Compact Object Binaries with Spinning Neutron Stars in Numerical Relativity

by

Nicholas A. Tacik

A thesis submitted in conformity with the requirements
for the degree of Doctor of Philosophy
Graduate Department of Astronomy & Astrophysics
University of Toronto

Abstract

Compact Object Binaries with Spinning Neutron Stars in Numerical Relativity

Nicholas A. Tacik

Doctor of Philosophy

Graduate Department of Astronomy & Astrophysics

University of Toronto

2016

The inspiral and merger of binary neutron stars (BNS) is one of the most promising potential sources of gravitational waves for ground-based detectors like Advanced LIGO. BNS mergers are also likely a source of counterpart electromagnetic radiation. It is important to perform simulations of BNS to better understand and model their gravitational wave emission as well as their electromagnetic emission. The parameter space of BNS binaries is quite large, and one aspect that has not been well studied in neutron star spin.

In this thesis, we focus on investigating spinning neutron stars in compact object binaries. Using the `SpEC` code, developed by the SXS collaboration, we begin by presenting a new code to create initial data for binary neutron stars with arbitrary spins. We introduce a novel method of measuring neutron star spin, and show that it is accurate and robust. We evolve several spinning binary configurations and show that their properties agree remarkably well with Post-Newtonian predictions. We also show that we are able to control the eccentricity of the binaries to $\sim 0.1\%$.

Thereafter, we proceed to extend our code to black hole–neutron star (BHNS) binaries. We create many data sets across the BHNS parameter space, varying neutron star spin magnitude, spin direction, compactness, and black hole mass, spin and spin direction. We are able to create initial data sets with neutron star spins near the mass-shedding limit, and nearly extremal black hole spins.

Finally, we investigate spurious gravitational radiation in binary black hole systems. We study its parameter space dependence, by introducing three diagnostics, investigating them as a function of black hole spin and black hole separation, and comparing two different methods of constructing initial data.

"Until now, we have only seen warped space-time when it is very calm - as though we had only seen the surface of the ocean on a very clam day, when it's quite glassy. We had never seen the ocean roiled in a storm, with crashing waves. All that changed on Sept. 14. The colliding black holes that produced these gravitational waves created a violent storm in the fabric of space and time."

Kip Thorne

Acknowledgements

There are many people I'd like to thank in helping me make this thesis.

First, thanks to my supervisor Harald Pfeiffer. Your patience, guidance and helpfulness and your willingness and ability to teach me is truly appreciated. Further thanks to my committee members, Ue-Li Pen and Marten van Kerkwijk for your guidance through the years.

Thanks to the many helpful people in the SXS collaboration who helped me learn how to use `SpEC`. Special thanks to Francois Foucart for answering so many of my questions.

Thanks to all the great people I've gotten to know as grad students in the department - Lisa Esteves, Stephanie Keating, Greg Paciga, Ilana Macdonald, Adam Atkinson, and so many more. Your friendship has always kept me going.

Thanks to CITA for providing me a great environment to work in, and for providing so many cups of coffee.

And finally, thanks to my parents, Brenda and Roman, for giving me so much encouragement over the years. I couldn't have done it without you.

Contents

1 Introduction **1**

1.1 Introduction 1

1.2 The two-body problem in General Relativity 5

1.3 The initial value problem in Numerical Relativity 10

1.4 Binary Neutron Star Systems 15

2 BNS with Arbitrary Spins in Numerical Relativity **22**

2.1 Chapter Summary 22

2.2 Introduction 23

2.3 Methodology 26

2.3.1 Formalism for Irrotational Binaries 26

2.3.2 Formalism for Spinning Binaries 32

2.3.3 Solving the Elliptic Equations 34

2.3.4 Construction of Quasi-Equilibrium Initial Data 35

2.3.5 Quasilocal Angular Momentum 37

2.4 Initial Data Results 40

2.4.1 Convergence of the Iterative Procedure 40

2.4.2 Convergence of the Solution 42

2.4.3 Convergence of the Quasilocal Spin 45

2.4.4 Quasilocal Spin 49

2.5 Evolution Results 52

2.5.1 Evolution Code . . . 53
2.5.2 Eccentricity Removal . . . 56
2.5.3 Aligned spin BNS Evolutions: NS Spin . . . 62
2.5.4 Precession . . . 65
2.5.5 Stellar Oscillations . . . 70
2.6 Conclusions . . . 77

Appendices **79**

3 Initial Data for BH-NS Binaries, with Rotating Stars **87**
3.1 Chapter Summary . . . 87
3.2 Introduction . . . 88
3.3 Initial Data Formalism . . . 90
3.4 Numerical Methods . . . 96
3.4.1 Domain Decomposition . . . 96
3.4.2 Diagnostics . . . 98
3.4.3 Iterative Procedure . . . 100
3.5 Results . . . 103
3.5.1 Initial Data Set Parameters . . . 103
3.5.2 Convergence of the Initial Data Solver . . . 107
3.5.3 Broader Exploration of Parameter Space . . . 113
3.6 Conclusion . . . 120

4 Spurious Radiation in BBH Simulations **123**
4.1 Chapter Summary . . . 123
4.2 Introduction . . . 124
4.3 Numerical Methods . . . 128
4.3.1 The Initial Value Problem . . . 128
4.3.2 Code . . . 130

4.3.3 Eccentricity Reduction 131
4.3.4 Simulations 132
4.4 Methodology 132
4.4.1 Pulse in the Gravitational Waveform 132
4.4.2 Uncertainty in E_J 135
4.4.3 Transient Behaviour in Black Hole Quantities 141
4.5 Results 149
4.5.1 Energy in Junk Radiation 149
4.5.2 Mass Increase 149
4.5.3 Spin Decrease 153
4.6 Conclusion 156

5 Conclusions & Future Work **159**
5.1 Conclusions 159

Bibliography **162**

List of Tables

1.1 The properties of known double neutron star systems. In particular we show the spin period of the neutron star, P, the orbital period of the binary, $P_{\rm orb}$, the eccentricity of the binary, e, the characteristic age of the neutron star, $\tau = \dot{P}/2P$, the time until binary coalescence, τ_c, and the expected final spin period of stars that will merge within a Hubble time, assuming a dipole spin-down model, P_f. 4

2.1 Parameters for the initial data sets used in test the initial data solver. . . 40

2.2 Detailed information about our three evolutions. 53

2.3 Eccentricity removal data for our three main runs. 59

3.1 Initial data set parameters for series of 36 BH-NS initial data sets. 106

List of Figures

1.1 Effect of gravitational waves on a ring of particles. 7

1.2 Illustration of the 3+1 decomposition. 11

1.3 Evolutionary scenarios of a typical high-mass binary. 16

1.4 Comparison of an equal mass BNS system and a non-equal mass BNS system. 21

2.1 Visualization of the BNS initial data domain decomposition. 34

2.2 Iterative convergence of the Euler constant. 41

2.3 Convergence of the Hamiltonian and Momentum constraints. 43

2.4 Convergence of the location of the stellar surface. 44

2.5 Convergence of ADM-energy and of the ADM-angular momentum magnitude. 46

2.6 Convergence of the quasilocal spin computation. 47

2.7 Stellar cross-section for a series of different spins. 48

2.8 Dimensionless angular momentum as a function of ωM_{odot}. 50

2.9 Dimensionless spin measured as measured on different coordinate spheres. 52

2.10 Binary separation as a function of time. 57

2.11 The derivative of the binary orbital frequency at different levels of eccentricity reduction. 58

2.12 Convergence of the derivative of the binary orbital frequency. 61

2.13 The spin measured on multiple coordinate spheres for the `S.4z` run. . . . 62

2.14 Neutron star spin during the two aligned-spin evolutions. 64
2.15 Accumulated orbital phase as a function of time for our aligned and anti-aligned runs. 66
2.16 The gravitational waveforms for our anti-aligned and aligned runs. 67
2.17 Spin-components of one of the neutron stars during the precessing simulation. 68
2.18 Components of the orbital frequency vectors during our evolutions. . . . 69
2.19 Gravitational waveforms of our precessing run. 71
2.20 The normalized maximum density in each of our runs. 72
2.21 The Fourier transforms of the central density in all three of our runs. . . 73
2.22 Fourier transforms of several different quantities in the `S.4z` run. 76
2..23 Density oscillations with corrected initial data. 82
2..24 Derivative of orbital angular frequency with corrected initial data. 83
2..25 Dimensionless spin during the evolution of corrected initial data. 84
2..26 χ vs. ω relation with corrected initial data. 85
2..27 Snapshot of a high-spin evolution using corrected initial data. 86

3.1 Visualization of the BH-NS domain decomposition. 97
3.2 Convergence of the Euler constant. 108
3.3 Convergence of black hole spin and mass. 109
3.4 Hamiltonian and momentum constraints of the `R14i60`$\Uparrow$ ID set 111
3.5 Neutron star surface and spin accuracy. 112
3.6 3d parameter space plot of BH-NS initial data sets. 113
3.7 $\chi_{\rm NS}$ as a function of $\omega_{\rm NS}$ for bh-ns binaries 114
3.8 Constraints for the $\chi_{\rm NS}$ sequence. 115
3.9 Hamiltonian and momentum constraints for the sequence in $\chi_{\rm BH}$. 117
3.10 Measured neutron star spin plotted as a function of black hole spin. . . . 118
3.11 Hamiltonian and momentum constraint for the q sequence. 119
3.12 $\chi_{\rm NS}$ as a function of mass ratio q. 120

4.1 A typical run illustrating junk radiation. 125
4.2 Junk radiation profiles for CF and SKS initial data. 134
4.3 The flux, $F(t)$, and the computation of E_J for CF and SKS initial data. . 136
4.4 E_J as a function of δt_C. 138
4.5 E_J as a function of 1_R/ex. 140
4.6 Normalized change in irreducible mass curves for CF and SKS data. . . . 142
4.7 Convergence of $M_{\rm irr})(t)$ for CF initial data. 143
4.8 Convergence of $M_{\rm irr})(t)$ for SKS initial data. 144
4.9 $\delta S(t)$ for CF and SKS initial data. 146
4.10 Convergence test of $\delta S(t)$ for CF initial data. 147
4.11 Convergence test of $\delta S(t)$ for SKS initial data. 148
4.12 E_J as a function of χ. 150
4.13 Log-log plot of E_J vs. D. 151
4.14 δM vs. D for CF initial data. 152
4.15 δM as a function of black hole spin χ. 154
4.16 δS vs. D for CF initial data. 155
4.17 Semi-log plot of δS as a function of χ for CF data. 157

Chapter 1

Introduction

1.1 Introduction

September 14th, 2015 marked the dawning of a new age in astronomy – the age of gravitational wave astronomy. The extraordinary detection of merging black holes by the Advanced Laser Interferometer Gravitational-Wave Observatory (LIGO) (Abbott et al. 2016b) left no doubt of this. After a second detection of merging black holes on December 26th, 2015, Abbott et al. (2016a), we are left anxiously waiting what will be in store for us next. The first detection was made just before Einstein's theory of general relativity (GR) (Einstein 1915) turned one hundred years old. Indeed, one of its most striking predictions is the existence of gravitational waves (GWs) - ripples in space-time that propagate at the speed of light. One of the ways these gravitational waves are generated is through the inspiral of compact object binaries. In these binaries, a neutron star (NS) or a black hole (BH), orbits with a NS/BH companion about their common centre of mass. Over time, through the emission of GW, the orbit shrinks and eventually the objects merge. Previously, these GW have never been directly detected, although their existence had been indirectly confirmed. Hulse and Taylor won the 1993 Nobel Prize for their observations of the Hulse-Taylor pulsar (Hulse & Taylor 1975a) - a binary pulsar system whose orbital decay was carefully measured and found to match

perfectly with the predictions of general relativity (Taylor & Weisberg 1982). Further observations have since strengthened these findings; see Berti et al. (2015) for a detailed review of current and future tests of GR.

Ground-based interferometric gravitational wave detectors are poised to make many more direct detections of GWs. With Advanced LIGO (Harry 2010; Aasi et al. 2015) already doing so, and Advanced Virgo (The Virgo Collaboration 2010; Acernese et al. 2015) and KAGRA (Somiya & the KAGRA Collaboration 2012) coming on soon, a wealth of results awaits. Advanced LIGO expects a realistic event rate ~ 20 binary black hole mergers per year at design sensitivity. Similarly, an event rate of ~ 10 mergers pear year is expected for BH-NS binaries and ~ 40 per year for binary neutron star mergers (Abadie et al. 2010). These detectors are sensitive to frequencies of $\sim 10\text{Hz} - 1\text{kHz}$, which we refer to as the LIGO band. Other detection methods, like pulsar timing arrays (Joshi 2013), are sensitive to very different frequency bands ($300\text{pHz} - 100\text{nHz}$).

These ground-based detectors use the technique of matched filtering (Owen & Sathyaprakash 1999) to make detections, in which the observed signal is matched against template waveforms to search for the astrophysical signal. The templates are generated either analytically, using, for example, Post-Newtonian (PN) theory (Blanchet 2006), a perturbative expansion of GR, or by using numerical relativity (NR)(see, e.g., Baumgarte & Shapiro (2010) for an overview), in which the Einstein Field Equations are solved numerically on supercomputers. PN waveforms are computationally inexpensive to produce but become increasingly inaccurate near merger, while NR waveforms are more accurate, but are costly to produce. Hybridization techniques (e.g., MacDonald et al. (2013)) "stitch" PN waveforms together with NR waveforms to get the best of both worlds.

The parameter space of numerical relativity simulations of non-eccentric black hole binaries is seven dimensional. Each black hole has a dimensionless spin vector $\vec{\chi} = \vec{S}/m^2$ with three components, where $\vec{S}$ is the angular momentum of the black hole and m is its mass, and their mass ratio $q \equiv m_1/m_2$, where m_1 is the mass of the larger hole, is

the 7th dimension. The total mass of the binary is scaled out of the numerical problem. Most compact object systems are expected to circularize (Peters & Mathews 1963; Peters 1964) before they enter LIGO's sensitivity band, so we do not regard orbital eccentricity as part of the parameter space. Spanning this parameter space is a difficult endeavor for numerical relativity collaborations and much of it remains uncovered (Mroue et al. 2013; Chu et al. 2015). Various dimensional reduction technqiues (Canizares et al. 2015) are used for Advanced LIGO template banks. Once matter is added to simulations, through neutron stars, the parameter space increases significantly. In addition to the seven parameters already present in the black hole binaries, the total mass of the system is now a parameter, as the maximum NS provides a natural mass scale. This can affect, for example, whether or not a hyper-massive neutron star is present after the merger of binary neutron stars or if direct collapse to a black hole occurs. In addition, the NS equation of state (EOS) becomes important to the system. Since the equation of state of dense nuclear matter is not currently known, constraining the NS EOS from gravitational wave observations is an important goal of advanced ground-based detectors. Additionally, once a neutron star is present, simulations can study additional physics such as neutrino transport, nuclear reactions, and magnetic fields (Baiotti & Rezzolla 2016). Such ingredients are crucial for understanding the electromagnetic emission likely to come from a binary neutron star (BNS) or black hole-neutron star (BHNS) merger.

NSNS binaries, unlike BHBH and BHNS binaries, have been observed and studied within our galaxy. The known binary neutron star population is summarized in table 1.1 (Postnov & Yungelson 2014). We report the spin periods, orbital periods, eccentricities, characteristic ages ($\tau = \dot{P}/2P$), time until merger, and the final spin periods of systems that will merge in a Hubble time. The system J0737-3039 is particluarly interesting, as one of its NSs will merge with a spin period of 22.4ms. This is comparable enough to the orbital timescale near merger, $P \sim 2ms$, to be relevant to GW data analysis. NSs in binaries are spinning, and thus it is important to do NR simulations

Table 1.1: The properties of known double neutron star systems. In particular we show the spin period of the neutron star, P, the orbital period of the binary, $P_{\rm orb}$, the eccentricity of the binary, e, the characteristic age of the neutron star, $\tau = \dot{P}/2P$, the time until binary coalescence, τ_c, and the expected final spin period of stars that will merge within a Hubble time, assuming a dipole spin-down model, P_f.

System	$P(ms)$	$P_{\rm orb}(d)$	e	$\log_{10}\tau(yr)$	$\log_{10}\tau_c(yr)$	$P_f(ms)$
J0737-3039	22.7	0.102	0.088	8.3	7.9	26.8
J0737-3039	2770	0.102	0.088	7.7	7.9	4453
J1518+4904	40.9	8.6	0.25	10.3	12.4	—
B1534+12	37.9	0.32	0.27	8.4	9.4	126
J1756-2251	28.5	0.32	0.18	8.6	10.2	—
J1811-1736	104.2	18.8	0.83	9.0	13.0	—
B1820-11	279.8	357.8	0.79	6.5	15.8	—
J1829+2456	41.0	1.18	0.14	10.1	10.8	—
J1906+0746	144.1	0.17	0.085	5.1	8.5	7224
B1913+16	59.0	0.3	0.62	8.0	8.5	120
B2127+11C	30.5	0.3	0.67	8.0	8.3	52.6

of spinning BNS binaries. For many years, spin was a largely unexamined dimension of the BNS parameter space, although there has been a significant interest lately. Note, however, that the spins would have to be innate, since neutron star viscosity is not nearly large enough for tidal torques to be effective in spinning the stars up (Bildsten & Cutler 1992).

This thesis is largely interested in spinning neutron stars in numerical relativity. The structure is as follows: In chapter 2, we discuss our work on initial data and evolutions of spinning BNS binaries using the SpEC code. In chapter 3, we discuss the extension of this initial data formalism to BHNS binaries with a spinning NS. In chapter 4, we shift focus

and discuss work we have done on understanding the nature of spurious gravitational radiation, commonly known as "junk radiation", in Binary Black Hole (BBH) systems. Finally, in chapter 5 we conclude and summarize the thesis and discuss future possibilities.

The remainder of this introduction is structured as follows: In Section 1.2 we review the 2-body problem in GR and discuss some basic Post-Newtonian theory. In section 1.3, we review the initial value problem in NR. Finally, in section 1.4 we discuss some basic astrophysical properties of binary neutron star systems and black hole–neutron star systems.

1.2 The two-body problem in General Relativity

In this section, we will review the basic scales and ideas that govern the two-body problem in general relativity. Specifically, when the bodies are of comparable mass, i.e., the mass ratio is not a perturbative parameter. Since the inspiral of two compact objects is driven by the emission of gravitational radiation, we being by reviewing gravitational waves (see, e.g., Carroll (2003) or Misner et al. (1973) for an introduction).

We consider a perturbation to a Minkowski background, so we write the full metric as

$$g_{\mu\nu} = \eta_{\mu\nu} + h_{\mu\nu} \qquad |h| \ll 1. \tag{1.1}$$

It is easily verified that the inverse metric is

$$g^{\mu\nu} = \eta^{\mu\nu} - h^{\mu\nu}, \tag{1.2}$$

where

$$h^{\mu\nu} = \eta^{\mu\rho}\eta^{\sigma\nu}h_{\rho\sigma}, \tag{1.3}$$

as the assumption that $|h|$ is small allows us to neglect terms that are higher than first order in $h_{\mu\nu}$. It is now helpful to consider the "trace-reversed" perturbation defined as,

$$\bar{h}_{\mu\nu} = h_{\mu\nu} - \frac{1}{2}h\eta_{\mu\nu}. \tag{1.4}$$

It is easily verified that $\bar{h} = -h$, hence the name "trace-reversed". Next, we exploit our coordinate freedom and work in the Lorentz gauge, defined by

$$\nabla_\mu \bar{h}^{\mu\nu} = 0. \tag{1.5}$$

In this gauge, the Einstein tensor is simply

$$G_{\mu\nu} = -\frac{1}{2}\nabla_\rho \nabla^\rho \bar{h}_{\mu\nu}, \tag{1.6}$$

and so in vacuum, the Einstein field equations are a wave equation

$$\Box \bar{h}_{\mu\nu} = 0. \tag{1.7}$$

Thus we see that gravitational waves propagate at the speed of light. Using further coordinate freedom, it is convenient to work in the transverse-traceless (TT) gauge, defined by

$$\bar{h}^{\mathrm{TT}}_{\mu 0} = 0, \qquad \bar{h}^{\mathrm{TT}} = 0. \tag{1.8}$$

The first condition guarantees that the non-zero components of $\bar{h}^{\mathrm{TT}}_{\mu\nu}$ are purely spatial, while the traceless condition guarantees that $\bar{h}^{\mathrm{TT}}_{\mu\nu} = h^{\mathrm{TT}}_{\mu\nu}$. For the rest of this section, we will work only in the TT gauge.

The Lorentz gauge condition, transverse condition, and traceless condition account for 8 of the 10 degrees of freedom in the gravitational field $h_{\mu\nu}$. The remaining two degrees of freedom correspond go the two polarization states of gravitational waves. These are known as the "+" and "×" polarizations, due to their particular distorting effects acting upon a ring of particles, as shown in Fig. 1.1. We can thus decompose a gravitational wave as

$$h^{\mathrm{TT}}_{ij} = h_+ e^+_{ij} + h_\times e^\times_{ij}. \tag{1.9}$$

When a matter source is present, the wave equation becomes

$$\nabla_\rho \nabla^\rho h_{\mu\nu} = -16\pi T_{\mu\nu}. \tag{1.10}$$

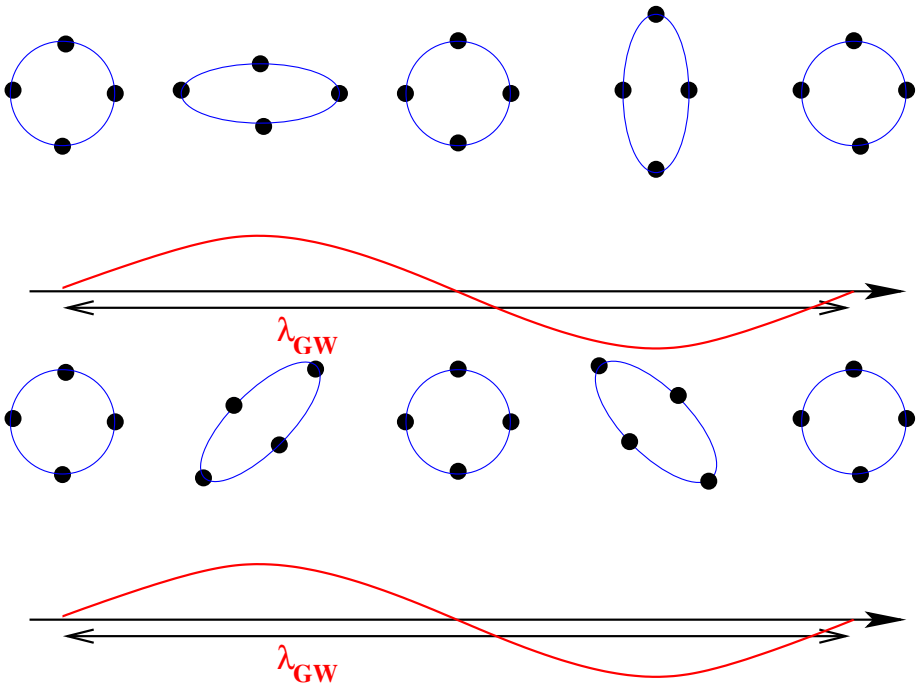

Figure 1.1: From Buonanno (2007). The top panel shows the effect of a + polarized gravitational wave passing through a ring of particles, in the direction perpendicular to the plane of the ring. The bottom panel shows the effect of a × polarized gravitational wave.

The solution to this equation can be written with the help of a Green's function,

$$h_{\mu\nu}(t, x^i) = 4 \int d^3y \frac{1}{|x-y|} T_{\mu\nu}(t_r, y^i), \tag{1.11}$$

where t_r is the "retarded" time, $t_r = t - |x - y|$. This integral can be evaluated in terms of the quadrupole tensor I^{ij} defined by

$$I^{ij}(t) = \int d^3x x^i x^j T^{00}(t, x^i), \tag{1.12}$$

and the reduced quadrupole moment

$$J_{ij} = I_{ij} - \frac{1}{3}\eta_{ij} I, \tag{1.13}$$

where $I = I^\mu_\mu$. To bring J_{ij} into the transverse-traceless gauge, we apply

$$J^{\mathrm{TT}}_{ij} = \left(P^k_i P^l_j - \frac{1}{2} P_{ij} P^{kl} \right) J_{kl}, \tag{1.14}$$

where

$$P_i^j = n_i n^j - n_i n^j \tag{1.15}$$

is a projection operator and n^i is a unit vector pointing in the wave's local direction of propagation.

The result is

$$h_{ij}(t, x^i) = \frac{2}{r}\ddot{J}_{ij}^{\mathrm{TT}}(t_r) \tag{1.16}$$

In other words, linear gravitational waves are sourced by an oscillating quadrupole. To study the energy content of these gravitational waves, note that the effective stress-energy tensor of this spacetime is

$$T_{\mu\nu} = \frac{1}{32\pi}\left\langle \partial_\mu h_{ij} \partial_\nu h^{ij} \right\rangle. \tag{1.17}$$

This can be integrated over a large sphere surrounding the source to find the energy output per unit time in gravitational waves,

$$L_{GW} = \frac{r^2}{16\pi}\oint \left\langle \dot{h}_\times^2 + \dot{h}_+^2 \right\rangle d\Omega \tag{1.18}$$

$$= \frac{1}{5}\left\langle \dddot{J}_{ij}^{\mathrm{TT}} \dddot{J}^{\mathrm{TTij}} \right\rangle. \tag{1.19}$$

Let us now consider a circular binary with total mass $M = M_1 + M_2$, reduced mass $\mu = \frac{M_1 M_2}{M_1 + M_2}$, separation R and orbital frequency ω. Direct computation of the quadrupole tensor gives the simple result

$$L_{GW} = \frac{32}{5}\mu^2 M^3 R^{-5}. \tag{1.20}$$

Using this, along with the Newtonian estimates $\omega = M^{1/2}R^{-3/2}$, $E = -\frac{\mu M}{2R}$, $dE/dt = -L_{\mathrm{GW}}$, allows us the compute the characteristic inspiral scales. The binary shrinks at a rate

$$\frac{dR}{dt} = \frac{dE/dt}{dE/dr} = \frac{-64}{5}M^2\mu R^{-3}. \tag{1.21}$$

Integrating this expression gives the time to coalescence where $R = 0$ as

$$\tau_c = \frac{5}{256}M^{-2}\mu^{-1}R^4. \tag{1.22}$$

As the binary separation decreases, the orbital frequency increases. By integrating

$$\frac{df_{\rm GW}}{dt} = \frac{1}{\pi}\frac{d\omega}{dt} = \frac{-3M^{1/2}}{2}R^{-5/2}\frac{dR}{dt}, \tag{1.23}$$

the frequency evolution is given by

$$f_{\rm GW}(t) = \frac{\omega}{\pi} = \frac{1}{8\pi}\left(\frac{5}{\mu M^{2/3}(\tau_c - t)}\right)^{3/8}. \tag{1.24}$$

The number of gravitational waves cycles, $N = \int f_{\rm GW} dt$, in a given frequency band $df_{\rm GW}$ is given by

$$\frac{dN}{d\log f_{\rm GW}} = \frac{5}{96\pi}\frac{1}{\left(\pi\mathcal{M}f_{\rm GW}\right)^{5/3}}, \tag{1.25}$$

where the quantity $\mathcal{M} = \mu^{3/5}M^{2/5}$ is called the "chirp mass". The explicit radiation pattern is given by

$$h_+ = \frac{4}{r}\mathcal{M}^{5/3}(2\omega)^{2/3}\cos(2\omega t + \phi)\left(\frac{1+\cos^2\theta}{2}\right), \tag{1.26}$$

$$h_\times = \frac{4}{r}\mathcal{M}^{5/3}(2\omega)^{2/3}\sin(2\omega t + \phi)\cos\theta, \tag{1.27}$$

where r is the distance to the source, θ is the angle between the observer and the axis normal to the orbital plane of the binary, and ϕ is the arbitrary phase of the binary. Detectors are sensitive to the strain h, rather than the energy flux, and therefore a factor of ξ improvement in sensitivity results in a factor of ξ^3 higher event rate (assuming a spatially uniformly distribution of sources).

These estimates were all made for a circular binary. If the binary has some eccentricity, e, then equation 1.18 is modified to (Peters & Mathews 1963)

$$L_{GW} = \frac{32}{5}\mu^2 M^3 R^{-5}\left(1 + \frac{73}{24}e^2 + \frac{37}{96}e^4\right)\left(1-e^2\right)^{-7/2} \tag{1.28}$$

However, eccentricity is radiated away as the inspiral proceeds. The classic reference Peters (1964) found that at leading Newtonian order

$$\left\langle\frac{de}{dt}\right\rangle = -\frac{304}{15}e\frac{\mu M^2}{R^4\left(1-e^2\right)^{5/2}}\left(1 + \frac{121}{304}e^2\right). \tag{1.29}$$

Thus even a highly eccentric binary will radiate away its eccentricity and circularize before merger, provided the compact objects started far enough away from each other. Most numerical relativity simulations consider only circularized binaries and use techniques to minimize any residual eccentricity (see, e.g., Pfeiffer et al. (2007); Buonanno et al. (2011a)).

The equations above in this section are valid only for a slowly-moving, weak-field system. As the system gets closer and closer to merger, these equations become increasingly inaccurate. Post-Newtonian theory (Blanchet 2006), by expanding to higher order, allows us to consider binaries with higher orbital frequencies. It is typically written as an expansion in the dimensionless parameter

$$x = \left(\frac{GM\omega}{c^3}\right)^{(2/3)}. \tag{1.30}$$

The evolution of the orbital phase, for example, can be written as

$$\phi = \frac{-x^{-5/2}}{32\nu}\left(1 + a_1 x + a_2 x^{3/2} + a_3 x^2 + a_4 x^{5/2} + a_5 x^3 + a_6 x^{7/2} + \mathcal{O}(1/c^8)\right) \tag{1.31}$$

where ν is the symmetric mass ratio, $\nu = \frac{m_1 m_2}{(m_1+m_2)^2}$, and each of the a_i are functions only of ν and $\log x$. This expression is said to be known to 3.5 Post-Newtonian order. Additional contributions come in at other PN orders, such as spin-orbit coupling at 1.5 PN order, spin-spin coupling at 2 PN order and tidal effects at 5 PN order. See Blanchet (2006) and references therein for an overview of PN results and methodology.

1.3 The initial value problem in Numerical Relativity

From the point of view of numerical relativity, it is natural to use a 3+1 decomposition of space-time. In this section, we will review this process (see, e.g., Baumgarte & Shapiro (2010) for a detailed overview). Note that we will use Greek letters to denote space-time indices (0,1,2,3), while Latin letters will represent spatial indices (1,2,3). The four-dimensional metric is denoted $g_{\mu\nu}$ and ∇ is the compatible connection. γ_{ij} and D_i are used for the metric and its compatible connection in a hypersurface Σ.

Given a globally hyperbolic spacetime $(\mathcal{M}, g_{\mu\nu})$, we foliate $\mathcal{M}$ by a family of non-intersecting spacelike hypersurfaces Σ_t, which are level sets of a scalar function t that can be understood as a global time function. This is illustrated in Fig. 1.2.

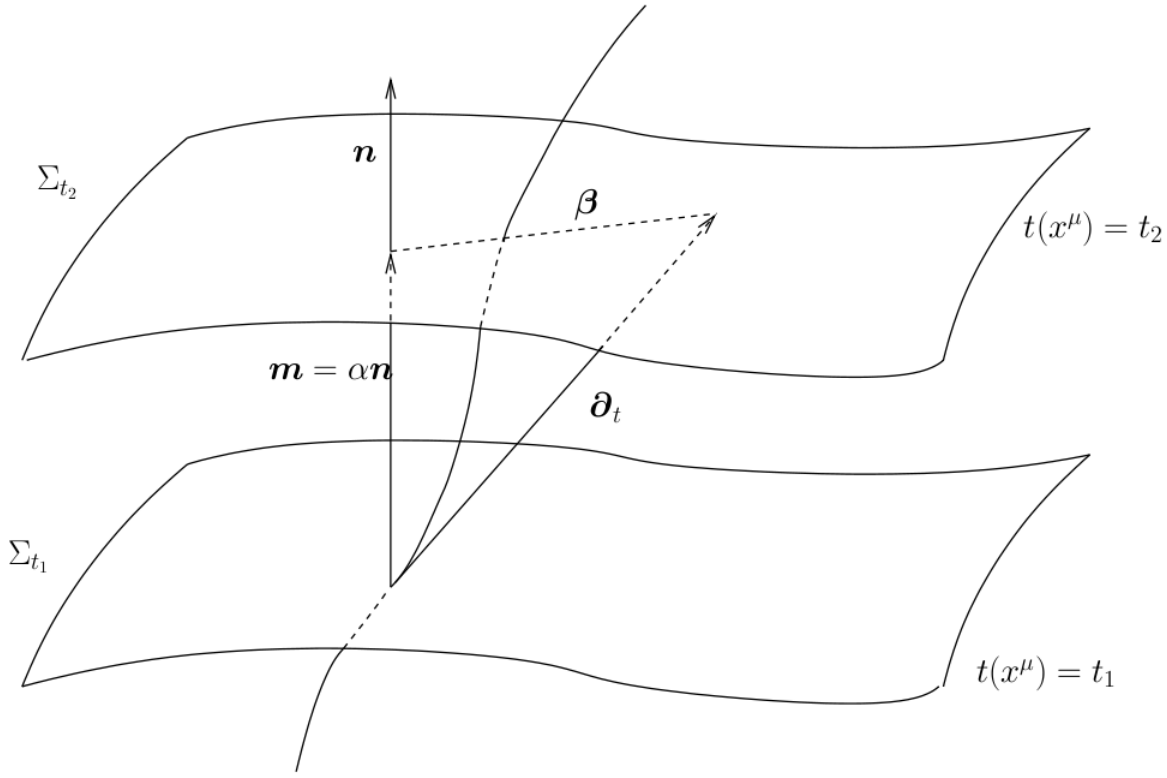

Figure 1.2: From Cardoso et al. (2014). An illustration of the foliation of spacetime by space-like hypersurfaces Σ_t, as well as illustrating the lapse, α, the shift, β^i, and the normal n^μ.

Each surface has a forward pointing unit normal

$$n^\mu = -g^{\mu\nu}\nabla_\nu t \left(g^{\mu\nu}\nabla_\mu t \nabla_\nu t\right)^{-1/2}, \tag{1.32}$$

induced metric

$$\gamma_{\mu\nu} = g_{\mu\nu} + n_\mu n_\nu, \tag{1.33}$$

and compatible derivative operator D. The induced metric measures curvature inside each hypersurface, while the extrinsic curvature $K_{\mu\nu}$ measures how the hypersurface is

curved inside the space-time manifold $\mathcal{M}$. It is defined by

$$K_{\mu\nu} = -\frac{1}{2}\mathcal{L}_n g_{\mu\nu}, \tag{1.34}$$

where $\mathcal{L}_n$ is the Lie derivative along the direction of the vector field n^μ. The space-time metric is written as

$$ds^2 = -\alpha^2 dt^2 + \gamma_{ij}\left(dx^i + \beta^i dt\right)\left(dx^j + \beta^j dt\right). \tag{1.35}$$

Here α is known as the lapse function - it measures the proper time between neighbouring hypersurfaces. β^i is known as the shift - it measures the proper distance within a spatial hypersurface. The lapse and shift are both arbitrary - their choice amounts to a choice of coordinates.

Similar to how Maxwell's equations can be written as a set of constraint equations that do not contain any time derivatives,

$$D_i E^i - 4\pi\rho = 0, \tag{1.36}$$

$$D_i B^i = 0, \tag{1.37}$$

and evolution equations,

$$\partial_t E_i = \epsilon_{ijk} D^j B^k - 4\pi j_i \tag{1.38}$$

$$\partial_t B_i = -\epsilon_{ijk} D^j E^k, \tag{1.39}$$

(where E^i is the electric field, B^i is the magnetic field, ρ is the charge density, j^i is the current density, and ϵ_{ijk} is the Levi-Civitia symbol, and the equations are written in Gaussian units), the same is true of Einstein's equations, $R_{\mu\nu} - \frac{1}{2}R g_{\mu\nu} = 8\pi T_{\mu\nu}$. The famous Hamiltonian and momentum constraints, obtained by projections of the Einstein equations, are

$$R + K^2 - K_{ij}K^{ij} = 16\pi\rho \tag{1.40}$$

and,

$$D_j K^j_i - D_i K = 8\pi S_i, \tag{1.41}$$

where ρ is the energy density measured by a normal observer, $\rho = n_i n_j T^{ij}$, and S_i is the momentum density measured by a normal observer $S_i = -\gamma_i^j n^k T_{jk}$. The general task of constructing initial data is to find $(\Sigma, g_{\mu\nu}, K_{\mu\nu})$ that satisfy the constraint equations and represent well the physical situation at hand (e.g., the inspiral of a compact object binary). The evolution equations are

$$\partial_t \gamma_{ij} = -2\alpha K_{ij} + D_i \beta_j + D_j \beta_i \tag{1.42}$$

and

$$\begin{aligned} \partial_t K_{ij} = &- D_i D_j \alpha + \alpha \left(R_{ij} - 2K_{ik} K^k_j + K K_{ij} \right) \\ &- 8\pi\alpha \left(S_{ij} - \frac{1}{2}\gamma_{ij} \left(S - \rho \right) \right) + \beta^k D_k K_{ij} + K_{ik} D_j \beta^k + K_{kj} D_i \beta^k. \end{aligned} \tag{1.43}$$

where S_{ab} is the spatial stress, $S_{ab} = \gamma_a^c \gamma_b^d T_{cd}$, and S is its trace. Once constraint-satisfying initial data has been constructed, the evolution equations determine the geometric quantities at all future times. Analytically, the evolution equations preserve the constraints, although numerically this may not always be the case (Kidder et al. 2001; Scheel et al. 2002).

There are many sets of data $(g_{\mu\nu}, K_{\mu\nu})$ that will satisfy the constraint equations. The task remains, then, to choose this free data appropriately. To do so, one typically begins with a conformal decomposition of the metric,

$$\gamma_{ij} = \Psi^4 \tilde{\gamma}_{ij}. \tag{1.44}$$

Here, Ψ is called the conformal factor, and $\tilde{\gamma}_{ij}$ is called the conformal metric. Objects associated with the $\tilde{\gamma}_{ij}$ will be denoted with a tilde as well. Next we break up the extrinsic curvature into its trace and trace-free parts,

$$K_{ij} = A_{ij} + \frac{1}{3}\gamma_{ij} K. \tag{1.45}$$

The Hamiltonian and Momentum constraints become

$$\tilde{D}^2 \Psi - \frac{1}{8}\Psi \tilde{R} - \frac{1}{12}\Psi^5 K^2 + \frac{1}{8}\Psi^5 A_{ij} A^{ij} = -2\pi \Psi^5 \rho \tag{1.46}$$

and

$$D_j A^{ij} - \frac{2}{3} D^i K = 8\pi j^i, \tag{1.47}$$

respectively. We now proceed according to the extended conformal thin sandwich formalism. We define

$$\tilde{u}_{ij} = \partial_t \tilde{\gamma}_{ij}, \tag{1.48}$$

and we introduce the scalings

$$\tilde{j}^i = \Psi^{10} j^i, \tag{1.49}$$

$$\tilde{\rho} = \Psi^8 \rho \tag{1.50}$$

$$\tilde{A}^{ij} = \Psi^{10} A^{ij}. \tag{1.51}$$

The Hamiltonian and Momentum constraints constraints can now be viewed as equations for the shift and conformal factor

$$\tilde{D}^2 \Psi - \frac{1}{8} \Psi \tilde{R} - \frac{1}{12} \Psi^5 K^2 + \frac{1}{8} \Psi^{-7} \tilde{A}_{ij} \tilde{A}^{ij} = -2\pi \Psi^{-3} \tilde{\rho}, \tag{1.52}$$

$$\tilde{D}_j \left(\frac{1}{2\tilde{\alpha}} \left(\mathbb{L}\beta \right)^{ij} \right) - \tilde{D}_j \left(\frac{1}{2\tilde{\alpha}} \tilde{u}^{ij} \right) - \frac{2}{3} \Psi^6 \tilde{D}^i K = 8\pi \tilde{j}^i, \tag{1.53}$$

where

$$\tilde{\alpha} = \Psi^6 \alpha \tag{1.54}$$

is the conformal lapse and

$$\left(\tilde{\mathbb{L}}\beta \right)^{ij} = \Psi^4 \left(D^i \beta^j + D^j \beta^i - \frac{2}{3} \gamma^{ij} D_k \beta^k \right) \tag{1.55}$$

is the conformal longitudinal operator. The lapse is given by the evolution equation of K,

$$\tilde{D}^2 \left(\tilde{\alpha} \Psi^7 \right) - \left(\tilde{\alpha} \Psi^7 \right) \left[\frac{1}{8} \tilde{R} + \frac{5}{12} \Psi^4 K^2 + \frac{7}{8} \Psi^{-8} \tilde{A}_{ij} \tilde{A}^{ij} + 2\pi \Psi^{-2} \left(\tilde{E} + 2\tilde{S} \right) \right] = -\Psi^5 \left(\partial_t K - \beta^k D_k K \right). \tag{1.56}$$

The free data are $\tilde{\gamma}_{ij}, \tilde{u}_{ij}, K, \partial_t K$. In a coordinate system corotating with the binary, it is natural to choose $\tilde{u}_{ij} = 0, \partial_t K = 0$. Common choices are conformal flatness, $\tilde{\gamma}_{ij} = \delta_{ij}$ and maximal slicing $K = 0$. With appropriate boundary conditions, the system of equations can now be solved.

1.4 Binary Neutron Star Systems

To begin our discussion of the properties of binary neutron stars, we should first briefly review how these systems form. We follow the discussion outlined in Postnov & Yungelson (2014). The standard formation scenario is illustrated in figure 1.3, and goes as follows:

- We begin with two high mass OB main-sequence stars undergoing standard binary evolution. Eventually the more massive (primary) star exhausts its central hydrogen, and a helium core is left over.
- The primary star then rapidly expands, overflows its Roche lobe, and begins a period of mass transfer onto the secondary star. This period lasts until most of the primary's Hydrogen envelope has been transferred, leaving behind a naked helium core.
- The primary star eventually collapses as a core-collapse supernova, leaving behind a neutron star. It is likely that the explosion disrupts the binary, but let us assume that it survives. We then have a massive main sequence star in orbit with a neutron star.
- Eventually the secondary star evolves off the main sequence, expands, and overflows its Roche lobe. It will then begin accreting mass onto the primary. This accretion spins up the neutron star, thus "recycling" it. It also leads to strong x-ray emission.
- The secondary further expands and a common envelope stage ensues. Eventually the secondary explodes as a supernova, and becomes a neutron star.

- If the binary system is not disrupted, it can then become a binary that will eventually merge due to the continuous emission of gravitational waves.

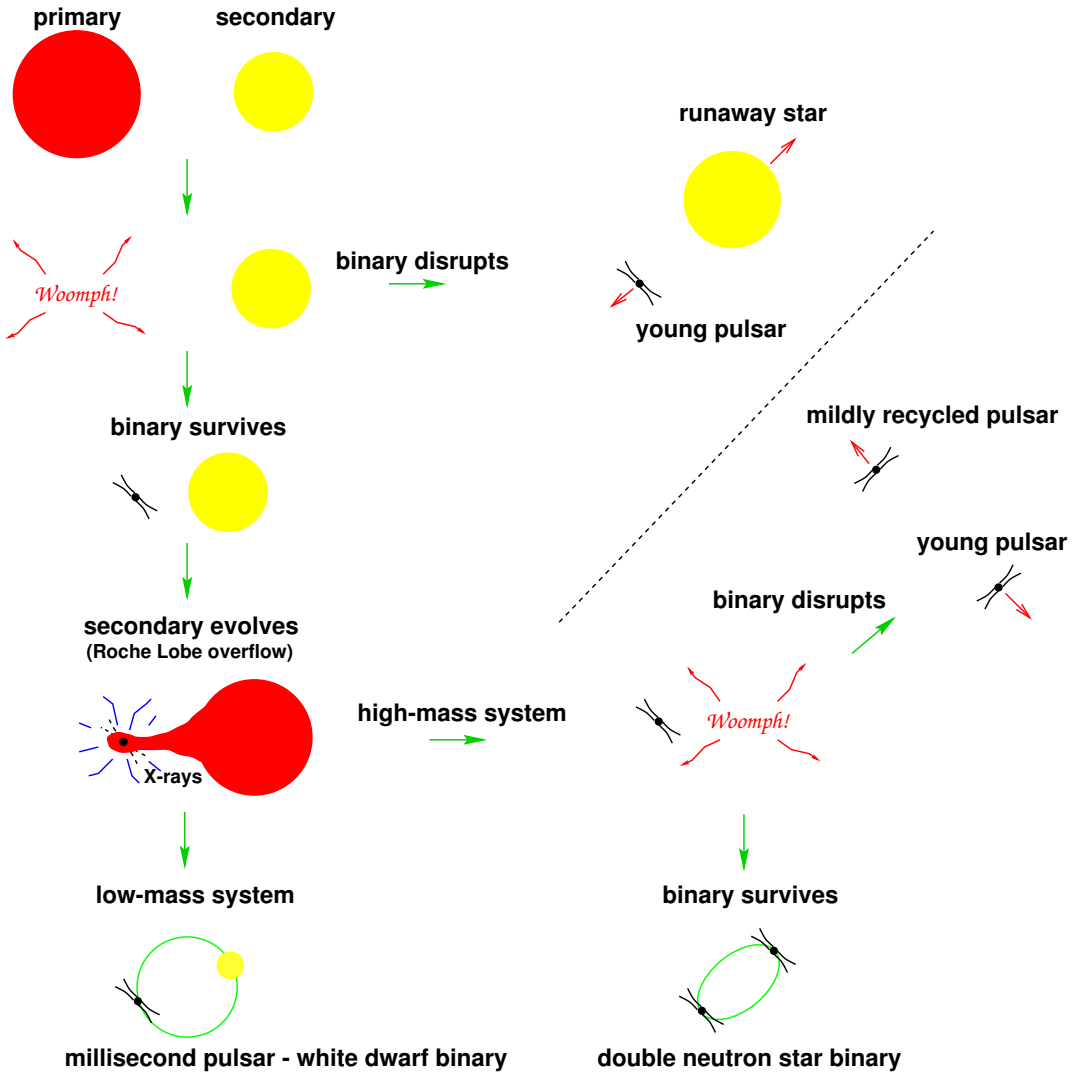

Figure 1.3: From Lorimer (2008). The possible evolutionary scenarios of a typical high mass binary are shown.

As discussed earlier, such systems are expected to be quasi-circular once they enter the LIGO band. There are, however, other ways of forming systems that are highly eccentric while in the LIGO band. For example, the dynamical capture in a close two-body encounter in a dense cluster environment, or a binary in a hierarchichal triple system whose eccentricity is enhanced by the Kozai mechanism (Kozai 1962; Thompson

2011; Seto 2013). Nonetheless, quasi-circular binaries are expected to constitute the large majority of gravitational wave sources.

The end state of a binary neutron star merger depends strongly on the properties of the two neutron stars. For systems with a combined mass less than the maximum mass allowed by the EOS, the final result would be a more massive neutron star. Otherwise, the final result will be a single Kerr black hole. Simulations have shown that these black holes will have a spin on the order of $\chi \simeq 0.7 - 0.8$ (Baiotti & Rezzolla 2016). The intermediate state is known as a hypermassive neutron star (HMNS). This is a NS whose mass is above the maximum mass allowed by the EOS, temporarily supported by differential rotation and thermal pressure. Over time, angular momentum is efficiently transported out of the system, and it collapses into a black hole. We can further subdivide these systems based on the timescale for callapse - prompt collapse or delayed collapse. In the prompt case, the pressure support is too low, and the system collapses on a $\sim$ freefall timescale. This is expected in systems with a large total mass ($\gtrsim 2.8 M_\odot$), although the details depend, of course, on the EOS (Hotokezaka et al. 2011). In the delayed collapse case, the collapse timescale depends on many factors. Angular momentum distribution by magnetic winding is an important factor - it operates on the Alfven timescale $\tau \sim R\sqrt{\rho}/B \simeq 10 - 100$ms, where ρ is the typical density of the hypermassive neutron star, R the radius, and B is the typical magnitude of the radial components of the magnetic field (Baumgarte et al. 2000). Transport driven by magneto-rotational instability is also important. It is of the order $\tau \sim 100$ms for $B \simeq 10^{15} G$. Cooling by neutrino or electromagnetic emission is also important, as it decreases thermal pressure, although it operates on a longer timescale, $\sim$ seconds. An accretion disk around the eventual BH, lying beyond the innermost stable circular orbit (ISCO), will form, with a mass of $\simeq 0.01 - 0.3 M_\odot$. The amount of material in the disk depends on the time to BH formation, as there is more time to distribute angular momentum ot the disk. HMNS systems emit gravitational waves at peak frequencies of approximately $2 - 4$kHz (see,

e.g., Hotokezaka et al. (2011)), unfortunately outside of the optimal frequency range of ground-based detectors.

The mass ratio of the system is another important factor. Figure 1.4 shows the post-merger remnant of an equal-mass system, and of a system with mass ratio $q \sim 1.38$ (Rezzolla et al. 2010). The equal mass system shows a "dumbell"-like structure, composed of two cores which, over time, turn into an ellipsoidal HMNS. The non-equal-mass case shows two asymmetric cores, which act like the smaller one orbiting the larger one. The stronger tidal forces in this case cause the outer layers of the smaller star to be stripped off and form an envelope around the HMNS. Higher disk mass correlates with higher deviations from $q = 1$, as well as with higher NS compactness.

The merger of two neutron stars is the site of the emission of a tremendous amount of electromagnetic energy (Eichler et al. 1989; Narayan et al. 1992; Nakar 2007; Patricelli et al. 2016). Their mergers are thought to be one of the most promising candidates to be the progenitors of short gamma ray bursts (SGRBs), although there is not yet definitive evidence for it (Nakar 2007). The engine of a rotating black hole, surrounded by a hot accretion torus and a collimiated magnetic field contains the necessary ingredients thought to be needed for a SGRB. Apart from this, another promising candidate for electromagnetic signature is the "kilonova" - emission powered by the radioactive decay of r-process elements formed in the merger, lasting on the time-scale of $\sim$ weeks. Multi-messenger astronomy (see Fan & Hendry (2015) for a review) seeks to combine information from gravitational waves, these electromagnetic events, and possible neutrino observations, to further elucidate the astrophysics of these mergers.

One of the most exciting prospects of the Advanced LIGO era is using gravitational wave observations to constrain the NS EOS. The EOS of dense nuclear matter is an open question of tremendous interest to nuclear physicists and astrophysicists alike. Tidal effects are parameterized by the tidal deformability paramter λ, which relates the induced

quadrupole field of one star, Q_{ij}, to the tidal field in which it is immersed, $\mathcal{E}_{ij}$:

$$Q_{ij} = -\lambda(m; \mathrm{EOS})\mathcal{E}_{ij}. \tag{1.57}$$

Or, likewise, by the second tidal Love number,

$$k_2 = \frac{3}{2}\frac{\lambda}{R^5}. \tag{1.58}$$

These enter the PN equations for binary phase at the very high 5PN order (i.e. proportional to $(v/c)^{10}$), but because of the large pre-factors, they are still very important in the late-stage inspiral dynamics. Much work has been done to estimate how well Advanced LIGO can measure these paramters (see Read et al. (2009); Hinderer et al. (2010); Damour et al. (2012); Lackey et al. (2012)). Del Pozzo et al. (2013) (further extended in Agathos et al. (2015)) used a Bayesian framework to show that λ could be constrained at the 10% level after a few tens of detections. There is also the question of more exotic NS matter. Chatziioannou et al. (2015) studied various possibilities and found, for example, that a detection with an SNR of ~ 20 could provide good evidence of the existence or non-existence of strange quark stars.

Numerical simulations of the mergers of binary neutron stars have been possible for at least fifteen years (Shibata & Uryū 2000). Since then, simulations have rapidly progressed, by adding more resolution (Hotokezaka et al. 2013), more orbits (Haas et al. 2016), radiative losses (Kiuchi et al. 2012; Neilsen et al. 2014; Palenzuela et al. 2015; Sekiguchi et al. 2015), studying different equations of state (Hotokezaka et al. 2011; Kiuchi et al. 2012; Neilsen et al. 2014), magnetic fields (Liu et al. 2008; Giacomazzo et al. 2011; Rezzolla et al. 2011; Anderson et al. 2008; Neilsen et al. 2014; Kiuchi et al. 2015a; Palenzuela et al. 2013; Palenzuela et al. 2013; Dionysopoulou et al. 2015), unequal mass ratios (Rezzolla et al. 2010; Kiuchi et al. 2010; Shibata et al. 2003; Dietrich et al. 2015a), ejecta (Wanajo et al. 2014; Sekiguchi et al. 2015; Radice et al. 2016) eccentric binaries (Gold et al. 2012), and spinning binaries Bernuzzi et al. (2014); Kastaun et al. (2013); Dietrich et al. (2015b); Tacik et al. (2015). Note that this is by no means an

exhaustive list of ongoing research – see Baiotti & Rezzolla (2016) for an up-to-date review. With the great increase in simulation technology, and the coincident start of the Advanced LIGO era, it is truly an exciting time for this field.

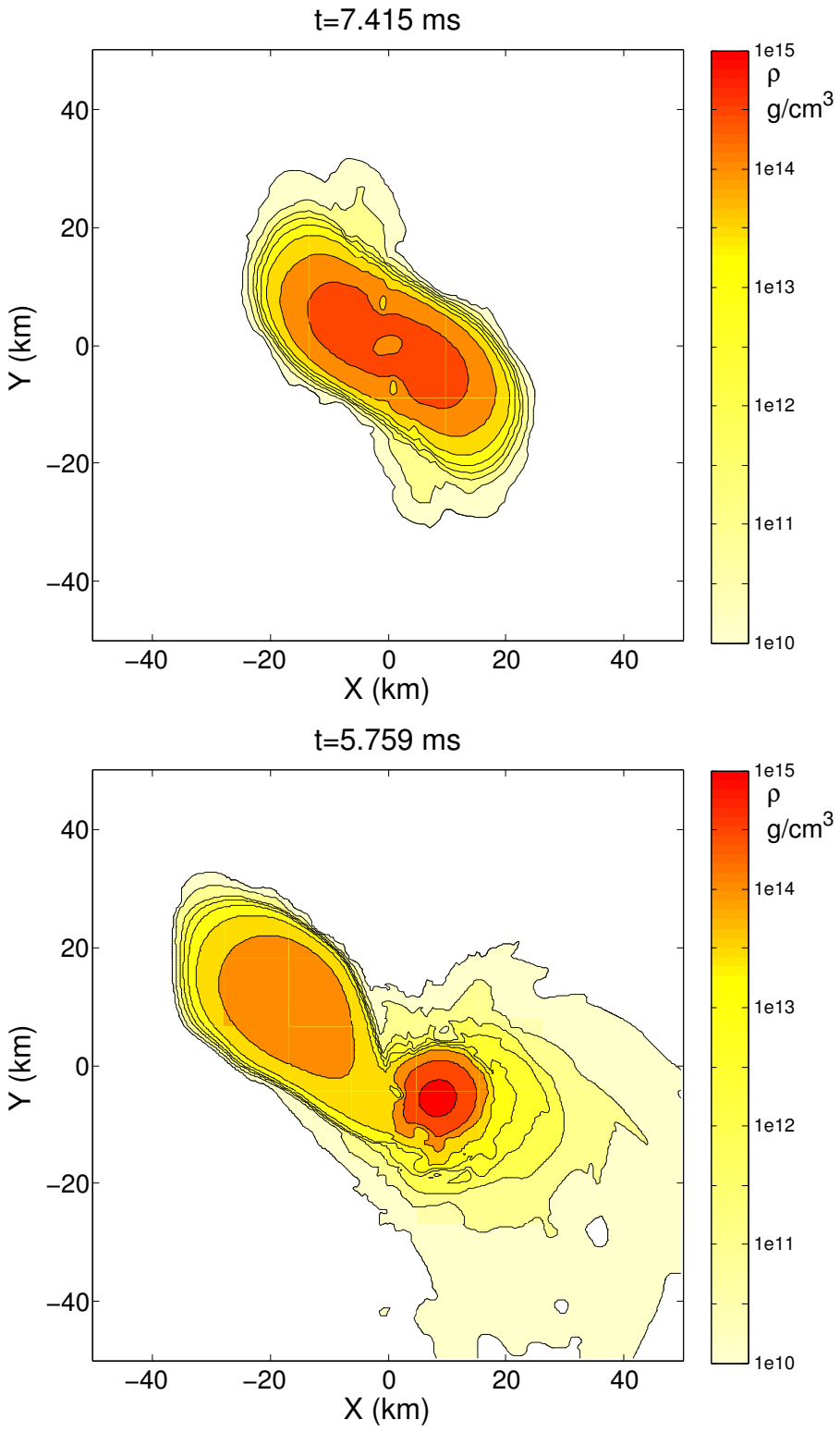

Figure 1.4: From Rezzolla et al. (2010). The top panel shows the iso-density contours of the HMNS from an equal mass system with baryon masses $M_1 = M_2 = 1.643 M_\odot$. The bottom panel shows the iso-density contours of the HMNS from a system with baryon masses $M_1 = 1.304 M_\odot$ and $M_2 = 1.805 M_\odot$.

Chapter 2

Binary Neutron Stars with Arbitrary Spins in Numerical Relativity

The material in this chapter is based on "Binary neutron stars with arbitrary spins in numerical relativity" by Nick Tacik, Francois Foucart, Harald P. Pfeiffer, Roland Haas, Serguei Ossokine, Jeff Kaplan, Curran Muhlberger, Matt D. Duez, Lawrence E. Kidder, Mark A. Scheel, Béla Szilágyi. Phys. Rev. D 92, 124012, December 2015. The material in the appendix of this chapter is based on an erratum to that article, submitted to Phys. Rev. D.

2.1 Chapter Summary

We present a code to construct initial data for binary neutron star systems in which the stars are rotating. Our code, based on a formalism developed by Tichy, allows for arbitrary rotation axes of the neutron stars and is able to achieve rotation rates near rotational breakup. We compute the neutron star angular momentum through quasilocal angular momentum integrals. When constructing irrotational binary neutron stars, we find a very small residual dimensionless spin of $\sim 2\times10^{-4}$. Evolutions of rotating neutron star binaries show that the magnitude of the stars' angular momentum is conserved, and

that the spin and orbit precession of the stars are well described by post-Newtonian approximation. We demonstrate that orbital eccentricity of the binary neutron stars can be controlled to $\sim 0.1\%$. The neutron stars show quasinormal mode oscillations at an amplitude which increases with the rotation rate of the stars.

2.2 Introduction

Several known binary neutron star (BNS) systems will merge within a Hubble time due to inspiral driven by gravitational radiation (Lorimer 2008), most notably the Hulse-Taylor pulsar (Hulse & Taylor 1975b). Therefore, binary neutron stars constitute one of the prime targets for upcoming gravitational wave detectors like Advanced LIGO (Harry 2010; Aasi et al. 2015) and Advanced Virgo (The Virgo Collaboration 2010; Acernese et al. 2015). The neutron stars in known binary pulsars have fairly long rotation periods (Lorimer 2008). The system J0737-3039 (Lyne et al. 2004) contains the fastest known spinning neutron star in a binary with a rotation period of 22.7ms. This system will merge within $\sim 10^8$ years through gravitational wave driven inspiral. Globular clusters contain a significant fraction of all known milli-second pulsars (Lorimer 2008), which through dynamic interactions, may form binaries (Lee et al. 2010; Benacquista & Downing 2013). Gravitational wave driven inspiral reduces (Peters & Mathews 1963; Peters 1964) the initially high eccentricity of dynamical capture binaries. Given the presence of milli-second pulsars in globular clusters, dynamically formed BNS may contain very rapidly spinning neutron stars with essentially arbitrary spin orientations. Presence of spin in BNS systems does influence the evolution of the binary. For instance, in order to avoid a loss in sensitivity in gravitational wave (GW) searches, one needs to account for the NS spin (Brown et al. 2012). Furthermore, early BNS simulations (Shibata & Uryū 2000) of irrotational and corotational BNS systems found that the spin of corotating BNS noticeably increased the size of accretion discs occurring during the merger of the two NS. The properties of accretion discs and unbound ejecta are intimately linked to electromag-

netic and neutrino emission from merging compact object binaries (Metzger & Berger 2012). Understanding the behavior of rotating BNS systems is therefore important to quantify the expected observational signatures from such systems. These considerations motivated a recent interest in the numerical modeling of rotating binary neutron star systems during their last orbits and coalescence. Baumgarte & Shapiro (2009), Tichy (2011), and East et al. (2012c) presented formalisms for constructing BNS initial data for spinning neutron stars. Tichy proceeded to construct rotating BNS initial data (Tichy 2012); and Bernuzzi et al. (2014) studies short inspirals and mergers of BNS with rotation rates consistent with known binary neutron stars (i.e. a dimensionless angular momentum of each star $\chi = S/M^2 \lesssim 0.05$), and rotation axes aligned with the orbital angular momentum. Very recently, Dietrich et al. (2015b) presented a comprehensive study of BNS, including a simulation of a precessing, merging BNS. East et al. (2015) investigate interactions of rotating neutron stars on highly eccentric orbit. Kastaun et al. (2013) determine the maximum spin of the black hole remnant formed by the merger of two aligned spin rotating neutron stars. Tsatsin & Marronetti (2013) present initial data and evolutions for non-spinning, spin-aligned and anti-aligned data sets. Tsokaros et al. (2015) presented initial data and quasi-equilibrium sequences of spin-aligned and anti-aligned binaries with a nuclear equation of state.

Previous studies differ in the type of initial data used: (Baumgarte & Shapiro 2009; Tichy 2011; 2012; Bernuzzi et al. 2014) construct and utilize constraint-satisfying initial data, which also incorporates quasi-equilibrium of the binary system. East et al. (2012c; 2015) construct constraint-satisfying data based on individual Tolman-Oppenheimer-Volkof (TOV) stars, without regard of preserving quasi-equilibrium in the resulting binary, but providing greatly enhanced flexibility in the type of configurations that can be studied, e.g. hyperbolic encounters. Kastaun et al. (2013); Tsatsin & Marronetti (2013), finally, only approximately satisfy the constraint equations. Previous studies also differ in the rigor with which the neutron star angular momentum is measured. Tichy

(2012) merely discusses the neutron stars based on a rotational velocity ω^i entering the initial data formalism (cf. our Eq. (2.49) below), whereas (Bernuzzi et al. 2014; Kastaun et al. 2013; East et al. 2015) estimate the initial neutron star spin either based on single star models or based on the differences in binary neutron star initial data sets with and without rotation, and thus neglecting the impact of interactions in the binary. All these studies measure the neutron star angular momentum in the initial data. Changes in the neutron star angular momentum that could happen during initial relaxation of the binary or during the subsequent evolution of the binary are not monitored.

In this chapter we study the construction of rotating binary neutron star initial data and the evolution through the inspiral phase. We implement the constant rotational velocity (CRV) formalism developed in Tichy (2012), and construct constraint satisfying BNS initial data sets with a wide variety of spin rates, as well as different spin *directions*. We apply quasilocal angular momentum techniques developed for black holes to our BNS initial data sets; the quasilocal spin indicates that we are able to construct BNS with dimensionless angular momentum exceeding 0.4. Evolving some of the constructed initial data sets through the inspiral phase, we demonstrate that we can control and reduce orbital eccentricity by an iterative adjustment of initial data parameters controlling orbital frequency and radial velocity of the stars, both for non-precessing (i.e. aligned-spin binaries) and precessing binaries. When monitoring the quasi-angular momentum of the neutron stars during the inspiral, we find that its magnitude is conserved, and the spin-direction precesses in a manner consistent with post-Newtonian predictions.

This chapter is organized as follows. Section 4.4 describes the initial data formalism and our numerical code to solve for rotating BNS initial data. In Sec. 2.4 we use this code to study a range of initial configurations, with a special emphasis on the behavior of the quasilocal spin diagnostic. We evolve rotating BNS in Sec. 2.5, including a discussion of eccentricity removal, the behavior of the quasilocal spin diagnostics, and a comparison of the precession dynamics to post-Newtonian theory. A discussion concludes the chapter

in Sec. 2.6. In this chapter, we work in units where $G = c = M_\odot = 1$.

2.3 Methodology

2.3.1 Formalism for Irrotational Binaries

To start, we will review a formalism commonly used for the construction of initial data for system of irrotational binary neutron stars. We will then discuss how to build upon this formalism to construct initial data for neutron stars with arbitrary spins.

We begin with the 3+1 decomposition of the space-time metric (see Gourgoulhon (2007) for a review),

$$ds^2 = -\alpha^2 dt^2 + \gamma_{ij}\left(dx^i + \beta^i dt\right)\left(dx^j + \beta^j dt\right). \tag{2.1}$$

Here, α is the lapse function, β^i is the shift vector and γ_{ij} is the 3-metric induced on a hypersurface $\Sigma(t)$ of constant coordinate time t. In this decomposition, the unit normal vector n^μ to $\Sigma(t)$ and the tangent vector t^μ to the coordinate line t are related by

$$t^\mu = \alpha n^\mu + \beta^\mu, \tag{2.2}$$

with $n_\mu = (-\alpha, 0, 0, 0)$ and $\beta^\mu = (0, \beta^i)$. The extrinsic curvature of $\Sigma(t)$ is the symmetric tensor defined as

$$K_{\mu\nu} = -\nabla_\nu n_\mu - n_\nu \gamma^\lambda{}_\mu \nabla_\lambda(\ln\alpha) = -\frac{1}{2}\mathcal{L}_n \gamma_{\mu\nu}, \tag{2.3}$$

where $\gamma_{\mu\nu} = g_{\mu\nu} + n_\mu n_\nu$ is the extension of the 3-metric γ_{ij} to the 4-dimensional spacetime, and $g_{\mu\nu}$ is the 4-metric of that spacetime. By construction, $K^{\mu\nu} n_\mu = 0$ and we can restrict $K^{\mu\nu}$ to the 3-dimensional tensor K^{ij} defined on $\Sigma \times \Sigma$. The extrinsic curvature K^{ij} is then divided into its trace K and trace-free part A^{ij}:

$$K^{ij} = A^{ij} + \frac{1}{3}\gamma^{ij} K. \tag{2.4}$$

We treat the matter as a perfect fluid with stress-energy tensor

$$T_{\mu\nu} = (\rho + P)\, u_\mu u_\nu + P g_{\mu\nu}, \tag{2.5}$$

where $\rho = \rho_0(1+\epsilon)$ is the energy density, ρ_0 the baryon density, ϵ the specific internal energy, P the pressure, and u_μ the fluid's 4-velocity. For the initial value problem, it is often convenient to consider the following projections of the stress tensor:

$$E = T^{\mu\nu} n_\mu n_\nu, \tag{2.6}$$

$$S = \gamma^{ij} \gamma_{i\mu} \gamma_{j\nu} T^{\mu\nu}, \tag{2.7}$$

$$J^i = -\gamma^i{}_\mu T^{\mu\nu} n_\nu. \tag{2.8}$$

We then further decompose the metric according to the conformal transformation

$$\gamma_{ij} = \Psi^4 \tilde{\gamma}_{ij}. \tag{2.9}$$

Other quantities have the following conformal transformations:

$$E = \Psi^{-6} \tilde{E}, \tag{2.10}$$

$$S = \Psi^{-6} \tilde{S}, \tag{2.11}$$

$$J^i = \Psi^{-6} \tilde{J}^i, \tag{2.12}$$

$$A^{ij} = \Psi^{-10} \tilde{A}^{ij}, \tag{2.13}$$

$$\alpha = \Psi^6 \tilde{\alpha}. \tag{2.14}$$

$\tilde{A}^{ij}$ is related to the shift and the time derivative of the conformal metric, $\tilde{u}_{ij} = \partial_t \tilde{\gamma}_{ij}$ by

$$\tilde{A}^{ij} = \frac{1}{2\tilde{\alpha}} \left[\left(\tilde{\mathbb{L}} \beta \right)^{ij} - \tilde{u}^{ij} \right], \tag{2.15}$$

where $\tilde{\mathbb{L}}$ is the conformal longitudinal operator whose action on a vector V^i is

$$\left(\tilde{\mathbb{L}} V \right)^{ij} = \tilde{\nabla}^i V^j + \tilde{\nabla}^j V^i - \frac{2}{3} \tilde{\gamma}^{ij} \tilde{\nabla}_k V^k, \tag{2.16}$$

and $\tilde{\nabla}$ is the covariant derivative defined with respect to the conformal 3-metric $\tilde{\gamma}_{ij}$.

In the 3+1 formalism, the Einstein equations are decomposed into a set of evolution equations for the metric variables as a function of t, and a set of constraint equations on each hypersurface $\Sigma(t)$. The initial data problem consists in providing quantities $g_{\mu\nu}(t_0)$ and $K_{\mu\nu}(t_0)$ which satisfy the constraints on $\Sigma(t_0)$ and represent initial conditions with the desired physical properties (e.g. masses and spins of the objects, initial orbital frequency, eccentricity, etc.).We solve the constraint equations using the Extended Conformal Thin Sandwich (XCTS) formalism (York 1999), in which the constraints take the form of five nonlinear coupled elliptic equations. The XCTS equations can be written as

$$2\tilde{\alpha}\left[\tilde{\nabla}_j\left(\frac{1}{2\tilde{\alpha}}\left(\tilde{L}\beta\right)^{ij}\right)-\tilde{\nabla}_j\left(\frac{1}{2\tilde{\alpha}}\tilde{u}^{ij}\right)-\frac{2}{3}\Psi^6\tilde{\nabla}^i K-8\pi\Psi^4\tilde{J}^i\right]=0, \tag{2.17}$$

$$\tilde{\nabla}^2\Psi-\frac{1}{8}\Psi\tilde{R}-\frac{1}{12}\Psi^5K^2+\frac{1}{8}\Psi^{-7}\tilde{A}_{ij}\tilde{A}^{ij}+2\pi\Psi^{-1}\tilde{E}=0, \tag{2.18}$$

$$\begin{aligned}\tilde{\nabla}^2\left(\tilde{\alpha}\Psi^7\right)-\left(\tilde{\alpha}\Psi^7\right)&\left[\frac{1}{8}\tilde{R}+\frac{5}{12}\Psi^4K^2+\frac{7}{8}\Psi^{-8}\tilde{A}_{ij}\tilde{A}^{ij}+2\pi\Psi^{-2}\left(\tilde{E}+2\tilde{S}\right)\right]\\&=-\Psi^5\left(\partial_tK-\beta^k\partial_kK\right).\end{aligned} \tag{2.19}$$

We solve these equations for the conformal factor Ψ, the densitized lapse $\tilde{\alpha}\Psi^7$ and the shift β^i. $\tilde{E}$, $\tilde{S}$ and $\tilde{J}^i$ determine the matter content of the slice. The variables $\tilde{\gamma}_{ij}$, $\tilde{u}_{ij}=\partial_t\tilde{\gamma}_{ij}$, K and ∂_tK are freely chosen.

If we work in a coordinate system corotating with the binary, $\tilde{u}_{ij}=0$ and $\partial_tK=0$ are natural choices for a quasi-equilibrium configuration. Following earlier work (Taniguchi et al. 2007; 2006; Foucart et al. 2008), we also choose to use maximal slicing, $K=0$, and a conformally flat metric, $\tilde{\gamma}_{ij}=\delta_{ij}$. Maximal slicing is a gauge choice that determines the location of the initial data hypersurface in the embedding space time. Conformal flatness is used for computational convenience; rotating black holes are known to be not

conformally flat (Garat & Price 2000), and so this simplifying assumption should be revisited in the future.

In addition to solving these equations for the metric variables, we must impose some restrictions on the matter. In particular, the stars should be in a state of approximate hydrostatic equilibrium in the comoving frame. This involves solving the Euler equation and the continuity equation. For an irrotational binary, the first integral of the Euler equation leads to the condition

$$h\alpha\frac{\gamma}{\gamma_0} = C, \tag{2.20}$$

where C is a constant, hereafter referred to as the Euler constant, the specific enthalpy h is defined as

$$h = 1 + \epsilon + \frac{P}{\rho_0}, \tag{2.21}$$

and we have introduced

$$\begin{aligned}
\gamma &= \gamma_n\gamma_0\left(1-\gamma_{ij}U^iU_0^j\right), && (2.22)\\
\gamma_0 &= \left(1-\gamma_{ij}U_0^iU_0^j\right)^{-1/2}, && (2.23)\\
\gamma_n &= \left(1-\gamma_{ij}U^iU^j\right)^{-1/2}, && (2.24)\\
U_0^i &= \frac{\beta^i}{\alpha}. && (2.25)
\end{aligned}$$

The 3-velocity U^i is defined by

$$\begin{aligned}
u^\mu &= \gamma_n(n^\mu + U^\mu), && (2.26)\\
U^\mu n_\mu &= 0. && (2.27)
\end{aligned}$$

The choice of U^i, which is unconstrained in this formalism, is an important component is determining the initial conditions in the neutron star. For irrotational binaries (non-spinning neutron stars), there exists a potential ϕ such that

$$U^i = \frac{\Psi^{-4}\tilde{\gamma}^{ij}}{h\gamma_n}\partial_j\phi. \tag{2.28}$$

The continuity equation can then be written as a second-order elliptic equation for ϕ:

$$\frac{\rho_0}{h}\nabla^\mu\nabla_\mu\phi + (\nabla^\mu\phi)\,\nabla_\mu\frac{\rho_0}{h} = 0. \tag{2.29}$$

Under the assumption of the existence of an approximate helicoidal Killing vector ξ (Teukolsky 1998; Shibata 1998), this equation becomes

$$\rho_0\left\{-\tilde{\gamma}^{ij}\partial_i\partial_j\phi + \frac{h\beta^i\Psi^4}{\alpha}\partial_i\gamma_n + hK\gamma_n\Psi^4 \quad + \left[\tilde{\gamma}^{ij}\tilde{\Gamma}^k_{ij} + \gamma^{ik}\partial_i\left(\ln\frac{h}{\alpha\Psi^2}\right)\right]\partial_k\phi\right\}$$
$$= \tilde{\gamma}^{ij}\partial_i\phi\partial_j\rho_0 - \frac{h\gamma_n\beta^i\Psi^4}{\alpha}\partial_i\rho_0. \tag{2.30}$$

Another simple choice for U^i is to enforce corotation of the star, i.e. $U^i = U^i_0$. This would be the case if neutron star binaries were tidally locked. However, viscous forces in neutron stars are expected to be insufficient to impose tidal locking (Bildsten & Cutler 1992), and the neutron star spins probably remain close to their value at large orbital separations.

Once we have obtained h from the metric and U^i, the other hydrodynamical variables can be recovered if we close the system by the choice of an equation of state for cold neutron star matter in β-equilibrium, $P = P(\rho_0)$ and $\epsilon = \epsilon(\rho_0)$. Throughout this work, we use a polytropic equation of state, $P = \kappa\rho_0^\Gamma$, with $\Gamma = 2$. The internal energy, $\epsilon\rho_0$, satisfies

$$\epsilon\rho_0 = \frac{P}{\Gamma - 1}. \tag{2.31}$$

The boundary conditions of our system of equations are quite simple. At the outer boundary of the computational domain (which we approximate as "infinity" and is in practice $10^{10}M_\odot$), we require the metric to be Minkowski in the inertial frame, and so in the corotating frame we have

$$\boldsymbol{\beta} = \boldsymbol{\Omega}_0 \times \boldsymbol{r} + \dot{a}_0\boldsymbol{r}, \tag{2.32}$$

$$\alpha = 1, \tag{2.33}$$

$$\Psi = 1, \tag{2.34}$$

with $\mathbf{\Omega}_0$ the initial orbital frequency of the binary and $\dot{a}_0 r = \dot{r}$ is the initial infall velocity of the binary (this quantity is negative for an inspiral). We choose $\mathbf{\Omega}_0 = (0, 0, \Omega_0)$, with Ω_0 and $\dot{a}_0$ as freely specifiable variables that determine the initial eccentricity of the binary.

At the surface of each star, the boundary condition can be easily inferred from the $\rho_0 = 0$ limit of equation (2.30):

$$\tilde{\gamma}^{ij}\partial_i\phi\partial_j\rho_0 = \frac{h\gamma_n\beta^i\Psi^4}{\alpha}\partial_i\rho_0. \tag{2.35}$$

Finally, we discuss how a first guess for the orbital angular velocity Ω_0 can be obtained for a non-spinning system. The force balance equation at the centre of the NS is

$$\nabla \ln\left(\frac{h\gamma_0}{\alpha\gamma}\right) = 0. \tag{2.36}$$

Neglecting any infall velocity, this condition guarantees that the binary is in a circular orbit. This is only an approximation as there is really some infall velocity, but this still leads to low eccentricity binaries with $e \sim 0.01$. Along with the assumption that the enthalpy is maximal at the centre of the NS,

$$\nabla \ln h = 0, \tag{2.37}$$

we can write this condition as

$$\nabla\left(\ln\frac{\gamma_0}{\alpha\gamma}\right) = 0, \tag{2.38}$$

or, by using the definitions of γ_0, and γ,

$$\nabla \ln\left(\alpha^2 - \gamma_{ij}\beta^i\beta^j\right) = -2\nabla \ln\gamma. \tag{2.39}$$

If we decompose β^i in its inertial component β_0^i and its comoving component according to

$$\boldsymbol{\beta} = \boldsymbol{\beta}_0 + \mathbf{\Omega}_0 \times \boldsymbol{r} + \dot{a}_0\boldsymbol{r}, \tag{2.40}$$

this can be written as a quadratic equation for the orbital angular velocity Ω_0 (neglecting the dependence of γ on the orbital angular velocity Ω_0). In practice, we solve for Ω_0 by projecting Eq. (2.39) along the line connecting the center of the two stars.[1]

The exact iterative procedure followed to solve in a consistent manner the constraint equations, the elliptic equations for ϕ, and the algebraic equations for h (including on-the-fly computation of Ω_0 and of the constant in the first integral of Euler equation) is detailed in Section 2.3.4.

Once a quasi-equilibrium solution has been obtained by this method, lower eccentricity systems can be generated by modifying Ω_0 and $\dot{a}_0$, following the methods developed by Pfeiffer et al. (2007).

2.3.2 Formalism for Spinning Binaries

We will now discuss how to alter the formalism discussed above to incorporate spinning BNS. Although several formalisms have been introduced in the past (Marronetti & Shapiro 2003; Baumgarte & Shapiro 2009), we will follow the work of Tichy (2011). A first obvious difference is that we can no longer write the velocity solely in terms of the gradient of a potential. Following Tichy, we break the velocity up into an irrotational part, and a new rotational part W:

$$U^i = \frac{\Psi^{-4}\tilde{\gamma}^{ij}}{h\gamma_n}\left(\partial_j\phi + W_j\right), \tag{2.41}$$

where it is natural, although not required, for W to be divergenceless.

Following the assumptions stated in Tichy (2011), the continuity equation becomes

$$\rho_0\left\{-\tilde{\gamma}^{ij}\partial_i\big(\partial_j\phi + W_j\big) + \frac{h\beta^i\Psi^4}{\alpha}\partial_i\gamma_n + hK\gamma_n\Psi^4 + \Big[\tilde{\gamma}^{ij}\tilde{\Gamma}^k_{ij} + \gamma^{ik}\partial_i\big(\ln\frac{h}{\alpha\Psi^2}\big)\Big]\big(\partial_k\phi + W_k\big)\right\}$$
$$= \tilde{\gamma}^{ij}\big(\partial_i\phi + W_i\big)\partial_j\rho_0 - \frac{h\gamma_n\beta^i\Psi^4}{\alpha}\partial_i\rho_0. \tag{2.42}$$

[1] Along the other directions, the specific enthalpy h is corrected so that force balance is enforced at the center of the star, according to the method described in Foucart et al. (2011)

Eq. 2.42 then is the same as in the irrotational case, cf. Eq. 2.30, under the replacement $\partial_i\phi \to \partial_i\phi + W_i$.

Taking the limit $\rho_0 \to 0$ in Eq. (2.42) yields the boundary condition at the surface of each star:

$$\tilde{\gamma}^{ij}\left(\partial_i\phi + W_i\right)\partial_j\rho_0 = \frac{h\gamma_n\beta^i\Psi^4}{\alpha}\partial_i\rho_0. \tag{2.43}$$

The solution of the Euler equation is no longer as simple as it was previously, in Eq. 2.20. As shown in Tichy (2011), the solution is now

$$h = \sqrt{L^2 - \left(\nabla_i\phi + W_i\right)\left(\nabla^i\phi + W^i\right)}, \tag{2.44}$$

where

$$L^2 = \frac{b + \sqrt{b^2 - 4\alpha^4\left(\left(\nabla_i\phi + W_i\right)W^i\right)^2}}{2\alpha^2}, \tag{2.45}$$

and

$$b = \left(\beta^i\nabla_i\phi + C\right)^2 + 2\alpha^2\left(\nabla_i\phi + w_i\right)w^i. \tag{2.46}$$

Finally, the method discussed previously of modifying the star's angular velocity is now no longer as simple. The equation is modified to

$$\nabla \ln\left(\alpha^2 - \gamma_{ij}\beta^i\beta^j\right) = -2\nabla\ln\Gamma, \tag{2.47}$$

where

$$\Gamma = \frac{\gamma_n\left(1 - \left(\beta^i + \frac{W^i\alpha}{h\gamma_n}\right)\frac{\nabla_i\phi}{\alpha h\gamma_n} - \frac{W_iW^i}{\alpha^2\gamma_n^2}\right)}{\sqrt{1 - \left(\frac{\beta^i}{\alpha} + \frac{W^i}{h\gamma_n}\right)\left(\frac{\beta_i}{\alpha} + \frac{W_i}{h\gamma_n}\right)}}. \tag{2.48}$$

Let us now discuss the choice of the spin term, W. This term is, in principle, freely chosen, and so we must choose it so as to best represent the physical situation at hand - namely a uniform rotation with constant angular velocity. As suggested by Tichy (2011) and Tichy (2012), a reasonable choice for W is

$$W^i = \epsilon^{ijk}\omega^j r^k, \tag{2.49}$$

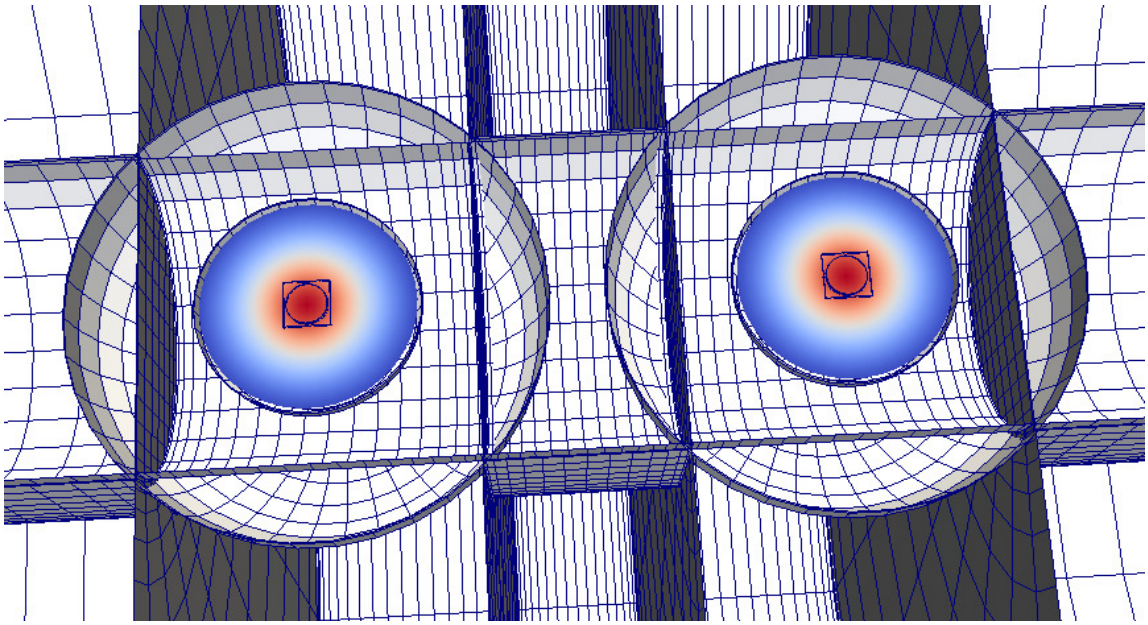

Figure 2.1: Visualization in the x-y plane of the domain decomposition used in our initial data solve. The colour map represents the density of the stars.

where r^k is the position vector centered at the star's centre, ω^j represents an angular velocity vector and $\epsilon^{ijk} = \{\pm 1, 0\}$. This leads to a vector field W^i with vanishing divergence in the conformal metric $\tilde{g}_{ij} = \delta_{ij}$. Alternatively, one might prefer a vector field V^i with vanishing divergence with respect to the physical metric $g_{ij} = \Psi^4 \delta_{ij}$. Owing to the conformal transformation properties of the divergence operator, V^i is given by

$$V^i = \Psi^{-6} W^i. \tag{2.50}$$

Here, we generally use W^i as we have found that it leads to initial data which is closer to being in equilibrium, as we will further discuss in section 2.5.5.

2.3.3 Solving the Elliptic Equations

In the previous sections, we have reduced the Einstein constraints, Eqs. (2.17)–(3.17), as well as the continuity equation (2.42) to elliptic equations. We solve these equations with the multi-domain pseudo-spectral elliptic solver developed in Pfeiffer et al. (2003), as modified in Foucart et al. (2008) for matter. The computational domain is subdivided

into individual subdomains as indicated in Fig. 2.1: The region near the center of each star is covered by a cube, overlapping the cube is a spherical shell which covers the outer layers of the star. The outer boundary of this shell is deformed to conform to the surface of the star. This places all surfaces at which the solution is not smooth at a subdomain-boundary, which preserves the exponential convergence of spectral methods. Another spherical shell surrounds each star. The inner shells representing the stars and their vicinity are embedded into a structure of five concentric cylinders with three rectangular blocks along the axis connecting the centers of the neutron stars, which overlap the inner spherical shells. The cylinders/blocks in turn are overlapped at large radius by one further spherical shell centered half-way between the two neutron stars. Using an inverse radial mapping, the outer radius of the outer sphere is placed at 10^{10}.

All variables are decomposed on sets of basis functions depending on the subdomain. The resolution of each domain (i.e., the number of collocation points used) is chosen at the start of the initial data solve, and then subsequently modified several times using an adaptive procedure described below. In this chapter, when discussing the total resolution of the domain, we use the notation

$$N^{1/3} = \left(\sum N_i\right)^{1/3}, \tag{2.51}$$

with N_i the number of collocation points in the ith subdomain. $N^{1/3}$ is thus the cube root of the total number of collocation points in all subdomains.

2.3.4 Construction of Quasi-Equilibrium Initial Data

Construction of initial data for rotating binary neutron stars begins with selecting the physical properties of the system: the equation of state of nuclear matter, the coordinate separation d between the neutron stars, the baryon masses M_1^b and M_2^b of the two stars, and their spin vectors $\boldsymbol{\omega}_{\rm rot,1}$ and $\boldsymbol{\omega}_{\rm rot,2}$. We also choose the orbital angular frequency Ω_0 and the initial inspiral rate $\dot{a}_0$.

We generally begin by setting Ω_0 to the value for the orbital frequency of a similar irrotational BNS (where Ω_0 is determined by the condition of quasi-circularity, Eq. (2.36)), and $\dot{a}_0 = 0$. These values are then adjusted following the eccentricity reduction method developed by Pfeiffer et al. (2007). Finally, we use a flat conformal metric, $\tilde{\gamma}_{ij} = \delta_{ij}$, and maximal slicing, $K = 0$.

Once all these quantities are fixed, we need to solve self-consistently Eqs. (2.17)–(3.17) for the Einstein-constraints, the continuity equation Eq. (2.42), while simultaneously satisfying conditions to enforce the desired masses of the stars. To do so, we follow an iterative procedure developed originally for black hole-neutron star binaries (Foucart et al. 2012).

First, we choose initial guesses for the conformal metric and hydrodynamical variables, using an analytical superposition of two isolated boosted neutron stars.

We then obtain constraint-satisfying initial conditions by applying the following iterative procedure, where n represents the iteration number:

1. Solve the nonlinear XCTS system for the set of metric variables $X = (\beta^i, \Psi, \alpha\Psi)$, assuming fixed values of the conformal source terms $(\tilde{E}, \tilde{S}, \tilde{J}^i)$. The new value X^{n+1} of the metric variables is obtained from their old value X^n and, following the relaxation scheme used in Foucart et al. (2008), the solution of the XCTS equations X^*, using
$$X^{n+1} = 0.3X^* + 0.7X^n. \tag{2.52}$$

2. Locate the surface of each star. Representing the surface in polar coordinates centered on each star as $R_s^n(\theta, \phi)$, we determine R_s^n to satisfy (Foucart et al. 2008) $h(R_{\rm s}^n(\theta, \phi), \theta, \phi) = 1$. To ensures that the grid-boundary R_b converges to the surface of the star, we occassionally modify the numerical grid such that $R_b(\theta, \phi) = R_s^n(\theta, \phi)$. Because this requires a re-initialization of the elliptic solver, the grid is only modified if the stellar surface has settled down, specifically, if
$$||R_{\rm s}^n - R_{\rm s}^{n-1}|| < 0.1||R_{\rm s}^n - R_b||. \tag{2.53}$$

Here $||\ .\ ||_2$ denotes the L2-norm over the surface.

3. For each neutron star, fix the constant in Euler's first integral so that the baryon mass of the neutron star matches the desired value. We compute the baryon mass as a function of the Euler constant C through

$$M^b_{\rm NS} = \int_{\rm NS} \rho_0 \Psi^6 \sqrt{\frac{1}{1-\gamma_{ij}U^iU^j}} dV, \tag{2.54}$$

and utilize the secant method to drive the mass to the desired value.

4. If desired, adjust the orbital frequency to ensure force-balance at the center of each star by solving Eq. (2.39). This step is skipped if the orbital frequency is fixed through iterative eccentricity removal, cf. Sec. 2.5.2.

5. Solve the elliptic equation for the velocity potential ϕ, and obtain the next guess for ϕ using the same relaxation method shown in Eq. 3.54.

6. Check whether all equations are satisfied to the desired accuracy. If yes, proceed. If no, return to Step 1.

7. Compute the truncation error of the current solution by examining the spectral expansion of the XCTS variables. If this truncation error is undesirably large (typically, if it is $> 10^{-9}$), then adjust the number of grid-points in the domain-decomposition and return to Step 1. The adjustment is based on the desired target truncation eror and the measured convergence rate of the solution, cf. Szilágyi (2014).

2.3.5 Quasilocal Angular Momentum

The goal of the present chapter is to construct spinning BNS initial data and to evolve it. Therefore, we need diagnostics to measure the NS spin, for which we use techniques

originally developed for black holes. It is common to discuss the spins of black holes in terms of their dimensionless spin χ,

$$\chi = \frac{S}{M^2}. \tag{2.55}$$

Here, S is the angular momentum of the black hole, and M is its Christodoulou mass (Christodoulou 1970),

$$M^2 = M_{\rm irr}^2 + \frac{S^2}{4M_{\rm irr}^2}. \tag{2.56}$$

The irreducible mass $M_{\rm irr}$ is defined based on the area of the hole's apparent horizon, $M_{\rm irr} = \sqrt{A/16\pi}$. The angular momentum is computed with a surface integral over the apparent horizon (Brown & York 1993; Ashtekar et al. 2001; Ashtekar & Krishnan 2003),

$$S = \frac{1}{8\pi} \oint_{\mathcal{H}} \phi^i s^j K_{ij} dA \tag{2.57}$$

where $\mathcal{H}$ is the black hole's apparent horizon, s^j is the outward-pointing unit-normal to $\mathcal{H}$ within the $t =$ const hypersurface, and ϕ^i is an azimuthal vector field tangent to $\mathcal{H}$. For spacetimes with axisymmetry, ϕ^i should be chosen as the rotational Killing vector. In spacetimes without an exact rotational symmetry (e.g. the spacetime of a binary black hole system), one substitutes an *approximate Killing vector*(AKV) (Cook & Whiting 2007; Lovelace et al. 2008). Lovelace et al. (2008) introduces a minimization principle to define ϕ^i, resulting in an Eigenvalue problem. The three eigenvectors with the lowest eigenvalues (i.e. smallest shear) are taken and used to compute the three components of the spin.

In this chapter, we explore the application of quasilocal spin measures to neutron stars. In the absence of apparent horizons $\mathcal{H}$, we need to choose different surface(s) to evaluate Eq. (2.57).

When constructing initial data, the stellar surface $\mathcal{S}$ is already determined, so one obvious choice is to integrate over the stellar surface $\mathcal{S}$. To estimate the ambiguity in quasilocal spin, we furthermore compute S by integrating over coordinate spheres with

radii ranging from just outside $\mathcal{S}$ to larger by about 70%. During the evolution, the stars change shape and may even loose mass in tidal tails. Because of these complications, the SpEC evolution code does not track the location of the stellar surface during the evolution, and we shall only monitor S on coordinate spheres.

It is useful to compute a dimensionless spin χ, for instance, for post-Newtonian comparisons. In the absence of a horizon, Eq. (2.56) is meaningless and we need a different choice for the mass-normalization. Instead, we normalize by each star's Arnowitt-Deser-Misner (ADM) mass, $M_{\rm ADM}$, i.e.

$$\chi \equiv \frac{S}{M_{\rm ADM}^2}. \tag{2.58}$$

The ADM mass is determined by computing the ADM mass of an equilibrium configuration of a single uniformly rotating polytrope in isolation with the same baryon mass and angular momentum as those measured in our binary systems.

The results of the quasilocal spin measures are described in section 2.4.4, which shows that this procedure is numerically robust.

Finally, let us discuss, from an order of magnitude perspective, how the star's dimensionless spin is related to its more commonly used physical properties. We start with the Newtonian relation $S = 2\pi I/P$ between angular momentum S, moment of inertia I, and rotational period P. Writing further $I = f\,R^2\,M$, with the dimensionless constant f depending on the stellar density profile, we have

$$\begin{aligned}\chi &\sim \frac{2\pi c}{G}\frac{f R^2}{P M} \\ &= 0.48 \left(\frac{f}{0.33}\right)\left(\frac{R}{12\text{km}}\right)^2\left(\frac{M}{1.4 M_\odot}\right)^{-1}\left(\frac{P}{1\text{ms}}\right)^{-1}.\end{aligned} \tag{2.59}$$

The factor c/G arises from the transition to geometric units.

This –quite simplistic– estimate shows that millisecond pulsars will have appreciable dimensionless spin χ. Centrifugal breakup of rapidly rotating neutron stars happens at a dimensionless spin in the range $0.65 - 0.70$ (Lo & Lin 2011), with only small dependence

Name	$M^b_{\rm NS}$	$\boldsymbol{\omega}$	D_0	$\Omega_0 \times 10^3$	$\dot{a}_0 \times 10^5$	$M_{\rm ADM}$	$\vec{\chi}$
`S.4z`	1.7745	$0.01525\hat{z}$	47.2	5.09594	-1.75	1.648	$0.3765\hat{z}$
`S-.05z`	1.7745	$-0.00273\hat{z}$	47.2	5.11769	-1.71	1.640	$-0.05018\hat{z}$
`S.4x`	1.7745	$0.01525\hat{x}$	47.2	5.10064	-2.36	1.648	$0.3714\hat{x}$

Table 2.1: Parameters for the initial data sets used in testing the initial data solver: $M^b_{\rm NS}$ and ω^i are baryon mass and rotational parameter for either neutron star (the same values are used); D_0, Ω_0 and $\dot{a}_0$ represent coordinate separation between the centers of the stars, the orbital frequency, and the radial expansion; $\vec{\chi}$ is the dimensionless spin vector computed from the initial data set. In each case we use a polytropic equation of state, $P = \kappa\rho_0^\Gamma$, with $\Gamma = 2$ and $\kappa = 123.6$.

on the equation of state and neutron star mass. Ansorg et al. (2003) studied in detail $\Gamma = 2$ polytropes, the equation of state we use here. They find a dimensionless spin at mass-shedding of $\chi = 0.57$.

2.4 Initial Data Results

In this section, we will demonstrate that our code can robustly construct contraint-satisfying initial data for BNS systems with arbitrary spins. As discussed in section 2.3.4, our code consists of a solver that runs for a number of iterations at constant resolution, and then the resolution is increased and this process restarts. We will therefore demonstrate that appropriate quantities converge with both the iterations of iterative scheme described above in Section 2.3.4 and with increasing resolution.

2.4.1 Convergence of the Iterative Procedure

At each step of the iterative procedure, the Euler constant of each star is modified to achieve a desired stellar baryon mass, based on the current matter distribution inside

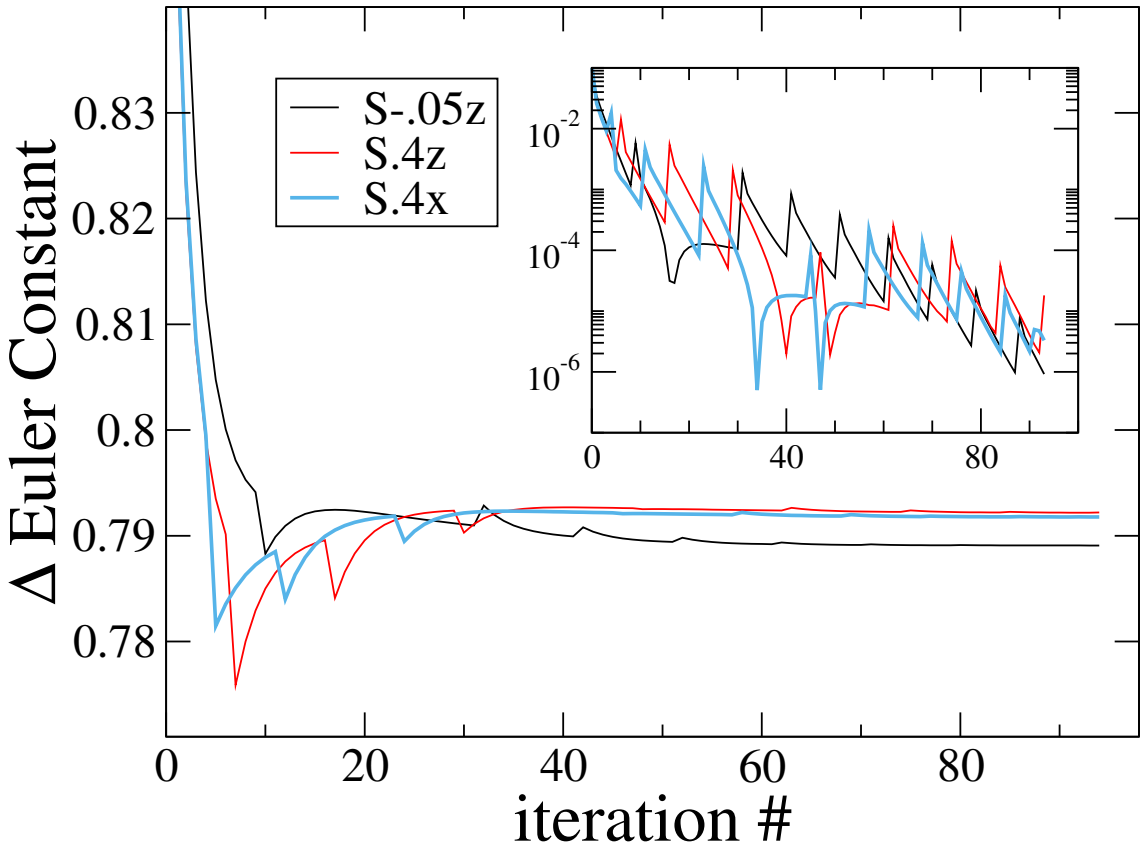

Figure 2.2: Convergence of the Euler constant during iteration at the lowest resolution R0. The inset shows the difference between values at subsequent iterations.

the star. We expect that the Euler constant converges during the iterations at a fixed resolution. Figure 2.2 shows the behavior of the Euler Constant during iterations at the lowest initial data resolution, R0. We show three runs of interest, one with large aligned spins (`S.4z`), one with large precessing spin (`S.4x`), and one with small anti-aligned spins (`S-.05z`). The properties of these configurations are shown in table 2.1. In all three cases we see agreement between neighboring iterations at the $10^{-5} - 10^{-6}$ level by the end of iterating at this resolution. At the highest resolutions, these differences are down to, typically, the $10^{-9} - 10^{-10}$ level. This can be compared to Fig. 3 of Gourgoulhon et al. (2001). Although not shown here, other free quantities converge similarly to the Euler constant.

2.4.2 Convergence of the Solution

Having established that our iterative procedure converges as intended, we now turn our attention to the convergence of the solution with resolution. To demonstrate it, we will look at the Hamiltonian and momentum constraints, and the differences between measured physical quantities - the ADM energy and ADM angular momentum, and the surface fitting coefficients of the stars. As our initial data representation is fully spectral, we expect that these quantities should converge exponentially with resolution. Note that when we discuss the value of a quantity at a certain resolution, we are referring to the value of that quantity after the final iterative step at that resolution.

Figure 2.3 shows the convergence of the Hamiltonian constraint and the Momentum constraint for our three runs of interest. These are computed during the last iterative solve at each resolution. The data plotted are computed as

$$H = ||\frac{R_\Psi}{8\Psi^5}||, \tag{2.60}$$

$$M = ||\frac{R_\beta}{2\alpha\Psi^4}||. \tag{2.61}$$

Here R_Ψ and R_β denote the residuals of Eqs. (2.18) and (2.17), respectively, and $||\,.\,||$ represents the root-mean-square value over grid-points of the entire computational grid. This plot demonstrates that our initial data solver converges exponentially with resolution, even for very high spins, which gives confidence that we are indeed correctly solving the Einstein Field Equations.

The surface of the star is represented by a spherical harmonic expansion:

$$R_s(\theta,\phi) = \sum_{l,m}^{l_{\max},m_{\max}} c_{lm} Y_{lm}(\theta,\phi), \tag{2.62}$$

where $l_{\max} = m_{\max} = 11$, unless stated otherwise. The stellar surface is located by finding a constant specific enthalpy surface, cf. Sec. 2.3.4, and the spherical subdomains

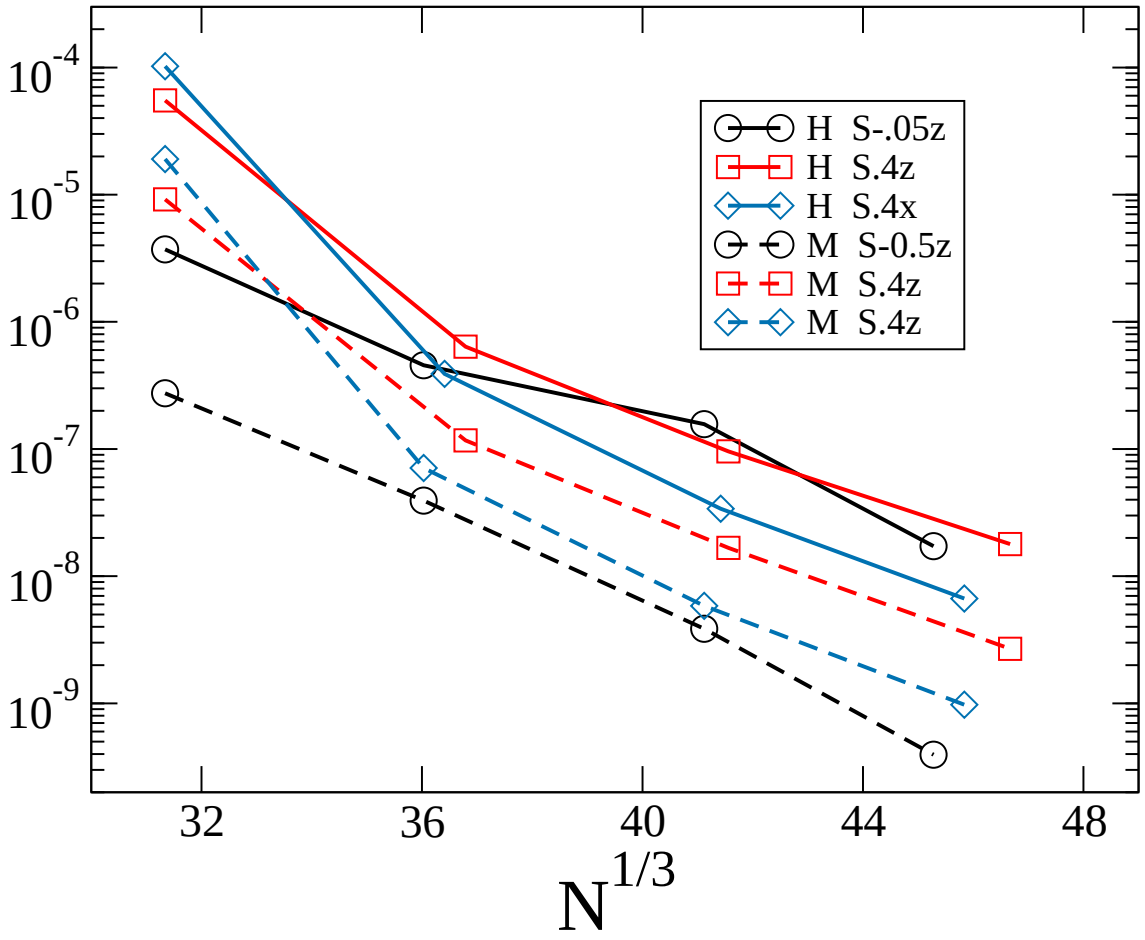

Figure 2.3: Hamiltonian and Momentum constraints as a function of resolution N. We see exponential convergence in all cases.

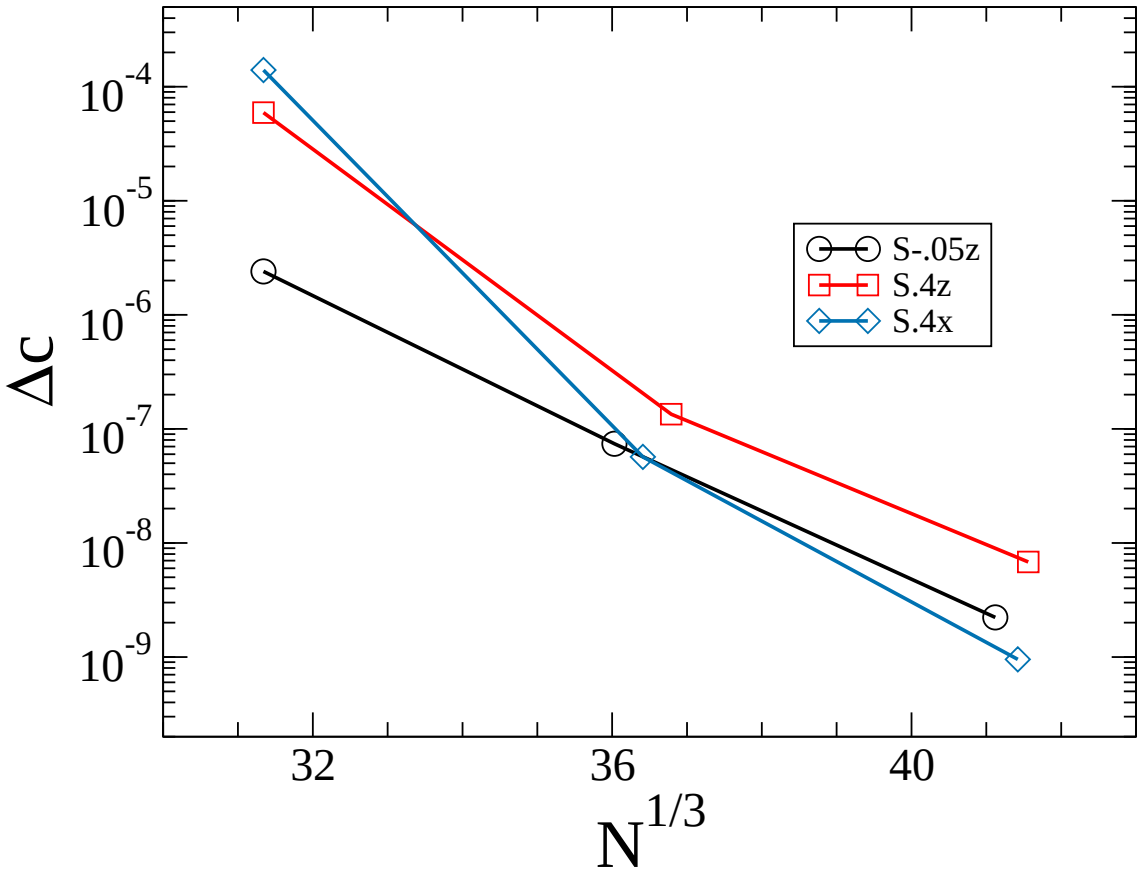

Figure 2.4: Convergence of the location of the stellar surface. Plotted is Δc as defined in Eq.(2.63), for three representative configurations.

that cover the star are deformed to conform to $R_s(\theta, \phi)$. To establish convergence of the position of the stellar surface we introduce the quantity

$$\Delta c(i) = \frac{1}{l(l+1)} \sqrt{\sum_{l,m}^{l_{\max}, m_{\max}} (c_{lm}(i) - c_{lm}(N))^2}. \tag{2.63}$$

Here i refers to the i^{th} resolution in the initial data, and N refers to the final resolution. Figure 2.4 plots $\Delta c(i)$ vs. resolution. The surface location converges exponentially to better than 10^{-8}.

Finally, we assess the overall convergence of the solution through the global quantities E_{ADM} and $|J^i_{\text{ADM}}|$. The surface integrals at infinity in these two quantities are recast using

Gauss' law (cf. (Foucart et al. 2008)):

$$\begin{aligned} E_{\rm ADM} &= -\frac{1}{2\pi}\oint_{S_\infty} \delta^i_j \partial_i \Psi \, dS_j \\ &= -\frac{1}{2\pi}\oint_{S} \delta^i_j \partial_i \Psi \, dS^j + \frac{1}{2\pi}\int_{\mathcal{V}} \delta^{ij}\partial_i\partial_j \Psi \, dV, \end{aligned} \tag{2.64}$$

and

$$\begin{aligned} J^z_{\rm ADM} &= \frac{1}{8\pi}\oint_{S_\infty} \left(xK^{yj} - yK^{xj}\right) dS_j \\ &= \frac{1}{8\pi}\oint_{S} \left(xK_{yi} - yK_{xi}\right) \delta^{ij}\Psi^2 \, dS_j. \end{aligned} \tag{2.65}$$

Here $\mathcal{V}$ is the volume outside S, and the integrals are evaluated in the flat conformal space. To obtain the other components of $J^i_{\rm ADM}$, cyclically permute the indices x,y,z. We define the quantities ΔE and ΔJ as the absolute fractional difference in these quantities between the current resolution and the next highest resolution. These are plotted in figure 2.5. In general, we find agreement at the $10^{-7} - 10^{-8}$ level by the final resolution.

2.4.3 Convergence of the Quasilocal Spin

We now turn to the angular momentum of the neutron stars, as measured with quasilocal angular momentum integrals on the stellar surface. We will discuss dimensionless spins χ, which depend on two distinct numerical resolutions: First, the resolution of the 3-dimensional grid used for solving the initial value equations. This resolution is specified in terms of N, the total number of grid-points. Second, the resolution used when solving the eigenvalue problem for approximate Killing vectors on the 2-dimensional surface, as given by L, the expansion order in spherical harmonics of the surface-parameterization $r_S(\theta,\phi) = \sum_{l=0}^{L}\sum_m r_{lm}Y^{lm}(\theta,\phi)$.

Throughout this chapter, we use $L = 11$. The top panel of Fig. 2.6 shows convergence of χ with grid-resolution N, at fixed $L = 11$. We find near exponential convergence.

The influence of our choice $L = 11$ is examined in the lower panel by computing the quasilocal spin at lower resolution $L = 8$ and at higher resolution $L = 14$. Changing

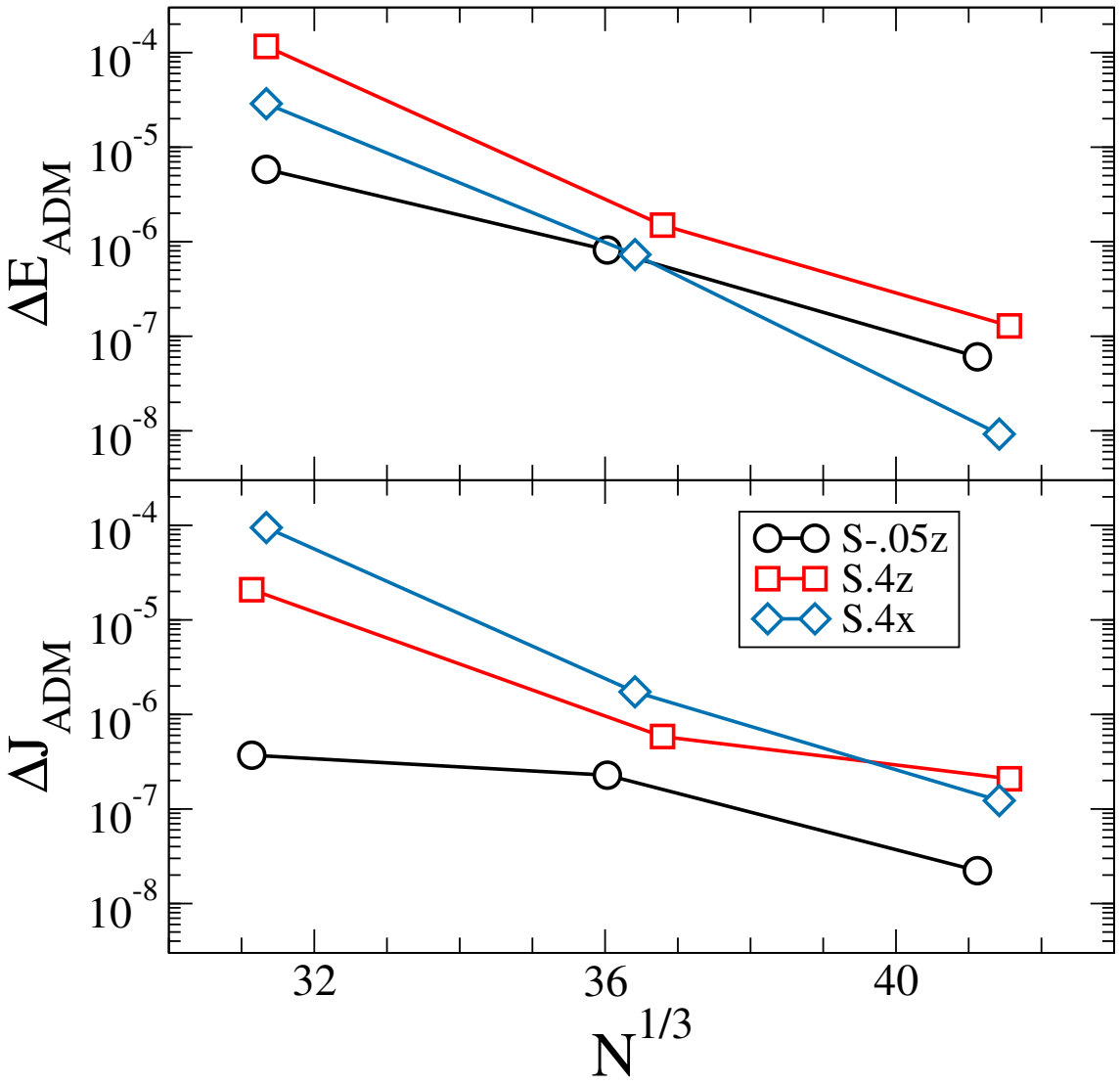

Figure 2.5: Convergence of ADM-energy and the magnitude of the ADM-angular momentum. Shown are the fractional differences between neighboring resolutions, as a function of the lower resolution.

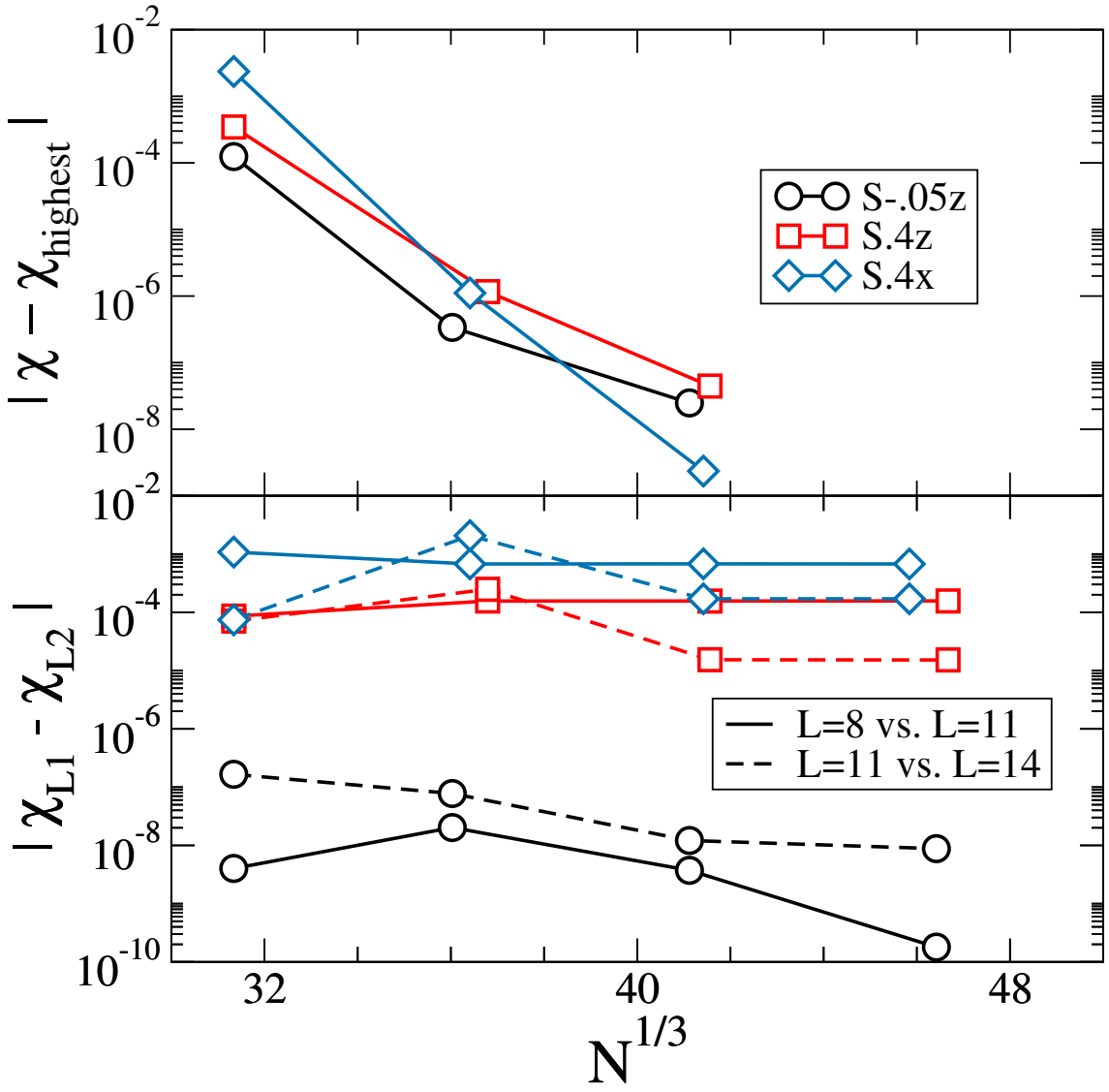

Figure 2.6: Convergence of the quasilocal spin computation. **Top panel:** difference of spin computed at resolution N with the spin computed at the highest resolution. **Bottom panel:** Difference between spins computed at different resolution L of the spin-computation. For `S-.5z`, we achieve an accuracy of $\sim 10^{-7}$, whereas for `S.4z` and `S.4x`, the accuracy is $\sim 10^{-4}$ due to finite L.

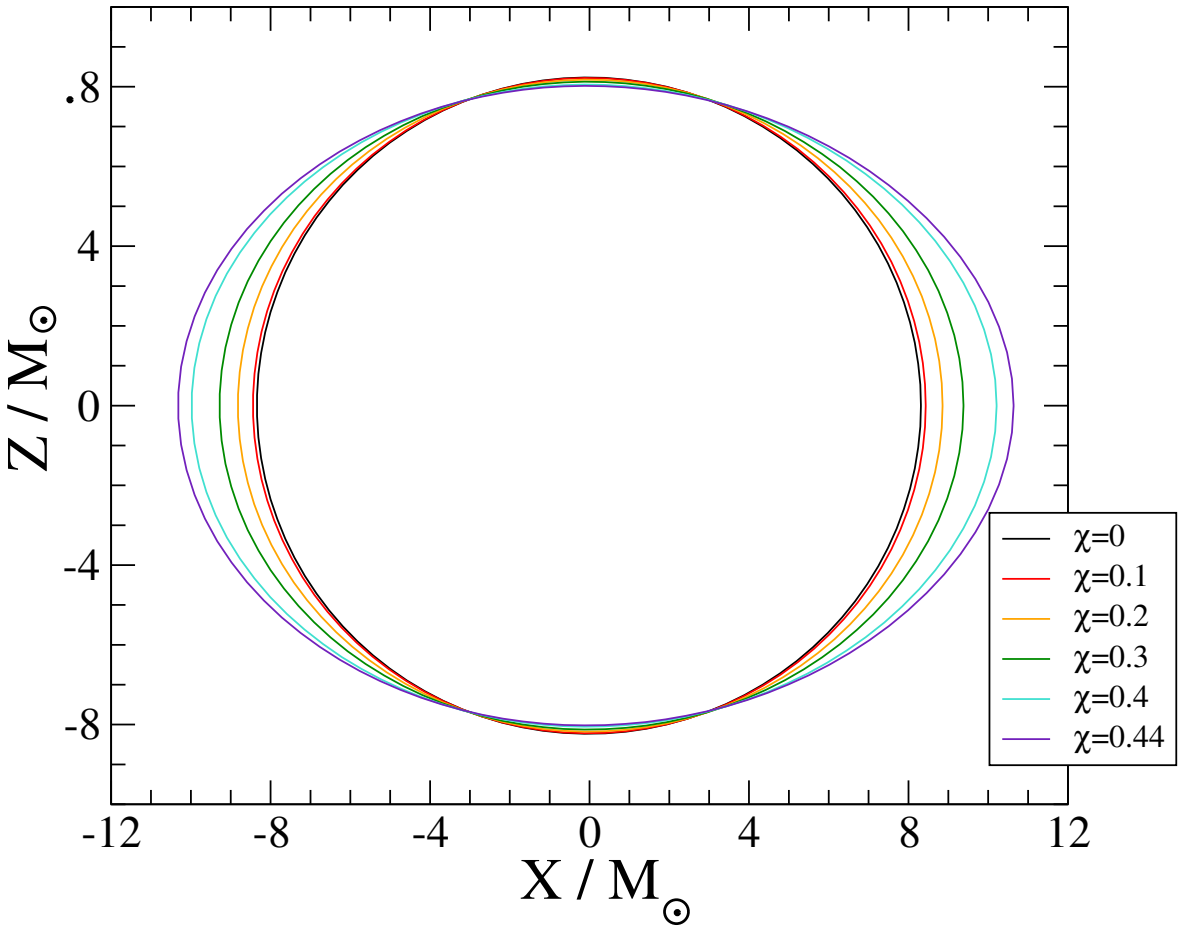

Figure 2.7: Stellar cross-sections in the X-Z plane for a series of different spins, aligned with the $\hat{z}$ axis, demonstrating that they bulge at the equator in the expected way with increasing spin.

L impacts χ by $\sim 10^{-8}$ for the low-spin case `S-.05z`, and by $\sim 10^{-4}$ for the high-spin cases `S.4z` and `S.4x`. For the high-spin cases, the spin measurement is convergent with increasing L, and the finite value of L dominates the error budget. For the low-spin case, numerical truncation error dominates the error budget and convergence with L is not visible. High NS spin leads to a more distorted stellar surface, and so a fixed $L = 11$ yields a spin result of lower accuracy. However, in all cases the the numerical errors of our spin measurements are still negligible for our purposes.

2.4.4 Quasilocal Spin

As discussed in section 2.3.5, we use a quasilocal spin to define the angular momentum carried by each neutron star. To our knowledge, this is the first application of this method to neutron stars in binaries.

In this section, we explore properties of the rotating BNS initial datasets and the employed quasilocal spin diagnostic.

To explore the spin-dependence of BNS initial data sets, we construct a sequence of equal-mass, equal-spin BNS binaries, with spins parallel to the orbital angular momentum. We fix the initial data parameters $M^b_{\rm NS}$, D_0, Ω_0 and $\dot{a}_0$ to their values for a configuration that we will also evolve below (specifically, `S.4z` - Ecc1)

Figure 2.7 shows cross-sections through one of the neutron stars in the xz-plane, i.e. a plane orthogonal to the orbital plane which is intersecting the centers of both stars. With increasing spin, the stars develop an increasing equatorial bulge, an expected consequence of centrifugal forces.

Figure 2.8 presents the dimensionless spin of either neutron star as a function of $\omega M_\odot$. χ increases monotonically with the rotation parameter ω. The spin χ increases linearly with ω for small ω. For larger ω, the dependence steepens, as the increasing equatorial radius of the stars increase the moment of inertia (Worley et al. 2008).

For $\omega = 0.01625 M_\odot^{-1}$ we achieve $\chi = 0.432$, the largest spin we are able to construct. This is reasonably close to the theoretical maximum value for $\Gamma = 2$ polytropes, $\chi \sim 0.57$ (Ansorg et al. 2003). Above $\omega = 0.01625 M_\odot^{-1}$, the initial data code fails to converge. The steepening of the χ vs. ω curve is reminiscent of features related to non-uniqueness of solutions of the extended conformal thin sandwich equations (Lovelace et al. 2008; Pfeiffer & York Jr. 2005; Baumgarte et al. 2007; Walsh 2007), and it is possible that our failure to find solutions originates in an analogous break-down of the uniqueness of solutions of the constraint equations.

While the focus of our investigation lies on rotating NS, we note that for $\omega = 0$ our data-sets reduce to the standard formalism for irrotational NS. For $\omega = 0$, we find a

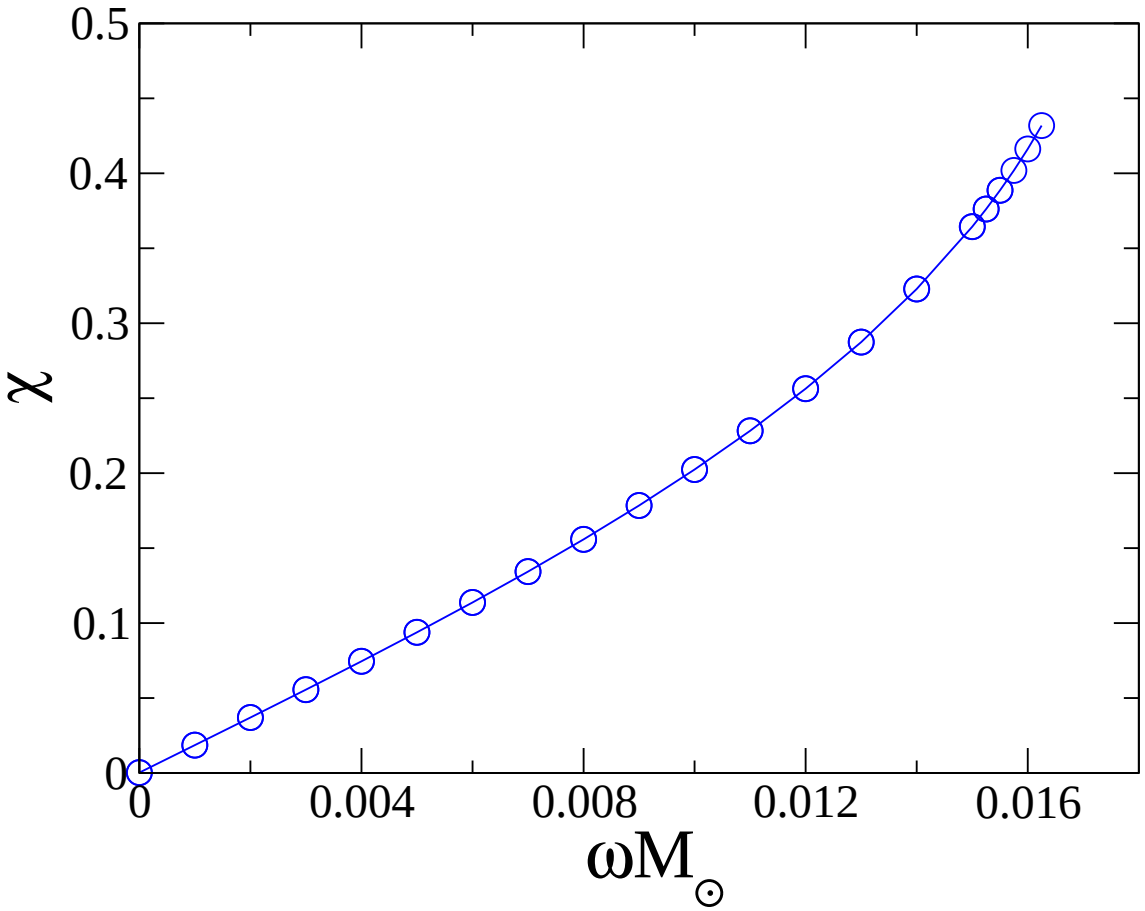

Figure 2.8: Dimensionless angular momentum χ as a function of $\omega M_{\odot}$ for a series of spin-aligned initial data sets with the same physical parameters as our runs of interest. We see, as expected, a linear relation between χ and ω at low-spins, which eventually becomes non-linear at higher spins.

quasilocal spin of the neutron stars is $\chi = 2\times10^{-4}$. This is the first rigorous measurement of the residual spin of irrotational BNS. Residual spin is, for instance, important for the construction and validation of waveform models for compact object binaries. The analysis in Boyle et al. (2007) indicates that spins of order 10^{-4} lead to a dephasing of about 0.01radians during the last dozen of inspiral orbits. This value is significantly smaller than the phase accuracy obtained by current BNS simulations, and so the residual spin is presently not a limiting factor for studies like Bernuzzi et al. (2015); Baiotti et al. (2011); Baiotti et al. (2010).

Finally, we demonstrate that the surface on which we compute the quasilocal spin, does not significantly impact the spin we measure: We choose coordinate spheres centered on the neutron star with radius R, and compute the quasilocal spin using these surfaces, rather than the stellar surface.

In Fig. 2.9, we plot the spin measured on various $R = \text{const}$ surfaces, for three different values of ω, from the same sequences shown in Fig. 2.8.

The circles denote spins extracted on coordinate spheres. The asterisks indicate the spins computed on the stellar surface. The asterisk is plotted at $R = R_{\rm eq}$, the equatorial radius of the neutron star under consideration. We find good agreement between spins extracted on coordinate spheres and the spin extracted on the stellar surface, as long as $R \geq R_{\rm eq}$. The maximum disagreement is seen in the high spin curve, where the two spins differ by $\sim 10^{-2}$.

For $R < R_{\rm eq}$, the coordinate extraction sphere intersects the outer layers of the neutron star and no longer encompasses the entire matter and angular momentum of the star. Therefore, $\chi(R)$ shows a pronounced decline for $R < R_{\rm eq}$ for each of the three initial-data sets considered in Fig. 2.9. For $R > R_{\rm eq}$, $\chi(R)$ continues to increase slightly, for instance, for the middle curve, $\chi(R = 9) = 0.202$ whereas $\chi(R = 11) = 0.204$.

In summary, Fig. 2.9 shows that the quasilocal spin extracted on coordinate spheres can serve as a good approximation of the quasilocal spin extracted on the stellar surface (as long as the coordiate sphere is outside the star, of course).

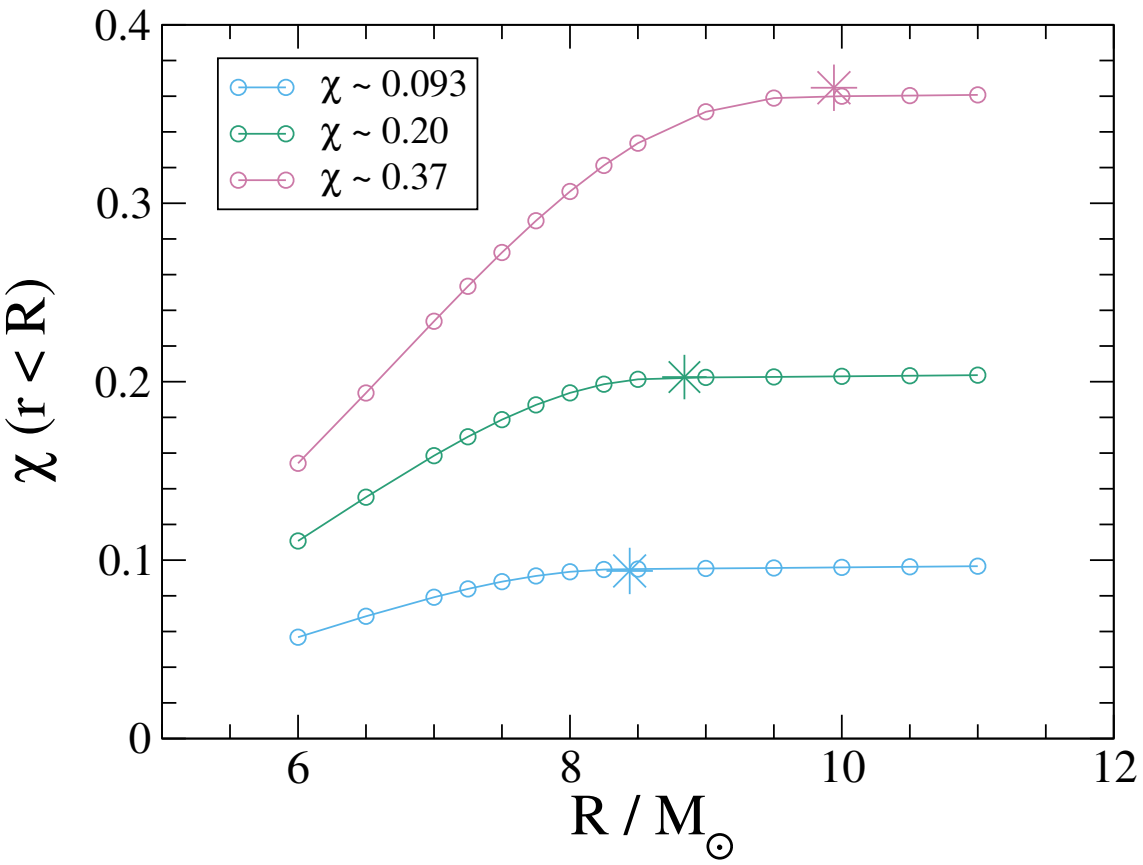

Figure 2.9: Dimensionless spin χ measured on coordinate spheres with radius R for three different aligned spin BNS systems. The asterik denotes the spin measured on the (non-spherical) stellar surface. Circles to the right of the asterik represent coordinate spheres entirely outside the neutron star, and circles on the left of the asterik indicate spin measurement surfaces that intersect the star or are entirely located inside the star.

This is important because during evolutions of the binary, we do not track the surface of the star. Instead, we will compute the spin on coordinate spheres, similarly to Fig. 2.9.

2.5 Evolution Results

We now evolve the three configurations discussed in Sec. 2.4. As indicated in Table 2.1, all three configurations are equal-mass binaries, with individual ADM masses $M_\star$ (in isolation) of $1.64M_\odot$ or $1.648M_\odot$ at initial separation of $D = 47.2M_\odot$, and using a

Name	k	e	$\vec{\chi}$	$f_0(Hz)$	$N_{\rm orb}$	t_f(ms)
`S.4z`	0,1,2	$\lesssim 0.001$	$0.381\hat{z}$	167.7	11.8	56.0
`S-.05z`	0,1,2	0.0006	$-0.050\hat{z}$	165.4	12.5	56.3
`S.4x`	0,1	$\lesssim 0.002$	$0.375\hat{x}$	164.8	9.1	45.7

Table 2.2: Information about our three evolutions. k indicates the numerical resolutions on which a simulation is performed, e indicates the smallest achieved orbital eccentricity. $\vec{\chi}$ and f_0 are the dimensionless spins at $t = 0$ and the initial orbital frequency. Finally, $N_{\rm orb}$ and t_f represent the number of orbits the configuration was evolved for, and the evolution time.

polytropic equation of state with $\Gamma = 2.0$ and $\kappa = 123.6$. Both stars have equal spins, and the three configurations differ in spin magnitude and spin direction. Configuration `S-0.05z` has spin-magnitudes ~ 0.05 anti-aligned with the orbital angular momentum, and the configurations `S.4z` and `S.4x` have spin magnitudes near 0.4, along the z-axis and x-axis, respectively.

Each configuration is evolved through $\gtrsim 10$ orbits, into the late-inspiral. In this chapter we focus on the inspiral of the neutron stars. Table 2.2 summarizes parameters for these runs.

2.5.1 Evolution Code

In our evolution code, SpEC (Buchman et al. 2012; Lovelace et al. 2012; M. A. Scheel, M. Boyle, T. Chu, L. E. Kidder, K. D. Matthews and H. P. Pfeiffer 2009; Kidder et al. 2000; Lindblom et al. 2006; Scheel et al. 2006; Szilágyi et al. 2009; Lovelace et al. 2011; Hemberger et al. 2013; Ossokine et al. 2013), we use a mixed spectral – finite-difference approach to solving the Einstein Field Equations coupled to general relativistic hydrodynamics equations. The equations for the space-time metric, $g_{\mu\nu}$ are solved on a spectral grid, while the fluid equations are solved on a finite difference grid, using a high-resolution shock-capturing scheme. We use a WENO (Jiang & Shu 1996; Liu et al. 1994) recon-

struction method to reconstruct primitive variables, and a Harten-Lax-van Leer (HLL) Riemann solver A. Harten (1983) to compute numerical fluxes at interfaces. Integration is done using a 3rd order Runge-Kutta method with an adaptive stepsize. We interpolate between the hydro and spectral grids at the end of each full time step, interpolating in time to provide data during the Runge-Kutta substeps (see Duez et al. (2008); Foucart et al. (2012); Foucart et al. (2013a); Muhlberger et al. (2014) for a more detailed description of the method).

Each star is contained in a separate cubical finite difference grid that does not overlap with that of the other star. The sides of the grids are initially 1.25 times the stars' diameters. We use grids that contain 97^3, 123^3 and 155^3 points for resolutions $k = 0, 1, 2$, respectively[2]. These resolutions correspond to linear grid-spacing of 340 m, 268 m and 213 m respectively for the `S.4z` case. The precessing evolution `S.4x` uses similar grid-spacing, whereas the anti-aligned run `S-.05z` has a slightly smaller grid-spacing because the stars themselves are smaller. The region outside the NS but inside the finite difference grid is filled with a low density atmosphere with $\rho = 10^{-13} M_\odot^{-2}$. The motion of the NSs is monitored by computing the centroids of the NS mass distributions

$$X^i_{\rm CM} = \int x^i u^0 \rho_0 \sqrt{-g^{(4)}} d^3x \tag{2.66}$$

for each of the grid patches containing a NS.

The grids are rotated and their separation rescaled to keep the centers of the NS at constant grid-coordinates (Scheel et al. 2006; Hemberger et al. 2013; Scheel et al. 2015). As the physical separation between the stars decreases, the rescaling of grid-coordinates therefore causes the size of the stars to increase in grid-coordinates. In order to avoid the stellar surfaces expanding beyond the geometric size of the finite difference grid, we monitor the matter flux leaving this grid along the x, y, and z-direction. If the matter flux is too large along a certain axis, we expand the grid in that direction. This procedure

[2]For aligned-spin configurations `S-.05z` and `S.4z`, we take advantage of, and enforce, z-symmetry, which halves the number of grid-points along the z-axis.

allows us to dynamically choose the optimal grid-size that limits matter loss to a small, user-specified level. When changing the size of the hydro grid, the number of grid-points is kept constant, so this process changes the effective resolution during the evolution.

The Einstein field equations are solved on a spectral grid using basis-functions appropriate for the shape of each subdomain. For rectangular blocks, Cheybyshev polynomials are used along each axis; for a spherical shell (i.e. where the center is excised), spherical harmonics in angles, and Chebyshev polynomial in radius are employed; and for an open cylinder (i.e. with the region near the axis excised), Chebyshev polynomials and a Fourier series. For full spheres and filled cylinders, multi-dimensional basis-functions respecting the continuity conditions at the orign/axis are employed (Matsushima & Marcus 1995; Verkley 1997). For more details see Muhlberger et al. (2014).

More specifically, our spectral grid, the central region of each star is covered by a filled sphere located at the center of the star. These have spherical harmonic modes up to $L = 12 + 2k$. The radial basis-functions are one-sided Jacobi polynomials with $7 + k$ collocation points. The filled spheres are surrounded by eight other spherical shells with the same radial and angular resolutions. At the start of the evolution, the stellar surface is generally located inside the third shell. The far field region is covered by 20 spherical shells starting at 1.5 times the inital binary separation and going out to 40 times that separation. These shells have angular resolution $L = 9 + 2k$ and radial resolution $6 + k$. The region between the innermost shell and the stars is covered by a set of cylindrical shells and filled cylinders.

We use a generalized harmonic evolution system (Pretorius 2006; 2005; Lindblom et al. 2006) with coordinates x^μ such that they satisfy a wave equation

$$\nabla^\nu \nabla_\nu x^\mu = H^\mu, \tag{2.67}$$

for some freely-specifiable source function H^μ. The initial source function H^μ_{initial} is determined by the initial data, assuming that the time derivatives of the lapse and shift functions initially vanish in the corotating frame. We then transition to a pure harmonic

gauge, $H^\mu = 0$ by using a transition function, i.e.

$$H^\mu = e^{-(t/\tau)^4}\, H^\mu_{\rm initial}. \tag{2.68}$$

The timescale τ is determined by $\tau = 2\sqrt{d^3/(2M_\star)}$. This is slow enough to avoid numerical gauge artifacts in the simulations.

2.5.2 Eccentricity Removal

Gravitational wave emission reduces orbital eccentricity rapidly during a GW-driven inspiral (Peters & Mathews 1963; Peters 1964). Therefore inspiraling binary neutron stars are expected to have essentially vanishing orbital eccentricity in their late inspiral, unless they recently underwent dynamical interactions. Our goal is to model non-eccentric inspirals. In this subsection we demonstrate that we can indeed control and reduce orbital eccentricity, using the techniques developed for black hole - black hole binaries (Pfeiffer et al. 2007; Boyle et al. 2007; Buonanno et al. 2011a) and also applied to black hole - neutron star binaries (Foucart et al. 2008).

For fixed binary parameters (masses, spins), and fixed initial separation D_0, the initial orbit of the binary is determined by two remaining parameters: The initial orbital frequency Ω_0, and the initial radial velocity, which we describe through an expansion parameter $\dot{a}_0 = \dot{r}/r$. These two parameters will encode orbital eccentricty and phase of periastron, and our goal is to determine these parameters to reduce orbital eccentricity. We accomplish this using an iterative procedure first introduced for binary black holes (Boyle et al. 2007; Buonanno et al. 2011a). An initial data set is evolved for a few orbits, the resulting orbital dynamics are analyzed, and then the initial data parameters Ω_0 and $\dot{a}_0$ are adjusted.

For binary neutron stars, we initialize the first iteration of eccentricity removal, with $\dot{a}_0 = 0$ and use Ω_0 determined from irrotational BNS initial data, based on the equilibrium condition in Eq. 2.39. Evolutions with these choices are labeled with the suffix "Ecc1",

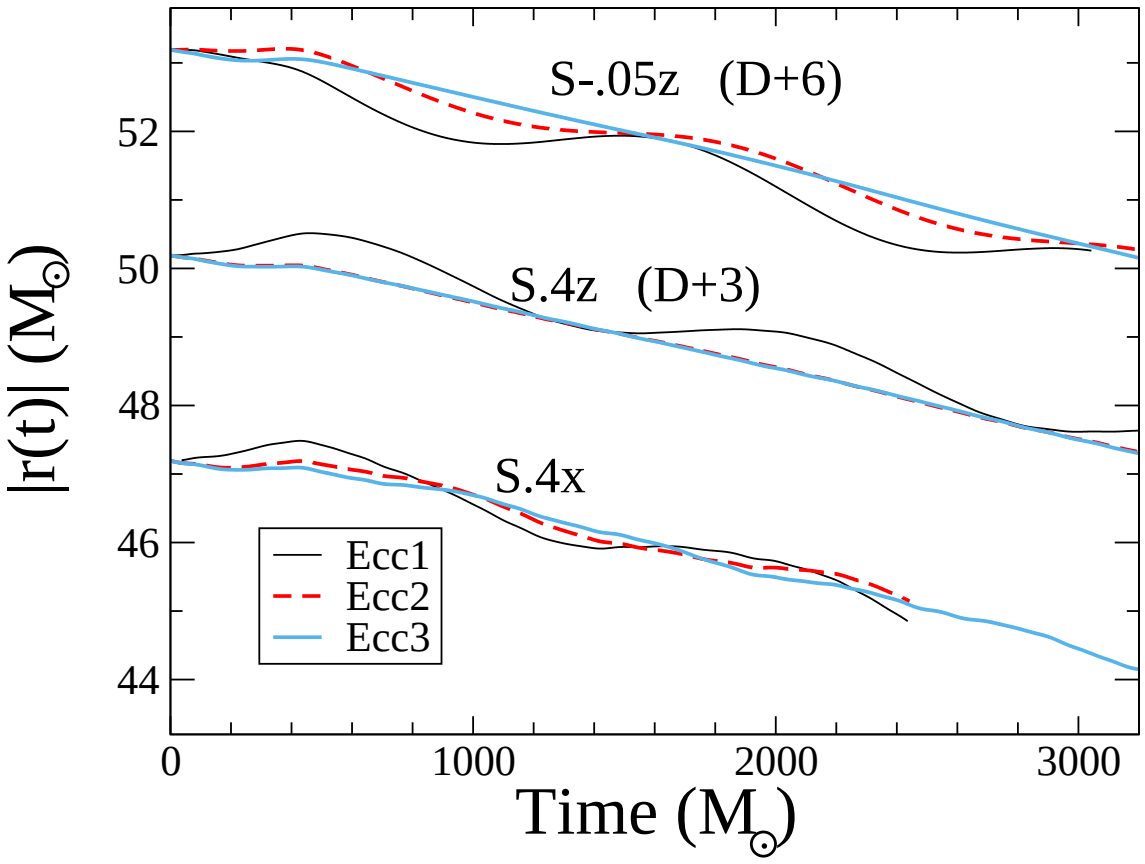

Figure 2.10: The binary separation as a function of time. Shown are three eccentricity removal iterations (Ecc1,Ecc2,Ecc3) for each of the three configurations studied. The data for `S-.05z` and `S.4z` is offset vertically by 6 and 3, respectively, for clarity of plotting.

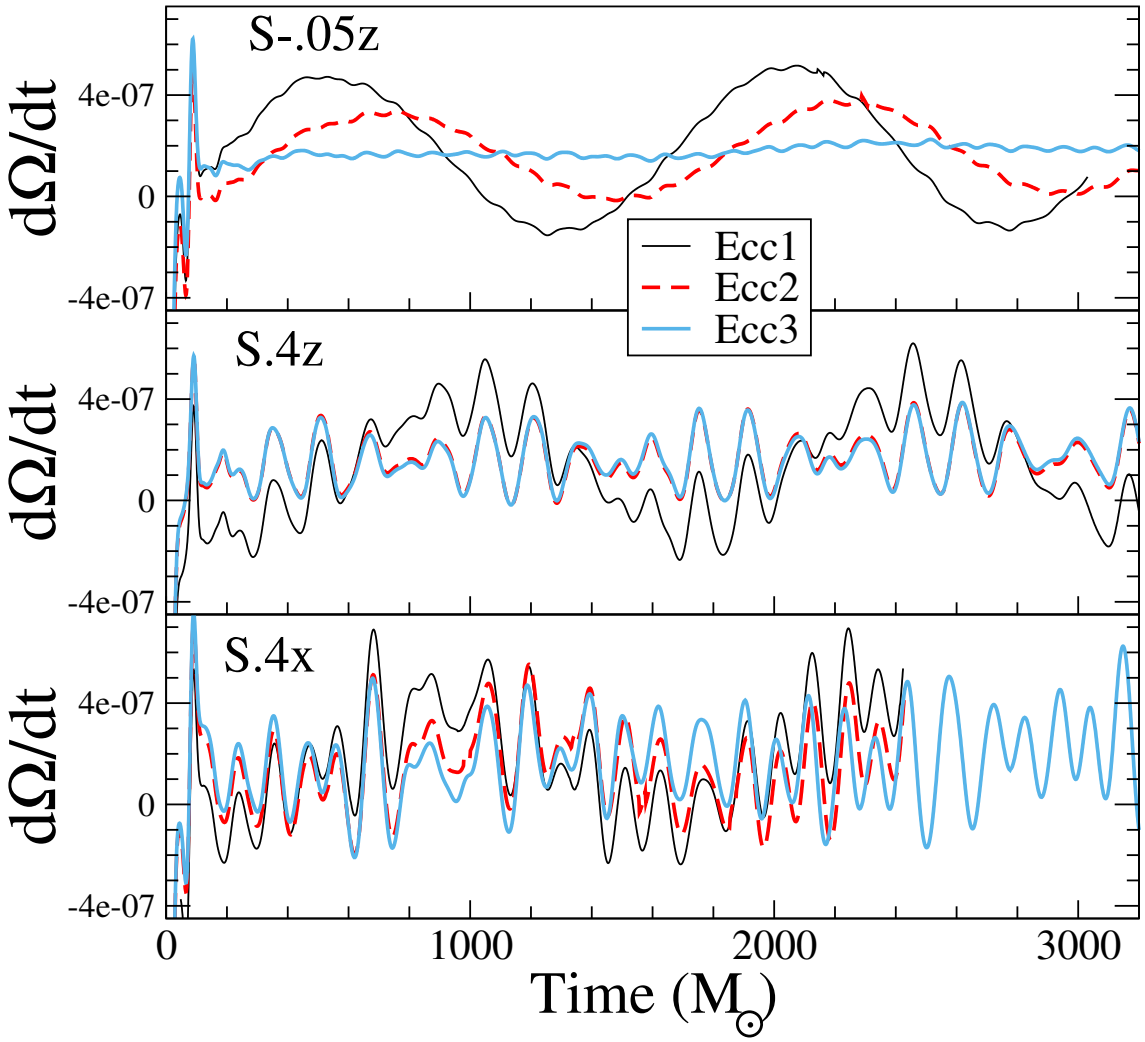

Figure 2.11: The derivative of the binary orbital frequency as a function of time for different levels of eccentricity reduction for our three runs of interest. Note that $d\Omega/dt$ has units of $M_{\odot}^{-2}$.

Name	$\Omega \times 10^3$	$\dot{a}_0 \times 10^5$	e
`S.4z` - Ecc1	5.10538	0	0.006
`S.4z` - Ecc2	5.09591	-1.60	$\lesssim 0.001$
`S.4z` - Ecc3	5.09594	-1.75	$\lesssim 0.001$
`S-.05z` - Ecc1	5.10538	0	0.008
`S-.05z` - Ecc2	5.11561	0	0.004
`S-.05z` - Ecc3	5.11769	-1.71	0.0006
`S.4x` - Ecc1	5.10538	0	0.007
`S.4x` - Ecc2	5.10429	-2.27	0.004
`S.4x` - Ecc3	5.10064	-2.36	$\lesssim 0.002$

Table 2.3: Eccentricity removal for the three main runs discussed in this chapter. Only initial orbital frequency Ω_0 and initial radial expansion factor $\dot{a}_0$ are changed between different EccN iterations. Recall that these quantities have units of $M_\odot^{-1}$.

and show noticeable variations in the separation between the two NS, cf. the solid black lines in Fig. 2.10.

We compute the trajectories of the centers of mass of each star, as determined by Eq. 2.66, $\vec{c}_1(t)$ and $\vec{c}_2(t)$, and using the relative separation $\vec{r} = \vec{c}_2(t) - \vec{c}_1(t)$, compute the orbital frequency

$$\Omega(t) = \frac{|\vec{r}(t) \times \dot{\vec{r}}(t)|}{r(t)^2}, \tag{2.69}$$

where an over-dot indicates a numerical time-derivative. Finally, we compute $\dot{\Omega}(t)$ and fit it to a function of the form

$$\begin{aligned}\dot{\Omega}(t) =& A_1(t_c - t)^{-11/8} + A_2(t_c - t)^{-13/8} \\ &+ B_0 \cos\left(B_1 t + B_2 t^2 + B_3\right).\end{aligned} \tag{2.70}$$

The power law parts of this fit represent the orbital decay due to the emission of gravitational waves, while the oscillatory part represents the eccentric part of the orbit. We

then update Ω_0 and $\dot{a}_0$ with the formulae (see Buonanno et al. (2011a) for a detailed overview)

$$\Omega_0 \leftarrow \Omega_0 - \frac{B_0 B_1}{4\Omega_0^2} \sin B_3, \tag{2.71}$$

$$\dot{a}_0 \leftarrow \dot{a}_0 + \frac{B_0}{2\Omega_0} \cos B_3. \tag{2.72}$$

We repeat this procedure twice, resulting in simulations with suffix Ecc2 and Ecc3. Table 2.3 summarizes the orbital parameters for the individual simulations, and Figs. 2.10 and 2.11 illustrate the efficacy of the procedure through plots of separation and time-derivative of orbital frequency. The eccentricity is successfully reduced from $e \sim 1\%$ to $\sim 0.1\%$. After two eccentricity reduction iterations, variations in $\dot{\Omega}(t)$ are so small that they are no longer discernible from higher-frequency oscillations in $\dot{\Omega}(t)$, cf. Fig. 2.11.

The high frequency oscillations in $\dot{\Omega}(t)$ are caused by the quasi-normal ringing of the neutron stars, as discussed in detail below in Sec. 2.5.5. Here, we only note that these oscillations are convergently resolved, cf. Fig. 2.12, and are therefore a genuine feature of our initial data. Figure 2.12 also confirms that the lowest resolution ($k = 0$) gives adequate resolution for eccentricity removal. Note that in Fig. 2.12 there are spikes in $\dot{\Omega}(t)$ at early times. Such transients are seen in every SpEC simulation - see, e.g., Fig. 5 of Buonanno et al. (2011b). These arise as the orbital frequency relaxes from that set in the initial data to that of a quasi-equilibrium inspiral, and as the gauge changes as described in Sec. 2.5.1.

The eccentricity removal algorithm attempts to isolate variations on the orbital time-scale as the signature of eccentricity. For `S.4z` - Ecc2, it reports $e = 0.0005$ and for `S.4z` - Ecc3, $e = 0.0002$. However, given the large amplitude of the quasi-normal mode ringing, we consider these estimates unreliable, and therefore quote an upper bound of 0.001 in Table 2.3. Similarly, for `S.4x` - Ecc3, the fitting reports $e = 0.001$, and we quote a conservative upper bound of 0.002.

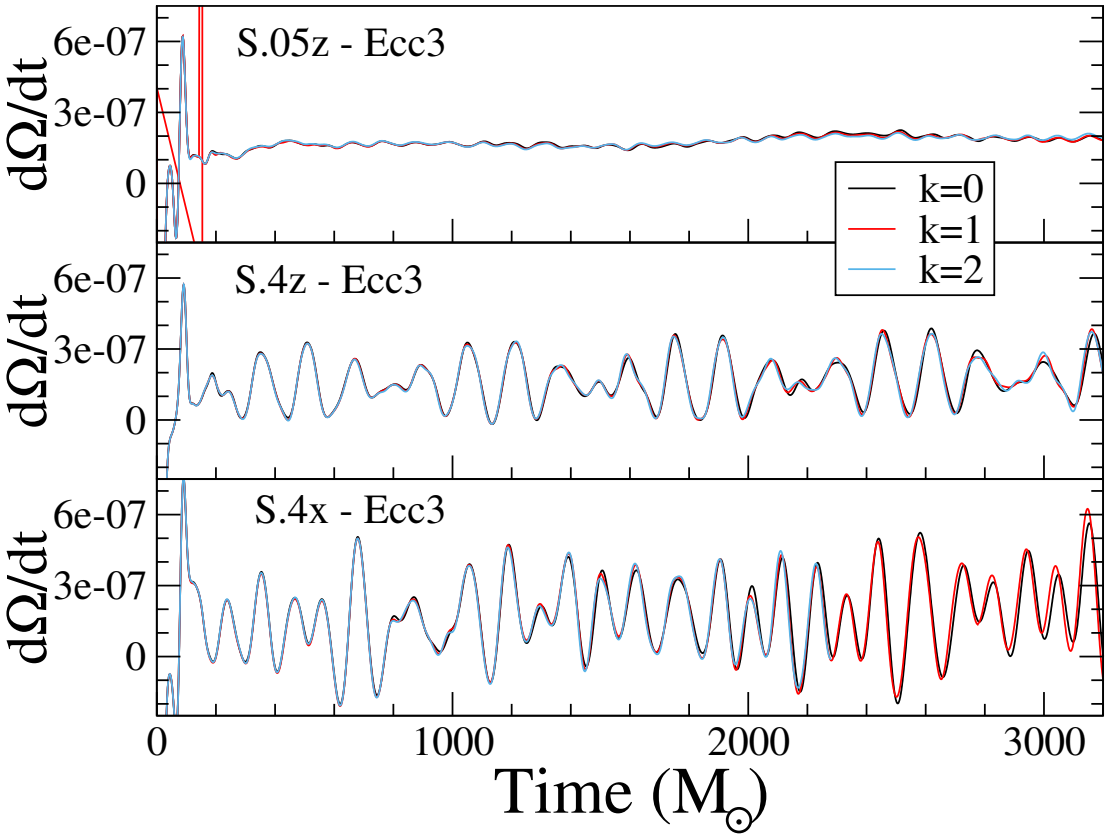

Figure 2.12: Convergence of $\dot{\Omega}(t)$. Shown are $\dot{\Omega}(t)$ at three different numerical resolutions ($k = 0, 1, 2$) for the final, lowest-eccentricity initial data. The oscillations in $\dot{\Omega}(t)$ are evidently not caused by numerical truncation error. Note that $\dot{\Omega}$ has units of $M_{\odot}^{-2}$.

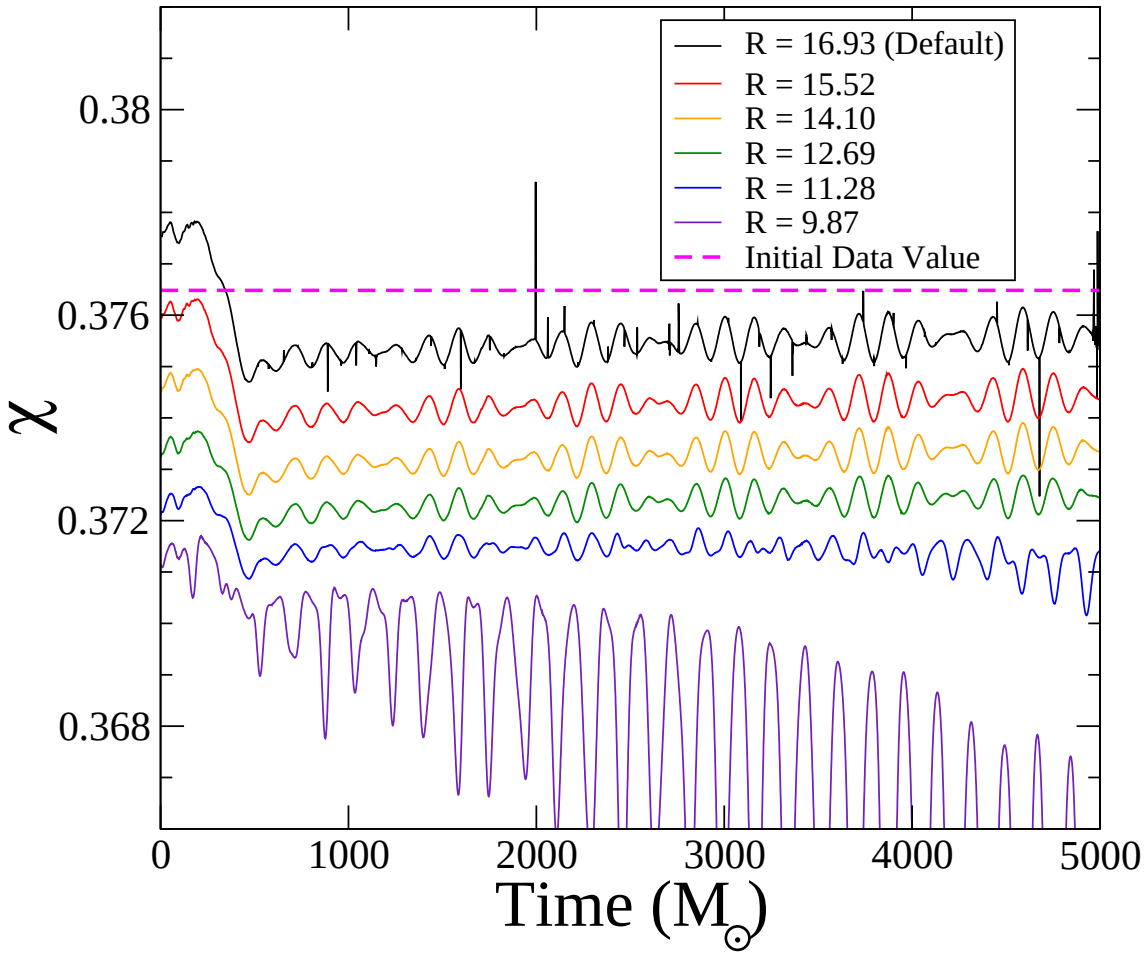

Figure 2.13: The spin measured on multiple coordinate spheres for the `S.4z` run.

2.5.3 Aligned spin BNS Evolutions: NS Spin

In this section, we will discuss the measurement of spins during our evolutions for the non-precessing cases, `S.4z` and `S-.05z`. Aligned spin binaries do not precess. Combined with the low viscosity we expect the NS spins to stay approximately constant during the evolutions. These systems therefore serve as a test on our spin diagnostics during the evolutions. In this section, and through the rest of this chapter, we always use the final eccentricity reduction, "Ecc3". For brevity, we will omit the suffix "-Ecc3", and refer to the runs simply as `S-.05z`, etc.

We do not track the surface of the star during the evolution. Instead we simply evaluate the quasilocal spin of the stars on coordinate spheres in the frame comoving

with the binary. We must therefore verify that the spin measured is largely independent of the radius of the sphere, and that it is maintained during the evolutions at the value consistent with that in the initial data. Figure 2.9 established that coordinate spheres can be used to extract the quasilocal spin in the initial data. Figure 2.13 shows the results for the high-spin simulation `S.4x` during the inspiral.

For coordinate spheres with radii $R = 11.28M_\odot$ to $R = 16.93M_\odot$ in grid coordinates, the spins remain roughly constant in time. The different extraction spheres yield spins that agree to about 1%, with a consistent trend that larger extraction spheres result in slightly larger spins (as already observed in the initial data). The horizontal dashed line in Fig. 2.13 indicates the spin measured on the stellar surface (i.e. not on a coordinate sphere) in the initial data. We thus find very good agreement between all spin measurements, and conclude that the quasilocal spin is reliable to about 1%.

The extraction sphere $R = 9.87M_\odot$ in Fig. 2.13 intersects the outer layers of the neutron star. Because the quasilocal spin captures only the angular momentum within the extraction sphere, the value measured on $R = 9.87M_\odot$ falls as our comoving grid-coordinates cause this coordinate sphere to slowly move deeper into the interior of the star. This behavior, again, is consistent with Fig. 2.9.

These tests of using multiple coordinate spheres were only run for about half of the inspiral – enough to establish that the method is robust. Subsequently, we report spins measured on the largest coordinate sphere, $R = 16.93M_\odot$.

The full behavior of the spin during the inspiral is shown in figure 2.14 for both the `S.4z` and `S-.05z` runs. Comparing the spin at different resolutions, we note that the data for $k = 1$ and $k = 2$ are much closer to each other than compared to $k = 0$, indicating numerical convergence. We note that the impact of numerical resolution (as shown in Fig. 2.14) is small compared to the uncertainty inherent from the choice of extraction sphere, cf. Fig. 2.13. We also note that for the first $10000M_\odot$ of the run, the measured spin behaves as a constant, as expected, albeit with some small oscillations.

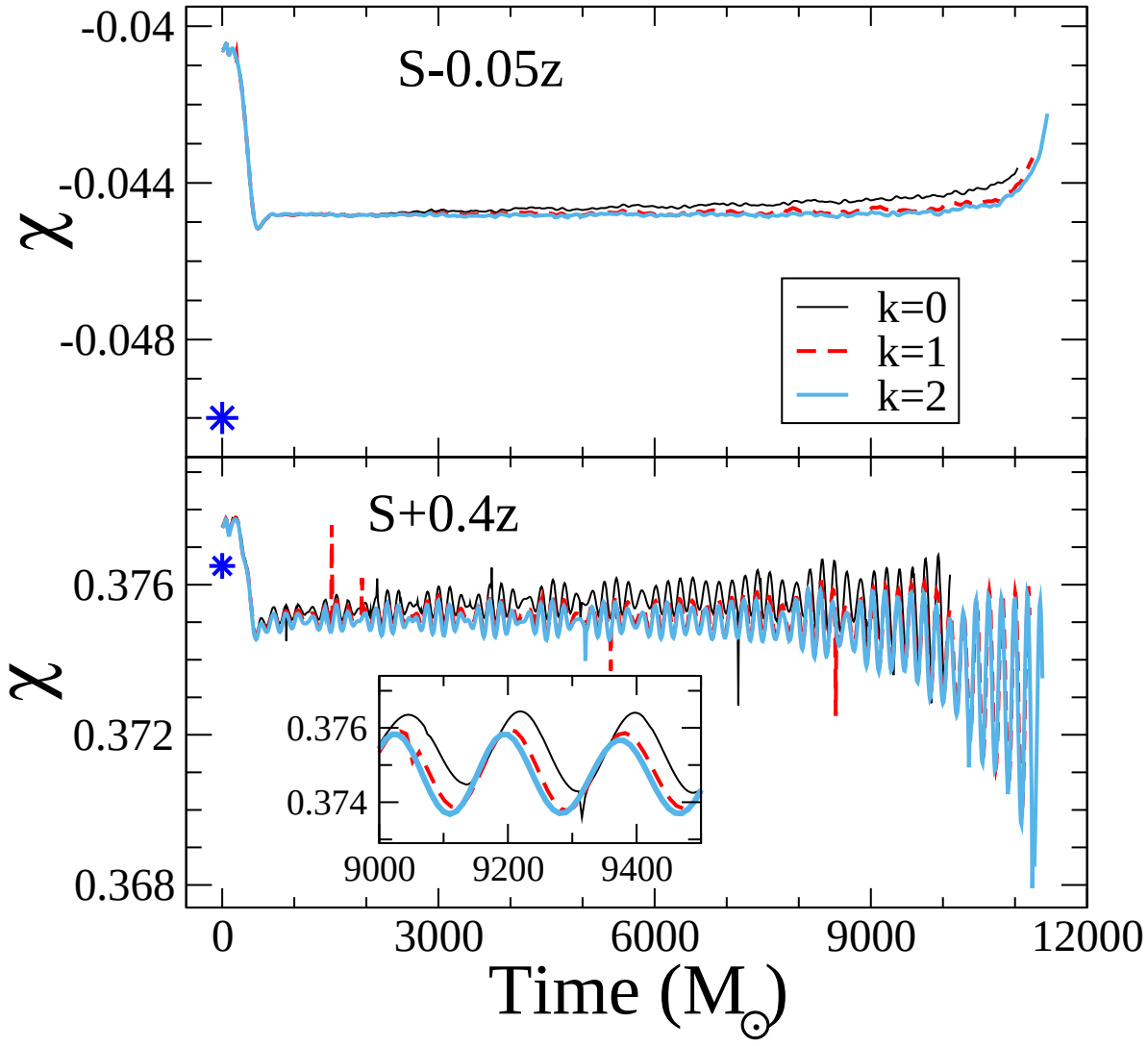

Figure 2.14: Neutron star spin during the two aligned-spin evolutions. Shown are three different numerical resolutions, $k = 0$ (lowest), $k = 1$, and $k = 2$ (highest). The asterisk indicates the spin measured on the stellar surface in the initial data.

However, afterward, we notice the absolute value of the spin starts to decrease in both cases. Finally, we note that in both cases, the spin measured in the inital data on the stellar surface is within $\Delta\chi = 0.008$ of the spin measured during the evolution.

Finally, we compute the orbital phase

$$\phi(t) = \int_0^t \Omega(t')\, dt', \tag{2.73}$$

where the orbital frequency $\Omega(t)$ is given by Eq. (2.69). The result is plotted in Fig. 2.15, along with the Post-Newtonian prediction for the same binary parameters (spins, masses and initial orbital frequencies). We use the Taylor T4 model (see e.g., Boyle et al. (2007)) at 3.5PN order expansion, with no tidal terms added, using the matching techniques described in Ossokine et al. (2015a). We find excellent qualitative agreement in both cases, thereby giving additional evidence that our numerical simulations are working as expected. We do find large late time growth in the phase difference, however this is expected because we do not model tidal effects, which become increasingly important at late times, in our Post-Newtonian equations.

Figure 2.16 shows the gravitational waveforms for our two non-precessing simulations. We extract the waves on a sphere of radius $R = 627M_\odot$.

2.5.4 Precession

We now turn to the precessing simulation, `S.4x`. Figure 2.17 shows the components of the spin-vector $\vec{\chi}$ of one of the neutron stars, as a function of time. The quasilocal spin diagnostic returns a spin with nearly constant magnitude, varying only by ± 0.002 around its average value 0.370. The spin components clearly precess, with the dominant motion in the xy-plane (the initial orbital plane), with the simulation completing about 2/3 of a precession cycle. A z-component of the NS spin also appears, indicating precession of the neutron star spin out of the initial orbital plane.

Fig. 2.17 shows a comparison of spin precession between numerical relativity and Post-Newtonain theory. We perform this comparison using the matching tecnhique in Ossokine

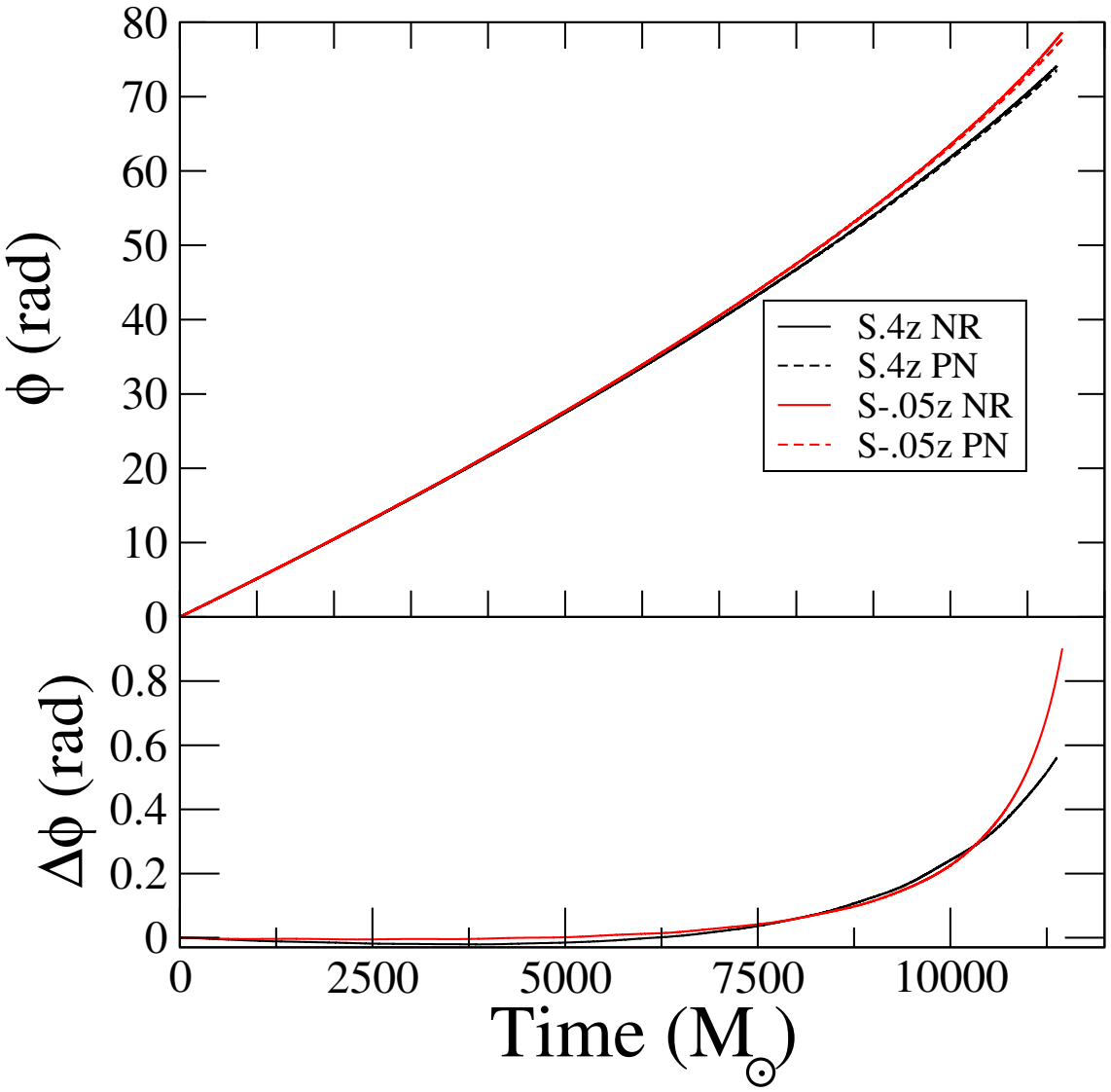

Figure 2.15: Accumulated orbital phase as a function of time for our anti-aligned, `S-.05z`, and aligned, `S.4z`, runs. The dashed lines are Taylor T4 Post-Newtonian (PN) simulations simulations. The PN simulations were matched to NR in the intervals [1109,3956] and [2090,4904] respectively. Qualitatively, there is excellent agreement with the numerical data. The lower panel shows the difference $\Delta\phi(t) = \phi_{\rm NR}(t) - \phi_{\rm PN}(t)$.

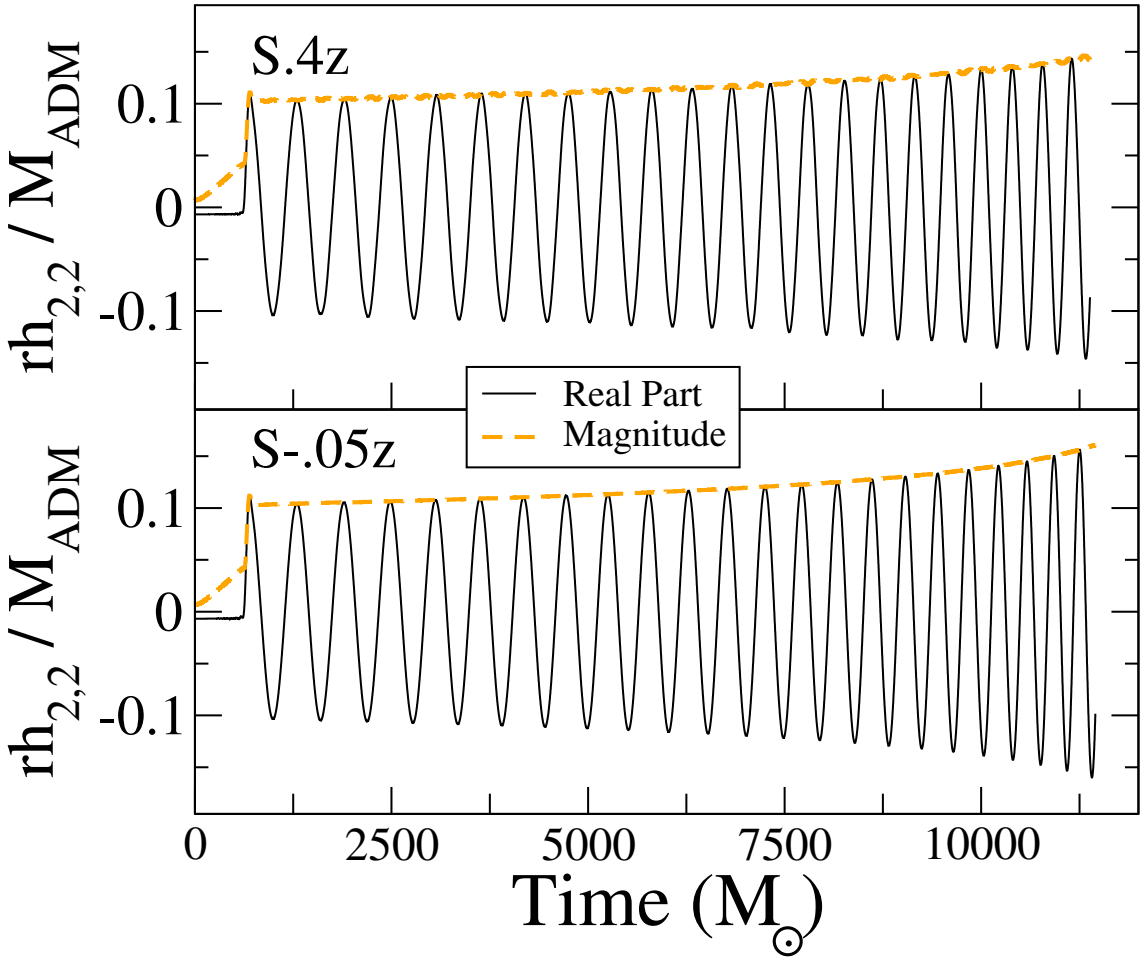

Figure 2.16: The gravitational waveforms for our anti-aligned, `S-.05z`, and aligned, `S.4z` runs. The black curve represents the real part of the waveform, $\Re(h_{2,2})$ while the orange curve represents the magnitude of the waveform.

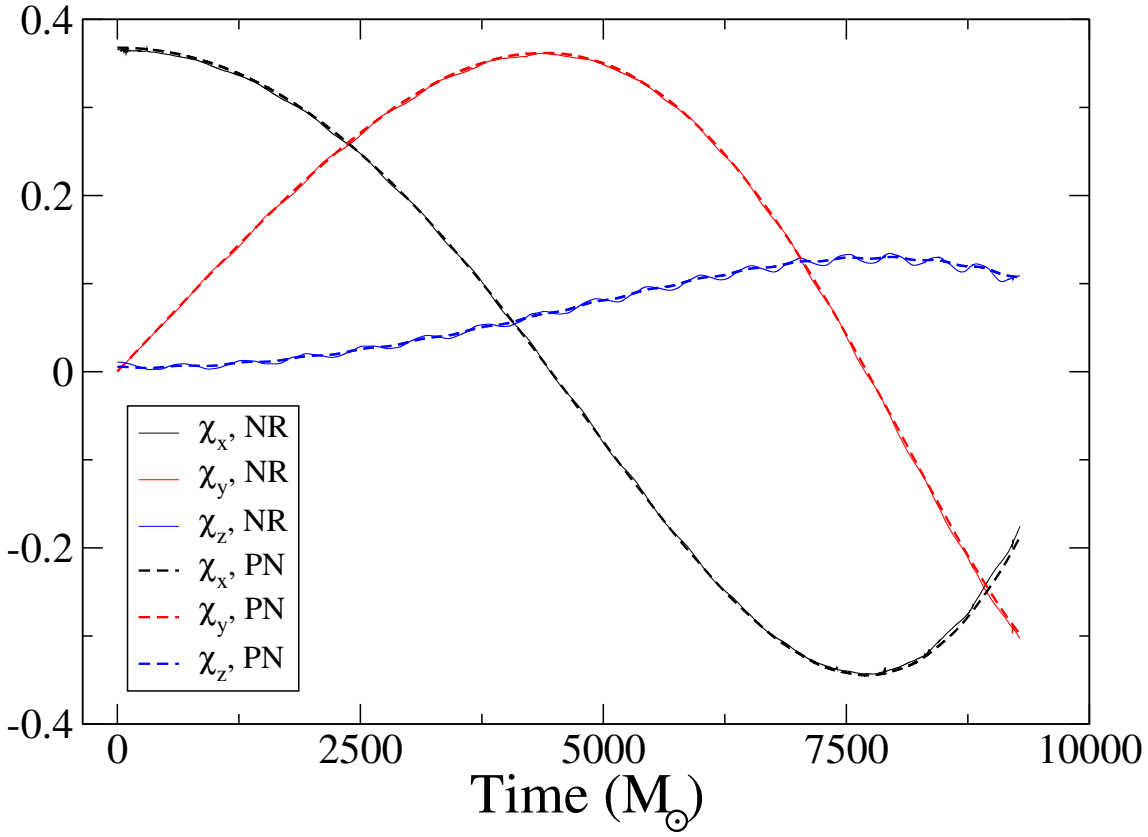

Figure 2.17: Spin-components of one of the neutron stars during the precessing simulation (thick, solid lines). The dotted and dashed lines represent the unmatched and matched PN results respectively. The agreement between PN and NR is good for both PN simulations. The orbital frequency was evolved using the Taylor T4 approximant. The matching was done in the interval [1892,4575].

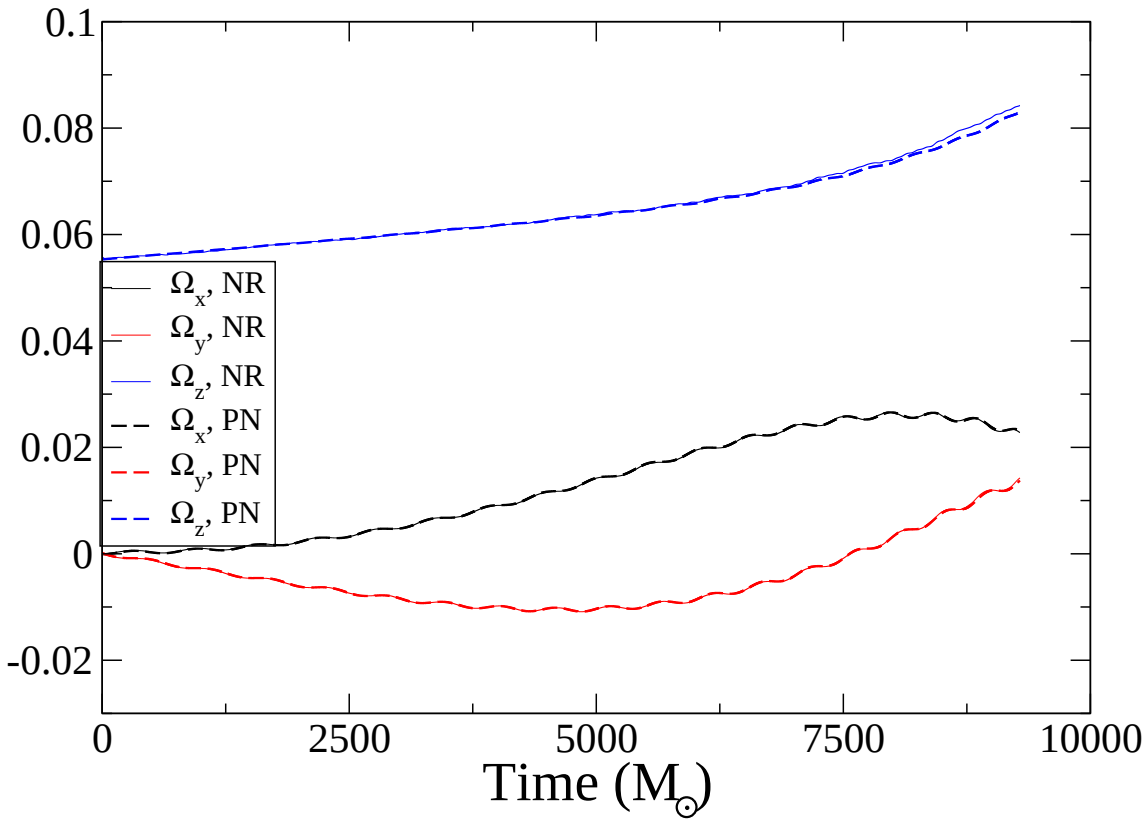

Figure 2.18: Components of the orbital frequency vector $\vec{\Omega}$. Thick solid lines represent the precessing BNS simulation and thin dashed lines represent the matched post-Newtonian simulations. The inclination reaches $\delta = 0.34$rad at $t = 7600 M_{\odot}$.

et al. (2015a). This gives very good agreement between PN (dotted) and NR (solid) as shown by Fig. 2.17. The NS spins indeed precess as expected, thus confirming both the quality of quasilocal spin measures, as well as the performance of the PN equations. Note that z-component of the spin in the NR data undergoes oscillations that are unmodelled by PN. These occur on a timescale of half the orbital timescale. Similar effects were found in Ossokine et al. (2015a). The origin of these oscillations remains unclear. The precession of the orbital angular frequency is shown in Fig. 2.18. We find substantial precession away from the initial direction of the orbital frequency $\vec{\Omega}_0 \propto \hat{z}$, with the angle δ between $\vec{\Omega}(t)$ and the z-axis reaching 20°. Once again, the PN equations reproduce the precession features successfully.

Finally, Fig. 2.19 shows the (2,2) and the (2,1) spherical harmonic modes of the gravitational wave-strain extracted at an extraction surface of radius $R = 647M_\odot$. The (l,m)=(2,1) mode would be identically zero for an equal-mass aligned spin binary with orbital frequency parallel to the z-axis, so the emergence of this mode once again indicates precession in this binary.

2.5.5 Stellar Oscillations

The rotating neutron stars constructed here show oscillations in the central density, as plotted in Fig. 2.20. In the low spin run, the density oscillations have a peak-to-peak amplitude of about 0.6%, whereas in the high-spin runs (`S.4z` and `S.4x`), the density oscillations reach a peak-to-peak amplitude of 20%. The two high-spin simulations show oscillations of nearly the same amplitude and frequency, therefore oscillating nearly in phase throughout the entire inspiral. The oscillation-period is about $177M_\odot \sim 0.87$ms, i.e. giving a frequency of 1.15kHz. It remains constant throughout the inspiral. The low-spin run `S-0.5z` exhibits a slightly smaller oscillation period of about $P \approx 170M_\odot \approx$ 0.84ms, i.e. a frequency of $\approx$ 1.19kHz.

To investigate the spectrum of the density oscillations, we perform a Fourier-transform

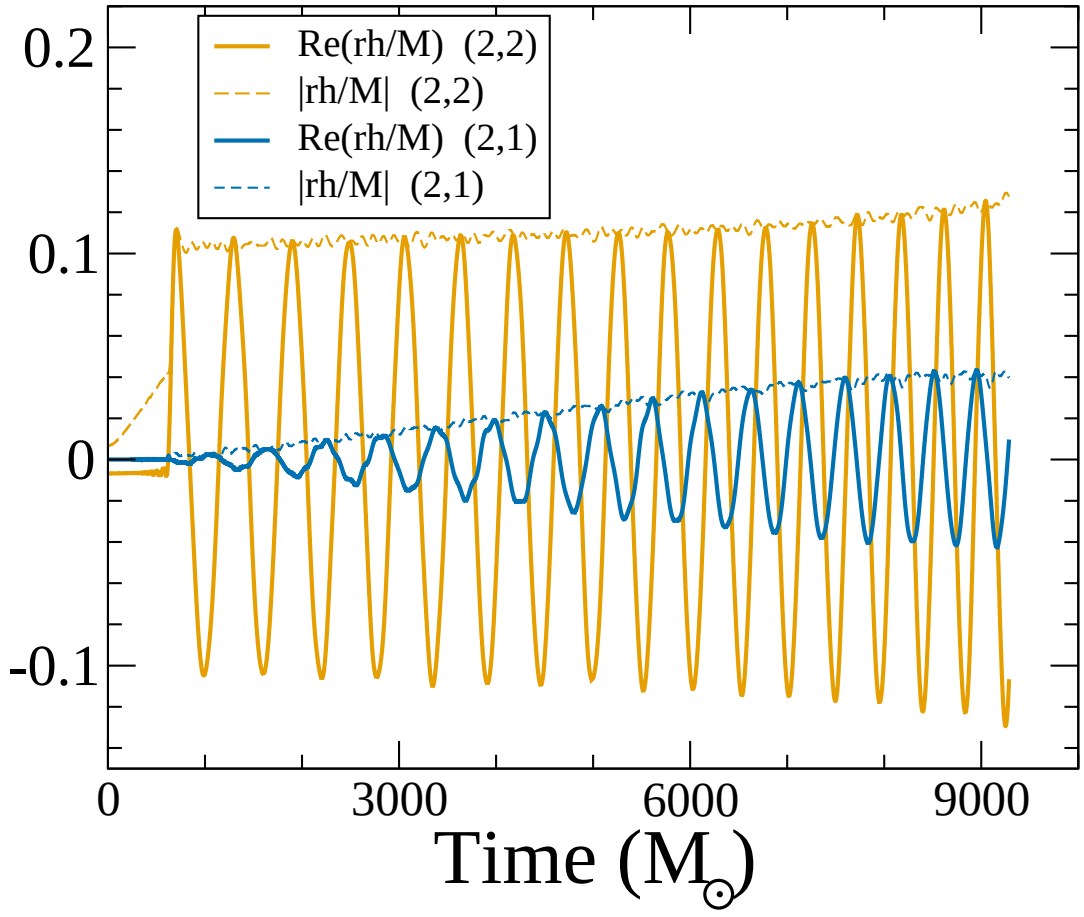

Figure 2.19: Gravitational waveforms of our precessing run. Shown are the $(l, m) = (2, 2)$ and $(2, 1)$ modes, as extracted in a spherical harmonic decomposition aligned with the z-axis. The emergence of the (2,1) mode indicates precession of the orbital plane away from the xy-plane.

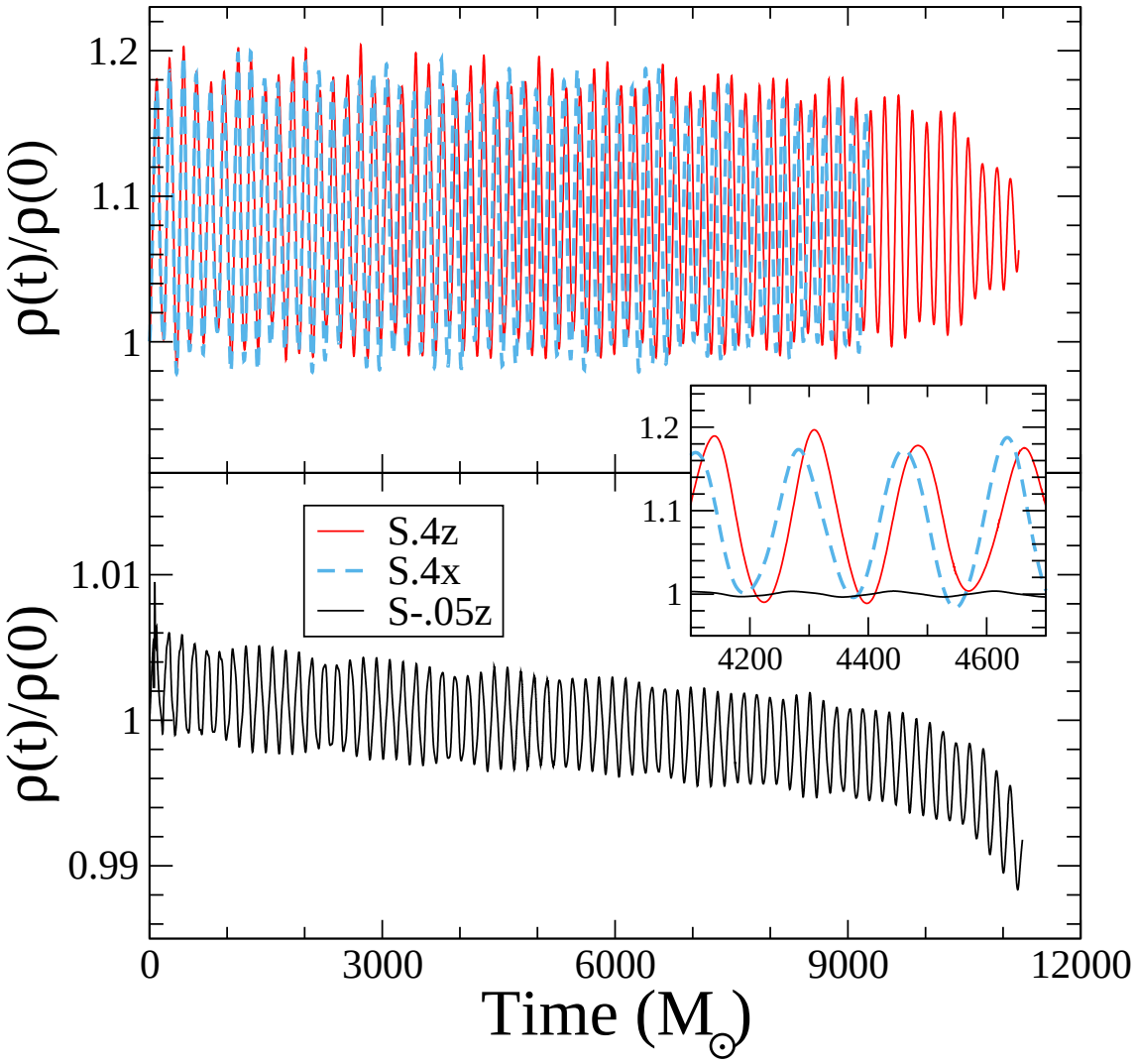

Figure 2.20: The maximum density $\rho(t)$ in each of our runs, normalized by the initial maximum density $\rho(0)$. The inset shows an enlargement of all three runs, illustrating that the oscillations are more pronounced in the high-spin simulations.

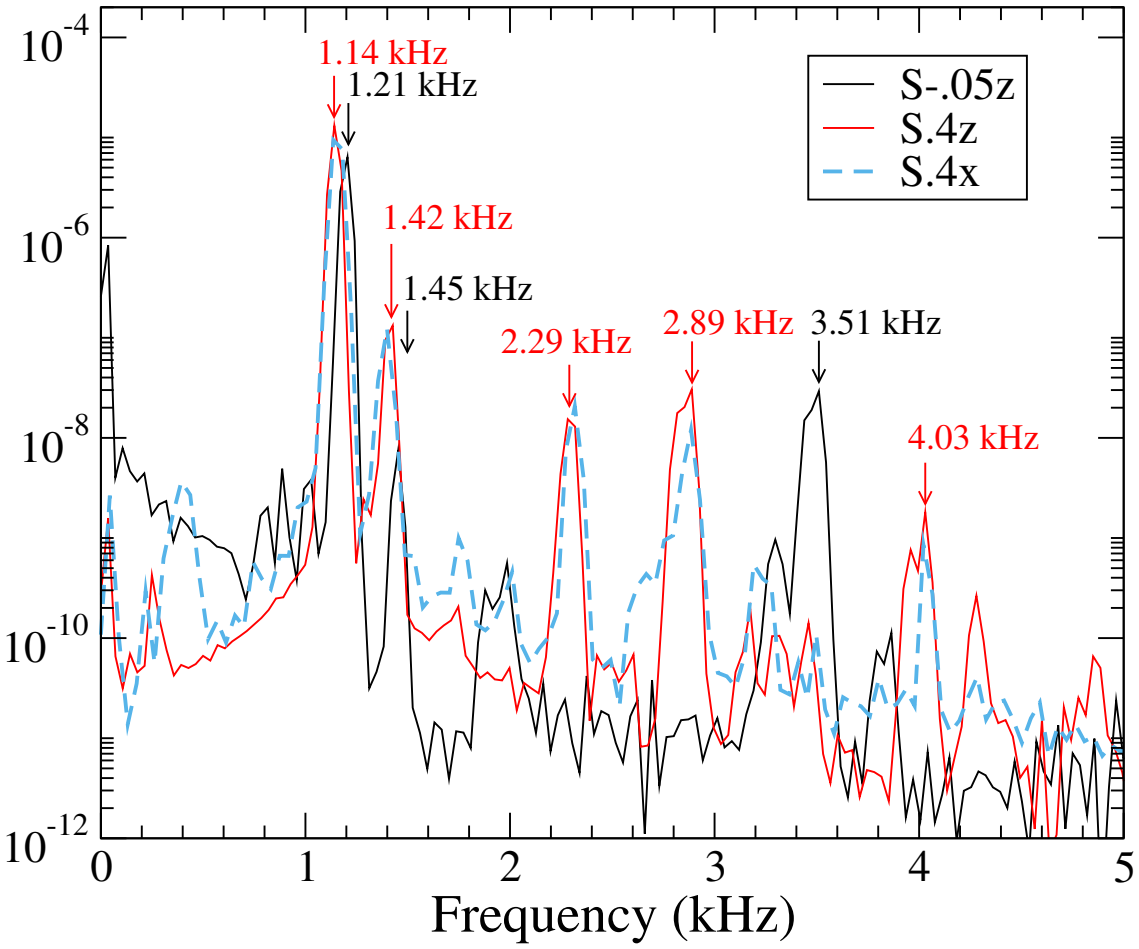

Figure 2.21: The Fourier transforms of the central density in all three of our runs. Labelled are the peak frequencies for the quasi-radial F mode and the $l = 2$, ${}^2f$ mode.

on $\rho(t)$. The result is shown in Fig. 2.21. The Fourier-transform confirms the dominant frequencies just stated, and reveals several more frequency components ranging up to 4kHz. The high spin evolutions `S.4z` and `S.4x` exhibit identical freqencies for all five discernible peaks. In contrast, the low-spin evolution `S-.05z` shows different frequencies.

We interpret these features as a collection of excited quasi-normal modes in each neutron star. The modes are excited because the initial data is not precisely in equilibrium. For the two high-spin cases the neutron stars have similar spin, and therefore the same quasi-normal modes, whereas in the low-spin model, the quasi-normal mode frequencies differ due to the different magnitude of the spin.

To strengthen our interpretation, we consider the series of rotating, relativistic, $\Gamma = 2$ polytropes computed by Dimmelmeier et al. (2006).

Dimmelmeier et al. (2006)'s model "AU3" has a central density of $1.074 \times 10^{-3} M_\odot^{-2}$ and its rotation is quantified through the ratio of polar to equatorial radius, $r_p/r_e = 0.780$. Meanwhile, our high-spin runs have a central density of $1.02 \times 10^{-3} M_\odot^{-2}$ (measured as time-average of the data shown in Fig. 2.20) and from our initial data, we find $r_p/r_e \sim 0.8$. Given the similarity in these values, we expect Dimmelmeier et al. (2006)'s "AU3" to approximate our high-spin stars `S.4x`, `S.4z`. Dimmelmeier et al. (2006) reports a frequency of $f_F = 1.283$kHz for the spherically symmetric ($\ell = 0$) F-mode, and a frequency $f_{2f} = 1.537$kHz for the axisymmetric $\ell = 2$ mode ${}^2f$. These frequencies compare favorably with the two dominant frequencies in Fig. 2.21, 1.14kHz and 1.42kHz.

Presumably, the small differences in these frequencies can be accounted for by the slight differences in stellar mass, radius, and rotation. Moreover, tidal interactions and orbital motion could factor in, as well. In our figure 2.21 we also see several other peaks at higher frequencies, which are reminiscent of the overtones and mode couplings in figure 10 of Dimmelmeier et al. (2006). If we identify our peak at $f_{H1} = 4.03$kHz with the H_1 mode, then (in analogy to Dimmelmeier et al. (2006) Fig. 10), $f_{H1} - f_F = (4.03 - 1.14)\text{kHz} = 2.89\text{kHz}$, and $2f_F = 2.28$kHz, two frequencies that are indeed present

in our simulations. Although we find clear indications of axisymmetric $\ell = 2$-modes, we note that their power is smaller by two orders of magnitude, compared to the spherically symmetric, dominant F mode.

Turning to the low-spin run `S.05z`, we note that if, to first order, these frequencies scale like $f \sim \sqrt{\rho}$ (on dimensional grounds), then we expect to see $F = 1.22$kHz and ${}^2f = 1.49$kHz. This is very close to what is seen.

The density oscillations discussed in this section are reflected in analogous oscillations in various other diagnostic quantities, for instance, the orbital frequency, Fig. 2.12 and the quasilocal spin as shown in Fig. 2.14. The dominant frequencies 1.14kHz and 1.42kHz can be robustly identified throughout our data analysis. In figure 2.22 we plot the Fourier transform of the density, the $(2,0)$ and $(2,2)$ gravitational wave strains, the orbital angular velocity time derivative $d\Omega/dt$ and the measured spin χ for the `S.4z` run. All show peaks in power at these two frequencies, $F \sim 1.14$kHz and ${}^2f \sim 1.4$kHz. In simulations of eccentric, irrotational BNS systems, Gold et al. (2012) find that the close encouters of the two stars excite f-modes in each star of frequency 1.586 kHz.

We believe that the stellar modes are excited because the initial data are not in perfect equilibrium. We expect the quasi-equilibrium approximations that enter the initial data formalism to become less valid at higher spins, consistent with our observation that the high spin models exhibit stronger oscillations. This interpretation is strengthened by additional simulations of neutron stars at larger separation. Increasing the intial separation by a factor 1.5, while keeping the same rotation parameter ω as in the `S.4z`-case, we find quasi-normal oscillations of similar amplitude than in `S.4z`. If the oscillations were caused by the neglect of tidal deformation, we would expect the amplitude to drop with the 3rd power of separation, inconsistent with our results.

Finally, we point out that the radial rotation profile, cf. Eq. (2.49) influences the amplitude of the induced quasi-normal oscillations. If the initial data is constructed with the rotation profile Eq. (2.50), instead of equation 2.49, then the amplitude of the density

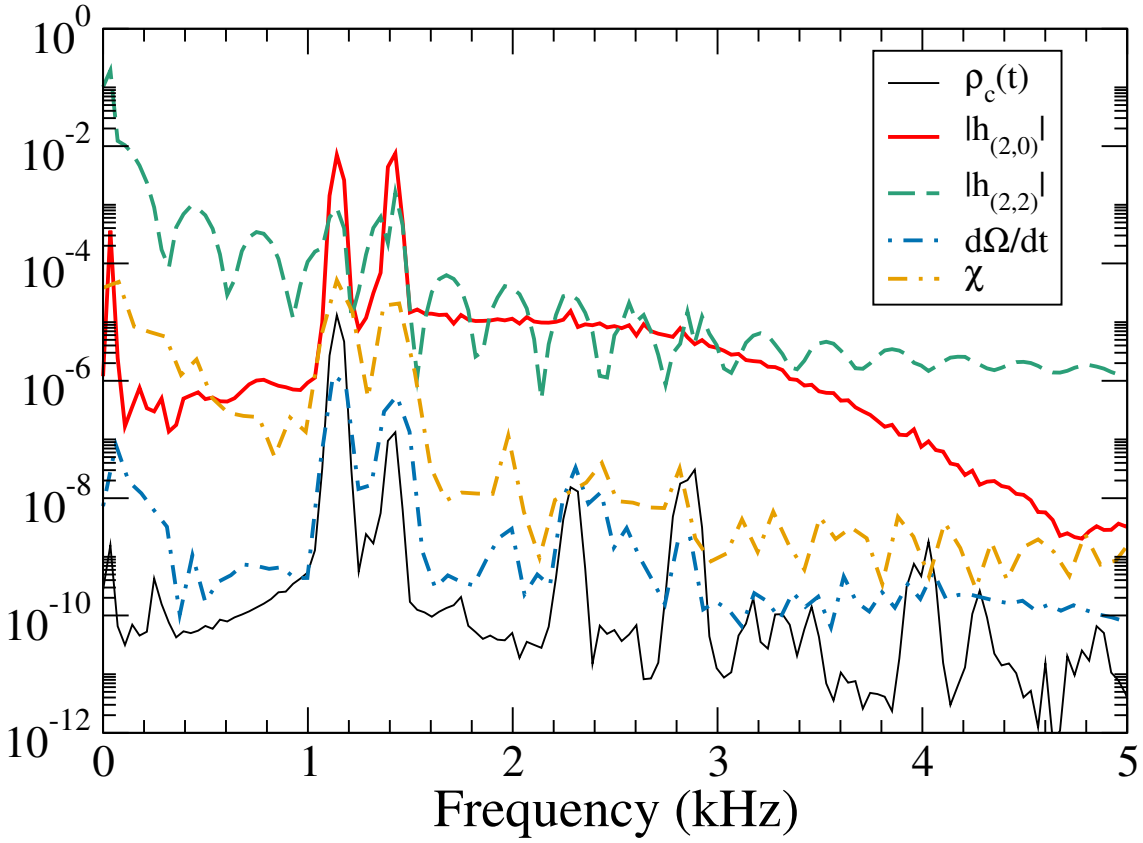

Figure 2.22: Fourier transforms of the central density $\rho_c(t)$, two modes of the magnitude of gravitational wave strain ($|h_{2,2}|$ and $|h_{2,0}|$), $\dot{\Omega}$ and χ for the `S.4z` run. All quantities show excess power at 1.14kHz and 1.4kHz, corresponding to the frequencies of excited neutron star quasi-normal modes.

oscillations for high spin doubles. This further supports our conjecture that the origin of this mode comes from non-equilibrium initial data.

2.6 Conclusions

In this chapter we implement Tichy's method (Tichy 2012) to construct binary neutron star initial data with arbitrary rotation rates. We demonstrate that our implementation is exponentially convergent, as expected for the employed spectral methods.

We measure the spin of the resulting neutron stars using the quasilocal angular momentum formalism (Brown & York 1993; Cook & Whiting 2007; Lovelace et al. 2008; Owen 2007). The resulting angular momentum is found to be nearly independent on the precise choice of extraction sphere, cf. Fig. 2.9, and provides a means to define the quasilocal angular momentum of each neutron star to about 1%, both in the initial data and during the evolution, cf. Fig. 2.13. We are able to construct binary neutron star initial data with dimensionless angular momentum of each star as large as $\chi = S/M^2 \sim 0.43$, both for the case of aligned spins, and also for a precessing binary where the initial neutron star spins are tangential to the initial orbital plane.

For irrotational BNS initial data sets, we find a quasilocal angular momentum of $\chi \sim 2 \times 10^{-4}$, cf. Fig. 2.8. This spin is small enough that present waveform modeling studies for BNS (e.g. (Bernuzzi et al. 2015; Baiotti et al. 2011; Baiotti et al. 2010)) are not yet limited by residual spin.

When evolving the initial data sets, the dimensionless spin measured in the initial data drops by about 0.004, and then remains constant through the 10 inspiral orbits for which we evolved the neutron star binaries. During these evolutions, we also demonstrated iterative eccentricity removal: By analyzing the orbital frequency $\Omega(t)$ during the first few orbits, we can correct the initial data parameters Ω_0 and $\dot{a}_0$, and thus decrease the orbital eccentricity from $e \approx 0.01$ to $e \lesssim 0.001$.

For the precessing simulation `S.4x`, we find precession of the neutron star spin directions. The numerically established precession of the spin axes and of the orbital angular momentum agrees well with post-Newtonian predictions.

The rotating neutron stars constructed here exhibit clear signals of exciting quasi-normal modes. We are able to identify multiple modes in the Fourier spectrum of the central density. The amplitude of the excited quasi-normal modes increases steeply with rotation rate of the neutron stars. For `S-.05z` (spin magnitude $\chi = 0.045$) the density oscillations have peak-to-peak amplitude of 0.6%, raising to 20% for the two runs with high spins (`S.4x` and `S.4z`).

As discussed in the appendix below, the results presented in this chapter have since been updated due to the correction of a code error. Now, the density oscillations, for $\chi \sim 0.4$*, have been decreased from* 20% *to* 0.5%*, and the highest neutron star spin we can create has increased from* $\chi \sim 0.43$ *to* $\chi \sim 0.65$*. The full results are summarized below.*

Appendix

Chapter 2 presented a computational code for the construction and evolution of binary neutron stars with arbitrary spin vectors. Following (Tichy 2012), the 3-velocity of the neutron star fluid in an inspiraling binary is written as the sum of an irrotational part and a rotational part,

$$U^i = \frac{\Psi^{-4}\tilde{\gamma}^{ij}}{h\gamma_n}\left(\nabla_j\phi + W_j\right). \tag{2.74}$$

Here Ψ denotes the conformal factor, $\tilde{\gamma}_{ij}$ the conformal spatial metric, h the specific enthalpy, γ_n the Lorentz term $\gamma_n = \left(1 - \gamma_{ij}U^iU^j\right)^{-1/2}$, and ϕ the irrotational velocity potential. The vector W_i represents a rotation term designed to endow a uniform rotation to the star,

$$W_i = \epsilon_{ijk}\omega^j r^k, \tag{2.75}$$

where ω^j is the rotation vector chosen by hand, and r^k is the distance to the center of the star. In this construction, the solution of the Euler equation is

$$h = \sqrt{L^2 - \left(\nabla_i\phi + W_i\right)\left(\nabla^i\phi + W^i\right)}, \tag{2.76}$$

where

$$L^2 = \frac{(x+y) + \sqrt{x^2 + 2xy}}{2\alpha^2}, \tag{2.77}$$

$$x = \left(\beta^i\nabla_i\phi + C\right)^2, \tag{2.78}$$

and

$$y = 2\alpha^2\left(\nabla_i\phi + W_i\right)W^i. \tag{2.79}$$

Here C denotes the Euler constant, α the lapse function and β^i the shift-vector.

The code reported in Chapter 2 has a mistake in the computation of h. Instead of Eq. 2.76, we computed the following quantity.

$$h' = \sqrt{L^2 - (\nabla_i \phi)\,(\nabla^i \phi)}, \tag{2.80}$$

and instead of Eq. (2.79), we computed

$$y' = (\nabla_i \phi + W_i)\, W^i. \tag{2.81}$$

This error causes h' to deviate from the correct h by

$$\begin{aligned} h'^2 - h^2 =& \frac{(y' - y)}{2\alpha^2} + \frac{\sqrt{x^2 + 2xy'} - \sqrt{x^2 + 2xy}}{2\alpha^2} \\ &+ W_i W^i + 2W^i \nabla_i \phi. \end{aligned} \tag{2.82}$$

For non-rotating stars, $W^i = 0$, the error disappears: $h' = h$. In the limit of fast rotation, i.e. large W, we expect this difference to be dominated by the terms quadratic in W,

$$h'^2 - h^2 \approx \frac{W^2}{2\alpha^2}. \tag{2.83}$$

This implies the constructed BNS had an enthalpy lower than the correct equilibrium configurations. This picture is consistent with Fig. 2.20 (and Fig. 2..23 below): for high NS spin, the central density $\rho(t)$ immediately *increases* in an evolution, and oscillates around values *larger* than the initial density.

We now construct initial data with the same input parameters as for the case `S0.4z - Ecc3` in chap. 2, and evolve it with the same evolution code. For this evolution, we find:

1. Convergence of the Hamiltonian and Momentum constraints, and of the ADM energy and ADM angular momentum do not appreciably differ. Convergence of the neutron star spin is somewhat improved.

2. As noted in Gourgoulhon & Bonazzola (1994), the absolute difference between the Komar mass M_K and the ADM energy $M_{\rm ADM}$ is an indicator of deviations from equilibrium, as $M_K = M_{\rm ADM}$ for equilibrium systems in circular orbits. The difference between the Komar mass M_K and ADM energy $E_{\rm ADM}$ is reduced by an order of magnitude, from $|M'_K - M'_{\rm ADM}| = 2.6\times10^{-3}$ to $|M_K - M_{\rm ADM}| = 2.1\times10^{-4}$. This supports the idea that the neutron stars themselves are closer to being in equilibrium.

3. Evolution of the corrected initial data yields substantially smaller density oscillations. Figure 2..23 shows the density oscillations for the evolution reported in chap. 2 and for the evolution of the corrected initial data. Peak-to-peak density oscillations are reduced from $\sim 20\%$ to about 0.5%. Density oscillations of $\sim 0.5\%$ also occur in our simulations of non-spinning binary neutron stars. The frequency of density-oscillation is unchanged, consistent with our interpretation that it represents a quasi-normal mode. We note that the phase of oscillation has changed by approximately half of a period.

4. The orbital frequency $\Omega(t)$ has significantly smaller oscillations at periods $\approx 200M_\odot$. Figure 2..24 compares $\dot{\Omega}(t)$ between evolutions of the old (erroneous) and new (corrected) initial data. High-frequency oscillations are strongly suppressed with the corrected initial data, allowing a clearer view of the lower-frequency sinusoidal features which are due to the overall trajectory of the binary.

5. The corrected code yields higher central density and therefore more compact stars (at same mass). At the same rotational frequency parameter ω (as defined in Eq. 2.75) we therefore expect the corrected code to yield stars with smaller angular momentum. This is indeed the case as is shown in Fig. 2..25. The subsequent evolution of the spin magnitude is comparable for both incorrect and corrected initial data (cf. inset of Fig. 2..25) although the oscillations present in the data are

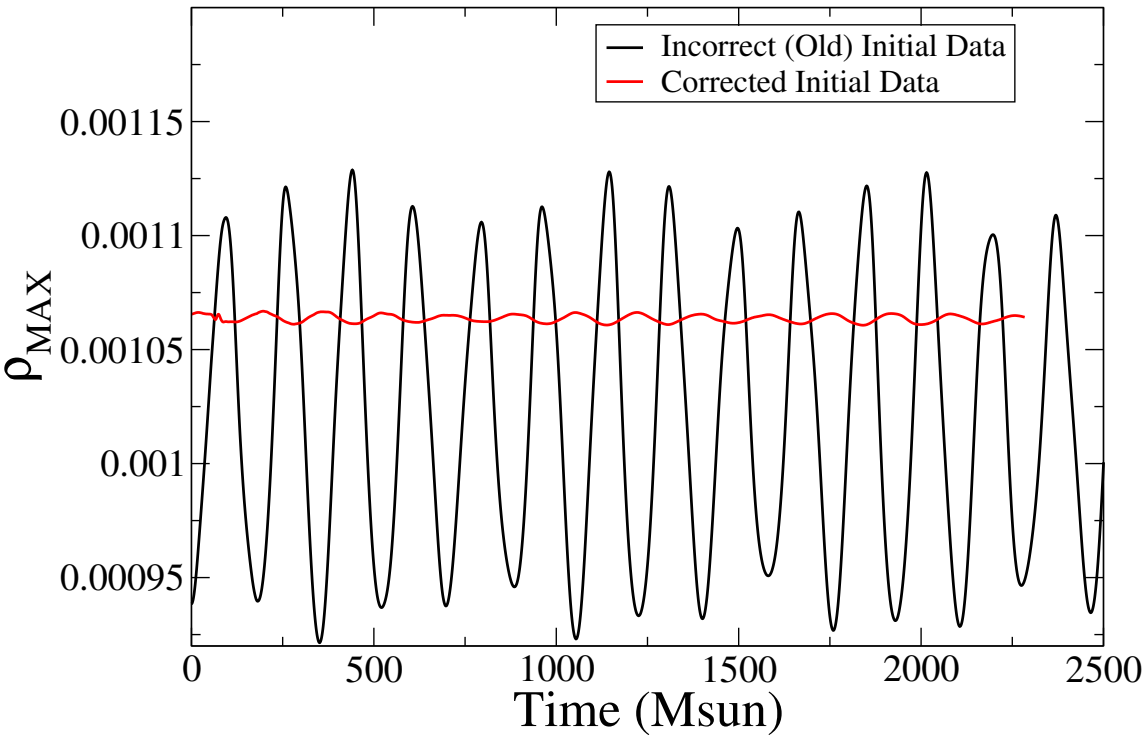

Figure 2..23: Density oscillations for the `S0.4z` run from chap. 2 and a new evolution of the corrected initial data.

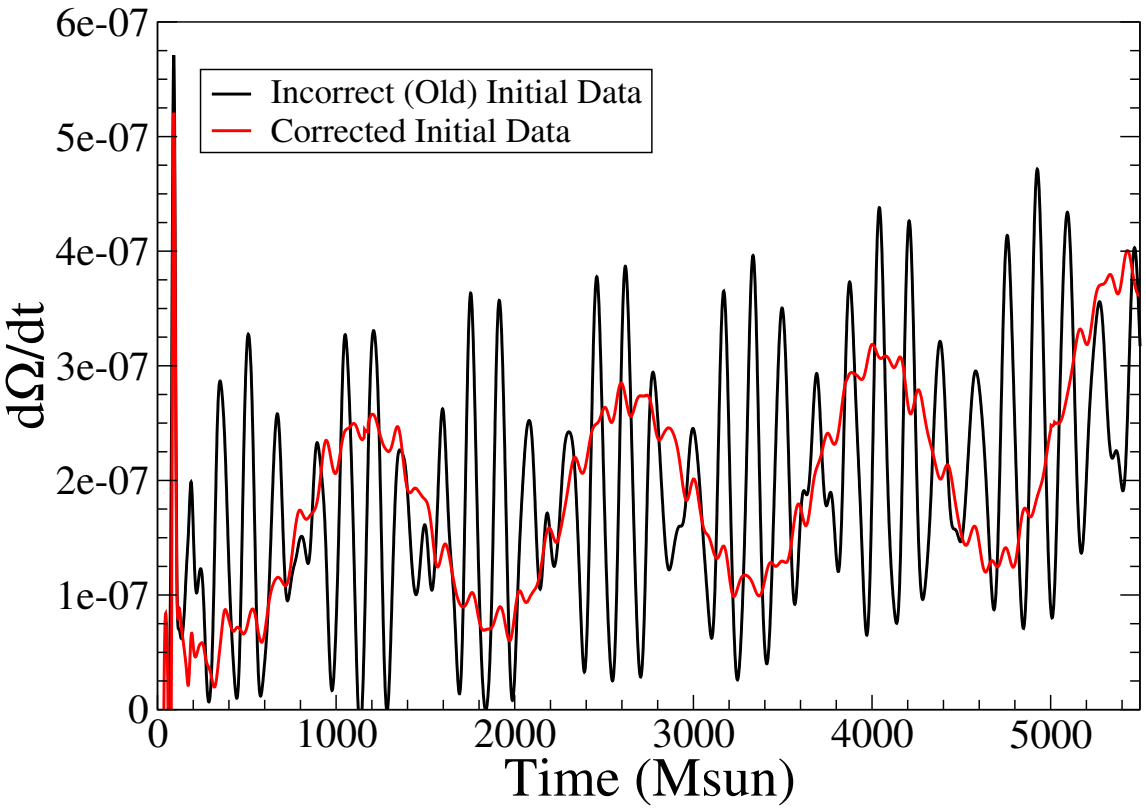

Figure 2..24: Derivative of the orbital angular frequency from the S0.4z run from chap. 2 and from a new run with the same parameters.

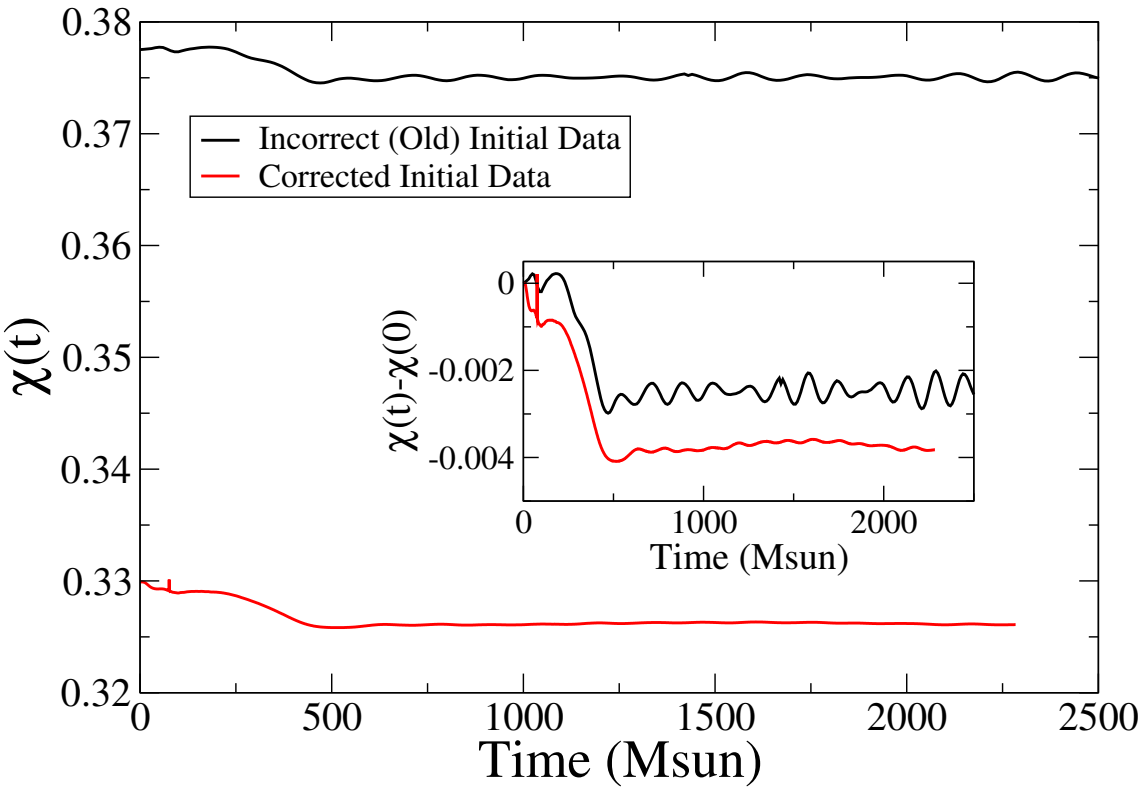

Figure 2..25: Dimensionless spin, $\chi = J/M_{\rm ADM}^2$, measured during the evolution of the S0.4z-Ecc3 run, computed from old and corrected initial data. The inset subtracts the value of the spin at $t = 0$ from both curves.

reduced. The cause of the early peak in spin in Fig. 2..25 is unclear.

We also find that the corrected code is capable of solving initial data sets for higher values of the NS rotation parameter ω. Figure 2..25 already showed that at the same rotation parameter ω, the corrected code yields smaller spin. Computing a sequence of initial data sets at different ω, we obtain Figure 2..26. For small ω, the $\chi(\omega)$ relation is unchanged, indicating that the low-spin evolution reported in Tacik et al. (2015) is probably only mildly affected. For large ω, the initial data solver can create ID at spins up to $\chi \sim 0.63$, a factor ~ 1.4 larger than the erroneous code. This is, in fact, greater than the break-up spin of $\chi = 0.57$ found for $\Gamma = 2$ polytropes found in Ansorg et al. (2003).

Being now able to construct ID at larger NS spins, we evolve an equal-mass, equal-

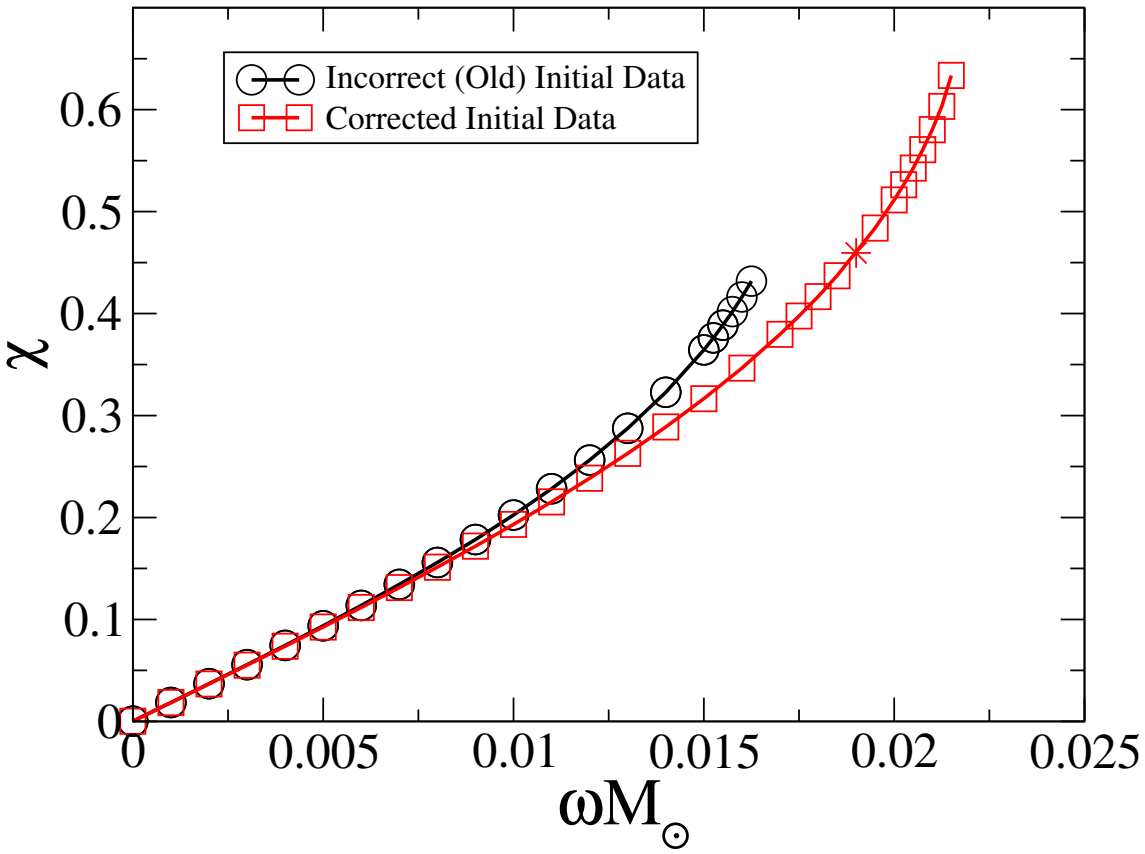

Figure 2..26: χ as a function of ω in the initial data. The black curve is from Fig. 8 of Tacik et al. (2015), while the red curve is generated with the corrected initial data. The astericks indicates the configuration we evolve in Fig. 2..27.

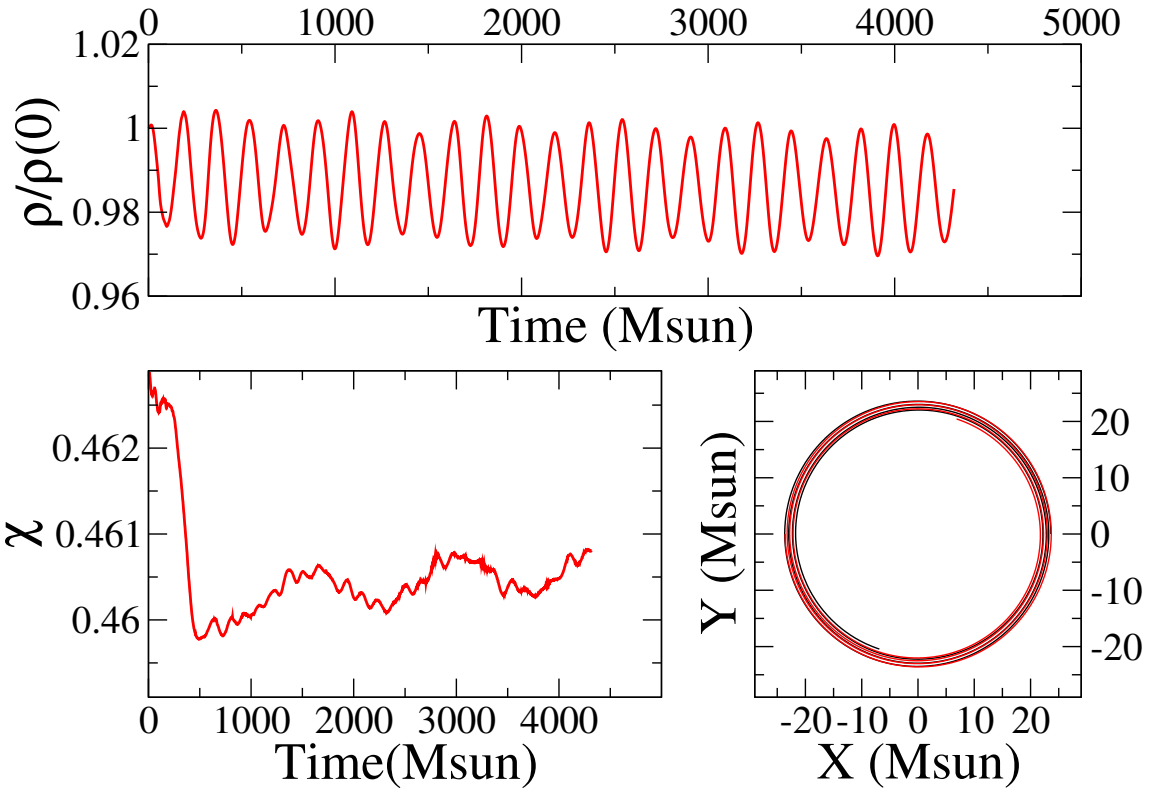

Figure 2..27: A snapshot of an evolution with $\omega = 0.019$. The top panel shows the normalized density oscillations. The bottom-left panel shows the measured spin of a star. The bottom-right panel shows the orbtis of the stars as they inspiral.

spin ID set with $\omega = 0.019 M_{\odot}^{-1}$, $\chi = 0.46$. In figure 2..27 we present a snapshot of the run, plotting the normalized density oscillations, spin, and the trajectories of the stars. The peak-to-peak density oscillations are now about 2%, higher than in the $\chi \sim 0.33$ evolution, but still much smaller than for the erroneous initial data despite the larger NS spin.

Chapter 3

Initial Data for Black Hole–Neutron Star Binaries, with Rotating Stars

The material in this chapter is based on "Initial data for black hole–neutron star binaries, with rotating stars" by Nick Tacik, Francois Foucart, Harald P. Pfeiffer, Curran Muhlberger, Lawrence E. Kidder, Mark A. Scheel, Béla Szilágyi. Submitted to Classical and Quantum Gravity. arXiv:1607.07962

3.1 Chapter Summary

The coalescence of a neutron star with a black hole is a primary science target of ground-based gravitational wave detectors. Constraining or measuring the neutron star spin directly from gravitational wave observations requires knowledge of the dependence of the emission properties of these systems on the neutron star spin. This chapter lays foundations for this task, by developing a numerical method to construct initial data for black hole–neutron star binaries with arbitrary spin on the neutron star. We demonstrate the robustness of the code by constructing initial-data sets in large regions of the parameter space. In addition to varying the neutron star spin-magnitude and spin-direction, we also explore neutron star compactness, mass-ratio, black hole spin, and black hole

spin-direction. Specifically, we are able to construct initial data sets with neutron stars spinning near centrifugal break-up, and with black hole spins as large as $S_{\rm BH}/M_{\rm BH}^2 = 0.99$.

3.2 Introduction

The spectacular detection of merging binary black holes by Advanced LIGO (Abbott et al. 2016a;b) marks the beginning of the era of gravitational wave astronomy. With binary black holes detected through gravitational waves, and binary neutron stars known from radio observations (Hulse & Taylor 1975b), mixed black-hole - neutron star (BH-NS) binaries are now the only compact object binary whose existence has not yet been directly observed.

BH-NS systems are an important potential source of gravitational waves for advanced ground-based detectors, with an expected event rate of approximately ten per year (Abadie et al. 2010), albeit with a large uncertainty. In addition to gravitational waves, BH-NS mergers can be an important source of electromagnetic radiation (Li & Paczynski 1998; Roberts et al. 2011; Metzger & Berger 2012; Piran et al. 2013; Rosswog et al. 2013; Tanaka et al. 2014) and give further clues to the violent processes that occur during the merger. If a massive disk is left from the merger, for instance, it could lead to a short-duration gamma ray burst (SGRB) and material ejected during the merger could radiate a signal such as a "kilonova" (Metzger & Berger 2012).

Direct numerical solutions are one of the primary means to explore coalescing compact object binaries (e.g. Baumgarte & Shapiro (2010); Lehner & Pretorius (2014); Pfeiffer (2012)). Such simulations are important to accurately study both the gravitational waves and electromagnetic emission produced by compact object mergers. Fully general relativistic simulations of mixed BH-NS binaries have been performed for about 10 years (Shibata & Uryu 2007; Faber et al. 2006) investigating the importance of mass-ratio (Foucart et al. 2014; 2013b; Foucart et al. 2012), black hole spin (East et al. 2012a; Shibata & Uryu 2006; Foucart et al. 2013a; Foucart et al. 2011; Kawaguchi et al. 2015;

Etienne et al. 2009), eccentricity (East et al. 2015; 2012b; Stephens et al. 2011), equations of state (Duez et al. 2010; Kyutoku et al. 2010; Kawaguchi et al. 2015; Foucart et al. 2013a), magnetic fields (Chawla et al. 2010; Paschalidis et al. 2015; Kiuchi et al. 2015b; Etienne et al. 2012; Etienne et al. 2012), neutrino physics (Foucart et al. 2015), disk formation (Lovelace et al. 2013; Shibata & Taniguchi 2008; Pannarale et al. 2015), outflows (Deaton et al. 2013; Kyutoku et al. 2013) and electromagnetic emission signatures (Paschalidis et al. 2013; Kawaguchi et al. 2016).

The parameter space for BH-NS binary simulations is relatively large. The mass ratio, q, NS compactness, C, and black hole spin, $\vec{\chi}$, have been of particular interest in numerical simulations, because they have the most profound impact of the evolution of the binary, and are the primary variables to control whether the neutron star tidally disrupts (Foucart 2012). One aspect that has not been studied, however, is the effect of neutron star spin. With the exceptions of Shibata & Uryu (2007); East et al. (2015), all simulations to date use irrotational neutron stars in their BH-NS binaries. For NS-NS binaries, in contrast, a significant number of studies investigate spinning neutron stars (Baumgarte & Shapiro 2009; Tichy 2011; East et al. 2012c; Tichy 2012; Bernuzzi et al. 2014; Kastaun et al. 2013; Tsatsin & Marronetti 2013; Dietrich et al. 2015b; East et al. 2015; Tsokaros et al. 2015; Tacik et al. 2015). Since no BH-NS binaries have been directly observed, the NS spins are, at least observationally, unconstrained. A spinning neutron star will affect the gravitational waveforms and cause the inspiral to proceed more slowly (for spin-aligned NS). The spin can be important for gravitational wave detection and can cause appreciable mismatch with non-spinning templates, especially at lower BH-NS mass ratios (Ajith 2011). We also expect the spin to also affect the time of NS disruption, as the stellar material will be less tightly bound to the stellar surface.

Any evolution must start with initial data, and so in this chapter, we consider the construction of fully general-relativistic initial data sets for BH-NS binaries with generic spin on the neutron star. We combine the techniques of constructing BH-NS initial

data without NS-spin (Foucart et al. 2008; Henriksson et al. 2016) with the rotating-NS formalism developed by Tichy (2012) as implemented in Tacik et al. (2015) (cf. chap. 2). We show that this approach, implemented in the Spectral Einstein Code `SpEC`[1], is robust and can construct BH-NS binaries with NS spin magnitudes up to nearly rotational break-up (dimensionless spin $\chi_{\rm NS} \sim 0.7$) and arbitrary rotation axis. The code also successfully constructs binaries with mass-ratios from 2 to 10, and with black hole spins $0 \leq \chi_{\rm BH} \leq 0.99$.

The structure of this article is as follows: In section 3.3, we review the standard numerical relativity initial data formalism, as well as the formalism developed in Tichy (2011) to create binaries with spinning NS, and discuss how this is extended to BH-NS systems. In section 3.4 we discuss the numerical methods used by our initial data solver. In section 3.5, we create a number of initial data sets to demonstrate the robustness of our solver by constructing BH-NS initial data sets with various values of neutron star spin, black hole spin, and mass ratio. We conclude with a discussion in section 3.6. Throughout this article we use units where $G = c = M_\odot = 1$.

3.3 Initial Data Formalism

In this section we will discuss the formalism used to solve the Einstein field equations and create quasi-equilibrium initial data for BH-NS binaries with spinning neutron stars. We employ the extended-conformal thin-sandwich formalism (Pfeiffer & York 2003; York 1999) to cast the Einstein constraint equations as a set of elliptic equations. Neutron star spin is incorporated with the approach developed in Tichy (2011), and the equations are solved by a generalization of the initial data solver developed in Foucart et al. (2008).

We begin with the $3+1$ decomposition of the space-time metric tensor,

$$g_{\mu\nu} dx^\mu dx^\nu = -\alpha^2 dt^2 + \gamma_{ij} \left(dx^i + \beta^i dt\right) \left(dx^j + \beta^j dt\right), \tag{3.1}$$

[1] http://www.black-holes.org/SpEC.html

where α is the lapse function, β^i is the shift vector, and γ_{ij} is the induced metric on a spatial hypersurface $\Sigma(t)$. The normal vector n^μ to $\Sigma(t)$ is related to the coordinate time t by $t^\mu = \alpha n^\mu + \beta^\mu$. The extrinsic curvature of $\Sigma(t)$ is given by $K_{\mu\nu} = -\frac{1}{2}\mathcal{L}_n \gamma_{\mu\nu}$, where $\gamma_{\mu\nu} = g_{\mu\nu} + n_\mu n_\nu$ and $\mathcal{L}_n$ is the Lie derivative in the direction of n^μ. By construction $K_{\mu\nu}$ is a purely spatial tensor, i.e. $K_{\mu\nu}n^\mu = 0 = K_{\nu\mu}n^\mu$, and so we restrict our attention to the spatial part of the extrinsic curvature, K^{ij}. It is convenient to decompose it into its trace and trace-free parts,

$$K^{ij} = A^{ij} + \frac{1}{3}K\gamma_{ij}. \tag{3.2}$$

The matter in the system is modelled with the stress-energy tensor of a perfect fluid

$$T_{\mu\nu} = (\rho + P)\, u_\mu u_\nu + P g_{\mu\nu}, \tag{3.3}$$

where ρ is the fluid's energy density, P is its pressure, and u^μ is its four-velocity. It is further useful to define the projections of the matter quantities,

$$E = T^{\mu\nu} n_\mu n_\nu, \tag{3.4}$$

$$S = \gamma^{ij}\gamma_{i\mu}\gamma_{j\nu}T^{\mu\nu}, \tag{3.5}$$

$$J^i = -\gamma^i_\mu T^{\mu\nu} n_\nu. \tag{3.6}$$

The spatial metric is conformally scaled,

$$\gamma_{ij} = \Psi^4 \tilde{\gamma}_{ij}, \tag{3.7}$$

where Ψ denotes the conformal factor and $\tilde{\gamma}_{ij}$ the conformal metric. Other quantities are conformally scaled as follows:

$$E = \Psi^{-6}\tilde{E}, \tag{3.8}$$

$$S = \Psi^{-6}\tilde{S}, \tag{3.9}$$

$$J^i = \Psi^{-6}\tilde{J}^i, \tag{3.10}$$

$$A^{ij} = \Psi^{-10}\tilde{A}^{ij}, \tag{3.11}$$

$$\alpha = \Psi^6 \tilde{\alpha}. \tag{3.12}$$

$\tilde{A}^{ij}$ is related to the shift and to the time derivative of the conformal metric, $\tilde{u}_{ij} = \partial_t \tilde{\gamma}_{ij}$, by

$$\tilde{A}^{ij} = \frac{1}{2\tilde{\alpha}} \left[\left(\tilde{\mathrm{L}}\beta \right)^{ij} - \tilde{u}^{ij} \right], \tag{3.13}$$

where $\tilde{\mathrm{L}}$ is the conformal longitudinal operator,

$$\left(\tilde{\mathrm{L}}V \right)^{ij} = \tilde{\nabla}^i V^j + \tilde{\nabla}^j V^i - \frac{2}{3}\tilde{\gamma}^{ij}\tilde{\nabla}_k V^k. \tag{3.14}$$

With these definitions and conformal rescalings, the Einstein constraint equations, and the Einstein evolution equation for the trace of the extrinsic curvature yield a set of five coupled elliptic equations, called the extended conformal thin sandwich (XCTS) equations (Pfeiffer & York 2003). They are written in the form

$$\tilde{\nabla}^2\Psi - \frac{1}{8}\Psi\tilde{R} - \frac{1}{12}\Psi^5 K^2 + \frac{1}{8}\Psi^{-7}\tilde{A}_{ij}\tilde{A}^{ij} = -2\pi\Psi^{-1}\tilde{E}, \tag{3.15}$$

$$2\tilde{\alpha}\left[\tilde{\nabla}_j \left(\frac{1}{2\tilde{\alpha}} \left(\tilde{L}\beta \right)^{ij} \right) - \tilde{\nabla}_j \left(\frac{1}{2\tilde{\alpha}} \tilde{u}^{ij} \right) - \frac{2}{3}\Psi^6 \tilde{\nabla}^i K \right] = 16\pi\tilde{\alpha}\Psi^4 \tilde{J}^i, \tag{3.16}$$

$$\tilde{\nabla}^2\left(\tilde{\alpha}\Psi^7 \right) - \left(\tilde{\alpha}\Psi^7 \right)\left[\frac{1}{8}\tilde{R} + \frac{5}{12}\Psi^4 K^2 + \frac{7}{8}\Psi^{-8}\tilde{A}_{ij}\tilde{A}^{ij} \right] + \Psi^5\left(\partial_t K - \beta^k \partial_k K \right) = -2\pi\tilde{\alpha}\Psi^5\left(\tilde{E} + 2\tilde{S} \right). \tag{3.17}$$

These equations are solved for the conformal factor, Ψ, the shift, β^i, and the densitized lapse, $\tilde{\alpha}\Psi^7$. Equations (3.15)–(3.17) constitute the gravitational sector of the initial data construction. The free data are $\tilde{\gamma}_{ij}$, $\tilde{u}_{ij}$, K and $\partial_t K$. Since we will be constructing initial data in a corotating coordinate system, the free data corresponding to time-derivatives can be naturally set to zero: $\tilde{u}_{ij} = \partial_t K = 0$. The choice of the conformal metric and K will be discussed in section 3.4.

Equations (3.15)–(3.17) require boundary conditions at large separation, and at the excision boundary of the black hole. At infinity[2] are the requirement of a Minkowski

[2]In practice we place the outer boundary of the computational grid at $R = 10^{10}$.

metric in the inertial frame (Foucart et al. 2008):

$$\boldsymbol{\beta}_0 = 0, \tag{3.18}$$

$$\alpha\Psi = 1, \tag{3.19}$$

$$\Psi = 1. \tag{3.20}$$

Here $\boldsymbol{\beta}_0$ is the shift in the inertial frame, which is related to the shift vector $\boldsymbol{\beta}$ by

$$\boldsymbol{\beta} = \boldsymbol{\beta}_0 + \boldsymbol{\Omega} \times \mathbf{r} + \dot{a}_0 \mathbf{r}, \tag{3.21}$$

where $\boldsymbol{\Omega}$ is the orbital angular velocity of the system and $\dot{a}_0$ is a term used to give the system an infall velocity $\mathbf{v} = \dot{a}_0 \mathbf{r}$. The interior of the black hole is excised from the computation domain. The boundary conditions at excision surface, $\mathcal{H}$, are (Cook & Pfeiffer 2004):

$$\tilde{s}^k \nabla_k \log \Psi = -\tfrac{1}{4}\left(\tilde{h}^{ij}\tilde{\nabla}_i \tilde{s}_j - \Psi^2 h^{ij} K_{ij}\right) \quad \text{on } \mathcal{H}, \tag{3.22}$$

$$\beta_\perp = \alpha \quad \text{on } \mathcal{H}, \tag{3.23}$$

$$\beta^i_\parallel = \Omega^{BH}_j x_k \epsilon^{ijk} \quad \text{on } \mathcal{H}, . \tag{3.24}$$

These derive from the assumption the black hole is in equilibrium and that the excision surface is an apparent horizon. In Eq. (3.22), $s^i = \Psi^{-2}\tilde{s}^i$ denotes the outward pointing unit normal to the apparent horizon surface and $h^{ij} = \gamma^{ij} - s^i s^j$ is the induced metric on the surface. In Eq. (3.24), $\epsilon^{ijk} = \{\pm 1, 0\}$, is the totally anti-symmetric symbol, x_i are the Cartesian coordinates relative to the center of the black hole and Ω^{BH}_j is a free vector that determines the spin of the black hole.

Let us next focus on the matter content of the neutron star, which enters through $\tilde{E}$, $\tilde{S}$, and $\tilde{J}^i$. The energy density of the fluid is $\rho = \rho_0\,(1+\epsilon)$, where ρ_0 is the baryon density and ϵ is the internal energy. The specific enthalpy of the fluid is

$$h = 1 + \epsilon + \frac{P}{\rho_0}. \tag{3.25}$$

It is convenient to introduce a three-velocity U^μ satisfying

$$U^\mu n_\mu = 0, \tag{3.26}$$

$$u^\mu = \gamma_n \left(n^\mu + U^\mu\right). \tag{3.27}$$

These conditions imply

$$\gamma_n = \left(1 - \gamma_{ij} U^i U^j\right)^{-1/2}. \tag{3.28}$$

Furthermore, we introduce

$$U_0^i = \frac{\beta^i}{\alpha}, \tag{3.29}$$

$$\gamma_0 = \left(1 - \gamma_{ij} U_0^i U_0^j\right)^{-1/2}, \tag{3.30}$$

$$\gamma = \gamma_n \gamma_0 \left(1 - \gamma_{ij} U^i U_0^j\right). \tag{3.31}$$

Following Tichy (2011), the three-velocity is written as the sum of an irrotational part (the gradient of a potential ϕ) and a rotational part W^i,

$$U^i = \frac{\Psi^{-4}\tilde{\gamma}^{ij}}{h\gamma_n}\left(\partial_j \phi + W_j\right). \tag{3.32}$$

W^i is a freely chosen, divergence-free vector field in this formalism; we will discuss the choice of W^i in section 3.4.

The matter fluid must satisfy the continuity equation and the Euler equation. Under the assumptions made in Tichy (2011), the continuity equation is a second order elliptic equation for the potential ϕ:

$$\frac{\rho_0}{h}\nabla^\mu \nabla_\mu \phi + \left(\nabla^\mu \phi\right)\nabla_\mu \frac{\rho_0}{h} = 0. \tag{3.33}$$

This can be re-written as

$$\begin{aligned}\rho_0 \left\{ -\tilde{\gamma}^{ij}\partial_i\big(\partial_j\phi + W_j\big) \right. &+ \left. \frac{h\beta^i\Psi^4}{\alpha}\partial_i\gamma_n + hK\gamma_n\Psi^4 + \left[\tilde{\gamma}^{ij}\tilde{\Gamma}^k_{ij} + \gamma^{ik}\partial_i\big(\ln\frac{h}{\alpha\Psi^2}\big)\right]\big(\partial_k\phi + W_k\big)\right\} \\ &= \tilde{\gamma}^{ij}\big(\partial_i\phi + W_i\big)\partial_j\rho_0 - \frac{h\gamma_n\beta^i\Psi^4}{\alpha}\partial_i\rho_0. \end{aligned} \tag{3.34}$$

Turning to the Euler equation, it can be solved for the specific enthalpy h as shown in Tichy (2011):

$$h = \sqrt{L^2 - \left(\nabla_i \phi + W_i\right)\left(\nabla^i \phi + W^i\right)}, \tag{3.35}$$

where

$$L^2 = \frac{b + \sqrt{b^2 - 4\alpha^4 \left(\left(\nabla_i \phi + W_i\right) W^i\right)^2}}{2\alpha^2} \tag{3.36}$$

and

$$b = \left(\beta^i \nabla_i \phi + C\right)^2 + 2\alpha^2 \left(\nabla_i \phi + W_i\right) W^i. \tag{3.37}$$

The boundary condition on ϕ at the surface of the neutron star are deduced from the $\rho_0 \to 0$ limit of the continuity equation:

$$\tilde{\gamma}^{ij} \left(\partial_i \phi + W_i\right) \partial_j \rho_0 = \frac{h \gamma_n \beta^i \Psi^4}{\alpha} \partial_i \rho_0. \tag{3.38}$$

Note that ϕ is only solved for inside the neutron stars, while the metric variables are solved for everywhere.

The force balance equation at the center of the neutron star, c^i is

$$\nabla \log h = 0 \qquad \text{at } x^i = c^i. \tag{3.39}$$

We can re-write this equation as Tichy (2011)

$$\nabla \ln\left(\alpha^2 - \gamma_{ij} \beta^i \beta^j\right) = -2 \nabla \ln \Gamma, \tag{3.40}$$

where

$$\Gamma = \frac{\gamma_n \left(1 - \left(\beta^i + \frac{W^i \alpha}{h \gamma_n}\right) \frac{\nabla_i \phi}{\alpha h \gamma_n} - \frac{W_i W^i}{\alpha^2 \gamma_n^2}\right)}{\sqrt{1 - \left(\frac{\beta^i}{\alpha} + \frac{W^i}{h \gamma_n}\right)\left(\frac{\beta_i}{\alpha} + \frac{W_i}{h \gamma_n}\right)}}. \tag{3.41}$$

Since $\beta^i = \beta_0^i + \vec{\Omega} \times \vec{r} + \dot{a}\vec{r}$, where β_0^i is the shift in the inertial frame, this is a second order equation for the orbital frequency Ω, when Γ is held constant. If desired, this equation can be solved to find a best guess for the orbital frequency. Alternatively, eccentricity removal techniques, such as those used in Buonanno et al. (2011a); Tacik et al. (2015) can be used to find the best value of the orbital frequency.

W^i is chosen so as to give the NS a uniform rotational profile. Following our work in Tacik et al. (2015), we use

$$W^i = \epsilon^{ijk}\omega^j r^k, \tag{3.42}$$

where r^k is the position vector relative to the center of the star, and ω^j is a freely chosen constant vector. Outside a radius larger than the neutron star size, W^i is set to zero, to avoid low density material at high radius leading to spurious large velocities. This is particularly important for large neutron star spins, or when the black hole mass is much larger than the neutron star mass.

3.4 Numerical Methods

3.4.1 Domain Decomposition

The XCTS equations 3.15, 3.16, and 3.17, combined with the continuity equation 3.34 form a set of six non-linear coupled elliptic equations that must be solved. We use the pseudo-spectral multi-domain elliptic solver developed in Pfeiffer et al. (2003) and enhanced to incorporate matter in Foucart et al. (2008); Tacik et al. (2015); Haas et al. (2016).

The computational domain has the black hole interior excised, and extends to some large outer boundary ($R = 10^{10}$ in practice). To cover this computational domain with spectral expansions, we split the domain into multiple subdomains as indicated in figure 3.1, each one with its own spectral expansion: The neutron star is covered by a spherical shell with outer boundary deformed to coincide with the boundary of the neutron star (cf. Eq. (3.55) below). To avoid having to deal with regularity conditions at the origin, this shell does not cover the origin; rather a small cube is placed there which overlaps the spherical shell. The neutron star is surrounded by one further spherical shell. The black hole is surrounded by two concentric spherical shells, where the inner boundary of the inner shell coincides with the apparent horizon, where the boundary

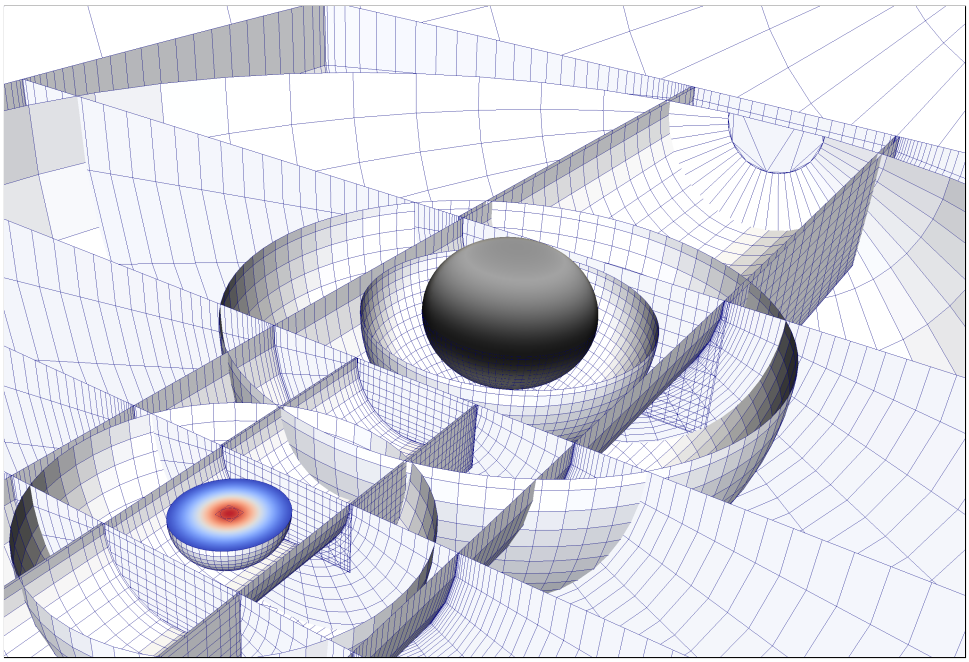

Figure 3.1: Visualization of the BH-NS domain decomposition. The object on the left is the neutron star, with the colours representing its density. The black object on the right represents the apparent horizon of the black hole. The blue wireframes represent the various spheres, cylinders and rectangular parallelepipeds in the domain.

conditions (3.22) – (3.24) are imposed. Three rectangular parallelepipeds surround the axis passing through the centers of the BH and the NS - one between them and one on each side of the objects. An additional eight cylindrical shells are placed around the same axis to cover the intermediate field region. The far-field region is covered by a large spherical shell whose outer boundary is placed at $R = 10^{10}$ using an inverse radial mapping.

All variables (metric and hydrodynamical) are decomposed on sets of basis functions on each subdomain. The type of basis function depends on the topology on the subdomain. Finite difference schemes are needed for hydrodynamical quantities during evolutions so as to capture shocks, but for initial data, where shocks are not present, spectral methods are suitable and exponential convergence can be achieved. The resolution of each domain is synonymous with the number of collocation points used. The resolution of each subdomain is initialized manually at the start of the initial data solve; subsequently, the resolution is adjusted several times using an adaptive mesh refinement (AMR) scheme (see step 13). To discuss the resolution of the computational domain for the purpose of convergence tests, we denote by N the total number of collocation points in all subdomains. $N^{1/3}$ is then a measure of linear resolution. A typical initial data solve starts with, $N^{1/3} \sim 33$ and ends with $N^{1/3} \sim 80$.

3.4.2 Diagnostics

The angular momentum of the black hole is computed as (Lovelace et al. 2008; Foucart et al. 2008)

$$S = \frac{1}{8\pi} \oint_{\mathcal{H}} \phi^i s^j K_{ij} dA. \tag{3.43}$$

In a space-time with aziumuthal symmetry, ϕ^i would represent the exact azimuthal Killing vector field generated by this symmetry. Since azimuthal symmetry is not present in a binary system, we instead use an *approximate* Killing vector. It is computed by solving a shear minimization eigenvalue problem - see Cook & Whiting (2007); Lovelace et al.

(2008) for details. The dimensionless spin is defined as

$$\chi = \frac{S}{M^2}, \tag{3.44}$$

where M is the Christodoulou mass,

$$M^2 = M_{\rm irr}^2 + \frac{S^2}{4M_{\rm irr}^2}. \tag{3.45}$$

The irreducible mass is related to the surface area of the apparent horizon, A,

$$M_{\rm irr} = \sqrt{A/16\pi}. \tag{3.46}$$

We employ similar surface integrals to compute the dimensionless spin of the neutron star. In particular we use Eq. 3.43, with $\mathcal{H}$ replaced by the neutron star's surface, as defined in Eq. 3.55 to compute the star's angular momentum $S_{\rm NS}$.

To define the neutron star's mass, we use the Arnowitt-Deser-Misner (ADM) mass $M_{\rm ADM,NS}$ of an *isolated* neutron star with same rotation. In particular, we use the methods described in Cook et al. (1994) to solve for the equilibrium state of an isolated neutron star with the same baryon mass, equation of state, and angular momentum, as the neutron star in our binary, and then compute its ADM mass. The dimensionless neutron star spin is defined as

$$\chi_{\rm NS} = \frac{S_{\rm NS}}{M_{\rm ADM,NS}^2}. \tag{3.47}$$

Tacik et al. (2015) showed that this method of computing neutron star spin was robust and accurate.

The ADM linear momentum is defined by a surface integral at infinity (Arnowitt et al. 1962; York 1979),

$$P^i_{\rm ADM} = \frac{1}{8\pi} \oint_{S_\infty} K^{ij} dS_j. \tag{3.48}$$

This integral relies on cancellation of leading order terms (Foucart et al. 2008; Ossokine et al. 2015b), which results in loss of accuracy when evaluated at finite numerical precision. Therefore, we use Gauss' law to rewrite (Foucart et al. 2008; Ossokine et al.

2015b) equation (3.48) as a surface integral over a sphere with smaller radius, $\mathcal{S}_0$, and a volume-integral over the volume V_0 outside $\mathcal{S}_0$,

$$P^i_{\rm ADM} = \frac{1}{8\pi}\oint_{S_0} P^{ij} dS_j - \frac{1}{8\pi}\int_{V_0} G^i dV, \tag{3.49}$$

where

$$P^{ij} = \Psi^{10}\left(K^{ij} - K\gamma^{ij}\right), \tag{3.50}$$

$$G^i = \tilde{\Gamma}^i_{jk} P^{jk} + \tilde{\Gamma}^j_{jk} P^{ik} - 2\tilde{\gamma}_{jk} P^{jk} \tilde{\gamma}^{il} \partial_l \left(\log \Psi\right). \tag{3.51}$$

3.4.3 Iterative Procedure

Construction of initial data begins by choosing the physical parameters of the BH-NS binary, which we aim to achieve. For the black hole, we specify:

- The black hole mass, $M_{\rm BH}$,
- The black hole's dimensionless spin vector, $\vec{\chi}_{\rm BH}$.

For the neutron star we specify:

- The neutron star's baryon mass, M_b,
- The neutron star's equation of state,
- The neutron star's spin vector, ω^i.

Finally, characterizing the orbit are:

- The separation between the centers of the BH and NS, D,
- The orbital angular velocity, Ω_0,
- The initial infall velocity parameter, $\dot{a}_0$.

Additionally, a prescription is required for the free metric variables, $\tilde{\gamma}_{ij}$ and K. Near the black hole, we would like these variables to approach the spatial metric $\gamma_{ij}^{\rm KS}$ and mean curvature $K^{\rm KS}$ of a single rotating black hole in Kerr-Schild coordinates. Away from the black hole (most notably in the vicinity of the neutron star), we desire conformal flatness and maximal slicing. Overall, therefore, we set

$$\tilde{\gamma}_{ij} = \delta_{ij} + e^{(-r/w)^4} \left(g_{ij}^{\rm KS} - \delta_{ij} \right), \tag{3.52}$$

$$K = e^{(-r/w)^4} K^{\rm KS}, \tag{3.53}$$

where r is the distance to the center of the black hole and w is the roll-off distance.

Once all physical parameters are specified an iterative procedure is used to solve the various elliptic equations and additional conditions, We proceed as follows:

1. Initialize two counters for nested iterative loops, $k = 0$ and $n = 0$. Here, k represents the AMR resolution iterations, and n represents iterations at constant AMR resolution.

2. If $k = 0$, at the first iteration (i.e. step 12 has not been reached yet), set $\omega^i = 0$. Otherwise set ω^i to its desired value, cf. above. This has been found to improve overall convergence, especially for high neutron star spins.

3. Solve the non-linear XCTS equations 3.16–3.17 for the metric variables $\beta^i, \Psi, \alpha\Psi$ assuming the matter source terms are fixed. For $n = 0$ this defines the metric variables $X^{(0)}$ at the 0-th iteration, where X indicates each of the metric variables. If $n \geq 1$, update the metric variables using a relaxation scheme

   $$X^{(n+1)} = \lambda X^* + (1 - \lambda) X^{(n)}, \tag{3.54}$$

   where X^* is the result found by solving the XCTS equations. We use $\lambda = 0.3$, as was previously used in chap. 2 and in Foucart et al. (2008).

4. If both the NS and BH have either aligned spin or zero spin, impose equatorial symmetry. This speeds up convergence and decreases computational cost.

5. If $k \geq 4$ go directly to step 9. (We generally find that after four resolution-updates, the stellar and black hole parameters are computed to sufficient accuracy. Skipping steps 6–8 decreases computational cost.)

6. Locate the surface of the star. The surface of the star is represented in terms of spherical harmonics

$$R(\theta,\phi) = \sum_{l=0}^{l_{\max}} \sum_{|m|\leq l} c_{lm} Y^{lm}(\theta,\phi). \tag{3.55}$$

The coefficients c_{lm} are determined by solving the relation $h\left(R\left(\theta,\phi\right)\right) = 1$. We generally use $l_{\max} = 11$.

7. Compute the ADM linear momentum $P_{\rm ADM}$ by evaluating Eq. 3.48. If its norm has changed by less than 10% in the last iteration, move the center of the BH by an amount $\delta\vec{c}$, designed to zero the in-plane components of $P^i_{\rm ADM}$, by finding $\delta\vec{c}$ such that $\delta\vec{c}\times\vec{\Omega}_0 = \vec{P}_{\rm ADM}$. Additionally, increase the radius of the excision surface $r_{\rm ex}$ to drive $M_{\rm BH}$ to the desired value by applying (Buchman et al. 2012)

$$\delta r_{\rm ex} = -r_{\rm ex}\frac{M_{\rm BH} - M^*_{\rm BH}}{M_{\rm BH}}, \tag{3.56}$$

where $M_{\rm BH}$ is the measured value in the initial data solve and $M^*_{\rm BH}$ is the desired value.

8. Compute the spin of the BH by evaluating Eq. 3.43. Then modify the vector $\Omega^i_{\rm BH}$ in Eq. 3.24 to drive the black hole spin to the target value, by applying (Buchman et al. 2012)

$$\delta\Omega^i_{\rm BH} = -\frac{\chi^i_{\rm BH} - \chi^{*i}_{\rm BH}}{4M} + \frac{M_{\rm BH} - M^*_{\rm BH}}{4M^2_{\rm BH}}\chi^i_{\rm BH}, \tag{3.57}$$

where $\chi^i_{\rm BH}$ is the computed black hole spin, and $\chi^{*i}_{\rm BH}$ is the target spin (see also (Ossokine et al. 2015b)).

9. If desired, adjust the orbital angular frequency using Eq. 3.40, which, after expanding the shift as $\beta^i = \beta^i_0 + \vec{\Omega}\times\vec{r} + \dot{a}\vec{r}$, is a second-order equation for Ω.

10. Fix the Euler constant by evaluating the integral

$$M_B = \int \rho_0 \Psi^6 \gamma_n dV \tag{3.58}$$

as a function of the Euler constant C (recall that C enters into h, cf. Eq. 3.35, and that ρ_0, in turn, depends on h, cf. Eq. 3.25). With the secant method, find the value of C that yields the desired baryon mass of the neutron star.

11. Solve the elliptic equation (3.34) for the velocity potential ϕ and update ϕ using the relaxation scheme in Eq. 3.54.

12. Check whether the Euler constant, black hole mass, black hole spin, ADM linear momentum, and the constraints are satisfied to the desired accuracy. If so, proceed to step 13. Otherwise increment n and return to step 3.

13. Compute the truncation error for the current solution by examining the spectral coefficients of the metric variables (Szilágyi 2014). If the truncation error is too large (generally we use 10^{-9} as the criterion), adjust the number of grid points. Then increment k, set $n = 0$, and return to step 2. This adaptive refinement is based on the target truncation error and the measured convergence rate of the solution. See Szilágyi (2014) for a complete description of this procedure.

3.5 Results

3.5.1 Initial Data Set Parameters

Our primary goal is to establish the performance of the initial data solver described in Sec. 3.4. The parameter space of BH-NS binaries is large, encompassing the masses of black hole and neutron star, their spin magnitudes and their spin directions, as well as the compactness of the neutron star. As our first stage in exploring this parameter space, we add neutron star spin to BH-NS initial data sets that already appeared in the

literature before (namely in Foucart et al. (2013a)). Our basis is six BH-NS configurations with different compactnesses of the neutron star, and with different orientations of the black hole spin relative to the orbital angular momentum. All base-configurations have mass ratio $q = 7$, black hole spin magnitude of $\chi_{\rm BH} = 0.9$ and neutron star mass of $M^{\rm NS}_{\rm ADM} = 1.4 M_\odot$ (recall that $M^{\rm NS}_{\rm ADM}$ is the mass of an individual neutron star of the same properties).

We explore three polytropic equations of state, $P = \kappa \rho^\Gamma$, all with $\Gamma = 2$. κ is chosen to achieve neutron star compactnesses $C = R/M = 0.170, 0.156$, 0.144, and radii of approximately 12km, 13km, 14km, respectively, for non-spinning neutron stars with ADM Mass $1.4 M_\odot$.

For all three equations of state, we consider BH spin-direction parallel to the orbital angular momentum. For the stiffest equation of state, we also vary the BH-spin direction and compute initial data sets for misalignment angles $\iota = 20^\circ, 40^\circ$, and 60°. The base-configurations are named `Rxxiyy`, where 'xx' denotes the approximate NS radius in kilometers and 'yy' denotes the inclination between BH spin direction and the orbital angular momentum in degrees (for instance `R14i20`).

Name	$\Theta_{\rm BH}$	$M^B_{\rm NS}$	$M\Omega_0$	$\vec{\omega}_{\rm NS}$	$\chi_{\rm NS}$
R12i0↑	0°	1.5212	0.0413	$0.00667\hat{z}$	0.0995
R12i0⇑	0°	1.5212	0.0413	$0.0225\hat{z}$	0.4093
R12i0↓	0°	1.5212	0.0413	$-0.00667\hat{z}$	-0.0895
R12i0⇓	0°	1.5212	0.0413	$-0.0225\hat{z}$	-0.4030
R12i0→	0°	1.5212	0.0413	$0.00667\hat{x}$	0.0936
R12i0⇒	0°	1.5212	0.0413	$0.0225\hat{x}$	0.3989
R13i0↑	0°	1.5128	0.0413	$0.00555\hat{z}$	0.0997
R13i0⇑	0°	1.5128	0.0413	$0.019\hat{z}$	0.3911
R13i0↓	0°	1.5128	0.0413	$-0.00555\hat{z}$	-0.0845
R13i0⇓	0°	1.5128	0.0413	$-0.019\hat{z}$	-0.3793
R13i0→	0°	1.5128	0.0413	$0.00555\hat{x}$	0.0913
R13i0⇒	0°	1.5128	0.0413	$0.019\hat{x}$	0.3771
R14i0↑	0°	1.5049	0.0413	$0.005541\hat{z}$	0.1188
R14i0⇑	0°	1.5049	0.0413	$0.017\hat{z}$	0.4109
R14i0↓	0°	1.5049	0.0413	$-0.005541\hat{z}$	-0.0965
R14i0⇓	0°	1.5049	0.0413	$-0.017\hat{z}$	-0.3915
R14i0→	0°	1.5049	0.0413	$0.005541\hat{x}$	0.1066
R14i0⇒	0°	1.5049	0.0413	$0.017\hat{x}$	0.3907
R14i20↑	20°	1.5049	0.0412	$0.005541\hat{z}$	0.1188
R14i20⇑	20°	1.5049	0.0412	$0.017\hat{z}$	0.4110
R14i20↓	20°	1.5049	0.0412	$-0.005541\hat{z}$	-0.0964
R14i20⇓	20°	1.5049	0.0412	$-0.017\hat{z}$	-0.3915
R14i20→	20°	1.5049	0.0412	$0.005541\hat{x}$	0.1064
R14i20⇒	20°	1.5049	0.0412	$0.017\hat{x}$	0.3905
R14i40↑	40°	1.5049	0.0412	$0.005541\hat{z}$	0.1193
R14i40⇑	40°	1.5049	0.0412	$0.017\hat{z}$	0.4117

R14i40↓	40°	1.5049	0.0412	-0.005541$\hat{z}$	-0.0961
R14i40⇓	40°	1.5049	0.0412	-0.017$\hat{z}$	-0.3908
R14i40→	40°	1.5049	0.0412	0.005541$\hat{x}$	0.1064
R14i40⇒	40°	1.5049	0.0412	0.017$\hat{x}$	0.3905
R14i60↑	60°	1.5049	0.0415	0.005541$\hat{z}$	0.1200
R14i60⇑	60°	1.5049	0.0415	0.017$\hat{z}$	0.4132
R14i60↓	60°	1.5049	0.0415	-0.005541$\hat{z}$	-0.0954
R14i60⇓	60°	1.5049	0.0415	-0.017$\hat{z}$	-0.3898
R14i60→	60°	1.5049	0.0415	0.005541$\hat{x}$	0.1061
R14i60⇒	60°	1.5049	0.0415	0.017$\hat{x}$	0.3903

Table 3.1: Full set of parameters of the 36 sets of initial data constructed here. Given are angle between the black hole spin and the orbital angular momentum $\theta_{\rm BH}$, baryon mass of the neutron star $M^B_{\rm NS}$, orbital frequency $M\Omega_0$, spin vector $\vec{\omega}_{\rm NS}$ of the neutron star (cf. Eq. 3.42), and the dimensionless spin of the neutron star, $\vec{\chi}_{\rm NS}$.

For the base-configurations, the following secondary choices are made: The non-parallel part of the black hole spin is set parallel to the $\hat{x}$ axis, i.e., the approximate axis between the BH and the NS. In each case the initial separation between the black hole and the neutron star is $D = 7.44M$, where $M = M_{\rm BH} + M^{\rm ADM}_{\rm NS}$ is the total mass of the binary. The initial infall velocity parameter $\dot{a}_0$ is set to 0. The orbital angular velocity, Ω_0, is the same as in Foucart et al. (2013a) and is indicated in table 3.1. The above constitutes 6 different configurations.

We combine each of the six base-configurations with six different configurations of neutron star spins for a total of 36 total configurations. In particular we choose three directions - aligned with the orbital angular momentum, anti-aligned with the orbital angular momentum, and parallel to the orbital plane (along the $+\hat{x}$ direction). For each of these three $\hat{\chi}_{\rm NS}$ directions, we consider "large" and "small" neutron star spin magnitude,

$\chi_{\rm NS} \sim 0.4$ and $\chi_{\rm NS} \sim 0.1$. In our naming notation, we use a double arrow ($\Uparrow$) for the large $\chi_{\rm NS}$ configurations and a single arrow ($\uparrow$) for the small $\chi_{\rm NS}$ configurations, with the direction of the arrow indicating the direction of the NS spin vector (e.g. `R14i20`$\rightarrow$). The full parameters of the initial data sets are summarized in Table 3.1.

In the present chapter, we do not perform evolutions of these initial data sets. Based on the evolutions in Foucart et al. (2013a) (for non-spinning NS), we expect these initial data sets to correspond to binaries that will proceed through ~ 7 to ~ 10 orbits before merger.

3.5.2 Convergence of the Initial Data Solver

To assess the convergence of the initial data solver we will begin by looking at the convergence of the iterative part of the solver. That is, the convergence of steps 1-12 in the iterative procedure described above. We will first focus on one particular initial data set of the 36 in Tab 3.1 - namely the `R14i60`$\Uparrow$ initial data set. The results we present for `R14i60`$\Uparrow$, however, are representative for all of the 36 sets considered.

First, we examine the convergence of the Euler constant, C. In figure 3.2 we plot the absolute difference in C between neighbouring iterations for the eight different resolutions used in the initial data solve. In the figure we see that at a given resolution these differences decrease exponentially with iteration as expected for the relaxation scheme employed (cf. Eq. 3.54). Meanwhile the differences also decrease with increasing resolution. We find similar results for all the other initial data sets we consider.

Next, we will look at the properties of the black hole to verify that they converge as expected in the presence of a spinning neutron star, using again `R14i60`$\Uparrow$ as our example. We focus on the black hole spin $\vec{\chi}_{\rm BH}$ which is controlled by the parameter $\Omega_j^{\rm BH}$ in Eq. 3.24, and the irreducible black hole mass, $M_{\rm irr}$ (cf. Eq. 3.46).

Figure 3.3 shows the fractional difference for these quantities to their desired target value. The difference is plotted as a function of iteration, for four different resolutions.

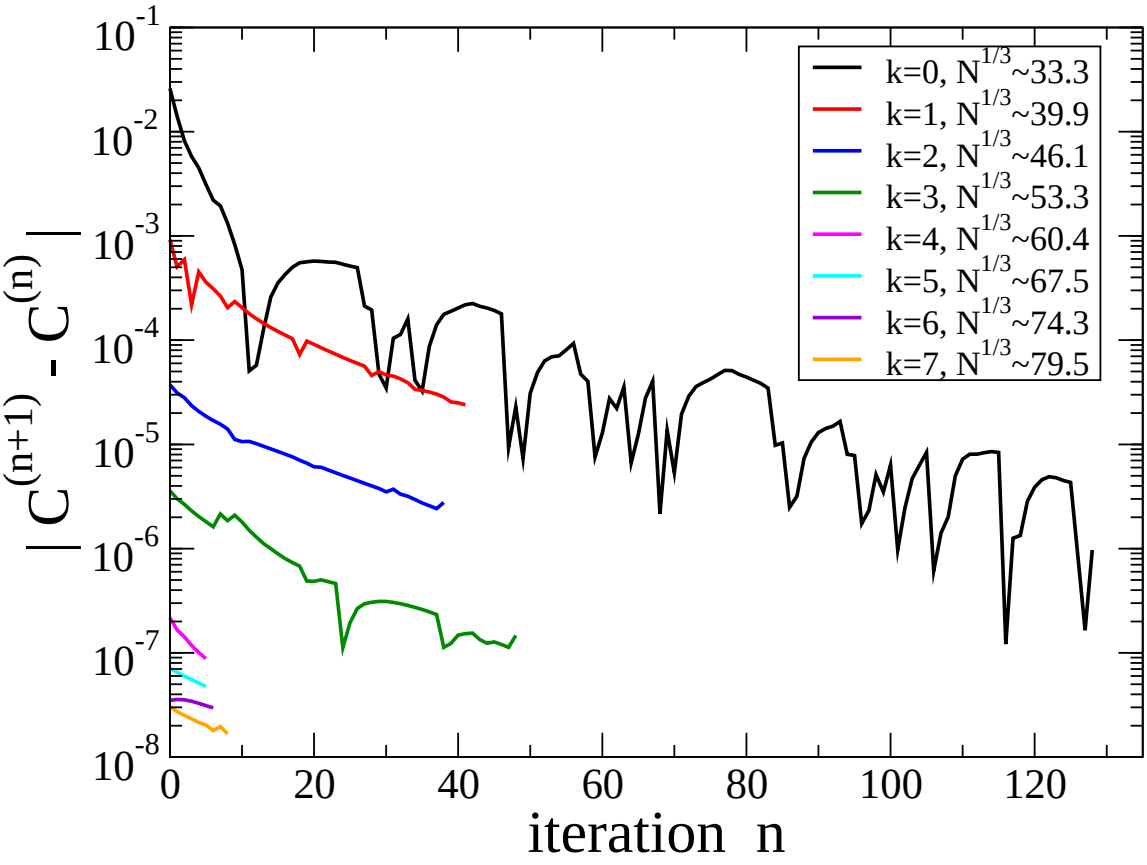

Figure 3.2: Absolute difference between neighbouring iterations of the Euler constant for the `R14i60`⇑ initial data set. k labels AMR adjustment iterations, and n the inner iterative loop at fixed grid-resolution.

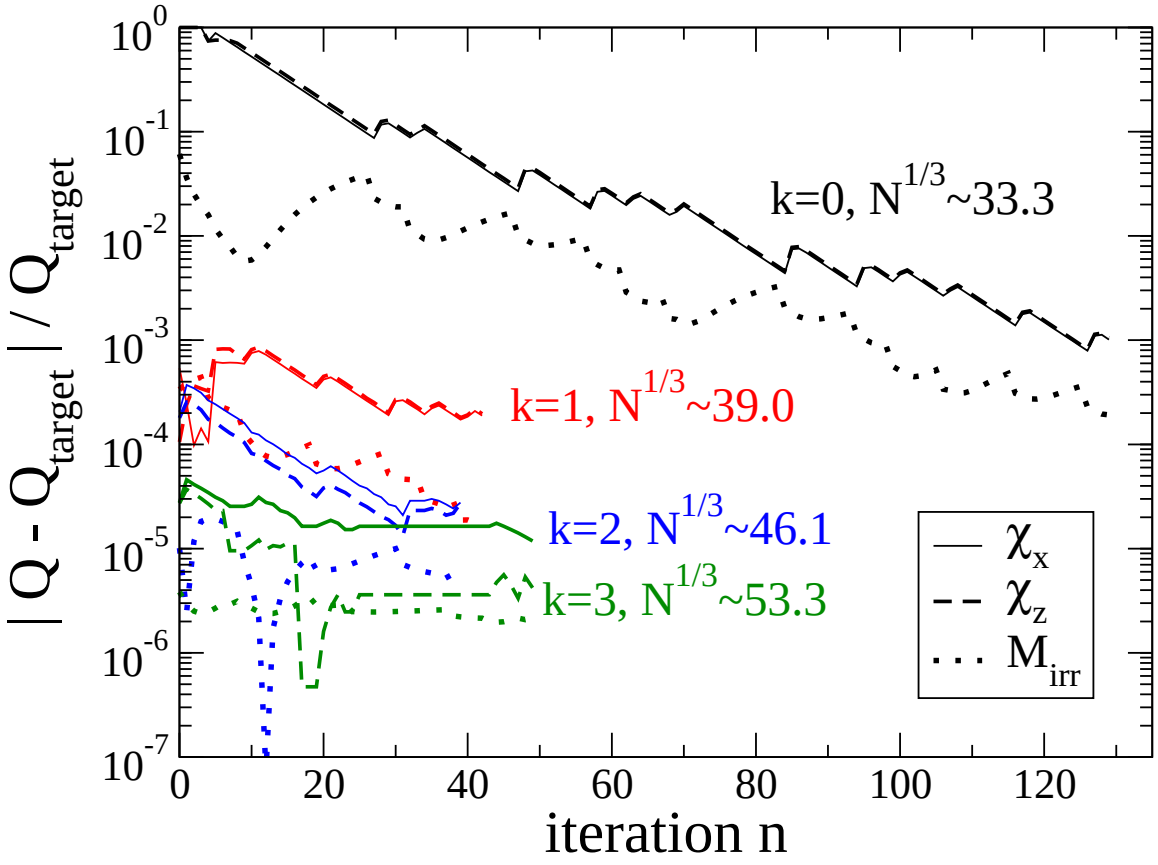

Figure 3.3: Fractional difference from desired values of black hole spin and mass. Shown is the solution of `R14i60`⇑ initial data set as a function of iteration count. The four colours represent the four different resolutions $k = 0, \ldots, 3$ at which the black hole spin is measured.

Recall that the BH spin is only adjusted on iterations $k = 0, 1, 2, 3$, and not thereafter (cf. Step 5). In general we see a decrease in this difference with iteration, especially at the first resolution, therefore showing that the iterative solver is correctly driving the the black hole properties to the target values. Furthermore, that this difference decreases with resolution, and we are able to achieve an accuracy of about 10^{-5} in the BH spin and mass. Note that the differences shown in Fig. 3.3 continue to remain small for $k > 3$.

Having established the convergence of the iterative procedure, we turn now to the global properties of the solution, continuing to focus on the `R14i60`$\Uparrow$ ID set. We first consider the Hamiltonian and momentum constraints, computed as

$$H = ||\tfrac{R_\Psi}{8\Psi^5}||, \tag{3.59}$$

$$M = ||\tfrac{R_\beta}{2\alpha\Psi^4}||, \tag{3.60}$$

where R_Ψ and R_β are the residuals of Eqs. 3.15 and 3.16, respectively, and $||.||$ represents the $L2$ norm over all collocation points of the computational domain. The constraints for this ID set are shown in figure 3.4. We find exponential convergence in the constraints, as expected for spectral methods. The increase at the second iteration ($k = 1$) arises because the neutron star spin is only activated in the second iteration (cf. step 2).

Finally, we look at the properties of the neutron star. As noted in Eq. 3.55, the neutron star surface is expressed as a sum of spherical harmonics. To evaluate the convergence of the surface location, we define the quantity

$$\Delta c^{(k)} = \sqrt{\sum_{l,m} \left(c_{lm}^{(k)} - c_{lm}^{(k_{\max})} \right)^2}, \tag{3.61}$$

where k represents the current resolution, and $k_{\max}$ represents the highest resolution. This quantity is plotted in figure 3.5. Similar to the black hole surface, the neutron star surface is only computed for the first four resolutions, and so we have three data points shown. We find exponential convergence in this quantity. We also look at the convergence of the neutron star spin $\chi_{\rm NS}$ measured at each resolution. In figure 3.5, we

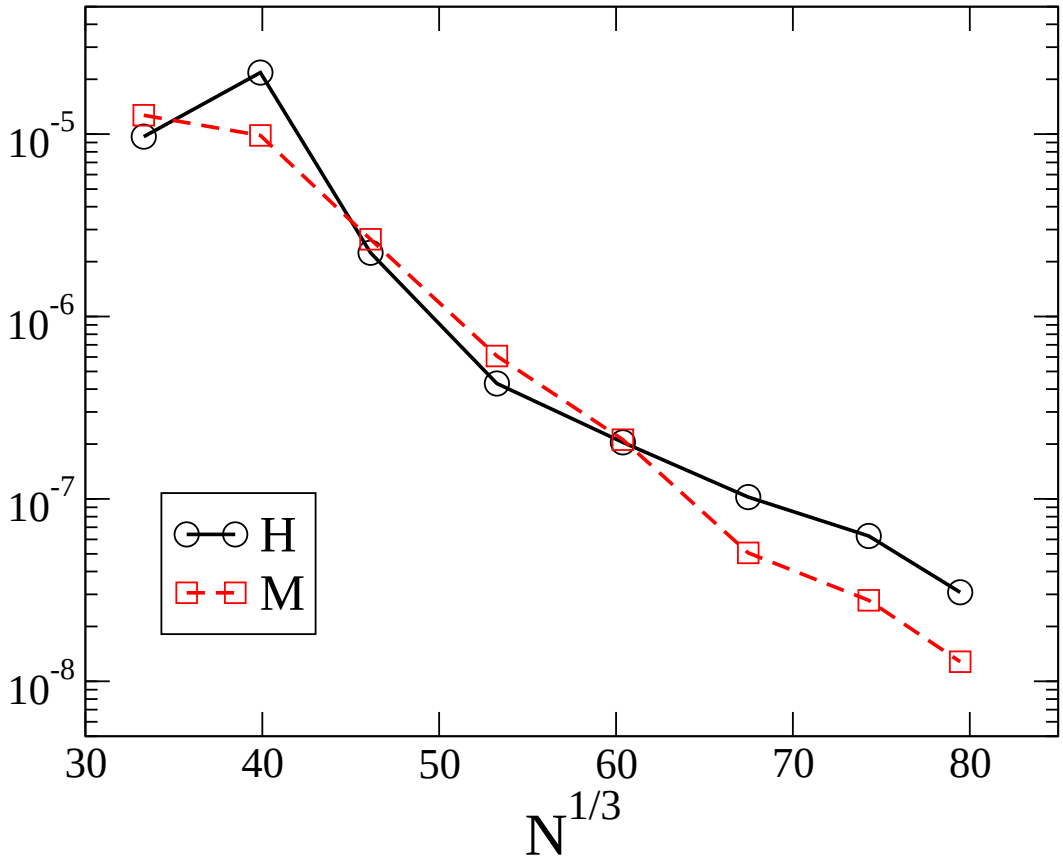

Figure 3.4: The Hamiltonian and momentum constraints for the `R14i60`$\Uparrow$ initial data set as a function of resolution. We find exponential convergence in both.

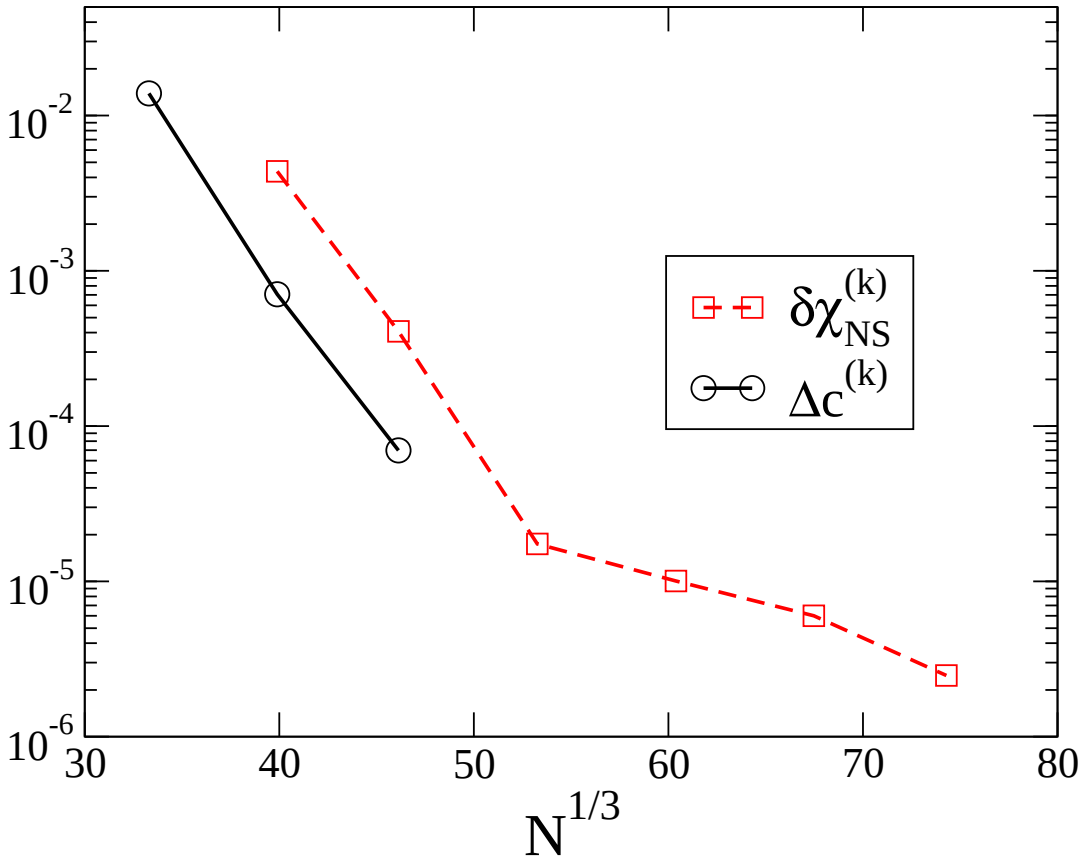

Figure 3.5: Accuracy of neutron star properties for the solution of `R14i60`⇑. Plotted are the accuracy of the NS surface, $\Delta c^{(k)}$, as defined in Eq. 3.61 and the fractional accuracy of the NS spin (equation 3.62).

plot the fractional difference in $\chi_{\rm NS}$ between neighbouring resolutions. That is, we plot

$$\delta\chi_{\rm NS}^{(k)} = \frac{|\chi_{\rm NS}^{(k+1)} - \chi_{\rm NS}^{(k)}|}{\chi_{\rm NS}^{(k)}}. \tag{3.62}$$

Figure 3.5 exhibits exponential convergence, although there are two distinctly different slopes in the data, once we cease to update the NS surface for $k \geq 4$. Nevertheless, we are able to measure the spin to an accuracy of about 10^{-6}. We have omitted the first data point of $\delta\chi_{\rm NS}^{(k)}$, because the NS spin is not activated for $k = 0$ (cf. Step. 2).

The above data all show that we have established the convergence of our initial data solver, by showing exponential convergence of the iterative solver, the black hole properties, neutron star properties, and the constraints.

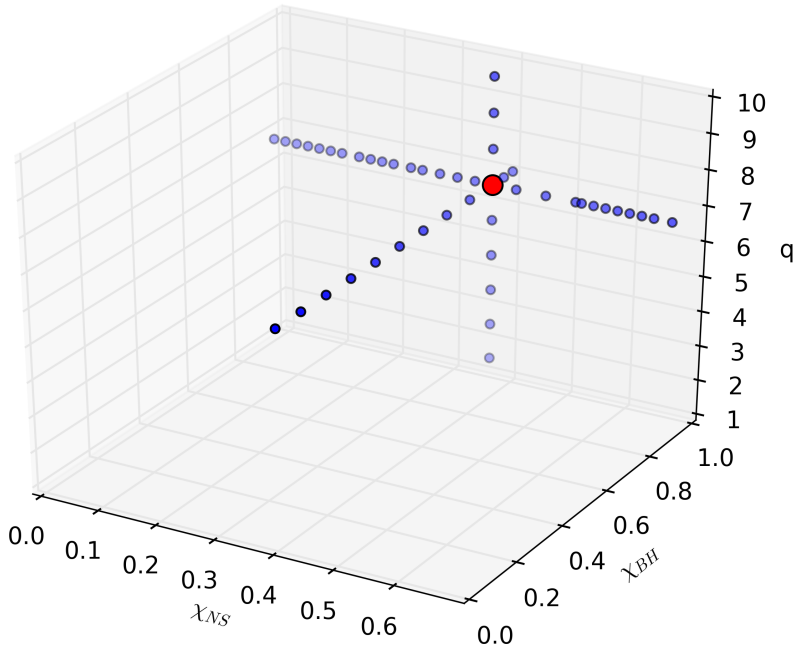

Figure 3.6: Parameter space exploration. Starting from `R14i0`⇑(large red circle) we vary (i) the BH spin $\chi_{\rm BH}$, (ii) the NS spin $\chi_{\rm NS}$ and (iii) the black hole mass $M_{\rm BH}$, indicated by the mass-ratio q.

3.5.3 Broader Exploration of Parameter Space

All initial-data sets constructed so far share the same black hole mass and black hole spin-magnitude, $M_{\rm BH} = 9.8_{\odot}$ and $\chi_{\rm BH} = 0.9$. In this section, we relax these restrictions, and also explore the range of possible neutron star spins our code is capable to construct. In total, we consider three additional sequences of initial-data sets:

First, we consider a sequence that varies the neutron star spin from $\chi_{\rm NS} = 0$ to $\chi_{\rm NS} \sim 0.7$, keeping it aligned with the orbital angular momentum. In these initial data sets, the other binary parameters are the same as in the `R14i0` runs. Namely, the neutron star mass, equation of state, black hole mass, black hole spin, initial separation and orbital angular frequency. Second, we consider a sequence of runs where we vary the black hole

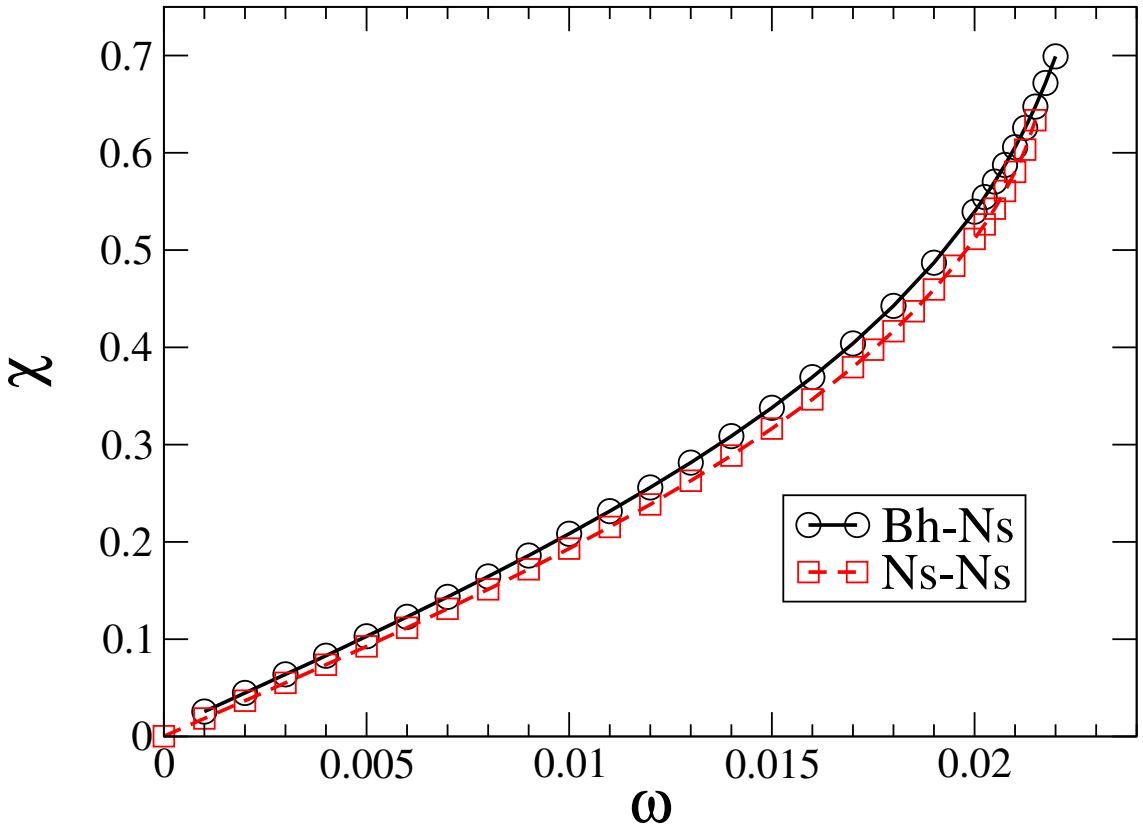

Figure 3.7: Neutron star spin χ as a function of neutron star spin parameter ω for a sequence of initial data sets. The black hole spin is constant at $\chi = 0.9$ and the mass ratio is $q = 7$. The dashed red curve is from NS-NS binaries, with somewhat different neutron star parameters.

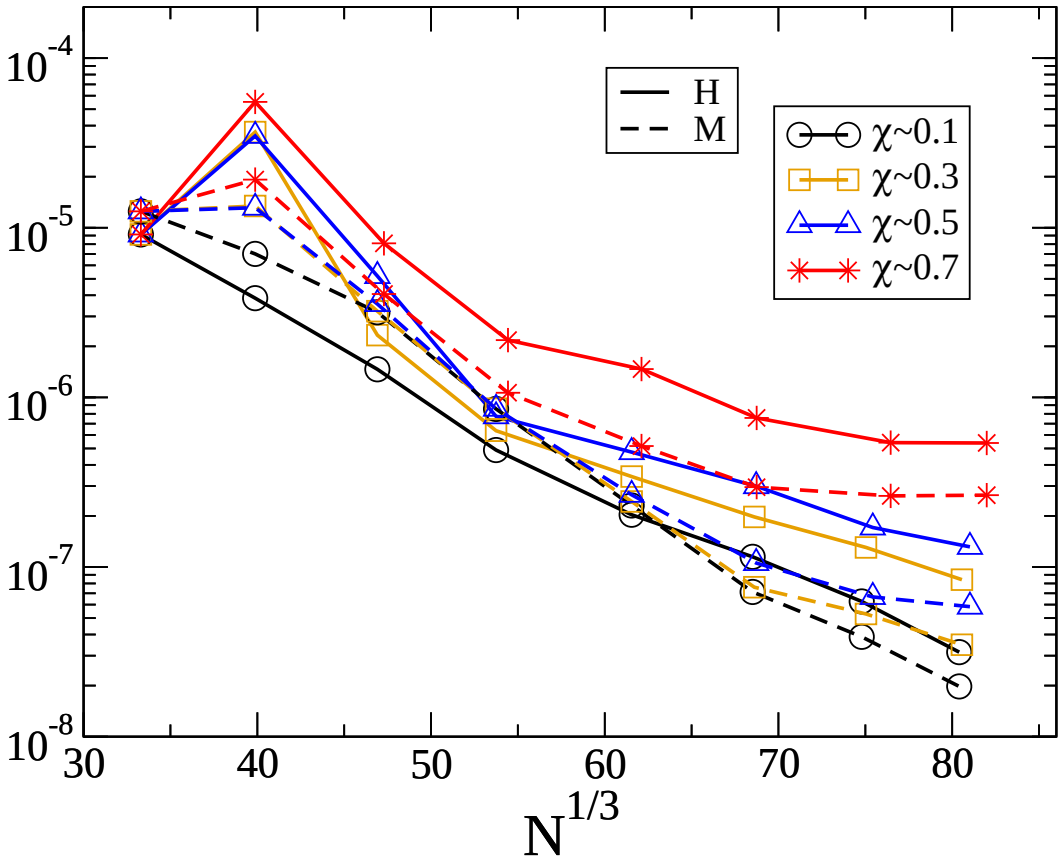

Figure 3.8: Hamiltonian (solid curves) and momentum (dotted curves) constraints for four different neutron star spins.

spin from $\chi_{\rm BH} = 0$ to $\chi_{\rm BH} = 0.99$, while keeping the other binary parameters as in the `R14i0`$\Uparrow$ run. Finally, we consider a sequence of runs where we vary the mass ratio from $q = 2$ to $q = 10$. Figure 3.6 summarizes all the initial data sets along the axes of $\chi_{\rm NS}$, $\chi_{\rm BH}$ and q.

We begin by varying the neutron star rotation parameter ω. The parameters in this sequence are otherwise the same as in the `R14i0` data sets, and the neutron star spin is kept aligned with the orbital angular momentum. In Fig. 3.7 we plot the measured neutron star spin $\chi_{\rm NS}$ as a function of the code parameter ω for the full sequence. As expected, we find a linear relationship at low ω, but the relationship becomes non-linear at higher ω, as the neutron star's size, and thus moment of inertia, becomes an appreciable function of spin. We find that the solver breaks down around $\chi_{\rm NS} \sim 0.7$, which is the

maximum spin parameter for neutron stars found in Lo & Lin (2011). Figure 3.7 also shows the corresponding $\chi_{\rm NS}$ vs. ω curve for a binary neutron star of mass-ratio $q = 1$ with both stars carrying the same aligned spin magnitude as presented in Tacik et al. (2015). The NS-NS data use different NS parameters, with mass $M_{\rm ADM} = 1.64 M_\odot$ and equation of state parameter $\kappa = 123.6$. Nevertheless, the curves remain very close to each other in shape, indicating that the method to impart NS rotation (Tichy 2011) performs similarly for mixed BH-NS binaries and for NS-NS binaries (Tacik et al. 2015).

To investigate numerical convergence of the initial-data sets presented in figure 3.7, we plot in figure 3.8 the Hamiltonian and momentum constraints for a subset of the generated initial data sets, with $\chi \sim 0.1, 0.3, 0.5, 0.7$. In general we find the expected exponential convergence, but there are a few features worth discussing in the data. The increase in the constraints between the lowest and second-lowest resolution ($k = 0$ vs. $k = 1$) arises because the spin is only activated at the second-lowest resolution, cf. step 2. This jump in constraints monotonically increases with the spin-parameter ω, as we might expect, because the solver has a more difficult task in adjusting to the abrupt activation of a larger spin. We also note that at high resolution, in the $\chi \sim 0.7$ curve, we lose exponential convergence and the curves flatten out around 10^{-6}. This is likely a sign that the accuracy of the solver is becoming limited, likely by approximations that go into the solver. $\chi \sim 0.7$ is around the maximum theoretical neutron star spin, so such difficulties are expected.

Continuing the exploration of parameter space, we next vary the black hole spin $\chi_{\rm BH}$. In particular, we vary the black hole spin from $\chi_{\rm BH} = 0$ to $\chi_{\rm BH} = 0.99$, keeping it aligned with the orbital angular momentum. The other binary parameters are kept the same as in the `R14i0` $\Uparrow$ initial data set, specifically $\vec{\omega}_{\rm NS} = 0.017\hat{z}$ and $q = 7$. In Figs. 3.9 we plot the Hamiltonian and momentum constraints, respectively, for this sequence. We find exponential convergence in all cases. It is interesting to note that the constraints seem to be lowest at the highest black hole spins, $\chi_{\rm BH} = 0.95$ and $\chi_{\rm BH} = 0.99$, while one might

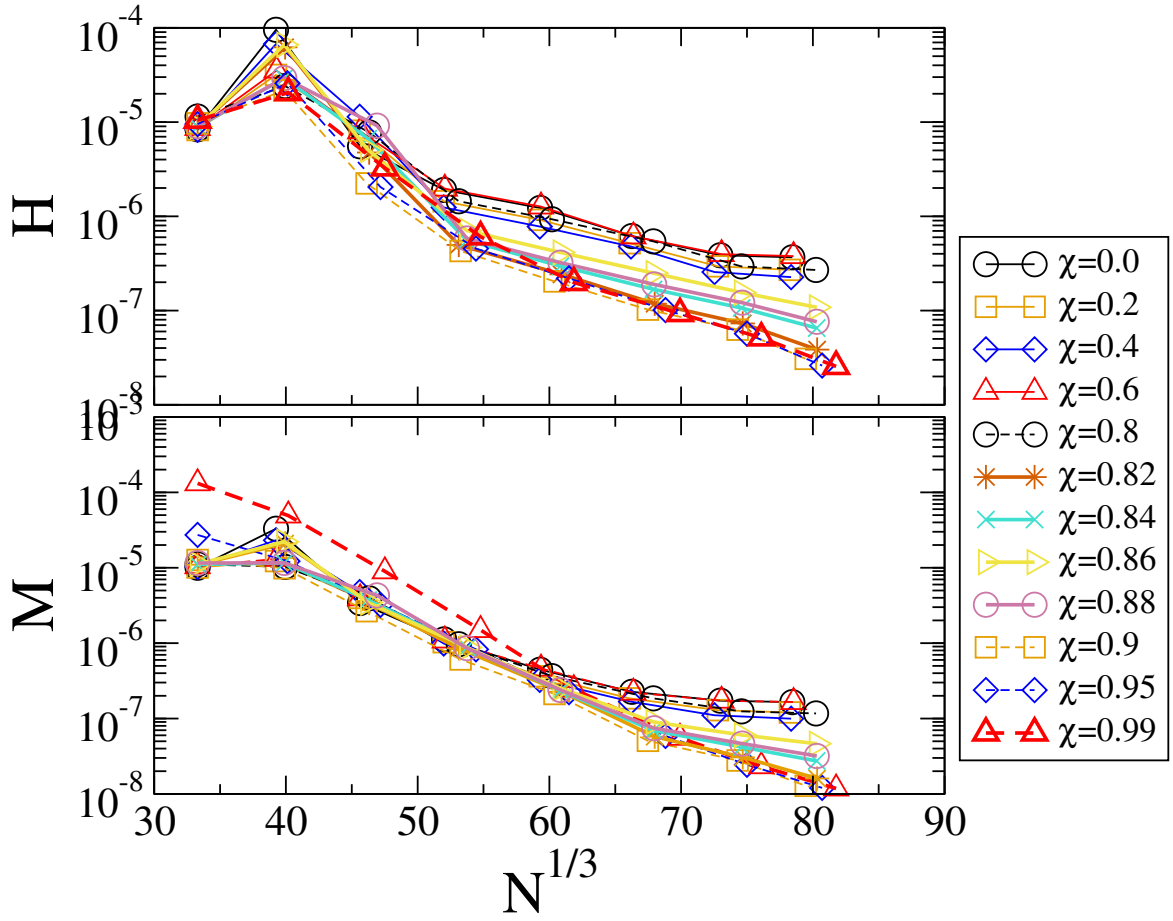

Figure 3.9: Hamiltonian constraint (top panel) and momentum constraint (bottom panel) versus resolution for our sequence of binaries where the black-hole spin is varied from $\chi_{\rm BH} = 0$ to $\chi_{\rm BH} = 0.99$. The NS spin parameter is kept constant at $\vec{\omega}_{\rm NS} = 0.017\hat{z}$ and the mass ratio is $q = 7$.

expect these to be the most challenging cases. In general we see a qualitative difference in the constraints that happens above $\chi = 0.8$. This seems to be an artifact of the initial data solver - for cases above $\chi = 0.8$, the solver takes more iterations to solve, and this pushes the constraints down.

Since this work focuses on neutron star spin, it is interesting to consider how the measured neutron star spin, $\chi_{\rm NS}$ couples to other binary parameters. To lowest order, it should depend only on $\omega_{\rm NS}$, but in practice it may also depend on the parameters of the black hole or of the orbit. For the sequence of initial data sets of varying $\chi_{\rm BH}$, figure 3.10

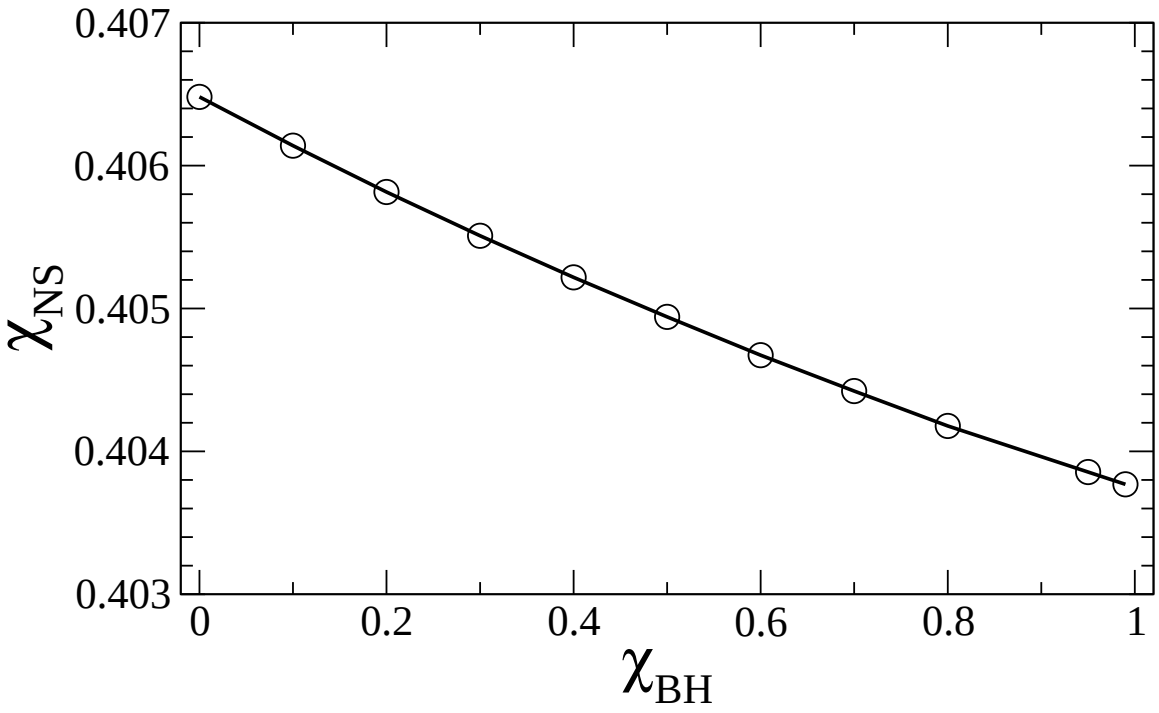

Figure 3.10: Neutron star spin $\chi_{\rm NS}$ as a function of black hole spin $\chi_{\rm BH}$ for this sequence. We notice a small downward linear trend.

presents the neutron star spin $\chi_{\rm NS}$ as a function of $\chi_{\rm BH}$. $\chi_{\rm NS}$ is nearly constant, dropping by less than 1% between $\chi_{\rm BH} = 0$ and $\chi_{\rm BH} = 0.99$, confirming that the spin specification for the neutron star almost completely decouples from the BH spin.

Finally, we consider a sequence of initial-data sets that varies the mass ratio from $q = 2$ to $q = 10$. In this sequence we keep the other binary parameters the same as in the `R14i0` $\Uparrow$ initial data set and we keep the orbital parameters $M\Omega$ and D/M constant.

As the mass-ratio changes, we expect that the orbital frequency needed to achieve low eccentricity will also somewhat change. We do not model this effect, but rather keep all other binary parameters the same as in the `R14i0`$\Uparrow$ run. In particular, the orbital parameters $M\Omega$ and D/M are constant. While not the most accurate way of choosing these parameters, as it is only correct to Newtonian order, it suffices for the present purpose of testing robustness of the initial-data solver.

To estimate the impact on the eccentricity of the constructed initial-data sets, we use

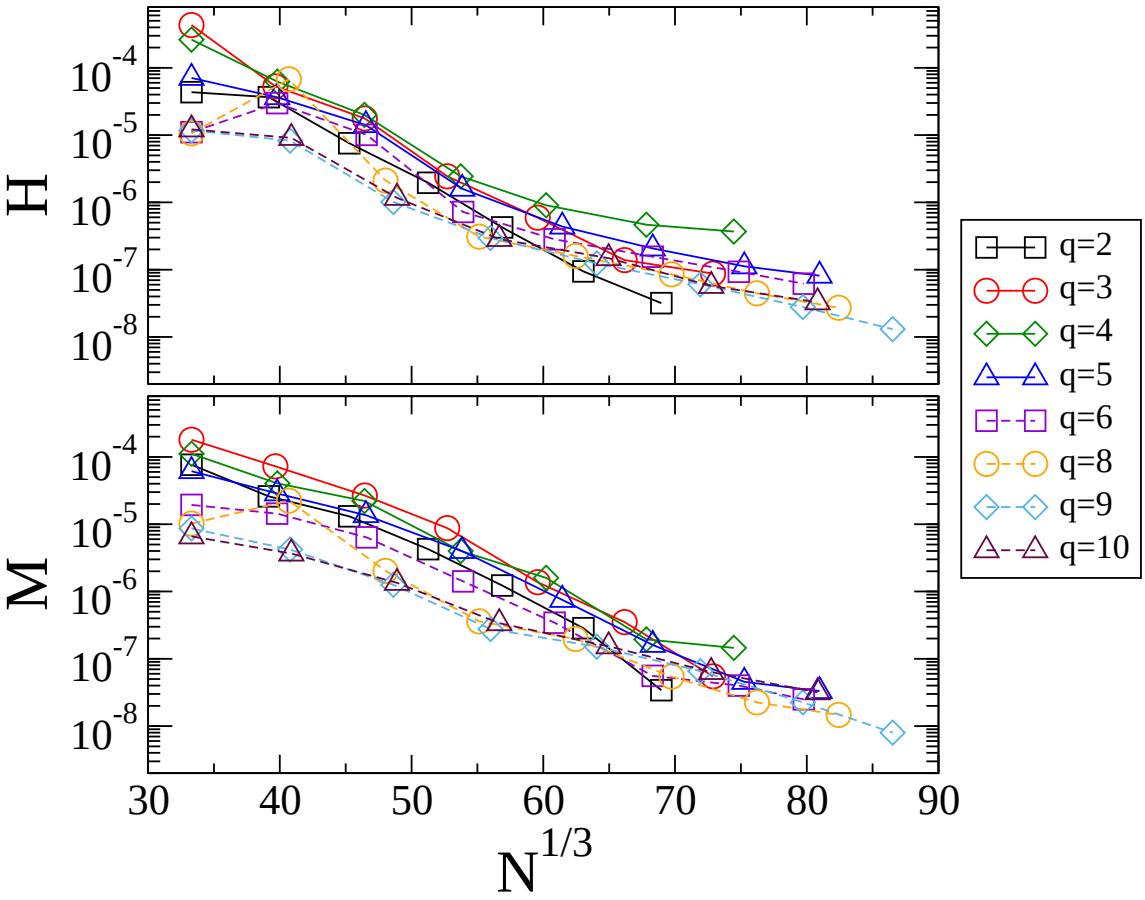

Figure 3.11: Hamiltonian constraint (top panel) and momentum constraint (bottom panel) versus resolution for our sequence of binaries where the mass ratio is varied from $q = 2$ up to $q = 10$. The NS spin parameter is kept constant at $\vec{\omega}_{\rm NS} = 0.017\hat{z}$ and the black hole spin is $\chi_{\rm BH} = 0.9$.

the post-Newtonian expansion of the orbital frequency of a BBH in a *circular* orbit (Eq. 228 of Blanchet (2006)):

$$\Omega^2 = \frac{GM}{r^3}\left(1 + (-3+\nu)\gamma + \left(6 + \frac{41}{4}\nu + \nu^2\right)\gamma^2 + ...\right). \tag{3.63}$$

Here $\nu = m_1 m_2/(m_1+m_2)^2 = q/(1+q)^2$ is the symmetric mass ratio, and $\gamma = GM/Dc^2$. Keeping D and M constant, the quantity $M\Omega$ varies by approximately 3% in the mass ratio range we consider. Therefore, we expect that the eccentricity of our initial-data sets varies by only a few percent between $q = 2$ and $q = 10$.

To assess convergence, we plot the Hamiltonian and momentum constraints for this

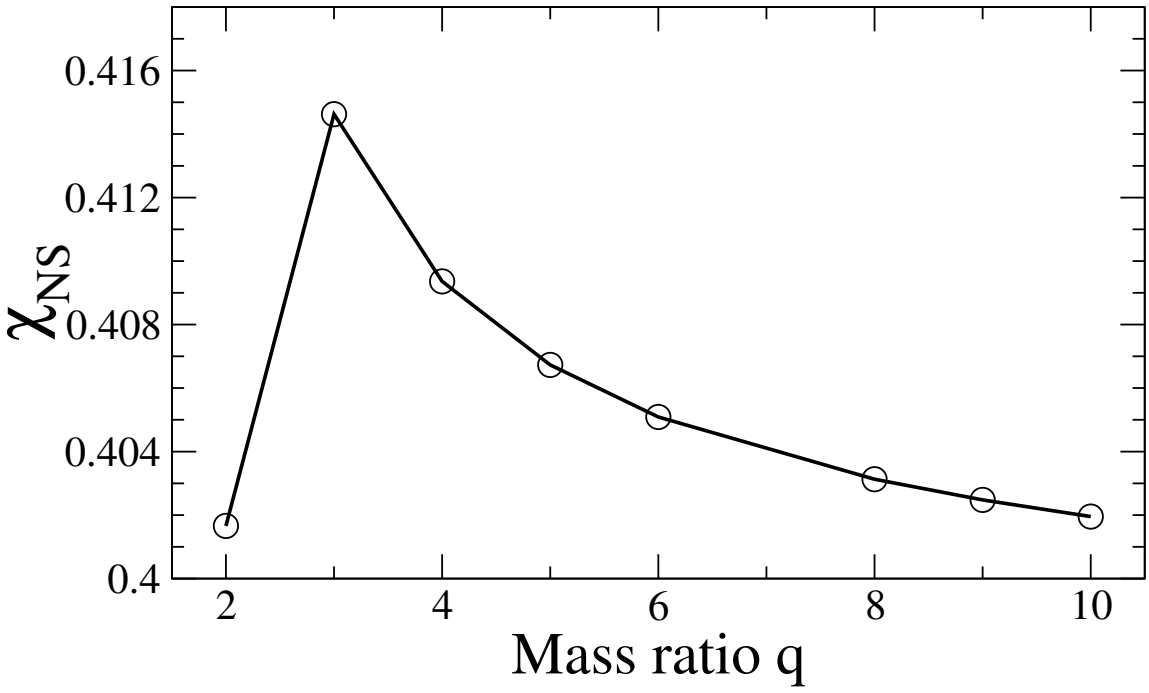

Figure 3.12: Neutron star spin $\chi_{\rm NS}$ as a function of mass ratio q for this sequence. We notice a small downward trend for $q \geq 3$.

sequence in Fig. 3.11. We find exponential convergence in all cases. Interestingly, no clear pattern in q-space emerges.

Figure 3.12 plots the neutron star spin as a function of mass-ratio. Having kept $\vec{\omega}_{\rm NS}$ constant across this sequence, we indeed find that the physical NS spin is approximately constant, too, varying less than 2 percent. Although there is not a great amount of variation, apart from $q = 2$, there is a clear trend of $\chi_{\rm NS}$ decreasing with q. Again, however, the effect is quite small and we do not seek to explain it.

3.6 Conclusion

In compact object binaries containing neutron stars, the spin of the neutron star(s) forms part of the parameter space of such binaries. In order to constrain neutron star spin *directly from gravitational wave observations*, one must know the impact of the neutron star spin on the evolution of the compact object binary, i.e. on the emitted waveforms

and on the electro-magnetic signature.

This chapter lays foundations for such studies by constructing initial-data sets of BH-NS binaries with arbitrary neutron star spins. To our knowledge, this is the first time initial data has been created for BH-NS binaries with spinning neutron stars. To impart spin on the neutron star, we carry over the formalism developed by Tichy (2011) and used in Bernuzzi et al. (2014); Tacik et al. (2015); Dietrich et al. (2015b) to create initial data for NS-NS systems with arbitrary spins.

Two new numerical tricks were found to be necessary to get convergent initial data - setting a maximum radius out to which to apply $W^i = \epsilon^{ijk}\omega^j r^k$, and only activating the neutron star spin after the first AMR-iteration of the initial data solver has completed. We create initial data sets across a large portion of the BH-NS binary parameter space.

First, we present a comprehensive study of initial-data sets with various NS spins, restricting to $q = 7$ and $\chi_{\rm BH} = 0.9$. This first study spans three different equations of state (all $\Gamma = 2$ polytropes), different neutron star spin magnitudes, different neutron star spin orientations, and four different black hole spin orientations. Subsequently, we construct initial data with spinning NS for mass-ratios from $q = 2$ to $q = 10$, and for black-hole spins $0 \leq \chi_{\rm BH} \leq 0.99$, the latter well exceeding the standard Bowen-York limit on black hole spin (Lovelace et al. 2008; Dain et al. 2008). Finally, we explore the range of possible NS spin magnitudes, and find that the presented numerical techniques can successfully construct initial data with neutron star spins ranging from $\chi_{\rm NS} = 0$ to $\chi_{\rm NS} \sim 0.7$ (near the maximum theoretical spin for neutron stars).

Future research will involve running evolutions of these, or similar, initial data sets. Some of the 36 initial data sets of our first study (Table 3.1) can be used to investigate how neutron star spin affects tidal disruption of the star by the black hole, and how it affects the disk that is formed. The orbital phase evolution can also be examined and compared to Post-Newtonian (Blanchet 2014) or other analytic predictions such as Effective-One-Body (EOB) (Buonanno & Damour 1999; Taracchini et al. 2014; Pan et al.

2013).

One can also explore the maximum mass of accretion disks and ejecta as a function of NS spin. Lovelace et al. (2013) finds a very large disk with a black hole spin of $\chi = 0.97$ and mass ratio $q = 3$. Keeping these BH and NS parameters, but adding spin on the neutron star will cause the NS' material to be less strongly bound and may increase the disk mass even further.

Chapter 4

Spurious Radiation in Binary Black Hole Simulations

4.1 Chapter Summary

In current numerical relativity binary black hole simulations, there is always a burst of non-astrophysical, spurious gravitational radiation at the start of the simulation, often called "junk radiation". To better understand junk radiation and to give insight on how to reduce it, we study its parameter space dependence. We use three different diagnostics for junk radiation - the energy contained in the pulse of radiation, and the transient increase in black hole mass and decrease in black hole spin due to junk radiation. Comparing conformally flat initial data and superposed Kerr-Schild initial data, we measure their dependence on the initial separation of the black holes and on the spins of the black holes, for equal-mass, equal-spin, spin-aligned systems. We find that the energy in junk radiation is relatively independent of spin, and is generally a factor of $2-3$ lower for SKS initial data. We find it has a power law dependence on initial separation. For SKS intial data, we are unable to directly quantify the transient quantities because of their low magnitude and lack of convergence. For CF data, we find the mass increase has a small dependence on initial separation and a strong power law dependence on spin. We

find similar results for the spin decrease, except with an exponential dependence on black hole spin.

4.2 Introduction

The detection of the inspiral and merger of binary black holes (BBH) by Advanced LIGO (Abbott et al. 2016a;b) has dawned the beginning of the era of gravitational wave astronomy. To make these kind of detections, and to learn about the properties of the source, gravitational waveform templates must be accurately modeled. Although analytic prescriptions like Post-Newtonian (PN) (Blanchet 2006)or Effective One-Body (EOB) (Buonanno & Damour 1999) can reproduce the early inspiral, Numerical Relativity (NR) simulations are needed to study the late inspiral and merger of the black holes.

In current NR simulations, there is always a burst of spurious gravitational radiation at the start of the simulation, often referred to as "junk radiation". This pulse always occurs at the start of the simulation, it is of much higher frequency and amplitude than the astrophysical gravitational radiation, and it has significant contributions from modes other than the $(l, m) = (2, \pm 2)$ spherical harmonic modes, which are the dominant contribution for the astrophysical part of the waveform. Therefore, this pulse is not astrophysical.

We illustrate this effect in Fig. 4.1, showing the gravitational waveform at the start of a typical simulation - non-spinning, equal-mass binary black holes, separated by $15M$[1]. The waves are extracted on a coordinate sphere at $r = 160M$, so the waves start appearing at $t \approx 160M$. We see the burst of junk radiation last about $100M$ in time, with significant contributions from both the $(2, 2)$ and $(2, 0)$ modes. The junk radiation then dies out, and subsequently, the expected sinusoidal $(2, 2)$ mode emerges.

[1]We use units where $G = c = 1$. The only natural length and time scale is then the total mass of both black holes, M.

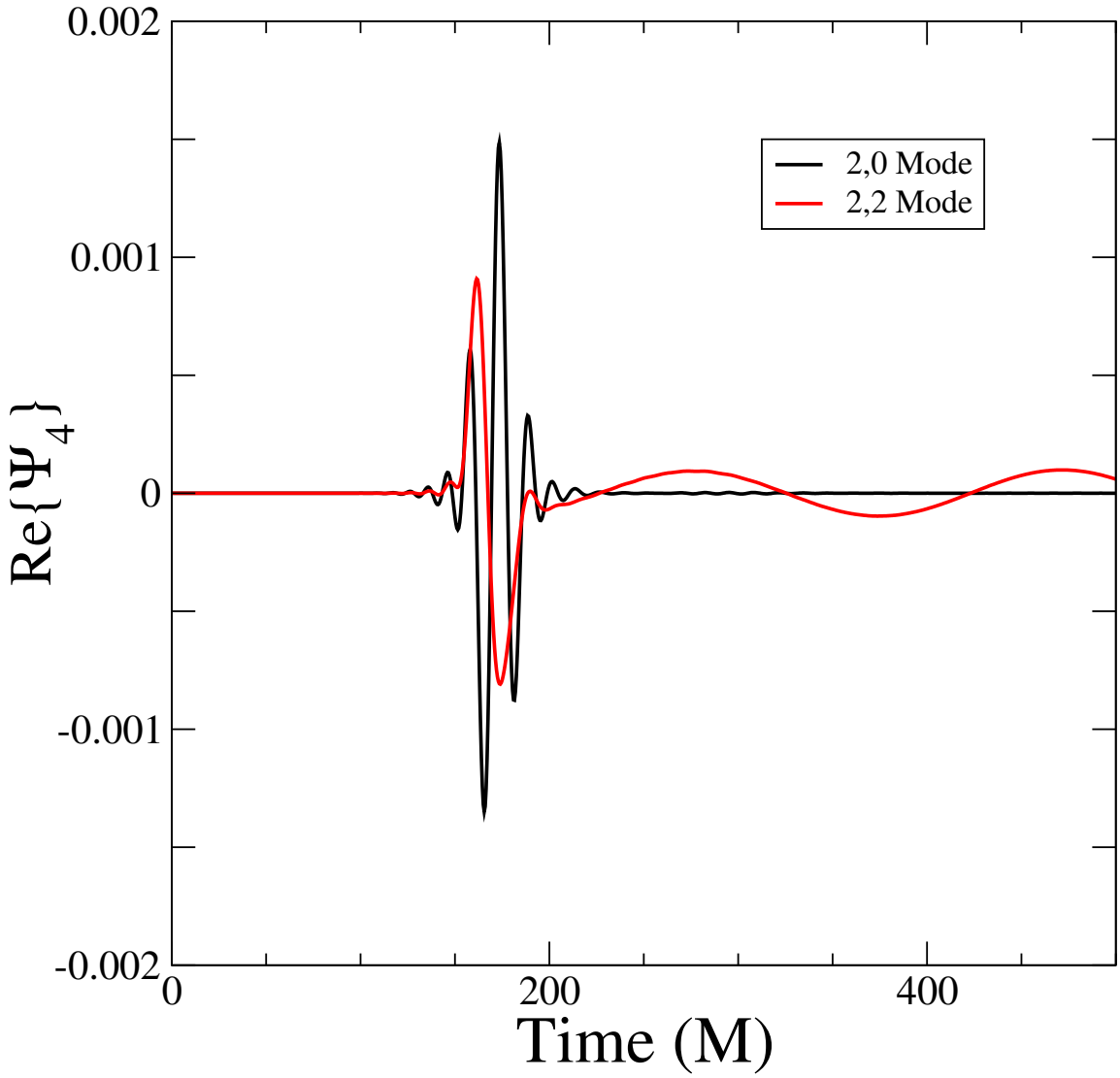

Figure 4.1: A typical run illustrating the spurious burst of junk radiation. At the very earliest times, no outgoing radiation has reached the extraction radius of $R = 160M$. Then at $t \sim 160M$, we see a burst of high-frequency, high-amplitude radiation. At later times, the $(2, 0)$ mode dies out, and the $(2, 2)$ mode settles into the usual inspiral radiation.

This junk radiation is undesirable in simulations for several reasons. It adds to the computational cost of the simulation as the junk radiation must leave the computational grid before any useful physical information can be extracted. It can unrealistically shorten the time until the black holes merge (Bode et al. 2008). It also must be carefully considered when comparing NR simulations with PN or EOB calculations (Damour et al. 2012), or when creating PN/NR hybrid waveforms (MacDonald et al. 2011). It is therefore a useful endeavor to better understand the junk radiation, how important it is, and how to reduce it.

Junk radiation is thought to be caused by assumptions made during the initial data construction, which are not compatible with binary black holes in perfect equilibrium. Specifically, black holes are generally treated in the initial data as independent and non-interacting, while in reality there should be some non-trivial tidal interactions between them which go unmodeled (see Chu (2014); Johnson-McDaniel et al. (2009) for examples of including tidal interactions). If we consider a sequence of initial data sets where the initial separation between the holes is decreasing, we would expect that these tidal interactions become more important as the initial separation decreases. Similarly, to fully model binary black holes at a late stage of the inspiral, there should already be some outgoing gravitational radiation already present in the initial data from its past history. However, this is generally not explicitly modelled in current initial data codes (see [Johnson-McDaniel et al. (2009); Kelly et al. (2010)] for efforts to model it). Moreover, the black holes in the initial data are often constructed with techniques that are incompatible a single, equilibrium black hole. Specifically, often, conformal flatness is assumed. As detailed in section 4.3.1, the construction of initial data has a free choice for the conformal metric, $\tilde{g}_{ij}$, on the initial hypersurface. A common choice is conformal flatness, i.e., $\tilde{g}_{ij}$ is equal to the flat Euclidean metric, f_{ij}. Since every spherically symmetric 3 geometry is conformally flat (Garat & Price 2000), this is fine for one Schwarzchild black hole. However, a binary system of compact objects is not conformally flat at second PN

order (Rieth 1997). Moreover, the Kerr space-time does not admit a conformally flat slicing that continuously approach Schwarzschild coordinates as the spin goes to zero (Garat & Price 2000). The former effect should decrease in importance with increasing separation of the binary. The latter is caused by a deficiency of conformally flat slicing that is present even for single spinning black holes, and so we expect its importance to be approximately independent of binary separation.

Superposed Kerr-Schild (SKS) (Matzner et al. 1998; Marronetti & Matzner 2000; Pfeiffer et al. 2002; Lovelace et al. 2008) (conformally curved) initial data is now a common alternative to conformally flat initial data for binary black hole simulations. The conformal metric is written as

$$\tilde{g}_{ij} = f_{ij} + e^{-(r_A/w)^2}\left(g^A_{ij} - f_{ij}\right) + e^{-(r_B/w)^2}\left(g^B_{ij} - f_{ij}\right), \tag{4.1}$$

where $r^{A,B}$ are the distances from black holes A and B, and $g^{A,B}_{ij}$ is the Kerr-Schild metric boosted in the direction of the black hole's motion. This has the effect that the metric looks like Kerr-Schild near the black holes, and looks flat far away. The Gaussian scalings help improve the convergence of the initial data. SKS initial data is now the standard choice for all BBH simulations with spin done by the SXS collaboration, and was used in the creation of large waveform catalogs (Mroue et al. 2013; Chu et al. 2015). It has also been used in simulating black holes with nearly extremal spins (Lovelace et al. 2012; Scheel et al. 2015; Lovelace et al. 2015). A similar approach has also been used for spinning black holes in BH-NS binaries(Foucart et al. (2008), cf. Chap. 3). In contrast, CF initial data is used for non-spinning and low-spin ($\chi < 0.5$) BBH simulations (Boyle et al. 2007; Buchman et al. 2012; Chu et al. 2015).

Lovelace (2009) investigated the effects on junk radiation of using SKS initial data for equal mass, non-spinning black holes. It was found that in general, the conformally curved initial data can decrease the amplitude of the junk radiation by a factor of ~ 2. Superposed Kerr-Schild initial data is built around the Kerr-Schild metric, which exactly

represents single spinning black holes. Therefore, one would expect that the advantages of superposed Kerr-Schild become particularly apparent for spinning black holes.

In this chapter we investigate the parameter space dependence of junk radiation. We measure its dependence on the spin of the black holes and on their initial separation, for low eccentricity, equal-mass, spin-aligned binaries. We also perform a comparison between conformally flat (CF) initial data and superposed Kerr-Schild (SKS) initial data. To quantify the amount of junk radiation we will use three diagnostics - the amount of energy present in the junk radiation, and the size of the transient effects of mass increase and spin decrease due to the junk radiation.

This chapter is organized as follows: section 4.3 presents the numerical methods, and section 4.4 describes how we quantify junk radiation and other initial transients in the BBH initial data sets. We present our results in Sec. 4.5 and close with a discussion in Sec. 4.6.

4.3 Numerical Methods

4.3.1 The Initial Value Problem

Employing the usual 3+1 decomposition (Arnowitt et al. 1962; York, Jr. 1979), spacetime is foliated by a family of spacelike hypersurfaces Σ_t. Each hypersurface has a future-pointing unit normal n^μ, induced metric g_{ij}, and extrinsic curvature $K_{\mu\nu} = -\frac{1}{2}\mathcal{L}_n g_{\mu\nu}$. The metric is written as

$$g_{\mu\nu} = -\alpha^2 dt^2 + g_{ij}\left(dx^i + \beta^i dt\right)\left(dx^j + \beta^j dt\right), \tag{4.2}$$

where α and β^i are the lapse function and the shift vector respectively. The lapse measures the proper time between neighbouring hypersurfaces, and the shift vector determines how coordinate labels move between neighbouring hypersurfaces. On the initial

hypersurface Σ_0, spatial metric and extrinsic curvature must satisfy the vacuum constraint equations

$$R + K^2 - K_{ij}K^{ij} = 0, \tag{4.3}$$

$$\nabla_j \left(K^{ij} - g^{ij}K \right) = 0. \tag{4.4}$$

To solve the constraint equations one writes (Lichnerowicz 1944) the metric in terms of a conformal metric $\tilde{g}_{ij}$ and a conformal factor Ψ:

$$g_{ij} = \Psi^4 \tilde{g}_{ij}. \tag{4.5}$$

We also split the extrinsic curvature into trace and trace-free parts

$$K^{ij} = A^{ij} + \frac{1}{3} g^{ij} K, \tag{4.6}$$

and employ the extended conformal thin sandwich formalism (York 1999; Pfeiffer & York 2003) to further decompose A^{ij}. One must then choose $(\tilde{g}_{ij}, \partial_t \tilde{g}_{ij}, K, \partial_t K)$ as the free data. Compared to the extrinsic curvature decomposition (Murchadha & York, Jr. 1974), the conformal thin sandwich formalism allows for physically motivated choices to a larger number of the free data. Elliptic equations with appropriate boundary conditions are then solved for Ψ, $\alpha\Psi$, and β^i, and the physical data is re-assembled. $\partial_t \tilde{g}_{ij} = \partial_t K = 0$ is chosen so that system is initially stationary in the co-rotating frame. This then leaves $\tilde{g}_{ij}$ and K as the free data to choose.

The two types of initial data we compare are described in detail in Lovelace et al. (2008): conformally flat, quasi-equilibrium initial data employs conformal flatness, $\tilde{g}_{ij} = f_{ij}$, maximal slicing, $K = 0$, and inner boundary conditions that enforce that the black holes are instantaneously in equilibrium (Caudill et al. 2006; Cook & Pfeiffer 2004; Cook 2002). Superposed Kerr-Schild initial data, first used in (Marronetti & Matzner 2000; Matzner et al. 1998)], takes the spatial metric and extrinsic curvature as superposition of elements of Kerr-Schild metrics (one for each black hole). As explained in Lovelace et al. (2008), we introduce Gaussian attenuation functions to ensure regularity at spatial

infinity. The details on the inner boundary conditions used can be found in Lovelace et al. (2008).

4.3.2 Code

The initial data is solved using the spectral solver `Spells` (Pfeiffer et al. 2003) of the Spectral Einstein Code `SpEC`[2]. This is a multi-domain elliptic PDE solver that uses pseudo-spectral methods, whereby quantities of interest are expressed as a linear summation of basis functions. This method gives exponential convergence (with the number of basis functions) as long as the quantities of interest are smooth. The black hole singularities are dealt with by excision from the computational grid. We evolve the initial data with the dual frame method described in Scheel et al. (2006). The domain decomposition and position of the black holes are fixed in a comoving frame, but the equations of motion are solved in an inertial frame that is asymptotically Minkowski. The frames are related by a rotation (due to orbital motion) and a radial rescaling (due to inspiral motion).

Gravitational waves are extracted on outer spheres using the Newman-Penrose scalar Ψ_4. Given a spacelike hypersurface with unit normal n^μ and a spatial unit vector in the direction of wave propagation r^μ, Ψ_4 is defined as

$$\Psi_4 = -C_{\alpha\mu\beta\nu} l^\mu l^\nu m^\alpha \bar{m}^\beta, \tag{4.7}$$

where $C_{\alpha\mu\beta\nu}$ is the Weyl tensor, $l^\mu = (n^\mu - r^\mu)/\sqrt{2}$ and m^μ is a complex null vector satisfying $m^\mu \bar{m}_\mu = 1$. We then expand Ψ_4 in spin-weighted spherical harmonics

$$\Psi_4(t, r, \theta, \phi) = \sum_{l=2}^{l_{\max}} \sum_{|m| \leq l} \Psi_4^{lm}(t, r) {}_{-2}Y_{lm}(\theta, \phi) \tag{4.8}$$

The number of terms used in this expansion is generally $l_{\max} \leq 8$ in our simulations. At large r, Ψ_4 is related to the gravitational wave amplitude, h, by

$$\Psi_4 = \frac{d^2}{dt^2} h_+ - i \frac{d^2}{dt^2} h_\times. \tag{4.9}$$

[2] `www.black-holes.org`

4.3.3 Eccentricity Reduction

Gravitational radiation tends to circularize in-spiralling compact binaries (Peters & Mathews 1963; Peters 1964). We reduce orbital eccentricity with an iterative method similar to the one described in (Boyle et al. 2007; Chu et al. 2009). One selects the initial orbital frequency Ω_0 from Kepler's third law or from a Post-Newtonian calculation, while assuming that the initial radial velocity, v_r is zero. After the first simulation has run for a sufficient length, about two orbits, we fit the time derivative of the orbital frequency, $\dot{\Omega}(t)$ as suggested in Buonanno et al. (2011a), to the function

$$\dot{\Omega}(t) = A_0 \left(\tau - t\right)^{-11/8} + A_1 \left(\tau - t\right)^{-13/8} + B \cos\left(\varphi + \omega t + q t^2\right). \tag{4.10}$$

Here $\{A_0, A_1, B, \varphi, \omega, q, \tau\}$ are the fitted parameters. The first two terms in Eq. 4.10 represent the smooth inspiral motion of the black holes, with functional form motivated by PN calculations (Blanchet 2011). The oscillatory term captures effects due to eccentricity. After the trajectories of an evolution have been analyzed via the fit in Eq. 4.10, we update the parameters with

$$\delta\Omega_0 = -\frac{B\omega \sin\varphi}{4\Omega_0^2}, \tag{4.11}$$

$$\delta v_r = \frac{B d_0 \cos\varphi}{2\Omega_0}, \tag{4.12}$$

where d_0 is the binary separation. These updates are designed to circularize low eccentricity Newtonian binaries. The eccentricity of the binary is estimated as (Buonanno et al. 2011a),

$$e = \frac{|B|}{2\Omega_0^2}. \tag{4.13}$$

This process is continued iteratively, typically another one or two times, until the eccentricity is reduced to $e \lesssim 0.002$. The effect of eccentricity on junk radiation is discussed in section 4.4.2.

4.3.4 Simulations

We run BBH evolutions using both conformally flat and SKS initial data. We consider five different initial separations for CF data, $D/M = \{12, 15, 20, 25, 30\}$, and $D/M = \{12, 15, 20\}$ for SKS data, where M is the total mass of the binary. At each separation we consider six different spins, $\chi = \{0, 0.1, 0.2, 0.3, 0.4, 0.5\}$. In each case the black holes are of equal mass, equal spin, and the spin is aligned with the orbital angular momentum, i.e., in the the $+\hat{z}$ direction. To test the convergence of our measurements, each run is done at four resolutions, which we will refer to as `N0` (lowest resolution) to `N3` (highest resolution). Each evolution is run to about $t \sim 1000M$, which is long enough to accurately measure the eccentricity, and make sure that it is sufficiently low for our purposes, i.e., $e \lesssim 0.002$.

4.4 Methodology

We employ three diagnostics to measure the initial relaxation of the initial data: the outgoing pulse of radiation (junk radiation), the change in black hole mass during relaxation, and the change in black hole spin during relaxation.

4.4.1 Pulse in the Gravitational Waveform

In this section we discuss our methods of quantifying the amount of junk radiation present in a given simulation. It is not immediately obvious what the best way to do this is. Lovelace (2009) considered the maximum value of the Newman-Penrose waveform, $\max\{R|\Psi_4^{lm}|\}$, where R is the extraction radius of the gravitational waves. The $(l, m) = (2, 2)$ and $(2, 0)$ modes were found to dominate. We find, however, that this method has some inadequacies. This is illustrated by comparing $R|\Psi_4^{lm}|(t_R)$, where t_R is the retarded time, $t_R = t - R$, in two different simulations. These use CF data, with the parameters $\{D = 15M, \chi = 0.2\}$; one is at our typical highest resolution `N3`, and another at an even

higher resolution, N7. In terms of the total number of basis functions X, $X^{1/3} \sim 58$ for N3 and $X^{1/3} \sim 78$ for N7. The $(2,0)$ and $(2,2)$ modes are shown in the top panel of Fig. 4.2. It is clear that the $(2,0)$ mode is significantly different between N3 and N7, in both the largest peak and in the subsequent smaller peaks, and that these differences are not well captured simply by using $\max\{R|\Psi_4|\}$. In Fig. 4.2 we also show these quantties for an SKS run with the same parameters. Because the waveform is significantly different from the CF waveform in both the number of peaks and their relative heights, it is clear that $\max\{R|\Psi_4^{lm}|\}$ does not encapsulate this waveform very well.

As a more robust quantity that incorporates the whole waveform, and is less resolution dependent than $\max\{R|\Psi_4^{lm}|\}$, we consider the total energy carried away from the system by gravitational waves. The gravitational wave energy flux is (Boyle et al. 2008)

$$F(t) = \frac{1}{16\pi} \sum_{l,m} \dot{h}^2_{lm}(t), \tag{4.14}$$

where

$$\dot{h}_{lm}(t) = \int_{t_0}^{t} \Psi_4^{lm}(t')dt' + H_{lm}. \tag{4.15}$$

The H_{lm} are integration constants. To measure the initial pulse of radiation, we use $t_0 = 0$ and $H_{lm} = 0$. The energy flux, $F(t)$, is shown in the red curves in Fig. 4.3 for conformally flat initial data (top panel) and SKS initial data (bottom panel). The initial burst is apparent in these figures; at late times $t_R \gtrsim 40M$, $F(t)$ approaches the nearly constant energy flux of the astrophysical inspiral. We are now faced with two problems: We would like to isolate the energy carried in junk-radiation from the energy-flux astrophysical inspiral. And, we would like to do so in a robust way, independent of arbitrary choices. We proceed as follows:

First, we assume that the astrophysical energy flux begins at a time t_{22}, i.e.

$$F_{22}(t) = F_0\, \theta(t - t_{22}). \tag{4.16}$$

Here, F_0 represents the value of $F(t)$ after the pulse of junk-radiation and θ represents the step-function. The choice of a constant value F_0 is reasonable since the timescale

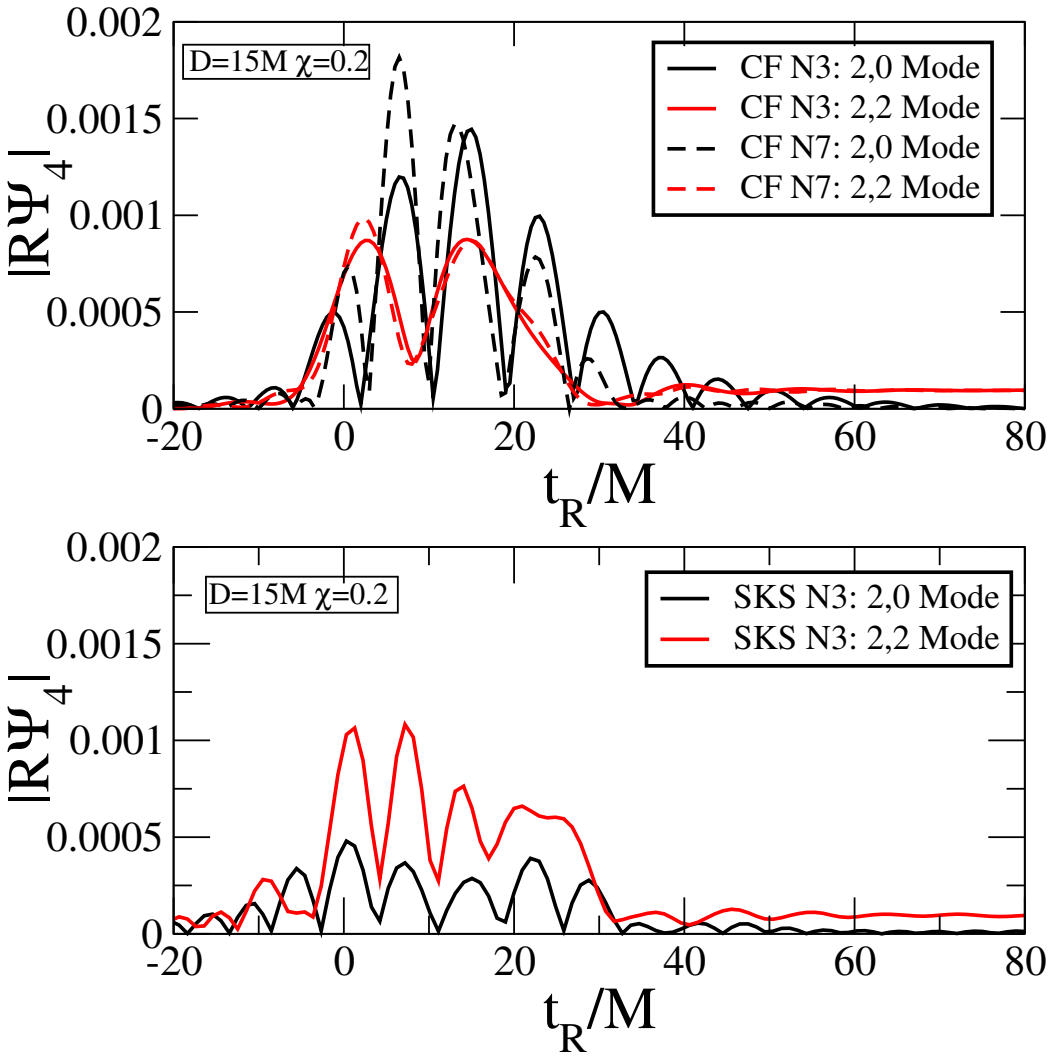

Figure 4.2: *Top Panel:* Comparison of the junk radiation profiles for our usual highest resolution (`N3`) and an additional run at a much higher resolution (`N7`). We see, especially for the $(2,0)$ mode, that the maximum peak of the junk radiation is much higher for `N7`, but additional peaks are comparable or higher for `N3`.

Bottom Panel: Junk radiation profile for an SKS run with the same parameters as in the top panel. The waveform is significantly different in structure from the CF waveform.

on which F_{22} changes significantly is much longer than the junk radiation timescale. We will discuss our choice for t_{22} shortly. The energy in the junk-radiation is now taken as

$$E_J = \int_0^{t_C} \big[(F(t) - F_{22}(t)\big] dt, \tag{4.17}$$

where the cut-off time t_C is chosen after the junk radiation has decayed, i.e. $t_C - R \gtrsim 50M$. In Fig. 4.3 we plot a representative example of the computation of E_J for CF (top panel) and SKS (bottom panel) data. The blue dashed curves represent $F_{22}(t)$, while the shaded area represents E_J. As already apparent from Fig. 4.3, the precise value of t_C is not extremely important, because at late times $F(t) - F_{22}(t) \approx 0$.

It remains to chose a prescription for the choice of t_{22}, the time when we deem the astrophysical waveform to "turn on". A simple method would be to choose t_{22} to correspond to $\max\{F(t)\}$. This seems reasonable for the conformally flat curve in Fig. 4.3, but the more wide double-peaked structure of the SKS curve shows that another approach is needed. Instead we take t_{22} to correspond to the flux weighted centre of the junk radiation waveform. The first moment of $F(t) - F_{22}(t)$, in other words. So,

$$t_{22} = \frac{\int_0^{t_C} t \left(F\left(t\right) - F_0 \theta\left(t - t_{22}\right)\right) dt}{\int_0^{t_C} \left(F\left(t\right) - F_0 \theta\left(t - t_{22}\right)\right) dt}. \tag{4.18}$$

This equation is solved iteratively for t_{22}.

4.4.2 Uncertainty in E_J

Several effects may influence the quantity E_J computed by Eqs. (4.17) and (4.18). *Numerical truncation error* can be estimated by performing the simulations with different numerical resolution. Our simulations show that in general, E_J increases with resolution. This is because junk radiation is a short wavelength feature, so greater resolution allows for more of the features present to be captured. To estimate the uncertainty in E_J, we compare our $\{D = 15M,\, \chi = 0.2\}$ runs at `N3` and `N7`, as discussed earlier. We find that at `N7`, E_J is about 13% greater than at `N3`. Since we don't have such high resolutions

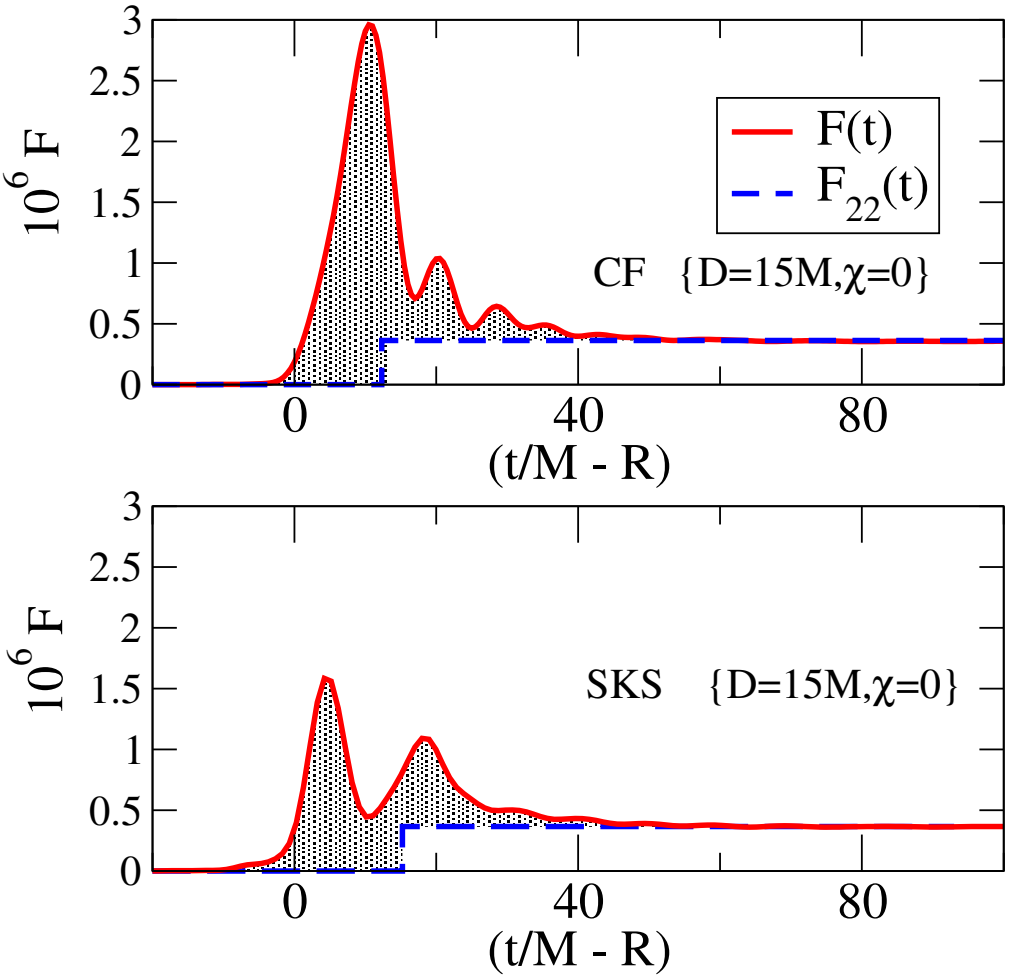

Figure 4.3: The flux $F(t)$ is plotted for two different runs, both with parameters $D = 15M$ and $\chi = 0$. Conformally flat initial data is in the top panel and SKS initial data is in the bottom panel. The solid red curve represents the total flux, $F(t)$. The dashed blue curve represents $F_{22}(t)$, the astrophysical flux that we subtract from $F(t)$. The shaded area between the two curves is the energy in junk radiation, E_J.

runs available for each of our cases, we assume that we can use this same 13% difference for each of our runs. We are also assuming that at `N7` the junk radiation is nearly fully resolved, so that this difference is a good indication of the true value. Finally, we use this same uncertainty of 13% for the SKS runs as well - while the technology is different for the SKS runs, it should still be a reasonably good estimate of the numerical truncation error in them.

A second uncertainty arises through the *choice of* t_C. This number is chosen manually for each run, introducing a subjective element into the analysis. Examining the flux curves in Fig. 4.3, for example, t_C could conceivably be chosen differently by $\sim 10M$ and still be a reasonable choice. Our definition Eq. (4.17) was meant to be robust to small changes in t_C. For E_J to be a robust measurement, it should therefore not change significantly in response to changes δt_C that are of that order. Indeed, this is enforced by our definition of E_J, which subtracts out the additional flux in the astrophysical $(2,2)$ mode. To verify this assertion, we compute E_J with t_C in Eq. (4.17) replaced by $t_C + \delta t_C$. Figure 4.4 shows that indeed E_J is almost independent of δt_C. In Fig. 4.4, E_J is plotted against t_C in the representative $\{D = 15M, \chi = 0\}$ case. For each run we define a fractional error parameter due to the choice of t_C, where we average the differences for $\delta t_C = -10M$ and $\delta t_C = 10M$:

$$\frac{\Delta E}{E} = \frac{|E_J(t_C + 10M) - E_J(t_C)| + |E_J(t_C) - E_J(t_C - 10M)|}{2E_J(t_C)} \tag{4.19}$$

This uncertainty ranges from $\sim 0.25\%$ to $\sim 3.75\%$ throughout all of our simulations.

A third error in E_J arises through *the finite radius of gravitational wave extraction.* In this study, gravitational waves are extracted at radii $R_{\rm ex} \sim 300 - 400M$. Gravitational waves extracted at finite radii are subject to near-field effects which may cause the extracted waveforms to differ from the one that would be observed at infinity. To estimate the error in E_J due to the finite extraction radius, we use the following procedure. For each of our simulations, we compute E_J at several extraction radii, and examine E_J as a

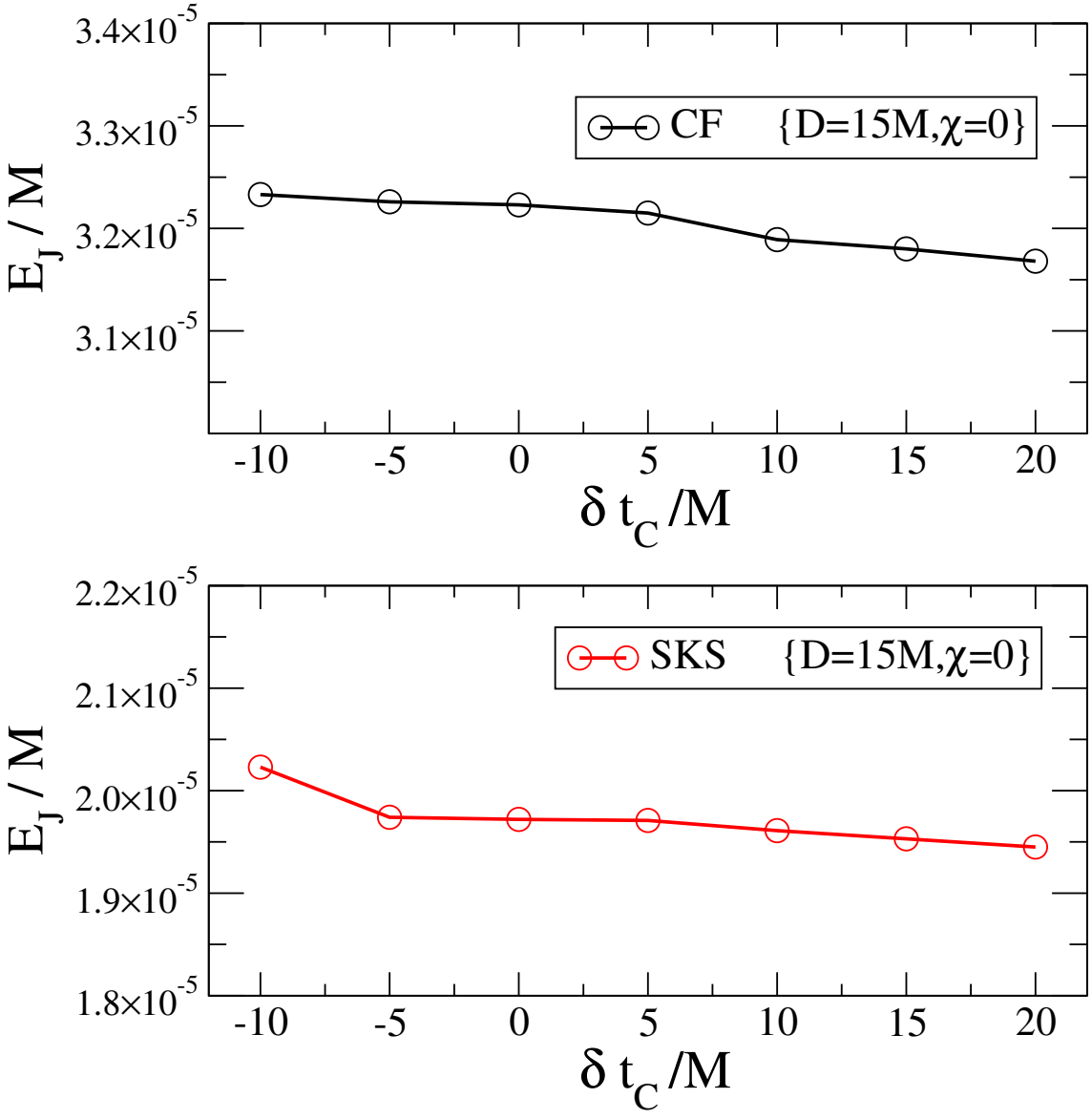

Figure 4.4: E_J is plotted against δt_C, representing changes to the selected value of t_C for runs where $D = 15M$, $\chi = 0$. The results for conformally flat initial data are shown in the top panel, and SKS initial data in the bottom panel. Typical changes in E_J are on the order of a few percent.

function of $1/R_{ex}$. We then extrapolate

$$E_\infty = \lim_{1/R_{ex}\to 0} E_J(1/R_{\rm ex}) \tag{4.20}$$

using a linear fit in $1/R_{\rm ex}$ to estimate the behaviour of E_J at infinity. We then take the fractional difference

$$\frac{\Delta E}{E} = \frac{E_\infty - E_J}{E_J} \tag{4.21}$$

as our error estimate. This parameter is on the order of 10% for most of our runs. Note, however, that we still use E_J and not E_∞ as our measure of energy in the pulse. In Fig. 4.5 we illustrate an example of this procedure, plotting E_J vs. $1/R_{ex}$ for one case, $\{D = 15M, \chi = 0\}$, for both CF and SKS data.

A final factor that could influence the estimated E_J is the *eccentricity of the orbit of the black holes*. Previously we argued that astrophysically realistic binaries have low eccentricity. Because our NR simulations cannot be run at precisely $e = 0$, we now consider how a small residual eccentricity affects the junk radiation, specifically the computed E_J. We examine the case $\{D = 25M, \chi = 0.1\}$ for CF data, as this particular case encountered a fairly large range of eccentricities in the eccentricity reduction process; $e \sim \{0.03, 0.008, 0.0006\}$. The measured E_J for these three cases is $10^6 E_J = \{7.053 \pm 0.38\%, 7.204 \pm 0.53\%, 7.174 \pm 0.58\%\}$. Here, the quoted uncertainty is purely due to the choice of t_C. The differences between the first two eccentricities is 2.10% and it is 0.42% for the last two. Because the latter difference is less than the uncertainty due to the choice of t_C, the two runs are effectively indistinguishable, and we conclude that we can safely ignore the effects of residual eccentricity once we have $e \lesssim 0.008$. However, to be "safe", we have generally reduced the eccentricity of all of our runs to $e \lesssim 0.002$.

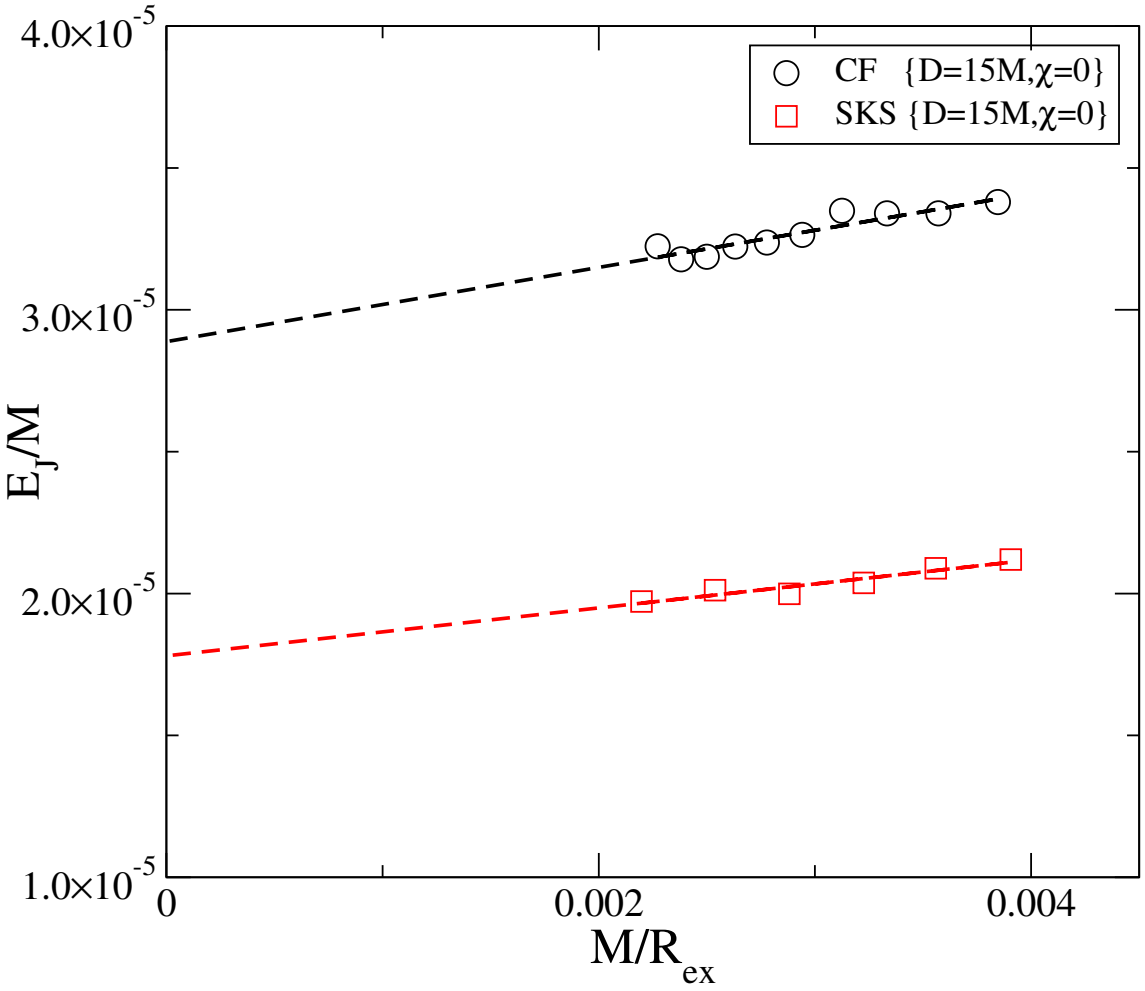

Figure 4.5: E_J as a function of $1/R_{ex}$, where R_{ex} is the extraction radius. This is for the case where $\{D = 15M, \chi = 0\}$, with CF data in black and SKS data in red. The dashed lines represent the best linear fit. The extrapolation to $1/R_{ex} \to 0$ allows us to estimate the error on E_J due to finite extraction radius effects.

4.4.3 Transient Behaviour in Black Hole Quantities

4.4.3.1 Mass Increase

In addition to the energy carried away in junk radiation, we utilize two further diagnostics of transients arising from imperfect initial data. The first diagnostic comes from the irreducible mass of the black hole, $M_{\rm irr} = \sqrt{A/16\pi}$, where A is the area of the black hole's apparent horizon. In the first few M during the evolution, the apparent horizon mass $M_{\rm irr}(t)$ increases by a small amount, before settling down to an approximately constant value. This effect is visible in Fig. 4.6 for $0 \leq\ t/M \leq 10$. We characterize the increase in mass due to initial transients by

$$\delta M(t) = \frac{M_{\rm irr}(t)}{M_{\rm irr}(0)} - 1 \tag{4.22}$$

and we define the equilibrium parameter $\delta M = \delta M(t_{\rm eq})$. Here $t_{\rm eq}$ is a time where the mass-increase is complete has and levelled off; typically $\sim 20M$.

For SKS initial data the behaviour of $M_{\rm irr}(t)$ is more complex. Within the first few M, $M_{\rm irr}(t)$ shows a rapid increase, presumably due to relaxation of the geometry in the immediate vicinity of the black holes. The trend here is similar to the CF initial data, in that larger spins result in a larger increase of $M_{\rm irr}(t)$, albeit the magnitude of the increase is about a factor of 50 smaller for SKS initial data. Subsequently, starting at $t \sim 40M$, the SKS simulations show a second set of features, oscillations with amplitude $\sim 2\times10^{-5}$ lasting about $60M$. The features of these oscillations are similar to each other even for runs with different spin black hole spin χ. Therefore, it is likely that these oscillations are caused by features in the initial data set *away* from the black holes.

There is a clear qualitative difference between the CF and SKS curves. The CF data forms an increasing sequence of δ_M with χ, and δ_M is clearly well-defined in each case. However, the SKS data exhibits oscillatory behavior that is relatively spin-independent, and there is not a clear way to robustly define δ_M. To further underscore the difficulties of the SKS data, figures 4.7 and 4.8 show convergence tests for one of the mass curves

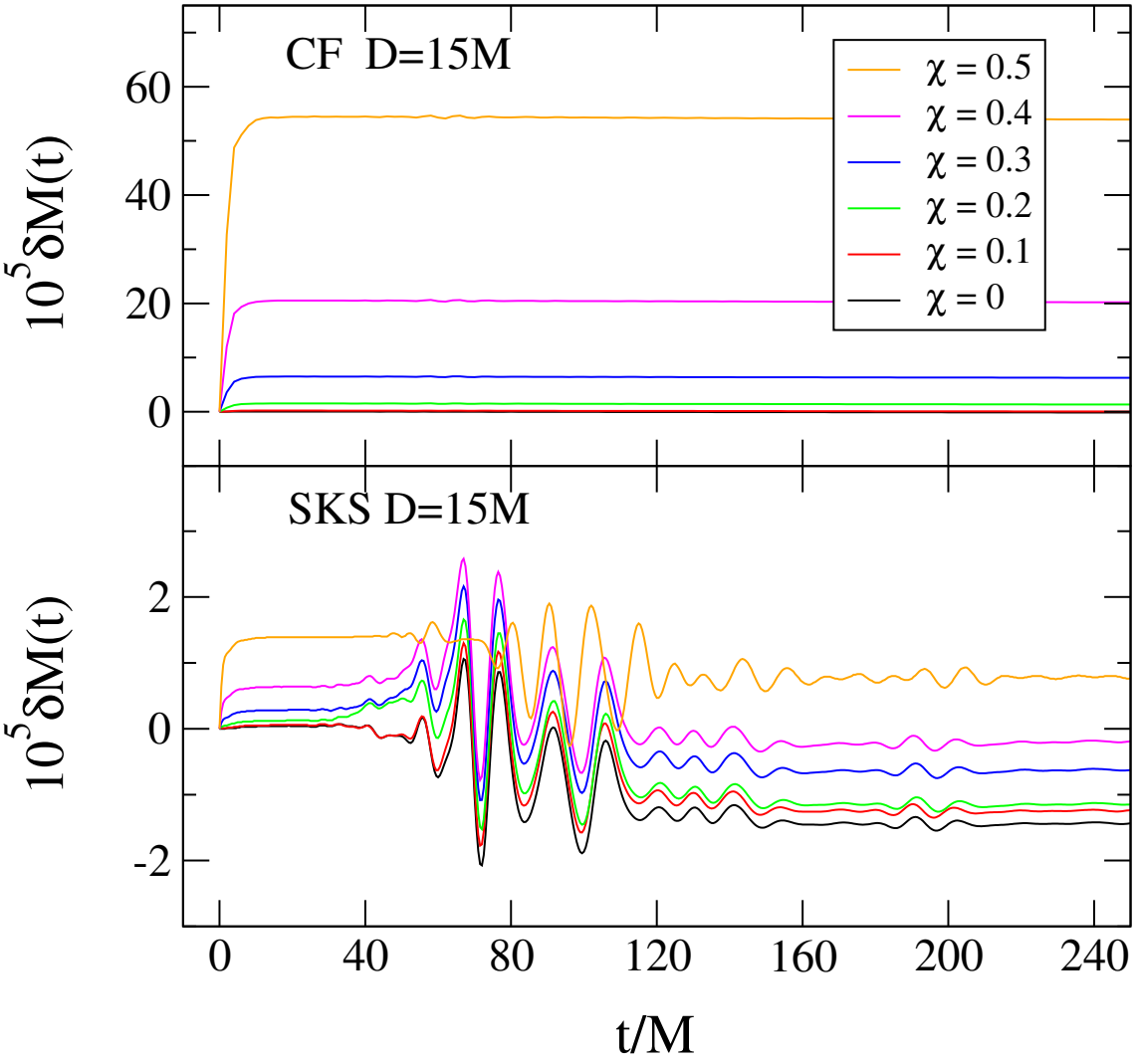

Figure 4.6: Normalized change in irreducible mass curves for CF data (top panel) and SKS data (bottom panel) for all of the different spins in the covered parameter space and $D = 15M$ remaining constant.

shown in fig. 4.6, $\{D = 15M, \chi = 0.3\}$. The top panels of Figs. 4.7 and 4.8 show $M_{\rm irr}(t)$ of one of the black holes computed at different numerical resolutions, and the bottom panels show differences in $M_{\rm irr}(t)$ computed at neighboring resolutions. Note that our parameter space studies presented in Sec. 4.5 were usually performed on resolution `N3`; we have run `N4-N6` for select cases to test convergence. The CF initial data shows rapid convergence and the features in the upper panel of Fig. 4.7 are well resolved. For

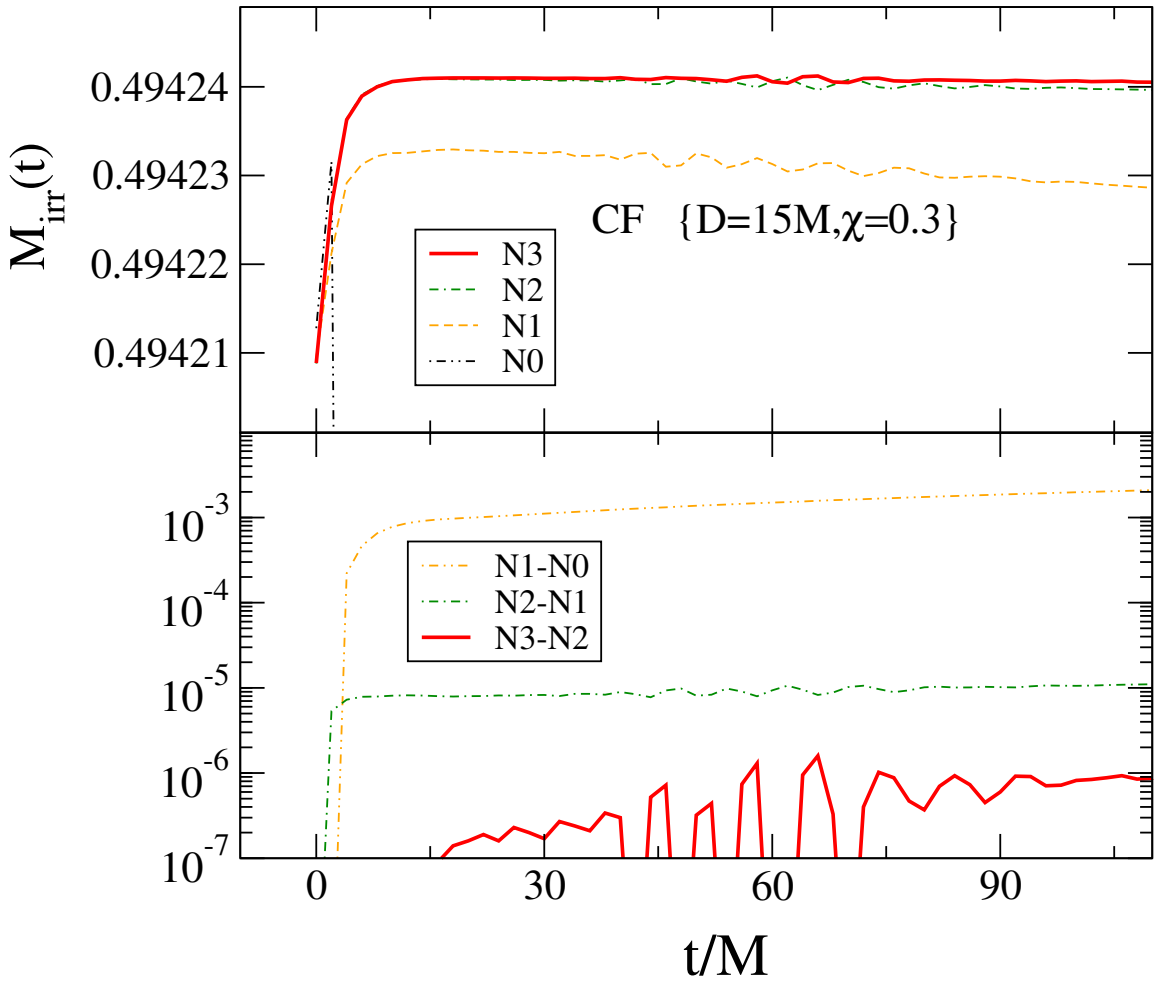

Figure 4.7: Convergence test of $M_{\rm irr}(t)$ for CF initial data in the case $\{D = 15M, \chi = 0.3\}$. The top panel shows $M_{\rm irr}(t)$ at different resolutions, and the bottom panel shows the difference between consecutive resolutions.

the SKS data shown in Fig. 4.8 we do not find convergence - the differences between resolutions do not strictly decrease with increasing resolution, and these differences are of similar order to the features that we are trying to quantify. Our conclusion is therefore that the magnitude of the change $M_{\rm irr}(t)$ for SKS initial data approaches our numerical truncation error, and are furthermore ambiguous due to the extra oscillatory features present in Fig. 4.6. In the parameter space survey of junk radiation in Sec. 4.5 below, we will not attempt to quantify them in detail, beyond giving upper bounds on δ_M for the SKS data.

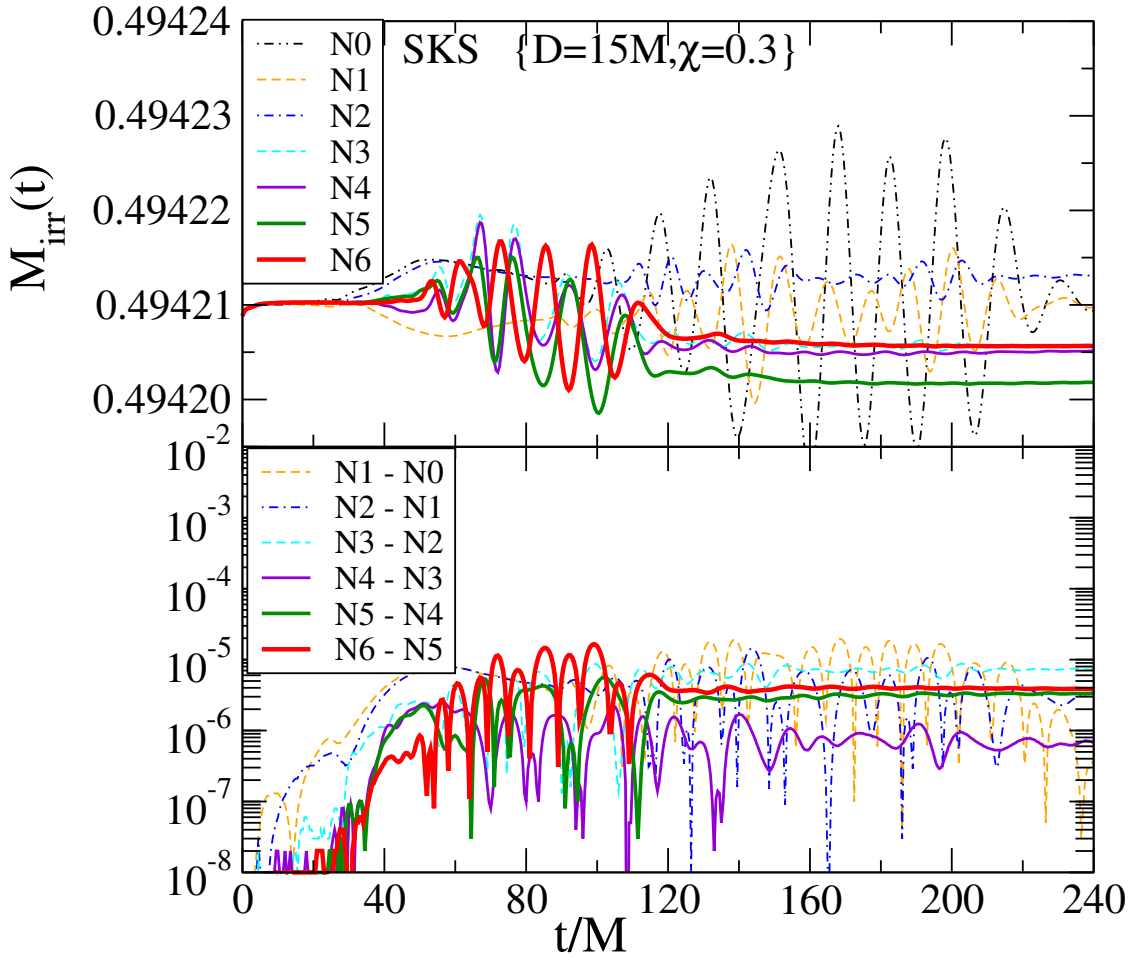

Figure 4.8: Convergence test of $M_{\rm irr}(t)$ for SKS initial data in the case $\{D = 15M,\ \chi = 0.3\}$. The top panel shows $M_{\rm irr}(t)$ at different resolutions, and the bottom panel shows the difference between consecutive resolutions.

4.4.3.2 Spin Decrease

Our third and final quantification of junk radiation comes from the black hole's spin $S(t)$. At early times in each simulation, the spin of each black hole decreases and oscillates rapidly. Eventually, at some time $t_{\rm eq}$, the spin reaches some approximately constant value, which is lower than the initial spin, $S(0)$. This effect can be interpreted as angular momentum being carried away from the system by junk radiation. Note that we use the dimensionful quasi-local angular momentum, measured with approximate Killing vectors as described in Lovelace et al. (2008). We use S rather than $\chi = S/M^2$ to de-couple the change in spin from the change in mass. This effect is illustrated in Fig. 4.9, where we plot $\delta S(t)$ for all of our simulations done at $D = 15M$.

Analogous to $\delta M(t)$, we define $\delta S(t)$ as the fractional spin decrease of the black hole:

$$\delta S(t) = \frac{S(t)}{S(0)} - 1, \tag{4.23}$$

and the equilibrium parameter $\delta S = \delta S(t_{eq})$, where t_{eq} the time when $\delta S(t)$ has reached an approximately constant value.

In Fig 4.9, the SKS data shows oscillatory behavior that makes it difficult to define δS, similar to the behavior of δM reported in Fig. 4.6. After the oscillations, δS does not neatly form a monotonic sequence in χ. Analogous to Figs. 4.7 and 4.8, Figs. 4.10 and 4.11 present convergence tests for $\delta S(t)$, again for the case $\{D = 15M, \chi = 0.3\}$. Similar to what was seen in the convergence test for $M_{\rm irr}(t)$, the CF data converges rapidly, while we see no clear convergence in the SKS data going up to `N6`, and the differences between the resolutions are of a similar order to the features we are trying to quantify. Thus we make a similar conclusion as we did for the mass transients: $\delta\ S$ is small for SKS data compared to CF data for the spins we consider ($\delta\ S \sim -2\times\ 10^{-5} vs. -5\times 10^{-4}$ at $\chi = 0.5$). But because of the confounding oscillatory features and the lack of convergence, we do not seek to further quantify δS for the SKS data.

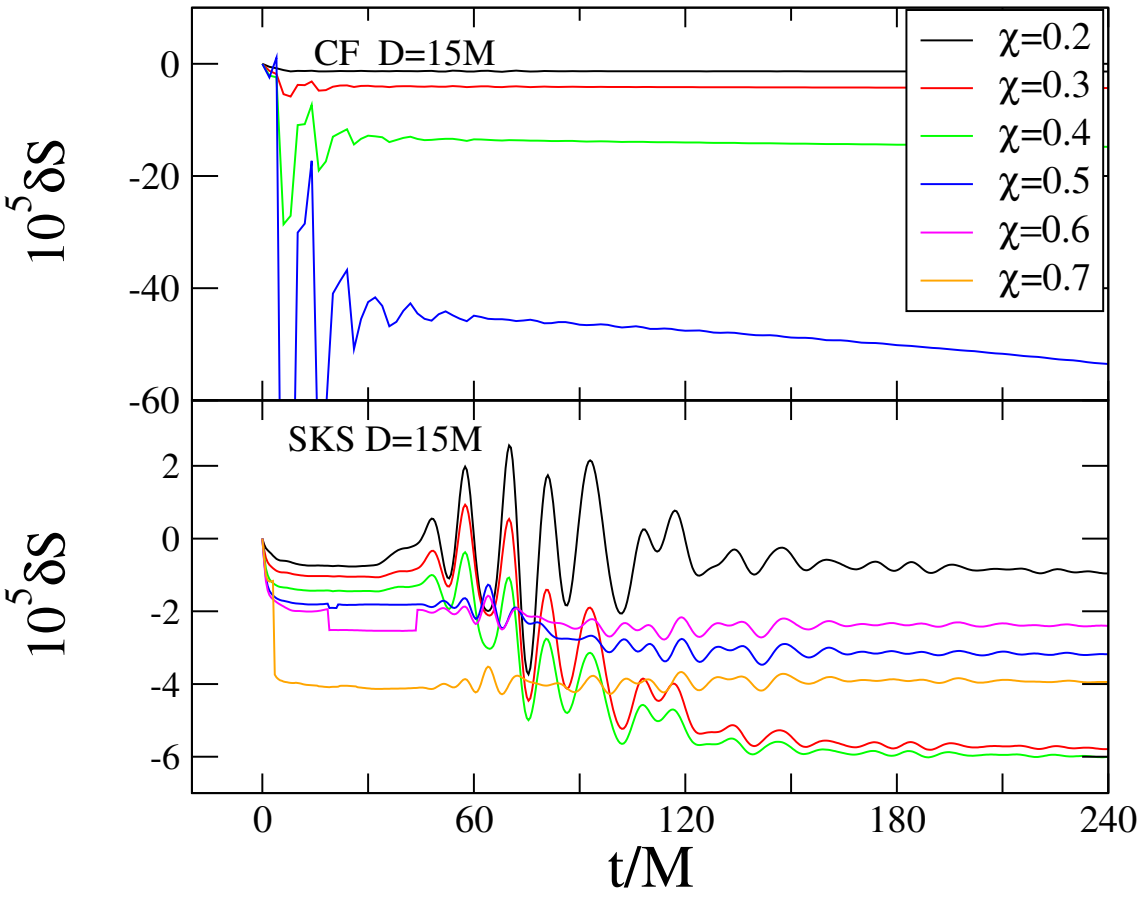

Figure 4.9: Fractional change in spin relative to $t = 0$, $\delta S(t) = S(t)/S(t = 0) - 1$. The top panel shows CF initial data and the bottom panel SKS data (note the different scale). All simulations shown are at $D = 15M$.

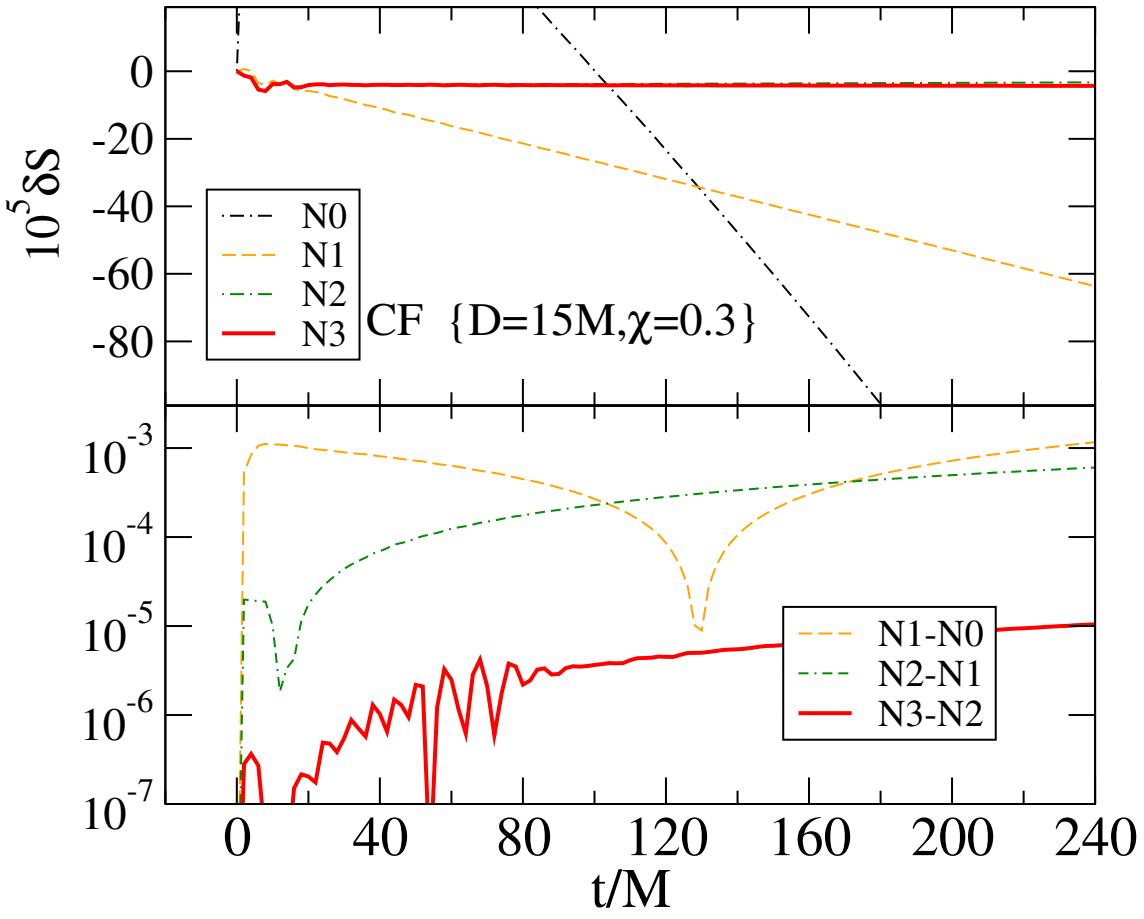

Figure 4.10: Convergence test of $\delta S(t)$ for CF initial data in the case $\{D = 15M, \chi = 0.3\}$. The top panel shows $\delta S(t)$ at different resolutions and the bottom panel shows the differences between consecutive resolutions.

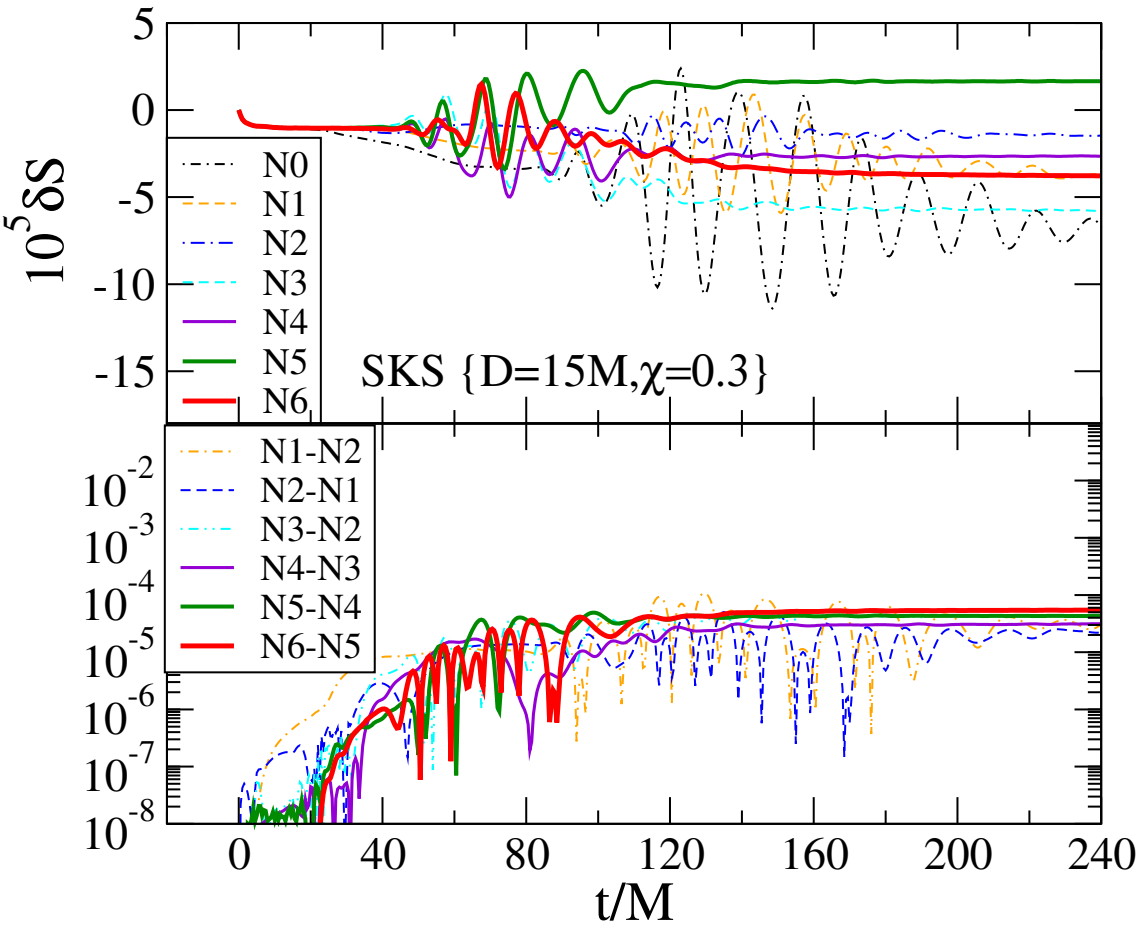

Figure 4.11: Convergence test of $\delta S(t)$ for SKS initial data in the case $\{D = 15M, \chi = 0.3\}$. The top panel shows $\delta S(t)$ at different resolutions and the bottom panel shows the differences between consecutive resolutions.

4.5 Results

4.5.1 Energy in Junk Radiation

Figure 4.12 shows the energy in the pulse of junk radiation, for all of our runs, as a function of spin. As was expected, the energy in junk radiation is a decreasing function of initial separation. We also see that at a given separation and spin, the E_J is always smaller for SKS intiail data than for CF intitial data; typically by about a factor of 2. Within the uncertainty of our simulations, E_J has virtually no dependence on the spins of the black holes. The only exception may be that for conformally flat data, E_J seems to increase as $\chi \to 0.5$. This is most visible in the $D = 12M$ case. Perhaps the dependence of E_J on χ could become important for $\chi > 0.5$ if this trend continues.

Figure 4.13 considers the dependence of E_J on the separation D of the black holes. Because there is virtually no dependence of E_J on χ (cf. Fig 4.12), we plot only $\chi = 0$ in Fig 4.13. E_J vs. D for both CF and SKS data are well approximated by power laws. For conformally flat data,

$$E_J^{\rm CF} \sim 0.062 \left(\frac{D}{M}\right)^{-2.79}, \tag{4.24}$$

and for SKS data

$$E_J^{\rm SKS} \sim 0.020 \left(\frac{D}{M}\right)^{-2.55}. \tag{4.25}$$

Note, however, the latter is a fit to three data points only.

4.5.2 Mass Increase

We now consider the spin and separation dependence of δM. As discussed earlier, we only consider the transient quantities for CF data, due to the small magnitude of δM and δS and their non-convergence in SKS data. We begin by looking at the dependence of δM on separation. In Fig. 4.14, we plot it for curves of constant χ[3].

[3] we omit $\chi = 0$ because the data is too noisy

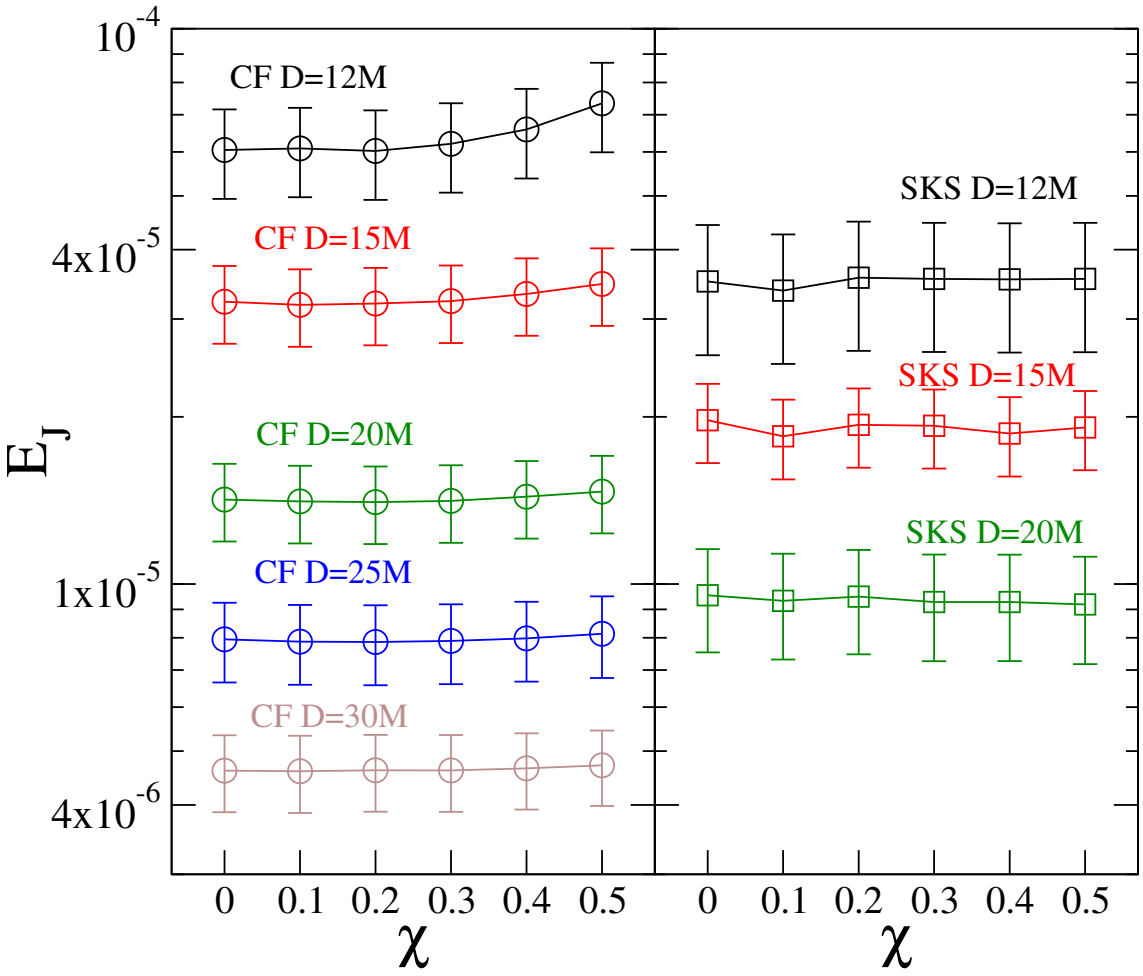

Figure 4.12: Energy in junk radiation as a function of χ at various initial separations, for conformally flat initial data (left panel) and SKS initial data (right panel). Within the uncertainty limit, there is virtually no dependence of E_J on χ.

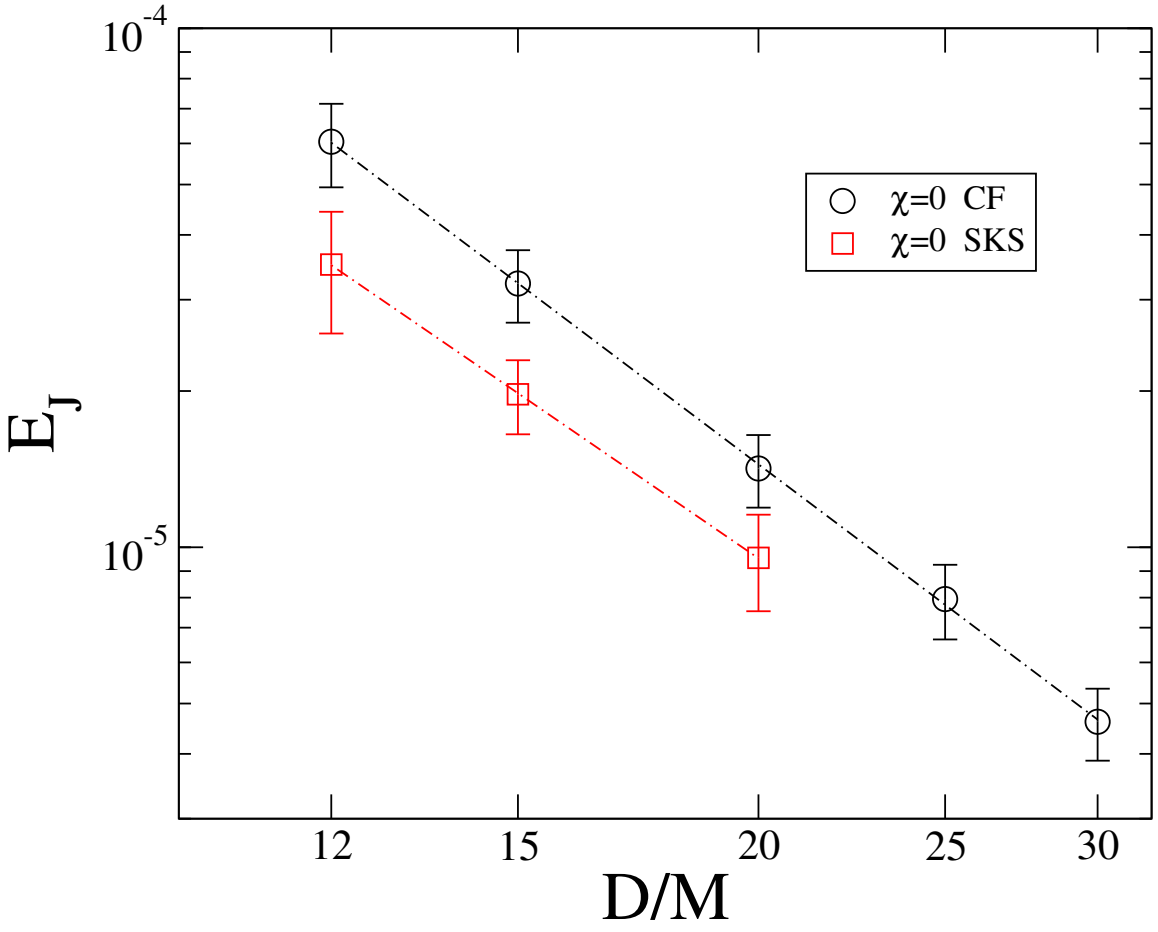

Figure 4.13: Log-log plot of the energy in junk radiation as a function of initial separation for binaries where $\chi = 0$. The black circles and red squares denote conformally flat and SKS initial data, respectively. The dotted lines are power law fits, with indices of ~ -2.79 and ~ -2.55 respectively.

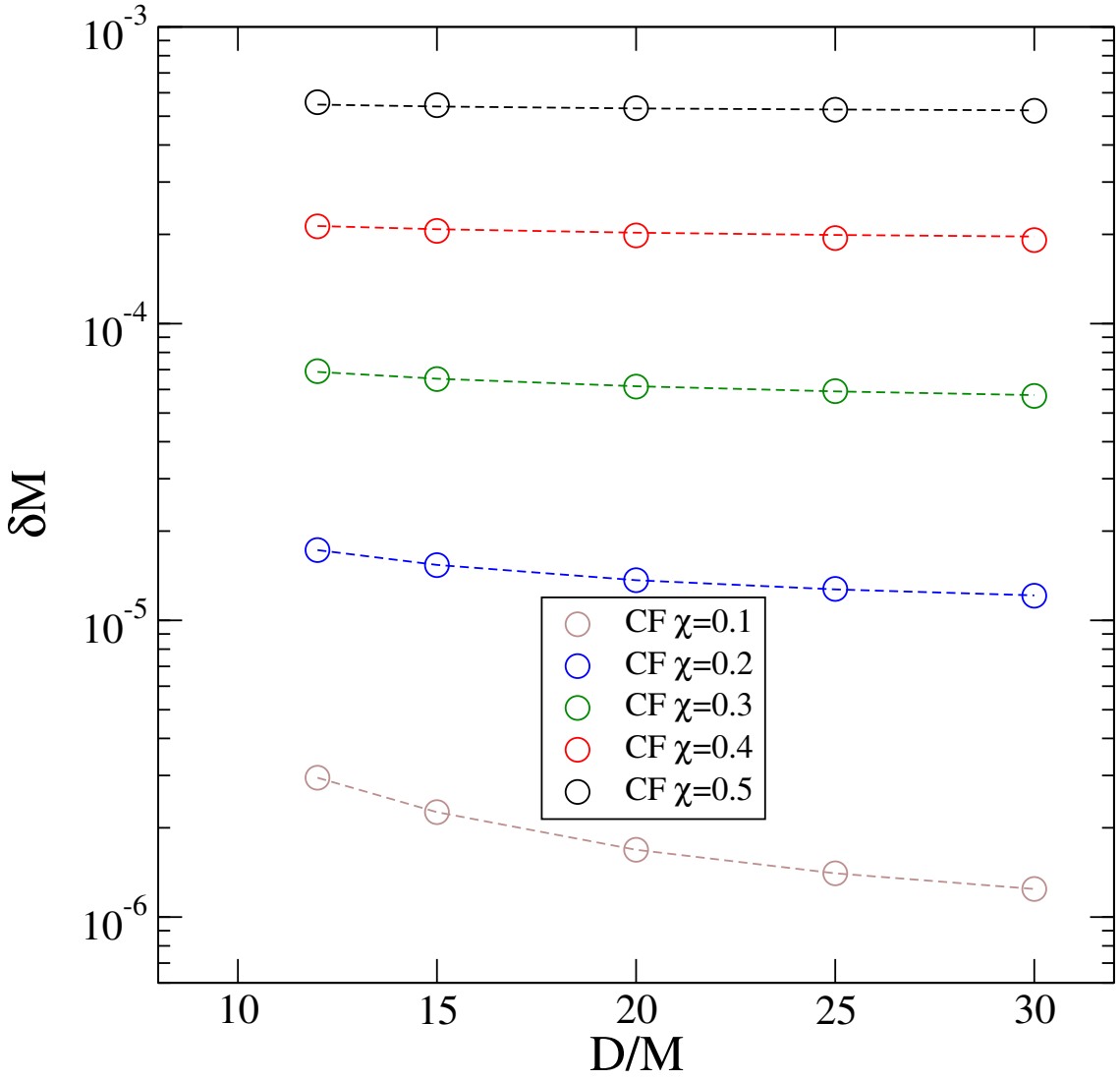

Figure 4.14: δM as a function of initial separation for CF initial data. The dotted lines are the best fits to a power law plus a constant offset.

The data are nearly independent of distance at high spin, while there is a clear dependence at lower spin. In each case, we fit the data to a power law plus a constant offset. The fits are

$$\begin{aligned}
\delta M^{\chi=0.1} &= 0.00017\,(D/M)^{-1.76} + 8.19\times10^{-7},\\
\delta M^{\chi=0.2} &= 0.00021\,(D/M)^{-1.36} + 1.01\times10^{-5},\\
\delta M^{\chi=0.3} &= 0.00015\,(D/M)^{-0.75} + 4.60\times10^{-5},\\
\delta M^{\chi=0.4} &= 0.00026\,(D/M)^{-0.87} + 1.83\times10^{-4},\\
\delta M^{\chi=0.5} &= 0.00047\,(D/M)^{-0.99} + 5.08\times10^{-4}.
\end{aligned}$$

In Fig. 4.15 we show a log-log plot of δM on χ for curves on constant D. In each case we compute the best fit power law to the data. These fits are

$$\begin{aligned}
\delta M^{D=12M} &= 0.0042\chi^{3.24},\\
\delta M^{D=15M} &= 0.0046\chi^{3.39},\\
\delta M^{D=20M} &= 0.0052\chi^{3.56},\\
\delta M^{D=25M} &= 0.0056\chi^{3.66},\\
\delta M^{D=30M} &= 0.0059\chi^{3.74}.
\end{aligned}$$

We see that the power law exponents are much larger in magnitude than the power law exponents found in the δM vs. D fits. This shows that the dependence of δM is much stronger on χ than it is on D. If we extrapolate these fits out to $\chi = 1$, then $\delta M \sim 0.004 - 0.006$, which would be an appreciable, although not necessarily limiting, effect.

4.5.3 Spin Decrease

As with the mass increase, we only attempt to calculate δS for CF data, as it was found to not be convergent for SKS data. In Fig. 4.16 we plot δS vs. D for curves of constant

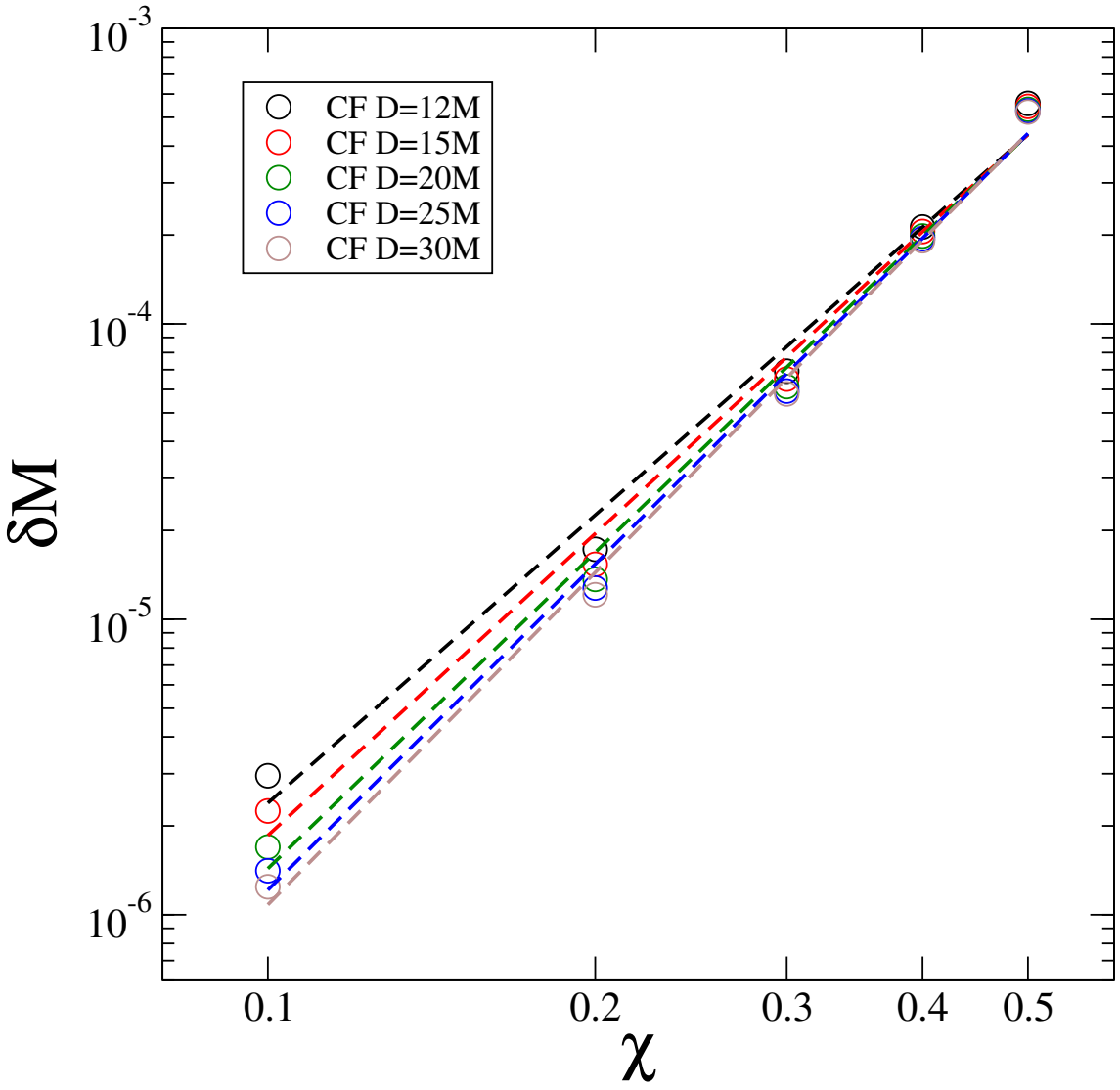

Figure 4.15: δM as a function of black hole spin χ for CF initial data, evaluated at each different initial separation. The dotted lines are the best fit power laws to the data.

χ. We omit $\chi = 0$ because δS is not well-defined, and we omit $\chi = 0.1$ because the data is too noisy. The data are similar to those in Fig. 4.14, although there seems to be a stronger dependence on initial separation.

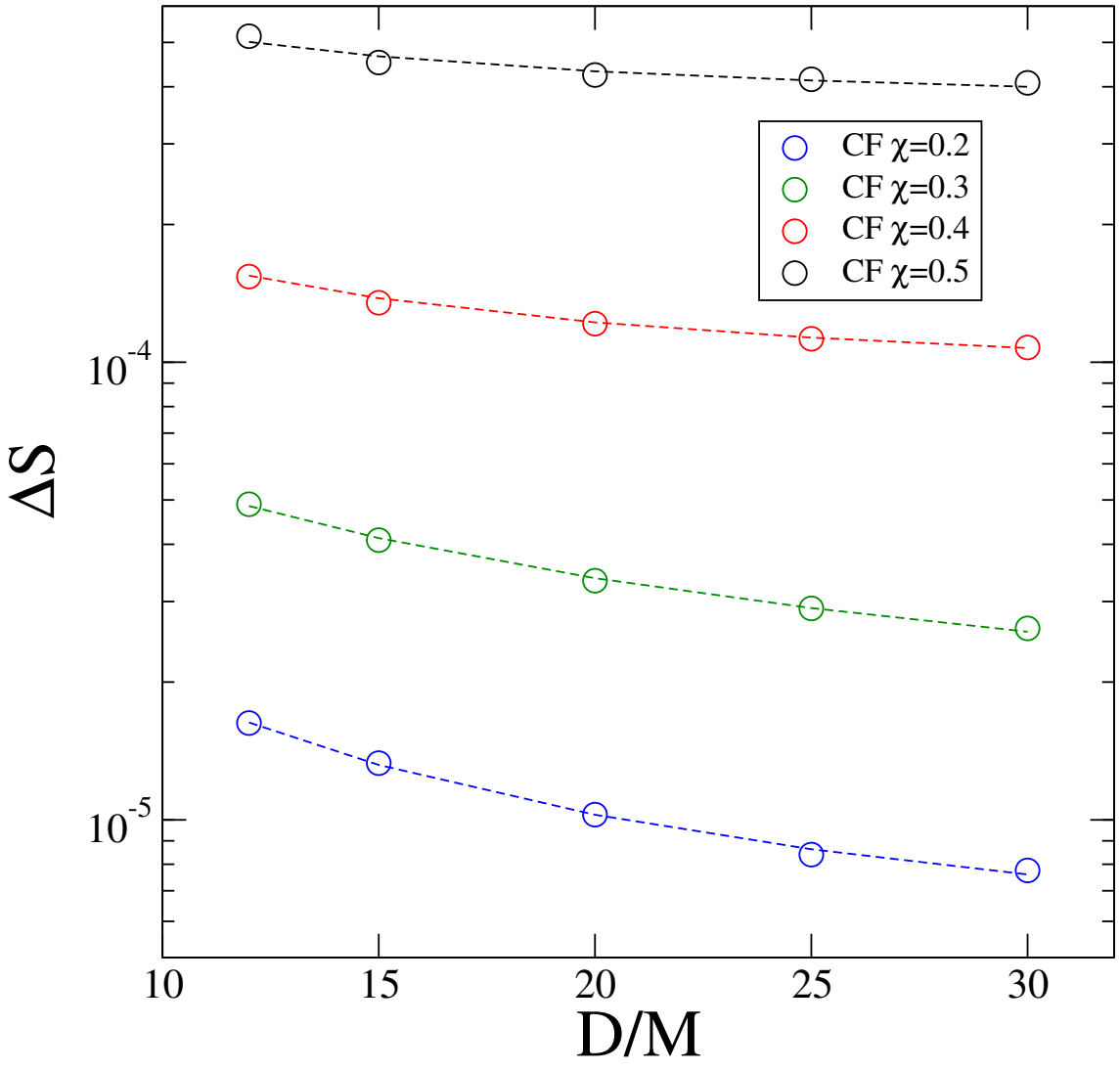

Figure 4.16: δS vs. D for CF initial data. The dotted curves are the best fit power law plus constant offsets.

In each case, we fit the data to a power law plus a constant offset. The fits are

$$\begin{aligned}
\delta S^{\chi=0.2} &= 0.00031\,(D/M)^{-1.28} + 3.70\times10^{-6},\\
\delta S^{\chi=0.3} &= 0.00034\,(D/M)^{-0.84} + 6.03\times10^{-6},\\
\delta S^{\chi=0.4} &= 0.0014\,(D/M)^{-1.19} + 8.35\times10^{-5},\\
\delta S^{\chi=0.5} &= 0.0026\,(D/M)^{-1.13} + 3.45\times10^{-4}.
\end{aligned}$$

In figure 4.17, δS is plotted as a function of χ, at different separations. In each case, the data is a good fit to an exponential; at $D = 15M$,

$$\delta S \sim 1.563\times10^{-6} e^{11.546\chi}. \tag{4.26}$$

Fig. 19 of Lovelace et al. (2008) found a similar result, noting an exponential relationship between $\Delta\chi$ (defined analogously to δS in this chapter) and $\chi(t_{\rm relax})$ for conformally flat initial data. Their relationship is shown from $\chi = 0.5$ to $\chi \sim 0.93$, however their $\Delta\chi$ matches the δS of this chapter in magnitude ($\sim 5\times10^{-4}$) at $\chi = 0.5$, indicating a convergent result between the two works. If we extrapolate the fit of Eq. 4.26 outwards, we find that $\delta S \sim 1$ at $\chi \sim 0.84$. Because this happens before $\chi = 1$, this would set a fundamental limit on the highest black hole spins that can be evolved using conformally flat initial data. Note that because we fit to S and χ, this limit is difficult to directly compute. We are only using five data points and extrapolating quite far, so this result must be taken cautiously. However, Lovelace et al. (2008) found a similar maximum spin limit to our extrapolated limit, as they could only evolve CF data with a maximum spin of $\chi \sim 0.93$.

4.6 Conclusion

We have performed a parameter space study of junk radiation in binary black hole simulations. We studied the effects of initial separation and spin magnitude, for spins up to

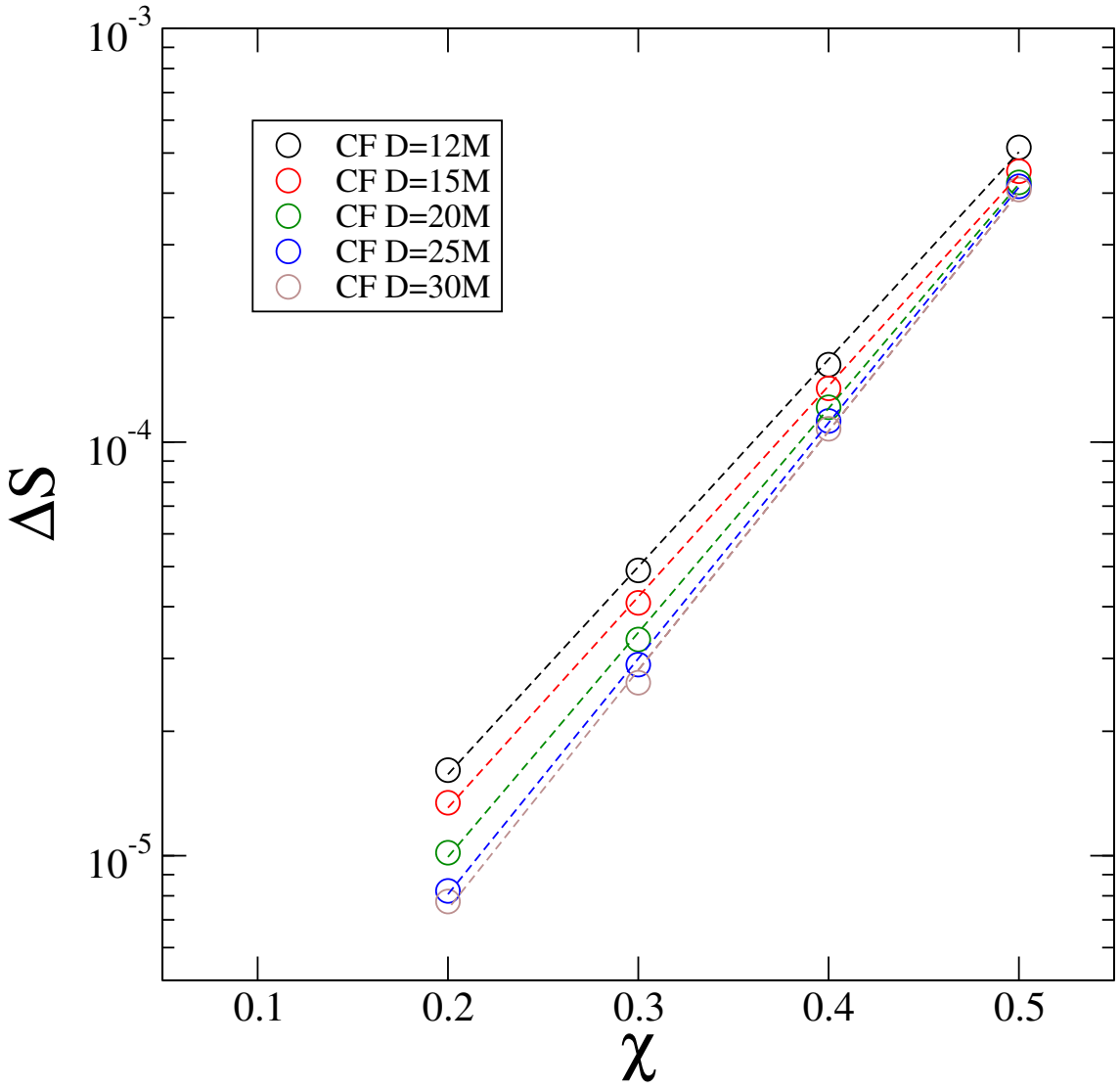

Figure 4.17: Semi-log plot of δS as a function of χ for CF data. The dotted lines are the best fit exponentials.

$\chi = 0.5$, for both conformally flat and superposed Kerr-Schild initial data sets. We used three diagnostics to quantify the amount of junk radiation — the energy carried away by junk radiation, the transient mass increase due to junk radiation and the transient spin decrease due to junk radiation.

For the energy present in the junk radiation, E_J, we found very little dependence on the spin of the black holes, but a power law dependence on the initial separations, with exponents of ~ -2.79 for CF initial data and ~ -2.55 for SKS initial data.

We were unable to directly quantify the mass and spin transients for SKS initial data because of their small magnitudes and a lack of convergence. However, we are able to say that they are below $\sim 2 \times 10^{-5}$ and $\sim 4 \times 10^{-5}$ respectively in the parameter space we study. These are well below the typical values for CF data, by factors of about 50.

For CF data, for both the mass and spin transients, we see very little dependence on initial separation. Instead however, we see very strong dependences on the spin of the black holes, finding an exponential dependence for δS and a steep power law dependence δM. Our curves for $\delta S(\chi)$ agree with a previous result found in Lovelace et al. (2008). The exponential dependence of δS on χ sets a fundamental limit on the maximum spin of black holes that can be evolved with conformally flat initial data.

Chapter 5

Conclusions & Future Work

5.1 Conclusions

With the recent direct detection of gravitational waves, it has never been more exciting to be in the numerical relativity community. Based on the preliminary event rate predictions, the first detection of gravitational waves from a neutron star cannot be far away - if no detections are made in the Advanced LIGO's next two observing runs, significant constraints will be placed on the BNS merger rate (Abbott et al. 2016c). With that comes the exciting possibility of the detection of an electromagnetic counterpart.

In this thesis we have largely focused on spinning neutron stars in compact object binaries. In chapter 2 we introduced our code and methodology for creating initial data for binary neutron star systems with arbitrary spins, and showed that we are able to created convergent, constraint-satisfying initial data. We introduced a novel method to directly measure the spin of the neutron stars using quasilocal approximate Killing vectors, and we showed that this method is accurate and robust. We also evolved three binary configurations, including one highly-spinning precessing system. We showed that the properties of these systems agree remarkably well with Post-Newtonian predictions, even without account for the neutron star tidal terms. We also showed that we are able to control the eccentricity of the systems to an accuracy of $\sim 0.1\%$. Upon evolving

the systems, we found large density oscillations in the neutron stars. We determined that these were due to an excited quasi-normal mode, due to imperfect initial data. As discussed in the appendix of chapter 2, however, we note that these oscillations were present because of an error that was present in the code. Upon fixing that error, the density oscillations drop by a factor of ~ 40, and that we are able to construct initial data with much higher spins than previously. The work done in chapter 2 leaves open maybe possible directions for future studies. At the time of writing chapter 2 the `SpEC` code had a difficult time merging binary neutron stars, and so we were only able to simulate orbits of the late inspiral. It remains an open, and interesting, question as to how high NS spin affects the dynamics of the merger. For example, how neutron star spin affects the properties of the hypermassive neutron star, how it affects the size of the disk, and how it affects the electromagnetic emission if magnetic fields are present are all interesting questions that could be investigated in the future. Given the results of the appendix, future studies should be able to use even higher spinning stars. One can then investigate how well Post-Newtonian match with the numerical relativity simulations at even higher spins. It is also interesting to ask how the spin interacts with neutron star compactness and binary mass ratio in the dynamics of the inspiral and merger.

In chapter 3 we extended the code of chapter 2 to create initial data for black hole–neutron star (BHNS) binaries. To show the robustness of the code, we create many different initial data sets across the BHNS paramter space. We vary the neutron star spin from $\chi_{\rm NS} = 0$ to $\chi_{\rm NS} \sim 0.7$, near the neutron star mass-shedding limit, the black hole spin from $\chi_{\rm BH} = 0$ to $\chi_{\rm BH} = 0.99$, and the mass ratio from $q = 2$ to $q = 10$. We also vary the directions of the neutron star spin and black hole spin, and consider three different compactnesses of the neutron star. An obvious extension of this work would be to evolve and merge some of these initial data sets. We created 36 initial data sets that vary from already published data sets (Foucart et al. 2013a), and so this would facilitate the comparison quite well. One could also use spinning NS in BHNS systems to try to

explore the maximum mass of accretion disks - adding spin on the neutron star should make the material less strongly bound and increase the disk mass further.

Finally, in chapter 4 we studied the paramter space dependence of spurious, "junk", radiation in binary black hole (BBH) simulations. To measure the amount of junk radiation present we introduced three diagnostics - the energy in the pulse of junk radiation, and the mass increase and spin decrease transient quantities. We considered how these depend on the spins and initial separations of the black holes, and we compared conformally flat (CF) initial data with superposed Kerr-Schild (SKS) initial data. In terms of the energy present, we found that it does not depend signficantly on spin, but found power law relations with the initial separations. The energy present in the CF data was larger by a factor of $2-3$. We were unable to directly quantify the transient quantities for SKS initial data beacuse of their small magnitude and their lack of convergence. For the CF data we found weak dependence on initial separation, but a strong power law dependence on spin for the mass increase, and an exponential dependence on spin for the spin decrease. There are several directions in which one could extend this research. The same sort of analysis could be performed using a different type of initial data, such as those adding tidal effects or outgoing gravitational radiation. One could also extend these methods further across the BBH paramter space - going to higher black hole spins, non-equal mass ratios, non-aligned spins, or further/closer separations.

Bibliography

A. Harten, P. D. Lax, B. v. L. 1983, SIAM Rev., 25, 35

Aasi, J., et al. 2015, Class. Quantum Grav., 32, 074001

Abadie, J., et al. 2010, Class. Quantum Grav., 27, 173001, arXiv:1003.2480

Abadie, J., et al. 2010, Class. Quantum Grav., 27, 173001

Abbott, B. P., et al. 2016a, Phys. Rev. Lett., 116, 241103

—. 2016b, Phys. Rev. Lett., 116, 061102

—. 2016c

Acernese, F., et al. 2015, Class. Quantum Grav., 32, 024001

Agathos, M., Meidan, J., Pozzo, W. D., Li, T. G. F., Tompitak, M., Veitch, J., Vitale, S., & Broeck, C. V. D. 2015, Phys. Rev. D, 92, 023012

Ajith, P. 2011, Phys. Rev. D, 84, 084037

Anderson, M., et al. 2008, Phys. Rev. Lett., 100, 191101

Ansorg, M., Kleinwachter, A., & Meinel, R. 2003, Astron.Astrophys., 405, 711

Arnowitt, R., Deser, S., & Misner, C. W. 1962, in Gravitation: An Introduction to Current Research, ed. L. Witten (New York: Wiley), 227–265

Ashtekar, A., Beetle, C., & Lewandowski, J. 2001, Phys. Rev. D, 64, 044016

Ashtekar, A., & Krishnan, B. 2003, Phys. Rev. D, 68, 104030

Baiotti, L., Damour, T., Giacomazzo, B., Nagar, A., & Rezzolla, L. 2010, Phys. Rev. Lett., 105, 261101

Baiotti, L., Damour, T., Giacomazzo, B., Nagar, A., & Rezzolla, L. 2011, Phys. Rev. D, 84, 024017

Baiotti, L., & Rezzolla, L. 2016

Baumgarte, T. W., O'Murchadha, N., & Pfeiffer, H. P. 2007, Phys. Rev. D, 75, 044009

Baumgarte, T. W., & Shapiro, S. L. 2009, Phys. Rev. D, 80, 064009

—. 2010, Numerical Relativity: Solving Einstein's Equations on the Computer (New York: Cambridge University Press)

Baumgarte, T. W., Shapiro, S. L., & Shibata, M. 2000, Astrophys. J. Lett., 528, L29

Benacquista, M. J., & Downing, J. M. 2013, Living Rev. Rel., 16, 4

Bernuzzi, S., Dietrich, T., Tichy, W., & Bruegmann, B. 2014, Phys. Rev. D, 89, 104021

Bernuzzi, S., Nagar, A., Dietrich, T., & Damour, T. 2015, Phys. Rev. Lett., 114, 161103

Berti, E., et al. 2015, Class. Quant. Grav., 32, 243001

Bildsten, L., & Cutler, C. 1992, Astrophys. J., 400, 175

Blanchet, L. 2006, Living Rev. Rel., 9, 4

—. 2011, Fundam.Theor.Phys., 162, 125

—. 2014, Living Rev. Rel., 17, 2

Bode, T., Shoemaker, D., Herrmann, F., & Hinder, I. 2008, Phys. Rev. D, 77, 44027

Boyle, M., Brown, D. A., Kidder, L. E., Mroué, A. H., Pfeiffer, H. P., Scheel, M. A., Cook, G. B., & Teukolsky, S. A. 2007, Phys. Rev. D, 76, 124038

Boyle, M., Buonanno, A., Kidder, L. E., Mroué, A. H., Pan, Y., et al. 2008, Phys. Rev. D, 78, 104020

Brown, D. A., Harry, I., Lundgren, A., & Nitz, A. H. 2012, Phys. Rev. D, 86, 084017

Brown, J. D., & York, J. W. 1993, Phys. Rev. D, 47, 1407

Buchman, L. T., Pfeiffer, H. P., Scheel, M. A., & Szilágyi, B. 2012, Phys. Rev. D, 86, 084033

Buonanno, A. 2007, in Les Houches Summer School - Session 86: Particle Physics and Cosmology: The Fabric of Spacetime Les Houches, France, July 31-August 25, 2006

Buonanno, A., & Damour, T. 1999, Phys. Rev. D, 59, 084006

Buonanno, A., Kidder, L. E., Mroué, A. H., Pfeiffer, H. P., & Taracchini, A. 2011a, Phys. Rev. D, 83, 104034

Buonanno, A., Kidder, L. E., Mroué, A. H., Pfeiffer, H. P., & Taracchini, A. 2011b, Phys. Rev. D, 83, 104034

Canizares, P., Field, S. E., Gair, J., Raymond, V., Smith, R., & Tiglio, M. 2015, Phys. Rev. Lett., 114, 071104

Cardoso, V., Gualtieri, L., Herdeiro, C., & Sperhake, U. 2014

Carroll, S. 2003, Spacetime and Geometry: An Introduction to General Relativity (New York: Addison Wesley)

Caudill, M., Cook, G. B., Grigsby, J. D., & Pfeiffer, H. P. 2006, Phys. Rev. D, 74, 064011

Chatziioannou, K., Yagi, K., Klein, A., Cornish, N., & Yunes, N. 2015, Phys. Rev. D, 92, 104008

Chawla, S., Anderson, M., Besselman, M., Lehner, L., Liebling, S. L., et al. 2010, Phys. Rev. Lett., 105, 111101

Christodoulou, D. 1970, Phys. Rev. Lett., 25, 1596

Chu, T. 2014, Phys. Rev. D, 89, 064062

Chu, T., Pfeiffer, H. P., & Scheel, M. A. 2009, Phys. Rev. D, 80, 124051

Chu, T., et al. 2015

Cook, G. B. 2002, Phys. Rev. D, 65, 084003

Cook, G. B., & Pfeiffer, H. P. 2004, Phys. Rev. D, 70, 104016

Cook, G. B., Shapiro, S. L., & Teukolsky, S. A. 1994, Astrophys. J., 422, 227

Cook, G. B., & Whiting, B. F. 2007, Phys. Rev. D, 76, 041501(R)

Dain, S., Lousto, C. O., & Zlochower, Y. 2008, Phys. Rev. D, 78, 024039

Damour, T., Nagar, A., Pollney, D., & Reisswig, C. 2012, Phys. Rev. Lett., 108, 131101

Damour, T., Nagar, A., & Villain, L. 2012, Phys. Rev. D, 85, 123007

Deaton, M. B., et al. 2013, Astrophys. J., 776, 47

Del Pozzo, W., Li, T. G. F., Agathos, M., Van Den Broeck, C., & Vitale, S. 2013, Phys. Rev. Lett., 111, 071101

Dietrich, T., Bernuzzi, S., Ujevic, M., & Brügmann, B. 2015a, Phys. Rev. D, 91, 124041

Dietrich, T., Moldenhauer, N., Johnson-McDaniel, N. K., Bernuzzi, S., Markakis, C. M., Bruegmann, B., & Tichy, W. 2015b, Phys. Rev. D, 92, 124007

Dimmelmeier, H., Stergioulas, N., & Font, J. A. 2006, Mon. Not. Roy. Astr. Soc., 368, 1609

Dionysopoulou, K., Alic, D., & Rezzolla, L. 2015, Phys. Rev., D92, 084064

Duez, M. D., Foucart, F., Kidder, L. E., Ott, C. D., & Teukolsky, S. A. 2010, Class. Quantum Grav., 27, 114106

Duez, M. D., Foucart, F., Kidder, L. E., Pfeiffer, H. P., Scheel, M. A., & Teukolsky, S. A. 2008, Phys. Rev. D, 78, 104015

East, W. E., Paschalidis, V., & Pretorius, F. 2015

East, W. E., Pretorius, F., & Stephens, B. C. 2012a, Phys. Rev. D, 85, 124009

—. 2012b, Phys. Rev. D, 85, 124009

East, W. E., Ramazanoglu, F. M., & Pretorius, F. 2012c, Phys. Rev. D, 86, 104053

Eichler, D., Livio, M., Piran, T., & Schramm, D. N. 1989, Nature, 340, 126

Einstein, A. 1915, Sitzungsber. Preuss. Akad. Wiss. Berlin (Math. Phys.), 1915, 778, [Addendum: Sitzungsber. Preuss. Akad. Wiss. Berlin (Math. Phys.)1915,799(1915)]

Etienne, Z. B., Liu, Y. T., Paschalidis, V., & Shapiro, S. L. 2012, Phys. Rev. D, 85, 064029

Etienne, Z. B., Liu, Y. T., Shapiro, S. L., & Baumgarte, T. W. 2009, Phys. Rev., D79, 044024

Etienne, Z. B., Paschalidis, V., & Shapiro, S. L. 2012, Phys. Rev. D, 86, 084026

Faber, J. A., Baumgarte, T. W., Shapiro, S. L., Taniguchi, K., & Rasio, F. A. 2006, Phys. Rev., D73, 024012

Fan, X., & Hendry, M. 2015

Foucart, F. 2012, Phys. Rev. D, 86, 124007

Foucart, F., Duez, M. D., Kidder, L. E., Scheel, M. A., Szilágyi, B., & Teukolsky, S. A. 2012, Phys. Rev. D, 85, 044015

Foucart, F., Duez, M. D., Kidder, L. E., & Teukolsky, S. A. 2011, Phys. Rev. D, 83, 024005

Foucart, F., Kidder, L. E., Pfeiffer, H. P., & Teukolsky, S. A. 2008, Phys. Rev. D, 77, 124051

Foucart, F., et al. 2013a, Phys. Rev. D, 87, 084006

—. 2013b, Phys. Rev. D, 88, 064017

—. 2014, Phys. Rev. D, 90, 024026

—. 2015, Phys. Rev. D, 91, 124021

Garat, A., & Price, R. H. 2000, Phys. Rev. D, 61, 124011

Giacomazzo, B., Rezzolla, L., & Baiotti, L. 2011, Phys. Rev. D, 83, 044014

Gold, R., Bernuzzi, S., Thierfelder, M., Brugmann, B., & Pretorius, F. 2012, Phys. Rev. D, 86, 121501

Gourgoulhon, E. 2007, 3+1 Formalism and Bases of Numerical Relativity

Gourgoulhon, E., & Bonazzola, S. 1994, Classical and Quantum Gravity, 11, 443

Gourgoulhon, E., Grandclément, P., Taniguchi, K., Marck, J.-A., & Bonazzola, S. 2001, Phys. Rev. D, 63, 064029

Haas, R., et al. 2016, Phys. Rev., D93, 124062

Harry, G. M. 2010, Class. Quantum Grav., 27, 084006

Hemberger, D. A., Scheel, M. A., Kidder, L. E., Szilágyi, B., Lovelace, G., Taylor, N. W., & Teukolsky, S. A. 2013, Class. Quantum Grav., 30, 115001

Henriksson, K., Foucart, F., Kidder, L. E., & Teukolsky, S. A. 2016, Class. Quant. Grav., 33, 105009

Hinderer, T., Lackey, B. D., Lang, R. N., & Read, J. S. 2010, Phys. Rev. D, 81, 123016

Hotokezaka, K., Kiuchi, K., Kyutoku, K., Muranushi, T., Sekiguchi, Y., Shibata, M., & Taniguchi, K. 2013, Phys. Rev. D, 88, 044026

Hotokezaka, K., Kyutoku, K., Okawa, H., Shibata, M., & Kiuchi, K. 2011, Phys. Rev. D, 83, 124008

Hulse, R. A., & Taylor, J. H. 1975a, Astrophys. J., 195, L51

—. 1975b, Astrophys. J., 195, L51

Jiang, G.-S., & Shu, C.-W. 1996, J. Comput. Phys., 126, 202

Johnson-McDaniel, N. K., Yunes, N., Tichy, W., & Owen, B. J. 2009, Phys. Rev. D, 80, 124039

Joshi, B. C. 2013, Int. J. Mod. Phys., D22, 1341008

Kastaun, W., Galeazzi, F., Alic, D., Rezzolla, L., & Font, J. A. 2013, Phys. Rev. D, 88, 021501

Kawaguchi, K., Kyutoku, K., Nakano, H., Okawa, H., Shibata, M., & Taniguchi, K. 2015, Phys. Rev. D, 92, 024014

Kawaguchi, K., Kyutoku, K., Shibata, M., & Tanaka, M. 2016, Astrophys. J., 825, 52

Kelly, B. J., Tichy, W., Zlochower, Y., Campanelli, M., & Whiting, B. F. 2010, Class. Quant. Grav., 27, 114005

Kidder, L. E., Scheel, M. A., & Teukolsky, S. A. 2001, Phys. Rev. D, 64, 064017

Kidder, L. E., Scheel, M. A., Teukolsky, S. A., Carlson, E. D., & Cook, G. B. 2000, Phys. Rev. D, 62, 084032

Kiuchi, K., CerdÃą-DurÃąn, P., Kyutoku, K., Sekiguchi, Y., & Shibata, M. 2015a, Phys. Rev., D92, 124034

Kiuchi, K., Sekiguchi, Y., Kyutoku, K., & Shibata, M. 2012, Class. Quantum Grav., 29, 124003

Kiuchi, K., Sekiguchi, Y., Kyutoku, K., Shibata, M., Taniguchi, K., & Wada, T. 2015b, Phys. Rev. D, 92, 064034

Kiuchi, K., Sekiguchi, Y., Shibata, M., & Taniguchi, K. 2010, Phys. Rev. Lett., 104, 141101

Kozai, Y. 1962, Astron. J., 67, 591

Kyutoku, K., Ioka, K., & Shibata, M. 2013, arXiv:1305.6309

Kyutoku, K., Shibata, M., & Taniguchi, K. 2010, Phys. Rev. D, 82, 044049

Lackey, B. D., Kyutoku, K., Shibata, M., Brady, P. R., & Friedman, J. L. 2012, Phys. Rev. D, 85, 044061

Lee, W. H., Ramirez-Ruiz, E., & van de Ven, G. 2010, Astrophys. J., 720, 953

Lehner, L., & Pretorius, F. 2014, Ann. Rev. of Astron. & Astroph., 52, 661

Li, L.-X., & Paczynski, B. 1998, Astrophys. J., 507, L59

Lichnerowicz, A. 1944, J. Math Pures et Appl., 23, 37

Lindblom, L., Scheel, M. A., Kidder, L. E., Owen, R., & Rinne, O. 2006, Class. Quantum Grav., 23, S447

Liu, X.-D., Osher, S., & Chan, T. 1994, J. Comput. Phys., 115, 200

Liu, Y. T., Shapiro, S. L., Etienne, Z. B., & Taniguchi, K. 2008, Phys. Rev., D78, 024012

Lo, K.-W., & Lin, L.-M. 2011, Astrophys.J., 728, 12

Lorimer, D. R. 2008, Living Rev. Rel., 11, 8

Lovelace, G. 2009, Class. Quantum Grav., 26, 114002

Lovelace, G., Boyle, M., Scheel, M. A., & Szilágyi, B. 2012, Class. Quantum Grav., 29, 045003

Lovelace, G., Duez, M. D., Foucart, F., Kidder, L. E., Pfeiffer, H. P., Scheel, M. A., & Szilágyi, B. 2013, Class. Quantum Grav., 30, 135004

Lovelace, G., Owen, R., Pfeiffer, H. P., & Chu, T. 2008, Phys. Rev. D, 78, 084017

Lovelace, G., Scheel, M. A., & Szilágyi, B. 2011, Phys. Rev. D, 83, 024010

Lovelace, G., et al. 2015, Class. Quantum Grav., 32, 065007

Lyne, A., Burgay, M., Kramer, M., Possenti, A., Manchester, R., et al. 2004, Science, 303, 1153

M. A. Scheel, M. Boyle, T. Chu, L. E. Kidder, K. D. Matthews and H. P. Pfeiffer. 2009, Phys. Rev. D, 79, 024003

MacDonald, I., Mroué, A. H., Pfeiffer, H. P., Boyle, M., Kidder, L. E., Scheel, M. A., Szilágyi, B., & Taylor, N. W. 2013, Phys. Rev. D, 87, 024009

MacDonald, I., Nissanke, S., & Pfeiffer, H. P. 2011, Class. Quantum Grav., 28, 134002

Marronetti, P., & Matzner, R. A. 2000, Phys. Rev. Lett., 85, 5500

Marronetti, P., & Shapiro, S. L. 2003, Phys. Rev. D, 68, 104024

Matsushima, T., & Marcus, P. S. 1995, J. Comput. Phys., 120, 365

Matzner, R. A., Huq, M. F., & Shoemaker, D. 1998, Phys. Rev. D, 59, 024015

Metzger, B. D., & Berger, E. 2012, Astrophys. J., 746, 48

Misner, C. W., Thorne, K. S., & Wheeler, J. A. 1973, Gravitation (New York, New York: Freeman)

Mroue, A. H., et al. 2013, Phys. Rev. Lett., 111, 241104

Muhlberger, C. D., Nouri, F. H., Duez, M. D., Foucart, F., Kidder, L. E., et al. 2014, Phys. Rev. D, 90, 104014

Murchadha, N. Ó., & York, Jr., J. W. 1974, Phys. Rev. D, 10, 428

Nakar, E. 2007, Phys. Rep., 442, 166

Narayan, R., Paczynski, B., & Piran, T. 1992, Astrophys. J. Lett., 395, L83

Neilsen, D., Liebling, S. L., Anderson, M., Lehner, L., O'Connor, E., & Palenzuela, C. 2014, Phys. Rev. D, 89, 104029

Ossokine, S., Boyle, M., Kidder, L. E., Pfeiffer, H. P., Scheel, M. A., & SzilÃągyi, B. 2015a, Phys. Rev. D, 92, 104028

Ossokine, S., Foucart, F., Pfeiffer, H. P., Boyle, M., & Szilágyi, B. 2015b, arXiv:1506.01689

Ossokine, S., Kidder, L. E., & Pfeiffer, H. P. 2013, Phys. Rev. D, 88, 084031

Owen, B. J., & Sathyaprakash, B. S. 1999, Phys. Rev. D, 60, 022002

Owen, R. 2007, PhD thesis, California Institute of Technology

Palenzuela, C., Lehner, L., Liebling, S. L., Ponce, M., Anderson, M., Neilsen, D., & Motl, P. 2013, Phys. Rev., D88, 043011

Palenzuela, C., Lehner, L., Ponce, M., Liebling, S. L., Anderson, M., Neilsen, D., & Motl, P. 2013, Phys. Rev. Lett., 111, 061105

Palenzuela, C., Liebling, S. L., Neilsen, D., Lehner, L., Caballero, O. L., O'Connor, E., & Anderson, M. 2015, prd, 92, 044045

Pan, Y., Buonanno, A., Taracchini, A., Kidder, L. E., Mroue, A. H., et al. 2013, Phys. Rev. D, 89, 084006

Pannarale, F., Berti, E., Kyutoku, K., Lackey, B. D., & Shibata, M. 2015

Paschalidis, V., Etienne, Z. B., & Shapiro, S. L. 2013, Phys. Rev. D, 88, 021504

Paschalidis, V., Ruiz, M., & Shapiro, S. L. 2015, Astrophys. J., 806, L14

Patricelli, B., Razzano, M., Cella, G., Fidecaro, F., Pian, E., Branchesi, M., & Stamerra, A. 2016, arXiv preprint arXiv:1606.06124

Peters, P. C. 1964, Phys. Rev., 136, B1224

Peters, P. C., & Mathews, J. 1963, Phys. Rev., 131, 435

Pfeiffer, H. P. 2012, Class. Quantum Grav., 29, 124004

Pfeiffer, H. P., Brown, D. A., Kidder, L. E., Lindblom, L., Lovelace, G., & Scheel, M. A. 2007, Class. Quantum Grav., 24, S59

Pfeiffer, H. P., Cook, G. B., & Teukolsky, S. A. 2002, Phys. Rev. D, 66, 024047

Pfeiffer, H. P., Kidder, L. E., Scheel, M. A., & Teukolsky, S. A. 2003, Comput. Phys. Commun., 152, 253

Pfeiffer, H. P., & York, J. W. 2003, Phys. Rev. D, 67, 044022

Pfeiffer, H. P., & York Jr., J. W. 2005, Phys. Rev. Lett., 95, 091101

Piran, T., Nakar, E., & Rosswog, S. 2013, Mon. Not. Roy. Astr. Soc., 430, 2121

Postnov, K. A., & Yungelson, L. R. 2014, Living Rev. Rel., 17, 3

Pretorius, F. 2005, Phys. Rev. Lett., 95, 121101

—. 2006, Class. Quantum Grav., 23, S529

Radice, D., Galeazzi, F., Lippuner, J., Roberts, L. F., Ott, C. D., & Rezzolla, L. 2016, ArXiv e-prints

Read, J. S., Markakis, C., Shibata, M., Uryū, K., Creighton, J. D. E., & Friedman, J. L. 2009, Phys. Rev. D, 79, 124033

Rezzolla, L., Baiotti, L., Giacomazzo, B., Link, D., & Font, J. A. 2010, Class. Quant. Grav., 27, 114105

Rezzolla, L., Giacomazzo, B., Baiotti, L., Granot, J., Kouveliotou, C., et al. 2011, Astrophys.J., 732, L6

Rieth, R. 1997, in Mathematics of Gravitation. Part II. Gravitational Wave Detection, ed. A. Królak (Polish Academy of Sciences, Institute of Mathematics, Warsaw), 71–74

Roberts, L. F., Kasen, D., Lee, W. H., & Ramirez-Ruiz, E. 2011, Astrophys. J. Lett., 736, L21

Rosswog, S., Piran, T., & Nakar, E. 2013, Mon. Not. Roy. Astr. Soc., 430, 2585

Scheel, M. A., Giesler, M., Hemberger, D. A., Lovelace, G., Kuper, K., Boyle, M., Szilágyi, B., & Kidder, L. E. 2015, Class. Quantum Grav., 32, 105009

Scheel, M. A., Kidder, L. E., Lindblom, L., Pfeiffer, H. P., & Teukolsky, S. A. 2002, Phys. Rev. D, 66, 124005

Scheel, M. A., Pfeiffer, H. P., Lindblom, L., Kidder, L. E., Rinne, O., & Teukolsky, S. A. 2006, Phys. Rev. D, 74, 104006

Sekiguchi, Y., Kiuchi, K., Kyutoku, K., & Shibata, M. 2015, Phys. Rev. D, 91, 064059

Seto, N. 2013, Phys. Rev. Lett., 111, 061106

Shibata, M. 1998, Phys. Rev. D, 58, 024012

Shibata, M., & Taniguchi, K. 2008, Phys. Rev., D77, 084015

Shibata, M., Taniguchi, K., & Uryu, K. 2003, Phys. Rev., D68, 084020

Shibata, M., & Uryū, K. ō. 2000, prd, 61, 064001

Shibata, M., & Uryu, K. 2006, Phys. Rev., D74, 121503

—. 2007, Class. Quantum Grav., 24, S125

Somiya, K., & the KAGRA Collaboration. 2012, Class. Quantum Grav., 29, 124007

Stephens, B. C., East, W. E., & Pretorius, F. 2011, Astrophys.J., 737, L5

Szilágyi, B. 2014, Int. J. Mod. Phys. D, 23, 1430014

Szilágyi, B., Lindblom, L., & Scheel, M. A. 2009, Phys. Rev. D, 80, 124010

Tacik, N., et al. 2015, Phys. Rev. D, 92, 124012

Tanaka, M., Hotokezaka, K., Kyutoku, K., Wanajo, S., Kiuchi, K., Sekiguchi, Y., & Shibata, M. 2014, Astrophys. J, 780, 31

Taniguchi, K., Baumgarte, T. W., Faber, J. A., & Shapiro, S. L. 2006, Phys. Rev. D, 74, 041502

—. 2007, Phys. Rev. D, 75, 084005

Taracchini, A., et al. 2014, Phys. Rev. D, 89 (R), 061502

Taylor, J. H., & Weisberg, J. M. 1982, Astrophys. J., 253, 908

Teukolsky, S. A. 1998, Astrophys.J., 504, 442

The Virgo Collaboration. 2010, Advanced Virgo Baseline Design, vIRâĂŞ027AâĂŞ09

Thompson, T. A. 2011, Astrophys. J., 741, 82

Tichy, W. 2011, Phys. Rev. D, 84, 024041

—. 2012, Phys. Rev. D, 86, 064024

Tsatsin, P., & Marronetti, P. 2013

Tsokaros, A., Uryū, K., & Rezzolla, L. 2015, Phys. Rev. D, 91, 104030

Verkley, W. T. M. 1997, J. Comput. Phys., 136, 100

Walsh, D. M. 2007, Class. Quantum Grav., 24, 1911

Wanajo, S., Sekiguchi, Y., Nishimura, N., Kiuchi, K., Kyutoku, K., & Shibata, M. 2014, Astrophys.J.Lett., 789, L39

Worley, A., Krastev, P. G., & Li, B.-A. 2008

York, J. W. 1999, Phys. Rev. Lett., 82, 1350

York, Jr., J. W. 1979, in Sources of Gravitational Radiation, ed. L. L. Smarr, 83–126

York, Jr., J. W. 1979, in Sources of Gravitational Radiation, ed. L. L. Smarr (Cambridge, England: Cambridge University Press), 83–126